Symmetries and correlations in solids probed by ultrafast high-harmonic spectroscopy

Dissertation

zur Erlangung des mathematisch-naturwissenschaftlichen Doktorgrades

"Doctor rerum naturalium" (Dr.rer.nat.)

der Georg-August-Universität Göttingen

–

im Promotionsprogramm Physik

der Georg-August University School of Science (GAUSS)

vorgelegt von

Herrn Tobias Gutberlet

geb. Heinrich

aus Herford

Göttingen, 2023

Betreuungsausschuss

Prof. Dr. Claus Ropers, IV. Physikalisches Institut und
Max-Planck-Institut für Multidisziplinäre Naturwissenschaften

Prof. Dr. Stefan Mathias, I. Physikalisches Institut

PD Dr. Salvatore Manmana, Institut für Theoretische Physik

Mitglieder der Prüfungskommission

Referent:	Prof. Dr. Claus Ropers, IV. Physikalisches Institut und Max-Planck-Institut für Multidisziplinäre Naturwissenschaften
Korreferent:	Prof. Dr. Stefan Mathias, I. Physikalisches Institut

Weitere Mitglieder der Prüfungskommission

Apl. Prof. Dr. Alexander Egner, Institut für Nanophotonik

DP Dr. Salvatore Manmana, Institut für Theoretische Physik

Prof. Dr. Thomas Weitz, I. Physikalisches Institut

Prof. Dr. Martin Wenderoth, IV. Physikalisches Institut

Tag der mündlichen Prüfung: 17. August 2023

Nothing in life is to be feared, it is only to be understood

Marie Skłodowska Curie

Abstract

Novel material systems with correlated and tunable properties promise to push the boundaries of current information processing and energy management technologies. Their investigation requires simultaneous access to multiple degrees of freedom at the fundamental timescales of electronic and lattice dynamics. High-harmonic generation (HHG) in gases offers such capabilities via absorption spectroscopy while solid-state HHG can probe the material properties via the nonlinear generation process. Although promising intriguing insights, studies of correlated solid systems with HHG remain challenging. The typically high noise floor of gas-phase HHG prohibits experiments of subtle dynamics in solids. Moreover, in the field of solid-state HHG, the access to fundamental observables such as chirality requires further development. In this cumulative thesis, we address both challenges by realizing and applying high-sensitivity absorption spectroscopy with gas-phase HHG as well as introducing circularly polarized HHG in solids with threefold driving fields.

In the first publication we extend solid-state HHG to chiral symmetry probing. By employing threefold driving fields, we achieve a material-independent generation of circularly polarized harmonics. This enables the investigation of surface magnetism in MgO and crystalline chirality in quartz. Additionally, by rotating the optical field, we gain access to the solid's space group, enabling the probing of prominent symmetry-breaking effects like phase transitions.

In the second publication we introduce an advanced referencing method for noise reduction in transient absorption experiments with a gas-phase HHG source. In comparison to other machine learning approaches, an artificial neural network best captures the non-polynomial noise of the HHG source and increases the sensitivity to absorption changes by one order of magnitude. With its general applicability for broadband sources, the presented approach is highly transferable to other beamlines including attosecond HHG, plasma sources, and free-electron lasers.

In the final study presented as part of this thesis, we apply the novel referencing technique to study absorption spectra in the correlated material system $1T$-$TiSe_2$ with high-sensitivity. Combined with *ab-initio* calculations the spectra allow deducing various electronic and structural components with high precision. Laser excitation of the charge-density-wave phase in this material triggers two coherent phonon modes. By analyzing the spectral response of the atomic vibrations, the amplitude mode is distinguished from

an optical phonon mode and linked to electronic screening.

In their entirety, these results pave the way for future time-resolved studies of novel material systems. The presented circularly polarized HHG in solids holds potential applications in ultrafast magnetism or valleytronics. Moreover, the highly transferable referencing scheme enables investigations of weak absorption changes associated with correlated electronic, lattice, and spin degrees of freedom.

Contents

List of Figures

Symbols and Abbreviations

Symbol	Meaning	Unit
A, OD	absorption	OD
A_{1g}, A^*_{1g}	phonon modes	
a,b,c	lattice constants	Å
a, $\mathbf{a}$	fit parameters	
B	mini-batch	
b	bias	
C	cost function	
c	vacuum speed of light	$\mathrm{m\,s^{-1}}$
D	data set	
d	diameter	m
e	elementary charge	C
E	energy	eV
E	error	
E_g	energy gap	eV
$\mathbb{E}$	expectation value	
f_H, f_{XC}	Hartree-, exchange-correlation kernel	
F, $\mathbf{F}$	electric field	$\mathrm{V\,nm^{-1}}$
F	fluence	$\mathrm{mJ/cm^2}$
f, F	model function	
f	frequency	Hz
f	Fermi (-Dirac) function	
$\mathfrak{F}$	Fourier-transformation	
$\mathbf{G}$	reciprocal lattice vector	$\mathrm{m^{-1}}$
g	physical function	
$g_{\mathbf{q}}$	electron-phonon coupling strength	eV

h	Planck constant	$\mathrm{m^2 kg/s}$
$\hbar$	reduced Planck constant	$\mathrm{J\,s}$
I	intensity	$\mathrm{W\,m^{-2}}$
i	imaginary unit	
k, $\mathbf{k}$	wave number, wave vector	$\mathrm{m^{-1}}$
k	imaginary part of the refractive index	
L	sample thickness	$\mathrm{m^{-1}}$
L	number of neuron layers	
m_e	electron mass	kg
M	atomic mass	kg
N	crystal rotational symmetry	
N	total umber of electrons	
N_{atm}	number density of gas at 1 atm pressure	
n	real part of the refractive index	
n	electron density	$\mathrm{m^{-3}}$
$\underline{n}$	refractive index	
P	pressure	$\mathrm{N\,m^{-2}}$
P	power	W
$\hat{P}$	parity operator	
q	harmonic order	
$\mathbf{q}$	wave vector	$\mathrm{m^{-1}}$
R	reflectivity	
R	retardance	
r	radius	m
$\mathbf{r}$	position vector	m
r_e	classical electron radius	m
T	optical period	s
T	relaxation timescale	s
t	time	s
U	potential	eV
u	lattice distortion amplitude	Å
V	potential	eV
V	crystal volume	$\mathrm{m^3}$
v	velocity	$\mathrm{m\,s^{-1}}$

$\mathbf{w}$	weights	
x, y, z	distances	m
$\mathbf{x}$, $\mathbf{X}$	feature vector, feature matrix	
$\mathbf{y}$, $\mathbf{Y}$	observable vector, observable matrix	
z	neuron activation	
γ	Keldysh parameter	
γ	momentum parameter	
Δ	difference	
Δ_j^l	derivative	
δ	absorption (extraction) length	m
δ	Dirac delta function	
ε	dielectric function	$\mathrm{F\,m^{-1}}$
ε_0	vacuum permittivity	$\mathrm{F\,m^{-1}}$
η	ionization fraction	
η	learning rate	
θ	angle between electric field and crystal	rad
θ_{step}	step function	
λ	wavelength	nm
λ	regularization parameter	
μ	absorption coefficient	$\mathrm{m^{-1}}$
ρ	density	$\mathrm{m^{-3}}$
σ	activation function	
σ_ε	standard deviation (Gaussian noise)	
τ	time delay	fs
φ, ϕ	relative phase	rad
χ	linear response function	
χ_0	non-interacting electronic susceptibility	
ψ	wave function	
Ω	unit cell volume	$\mathrm{m^3}$
ω	optical (angular) frequency	Hz
∇	differential operator	

Abbreviation	**Meaning**
ARPES	angle-resolved photoemission spectroscopy
BBO	β-barium borate
BSE	Bethe-Salpeter equation
CB	conduction band
CCD	charge-coupled device
CDI	coherent diffractive imaging
CDW	charge density wave
DFT	density functional theory
DOS	density of states
FWHM	full-width-of-half-maximum
GD	gradient descent
GGA	generalized gradient approximation
H	harmonic
HH	high harmonic
HHG	high-harmonic generation
IP	independent particle approximation
KS	Kohn-Scham
(FP-)LAPW	(full-potential) linearized augmented plane wave method
LDA	loacal density approximation
LHC	left-handed circular
MAZEL-TOV	Mach-Eehnder-less for threefold optical virginia spiderwort
ML	machine learning
MSE	mean squared error
OPA	optical parametric amplifier
PLD	periodic lattice distortion
ReLU	rectified-linear-unit activation function
RHC	right-handed circular
RPA	random phase approximation
SGD	stochastic gradient descent
SHG	second harmonic generation
TDDFT	time-dependent density functional theory
TMDC	transition-metal dichalcogenide

VB	valance band
VUV	vacuum ultraviolet
XUV	extreme ultraviolet

Chapter 1

Introduction

Emergent functional properties present a new era in the field of solid-state research and open a rich playground for technologically relevant applications [1, 2]. The so-called quantum materials possess strong correlations or unique topological properties, which lead to a wealth of phenomena such as superconductivity [3, 4, 5], ultrafast metal-to-insulator transitions [6, 7], and charge density waves [8]. This scientific area was significantly expanded by the discovery of atomically thin graphene [9] which started the search for two-dimensional materials that show unconventional traits [10, 11, 12, 13]. In this ongoing research of the last two decades, materials with correlated properties have been extensively studied. Due to the strong link between electronic, spin, and structural degrees of freedom in such sample systems, utilization of probes with simultaneous access to multiple observables and the combined use of multiple tools rapidly expanded.

Particularly promising are time-resolved experiments that study the underlying microscopic mechanisms at their fundamental timescales in the picosecond to attosecond regime. Ultrafast versions of electron diffraction and microscopy [14, 15, 16], X-ray scattering [17, 18], photoemission [19, 20, 21, 22], and spectroscopy [23, 24] expand the toolbox of conventional control parameters like temperature, pressure, external electric fields, and doping. By introducing the time coordinate to experiments, a twofold goal is pursued. Real-time studies provide unique insights into material dynamics which allow to build a more thorough understanding of intricate material properties. In addition, the use of pulsed laser fields offer an unprecedented potential for control at ultrafast time scales. In this regard, great success was presented in disentangling charge order [20], understanding collective excitations such as phonon modes [25], observing hidden phases [26], realizing Floquet engineering [27, 28, 29], driving metal-to-insulator transitions [30, 31, 32],

and tracking ultrafast demagnetization [33]. However, many questions in the field of novel material systems have not been fully answered. In particular, correlated effects between multiple degrees of freedom, such as the details of the multifaceted driving forces that stabilize charge-density-wave states, remain unsolved.

By offering unmatched time resolution [34] and unique possibilities to measure a variety of different properties, time-resolved spectroscopy with the use of high-harmonic generation (HHG) is strongly expanding in the field of solid-state research. Here, light in the visible to extreme ultraviolet (XUV) or even soft X-ray region is generated through photon upconversion of intense laser fields in noble gases or solid media. Accelerated by the external laser field, the electrons in the generating medium gain momentum and release higher energy photons upon recombination when the field reverses. The emitted light from gas sources may be used for transient absorption spectroscopy with potential attosecond temporal resolution [35, 36]. Alternatively, solid-state HHG offers intrinsic information about the generating medium by the non-perturbative process or through subsequent absorption [37, 38, 39, 36]. Both experiments offer a wealth of information suited for studying novel quantum materials. In particular, by combining attosecond temporal and millielectronvolt energy resolution, transient absorption spectroscopy is a remarkable tool for band structure investigations. In addition, photon energies in the XUV region excite core level electrons, which allow studies of element specific dynamics such as the probing of spin transfer between atomic species [40, 41]. This tool set is complemented by solid-state HHG, which is an all-optical probe that poses fewer restrictions on sample preparation and vacuum conditions in comparison to techniques like photoemission spectroscopy. In contrast to classical spectroscopy, the HHG process spans the whole Brillouin zone and encodes full band structure information in the emitted light. At the same time, orientational information such as symmetry groups are easy to obtain and can be used to probe symmetry breaking effects which relate to ultrafast phase transitions [42, 43, 44, 45, 46, 47, 48, 49]. The various accessible observables of both techniques are summarized in Fig. 1.1 and include:

- Lattice: Collective excitations of individual phonon modes and the lattice temperature are accessible [50, 51, 52, 53, 54, 55, 56].

- Electronic: The relaxation of carriers including electrons, holes or excitons can be traced in real time [57, 58, 59, 60, 51, 61, 54, 55, 62, 63].

- Spin: Magnetization dynamics can be probed by circularly polarized high-harmonic radiation [40, 41, 64].
- Chirality: Circularly polarized light offers a probe of crystalline and molecular helicities [65, 66, 67].
- Symmetry: Crystal symmetries are probed by solid-state HHG through rotation of the driving field [68, 69, 70, 71].
- Element specificity: Absorption spectroscopy in the XUV regime probes element specific core levels [72, 73, 40, 51, 54].

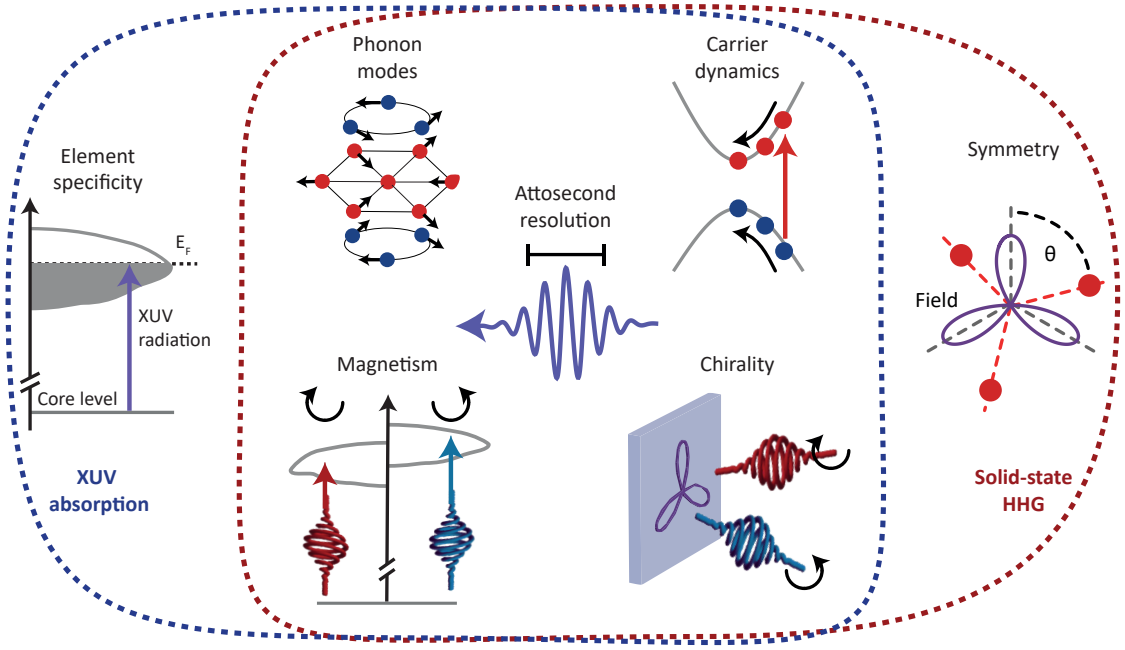

Figure 1.1: Observables in ultrafast spectroscopy with HHG sources. Solid-state HHG and XUV absorption spectroscopy with gas-phase HHG sources are versatile tools for the investigation of solid samples at potential attosecond time resolution. Both techniques offer simultaneous excess to electronic, structural, and spin degrees of freedom. In addition, absorption spectroscopy can be used to obtain element-specific information while solid-state HHG allows probing of the crystal symmetry.

Most of the different degrees of freedom have already been studied by time-resolved versions of absorption spectroscopy and solid-state HHG. While attosecond studies are

achievable for both techniques [74, 39], a femtosecond temporal resolution is already sufficient to study a broad range of phenomena in solids, such as lattice dynamics. Since simultaneous access to multiple observables is key in the field of strongly correlated materials, spectroscopy with HHG sources is ideally suited for the investigation of quantum materials.

Despite the many great works that have been presented in the context of HHG and quantum materials, this field warrants further development. In XUV absorption spectroscopy, the biggest challenge is the high noise floor which is induced by the strong intensity fluctuations of HHG sources. In comparison to spectroscopy in the visible regime, the sensitivity to small changes of the XUV spectrum is significantly worse. A second challenge in the study of strongly correlated materials is the extraction of material properties from the absorption coefficient. The complex entangled spectra are not trivial to decode and require further methodical and theoretical advances in order to take full advantage of the rich material information [75]. Likewise, solid-state HHG is still an emerging field and many applications have not yet been fully developed. As an example, the generation of circularly polarized harmonics, which is well established for gas sources, has not been completely transferred to the field of solid targets. In order to study magnetization dynamics and chirality, an efficient and reliable means of generating circularly polarized high harmonics is required.

In this study, we broadly expand the current state of HHG as a probe for solid-state research. Specifically, the field of solid-state HHG is extended to the investigation of symmetries with threefold driving fields. This allows for efficient generation of circularly polarized high harmonics and studies of crystalline chirality, magnetization, and the pseudo spin in two-dimensional materials [11, 76]. Our work opens the pathway for time-resolved studies of these observables in complex and correlated material systems with solid-state HHG. In the context of XUV absorption spectroscopy, we introduce a new method for tenfold noise reduction by using a reference spectrum in combination with machine learning. This significant improvement of the sensitivity facilitates experiments of small spectral changes that occur in weakly excited materials. We apply the presented method to the transition-metal dichalcogenide 1T-$TiSe_2$ in order to resolve its charge-density-wave dynamics. Here, we address the additional problem of disentangling various electronic and structural contributions in the data by performing *ab-initio* simulations of the spectra.

Outline

The presented work is a multi-faceted, interdisciplinary, cumulative thesis based on three original publications shown in chapters 6, 7, and 8. Therefore, extensive background information is provided in chapters 2 to 5 in order to put the results of the presented publications into context. Each publication is preceded by an individual introduction and includes a methods section, experimental results, as well as a discussion.

Chapter 2 introduces the theory of HHG in the gas and solid phase. In the succeeding chapter 3 the principles of absorption spectroscopy with a focus on the XUV spectrum is presented. The theory of *ab-initio* calculations of core level spectra will be discussed. In chapter 4 the basics of machine learning are presented along with neural network methods. Furthermore, chapter 5 briefly introduces the basics of charge density wave formation and highlights relevant time-resolved studies on the transition-metal dichalcogenide (TMDC) $1T$-$TiSe_2$.

Chapter 6 presents experimental realization of generating circularly polarized high-harmonics in solid systems. Magnesium oxide and quartz have been irradiated with a threefold symmetric driving field to generate harmonics in the vacuum-ultraviolet (VUV) regime. By comparing left-handed-circularly and right-handed-circularly polarized radiation, surface magnetism in MgO and crystalline chirality in quartz could be observed along with the crystal symmetries.

Chapter 7 discusses machine learning enhanced referencing for XUV absorption spectroscopy. By introducing a reference spectrum which traces the HHG source fluctuations, the sensitivity to weak absorption changes was substantially improved. The combined use of a reference spectrum and a neural network lead to a reduction of the noise level by more than one order of magnitude.

Chapter 8 presents high-sensitivity transient absorption spectroscopy of the strongly correlated material $1T$-$TiSe_2$. By spectrally separating the contribution of different phonon modes, the charge density related amplitude mode was studied. With the help of *ab-initio* simulations, the real space displacements of the amplitude mode were extracted.

All of the presented results are summarized in chapter 9 and put in perspective. Finally, an outlook of this work within the field of ultrafast spectroscopy with HHG sources is discussed.

Den langen Weg zur Promotion haben mich meine Freunde aus dem ersten Semester begleitet. Ich möchte mich bei euch für die vielen tollen Stunden und die Unterstützung während des Studiums bedanken.

Chapter 2

High-harmonic generation in gases and solids

Soon after the demonstration of the first working rubidium laser [77], Franken *et al.* and shortly after Kaiser *et al.* showed the conversion of two photons to one photon with doubled energy, which is now termed second harmonic generation (SHG) [78, 79]. This discovery is seen as the beginning of the field of nonlinear optics which describes processes in material systems that scale nonlinearly to the applied optical field strength [80]. In this manner, the second harmonic generation is governed by the quadratic term of the atomic susceptibility which is a perturbative correction of the linear response. More generally, photon upconversion to multiples of the laser frequency is referred to as harmonic radiation. In the perturbative regime with laser intensities in the range of $10^8\,\mathrm{W/cm^2}$, the intensity of the q^{th} harmonic scales with the fundamental intensity by the power law I^q [81]. As the nonlinear conversion efficiency decreases exponentially with higher orders [80] the perturbative harmonic generation is practically limited to order of less than five [82].

The high-harmonic generation (HHG) refers to non-perturbatively generated higher orders of harmonics which can cover the visible to X-ray region [83, 84] and were first observed in the 1980s [85, 86] with a noble gas medium. This process was made accessible by the development of high-intensity pulsed laser sources based on chirped pulse amplification [87]. These light sources are capable of extremely high intensities of more than $10^{13}\,\mathrm{W/cm^2}$ at which the influence of the light field on the electrons becomes comparable to the atomic Coulomb potential [88]. Today, HHG is feasible in a vast variety of media including gas, solid and even liquid phase [37, 89]. Figure 2.1(a) depicts HHG from noble gases with a femtosecond (fs) infrared driving laser at typical peak intensities of $I \approx 10^{14}\,\mathrm{W/cm^2}$. In solid targets [Fig. 2.1(a), bottom], which possess a much

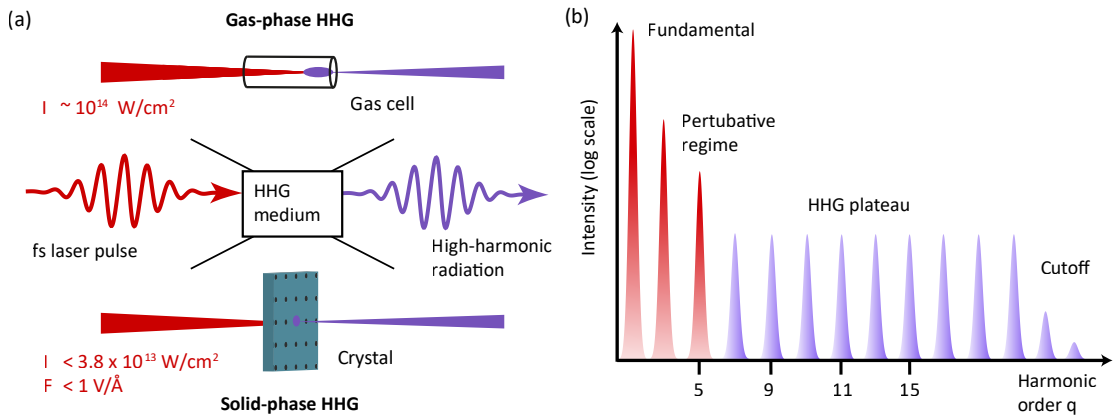

Figure 2.1: High-harmonic generation (HHG) in gas and solid media. (a) HHG is achieved by a fs laser pulse at high intensities (I) in various media. Noble gasses in a cell as well as solid crystals can be used to generate high-harmonic radiation. (b) A typical HHG spectrum showing perturbative harmonics and a plateau of high harmonics.

smaller damage threshold, HHG is usually achieved at lower field strengths of $F < 1\,\mathrm{V/\AA}$ which correspond to intensities of $I < 3.8 \times 10^{13}\,\mathrm{W/cm^2}$ [37]. A typical high-harmonic spectrum is depicted in Fig. 2.1(b). It shows the rapid exponential intensity decrease of perturbative harmonics followed by a plateau of similar intense high harmonics that span up to a certain cutoff energy.

High-harmonic emission from gas sources is fairly well understood and routinely used in numerous experiments for absorption spectroscopy [35, 90], nanoscale imaging [91], and photoemission [92, 93]. It is the workhorse of lab scale core-level spectroscopy and presents the forefront of attosecond materials studies. The microscopic mechanism is well-described by the semiclassical three-step model which captures all aspects of the HHG process [88, 94, 95, 96]. In contrast to gaseous media, there is no unified model for HHG in solids and different processes simultaneously contribute [37, 38]. In the literature, two mechanisms are currently discussed: The inter- and intra-band mechanism. The interband mechanism is the extension of the three-step model to the solid phase and describes the emission of light by conceptually similar processes. On the other hand, the intraband mechanism results from currents within a nonlinear band dispersion only found in the solid phase. So far no unified picture has emerged and the mechanisms of HHG in solids remain an active research field.

In the following, the microscopic generation mechanisms of high harmonics from gases and solids are elaborated, along with a discussion of the harmonic properties.

2.1 The three-step model of high-harmonic generation

The most intuitive way, in which high-harmonic generation is explained for the gas phase is the semiclassical three-step model which is also called the recollision model [88, 94, 95, 96]. It describes the three steps: Excitation, acceleration, and recombination of an electron in an intense laser field, whereas the last process is accompanied by the emission of the high-harmonic radiation. This model can be, to some degree, extended to describe the HHG in solid-state media [37, 38]. However, the real-space description that is commonly used for describing the gas-phase HHG cannot be easily transferred to the condensed phase. In translational symmetric solid-state systems, the electrons are described by delocalized Bloch wave functions and form energy bands. This band structure is represented in the momentum space. Therefore, HHG in solids is best described in the momentum space, but it was shown that a real space picture based on localized wave functions can also be used to accurately describe the mechanism. In this representation, solid-state HHG shows many similarities with the recollision model of the gas phase.

In this section, we will discuss the gas-phase HHG and the interband mechanism of solid-state HHG in the real and momentum space. The intraband currents of solid-state HHG result from acceleration of electrons within the bands and are discussed in Sec. 2.1.2. All three steps of the recollision model will first be described for the gas-phase HHG followed by a discussion of differences in solid media. Figure 2.2 illustrates the three-step model in real and momentum space and can be used as a guide through the individual steps.

2.1.1 Excitation

At first, the intense laser excites a bound electron in the generating medium. In the case of gases, the electron is ionized through the deformation of the atomic potential by the laser field as shown in Fig. 2.2(a). Superimposing atomic coulomb attraction and the external electric field of the laser $F_L(t)$ yields the total potential of the electron:

$$U_{tot}(r,t) = -\frac{e^2}{4\pi\varepsilon_0 r} + eF_L(t)r, \tag{2.1}$$

where r is the distance of the electron to the nucleus. By lowering of the potential barrier the time dependent external field ionizes the bound electron via different mechanisms.

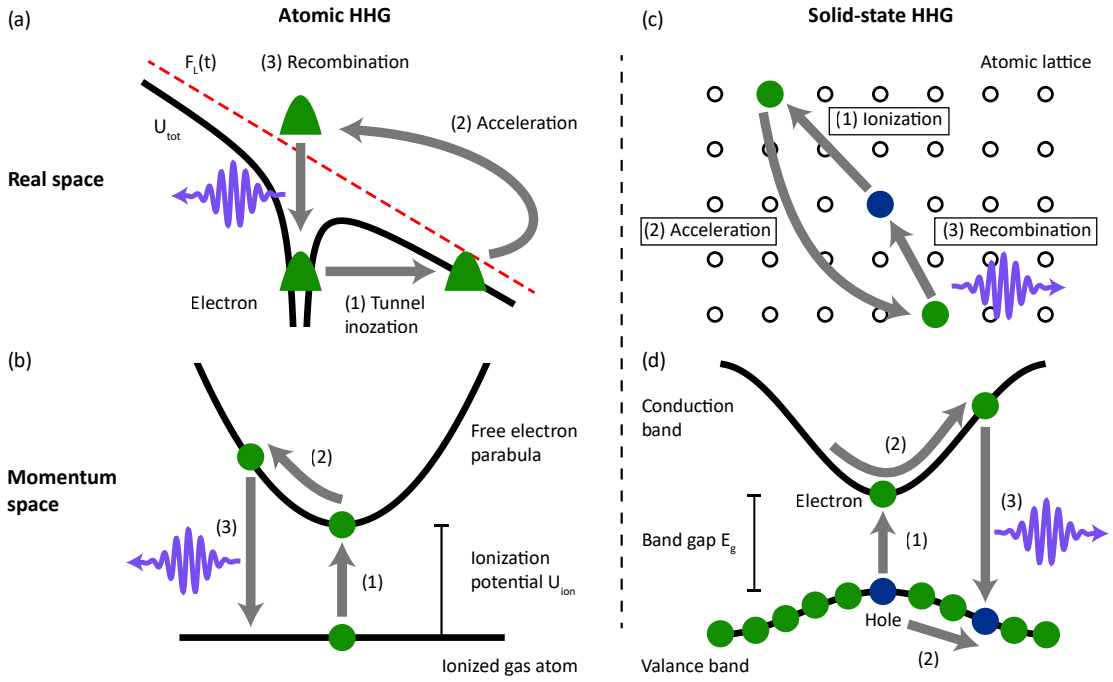

Figure 2.2: Three-step model of high-harmonic generation in gases and solids. (a) and (b) In the gas phase the bound electron is ionized by the laser and subsequently accelerated in free space. In the third step it recombines with the parent ion. (c) In solid media, the electron is excited to a potentially different lattice site leaving behind a hole. Both quasi-particles are accelerated and recombine eventually. (d) In momentum space, the electron is excited from the valance to the conduction band and the acceleration is equivalent to a propagation along the bands.

The exact process depends on the intensity $I_L = |F_L|^2$ and the frequency ω_L of the driving laser and is estimated by the *Keldysh parameter* [97]

$$\gamma = \sqrt{\frac{U_{Ion}}{2U_p}}, \tag{2.2}$$

with the material dependent ionization potential U_{Ion} and the ponderomotive potential $U_p = \frac{e^2 I_L}{4 m_e \omega_L^2}$. Here, e is the electron charge and m_e its mass. Equation 2.2 balances the strength of the atomic binding potential in terms of U_{Ion} and the energy of an electron in the laser field expressed by the ponderomotive energy. The latter is defined as the cycle-averaged quiver energy of a free electron in an alternating electromagnetic field. At $\gamma >> 1$, the atomic potential is only perturbatively disturbed and multi-photon ionization dominates. On the contrary, at $\gamma \approx 1$, the energy of the electric field and the atomic attraction are of similar magnitude and tunnel ionization is predominant. Even larger

field strengths ($\gamma << 1$) allow for over-the-barrier ionization of electrons and can lead to excitation of deeper-level electrons. Most experiments that use harmonic emission as a probe rely on moderate intensities of approximately $I = 10^{14}\,\mathrm{W/cm^2}$ in the tunnel ionization range. Electrons can, in principle, be ionized at various tunnel times t_{tunnel}, but the tunnel probability strongly depends on the barrier height and the shape of the potential. Both are determined by the alternating laser field and the highest tunnel probability is reached around the intensity peaks every laser half-cycle.

In solids, the initial electron excitation step of the recollision model is the tunneling of a conduction band electron to the valance band. In a simplified picture depicted in Fig. 2.2(d), the band structure consists of a single valence band that is completely filled with electrons and one empty conduction band. In semiconductors and insulators, these bands are separated by the band gap energy E_g. When the electron is extracted from the conduction band, it leaves an electron hole that is screened by the remaining electrons and can be treated as a quasiparticle with a positive charge. The electron and the hole form a pair and are typically generated at the lowest band gap energy E_g due to the exponential dependence of the tunnel probability on the gap size.

To some extent it is possible to describe the same process in real space with *Wannier-functions* which are Fourier-transformed Bloch functions. These states describe localized electrons at atomic lattice sites and can be used to project the three-step model of solids into the real space [98] as schematically shown in Fig. 2.2(c). On the contrary to the gas phase, tunneling of the electron can take place between different lattice sites such that an electron is created in the conduction band some lattice sites away from the hole generated in the valance band. The tunneling probability is defined by the Wannier dipole moment and an additional exponent which scales with the distance, the electric field strength, and the band gap energy. Similar to gas-phase HHG, electrons are preferably excited near the intensity peaks of the driving laser. However, in solids the electron-hole pair in the electric field of the laser possesses an energy of $\mathbf{F}_L \cdot \mathbf{x}_l$. The distance vector $\mathbf{x}_l$ corresponds to an electron hole separation by l lattice sites. Hence, pair creation at unequal lattice sites may be energetically favorable.

2.1.2 Acceleration

The second step is the acceleration of the electron in the alternating electric field $F_L(t)$. In gases the electron can be classically described by Newton's equation of motion [88].

The electron is accelerated in the direction of the laser field and after its reversal driven back in the opposite direction. Figure 2.3(a) depicts possible trajectories which depend on the time of ionization with respect to the phase of the external field. Some trajectories correspond to a complete removal of the electron while others intercept the position of the parent atoms (0 position). Remarkably, only linearly polarized driving fields lead to a high recollision probability. Even a slightly elliptical polarization drives the electrons on circular trajectories and leads to a drastic reduction in the recombination probability and consequentially prohibits high-harmonic emission.

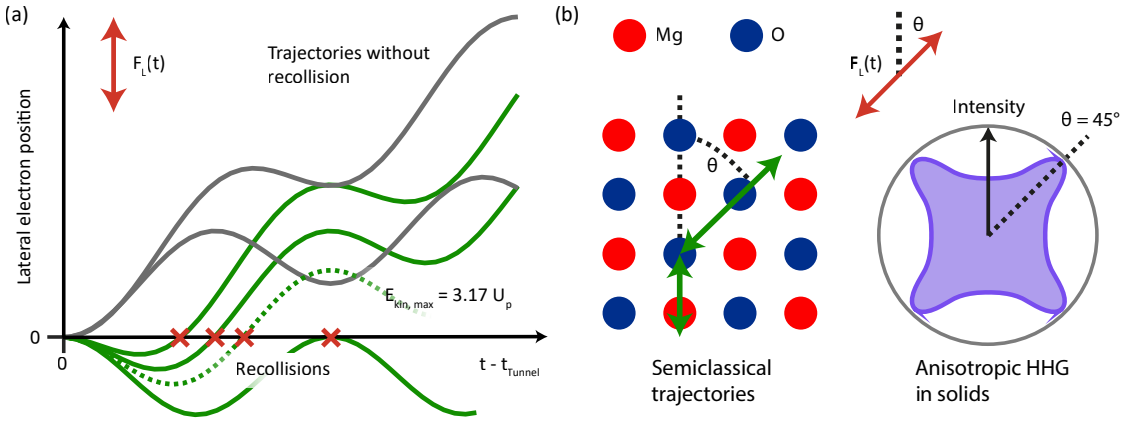

Figure 2.3: Electron trajectories in gases and solids. (a) In gas-phase HHG, the free electrons are accelerated in the laser field F_L and, depending on the tunnel time t_{tunnel}, some electrons drift away (gray lines) while others recollide (green lines and red marks). The maximal kinetic energy of $E_{kin,max} = 3.17\,U_p$ is achieved by a trajectory with a relative phase of 17° at the time of tunneling. (b) In solids, the electrons can be described by semiclassical trajectories. Since solids like MgO are non-isotropic, the intensity of the high harmonics is strongly dependent on the angle θ of the light field with respect to the crystal orientation.

At recollision with the parent atom the electron releases its kinetic energy which is determined by the trajectory. A maximal kinetic energy of $E_{kin,max} = 3.17\,U_p$ is reached for tunneling at a relative phase of 17°. This energy is roughly three times the average quiver energy of an electron in the light field. A fully quantum mechanical description treats the electrons as wave packets and replaces the classical trajectory by possible quantum paths [96]. The expectation value of the path coincides with the classical description, but in the quantum representation, the electron wave packet experiences quantum diffusion that scales with the time spend in the continuum.

In solids, the process is somewhat similar, but the electron can not be described as a

free particle since it is bound to the atomic lattice. In momentum space, the movement can be described by the Houston picture, where the quasiparticle is accelerated within a single band by an increase of the k vector: $k(t) = k + e/\hbar \int F_L(\tau) d\tau$ [99]. Electrons and holes are both mobile and accelerated in opposite directions due to the opposing charge. Upon field reversal, the two carriers are driven back together. In general, the group velocity of a particle is determined by the curvature of the dispersion via $v(k) = \hbar^{-1} \nabla_k E(k)$. In contrast to the free space parabola [see Fig. 2.2(b)] solids possess a complex band structure which leads to a non-trivial relation between k and the velocity. These nonlinearities of the intraband current can itself lead to emission of high-harmonic radiation. For example, at high field strengths, the electron velocity oscillates in the periodic bands of a solid [e.g. cosine bands shown in Fig. 2.2(d)] when driven with a constant electric field. As alternating charges induce a dipole moment, the accelerated electrons and holes themselves will emit radiation. This photon emission induced by nonlinear bands is called the intraband mechanism of solid-state HHG and possesses no analog in the gas phase [100, 101, 102, 103, 104].

The electron and hole acquire energy by traveling through the band structure and moving away from the minimal band gap [Fig. 2.2(d)]. This energy releases upon recombination and corresponds to the kinetic energy in the recollision model of gas-phase HHG. A soft cutoff for the maximal energy is reached at the largest band gap between the conduction and the valance band, but even higher bands can be populated by inter-band tunneling at high field strengths.

In real space, the trajectories of the electrons and holes can be described by semiclassical paths through the crystal lattice. Calculations with inclusion of quantum mechanical correction obtain the path by saddle-point integration [98] and model HHG in solids using a trajectory picture. As the solid structure is highly anisotropic, the direction of the electron path strongly influences the HHG. Figure 2.3(b) depicts the HHG in magnesium oxide (MgO) with varying angle θ of the laser polarization with respect to the crystal. The semiclassical electron trajectories (green arrows) are aligned with the electric field and can cover the distance of multiple lattice constants [68]. Consequentially, the moving electrons and holes acquire information of the directional band structure, which leads to highly anisotropic high-harmonic emission [68]. This effect has been observed in various experiments and is applied in band reconstructions [62] and tomography of electron orbitals [105]. For MgO a schematic intensity of the emitted harmonic radiation as a function of the angle θ is shown in Fig. 2.3(b). The high harmonic intensity exhibits the

same rotational symmetry as the crystal, but varies with the harmonic order, as will be discussed in chapter 6.

2.1.3 Recombination

In the last step, the excited and accelerated electron interacts and recombines with the ion or the corresponding hole and emits the access energy as high-harmonic radiation. In gases the free electron wave packet overlaps with the parent ion and emits the kinetic energy plus the ionization potential:

$$\hbar\omega_{HHG} = U_{Ion} + E_{kin}. \tag{2.3}$$

The kinetic energy depends on the trajectory which is defined by the laser phase at the time of tunneling. By inserting the maximal kinetic energy and the definition of the ponderomotive potential into Eq. (2.3) the high-harmonic cutoff energy is found to depend quadratically on the wavelength and the driving field strength:

$$E_{cutoff} \propto F_L^2 \lambda_L^2. \tag{2.4}$$

Within the quantum-mechanical description, the electron wave packet returns to the parent atom and interferes with the portion of the electron wave function that did not tunnel out of the atomic potential. The interference is caused by the difference in energy of the two wave packets and leads to dipole oscillations that emit the harmonic radiation. As mentioned, the electron in the continuum experience quantum diffusion which can significantly decrease the recollision probability.

In solid media, electron and hole may recombine from different lattice sites with exponentially decreasing probability as a function of the distance. The energy that is emitted in form of a photon corresponds to the energy difference of electron and hole and consists of the kinetic energies plus the minimal band gap energy E_g. An additional but small energy contribution stems from the electric dipole of electron and hole in the external field. This allows photon energies slightly larger than the maximal band gap of conduction and valance band. The described emission of radiation by electron hole recombination is called the interband mechanism of solid-state HHG and is the analogue to the three-step-model of gas-phase HHG.

2.2 Properties of high-harmonic radiation from gases and solids

High-harmonic emission from gas and solid sources possesses many intriguing properties that renders it ideal for application in spectroscopy, microscopy, and photoemission. In this section we will briefly discuss these properties and their implications for the use in solid-state research with a focus on spectroscopy.

Gas-phase HHG is a reliable source of coherent extreme ultraviolet (XUV) radiation on a laboratory scale. This wavelength region offers spectroscopic access to core level transitions which is discussed in Sec. 3.1.1 and enables element specific sensitivity to lattice, electronic, and spin degrees of freedom [8, 6, 106, 107]. Furthermore, the short wavelength and the exceptional high coherence provides an ideal platform for microscopy with nanometer resolution. In studies of cobalt palladium multilayer structures, Zakyo *et al.* showed the imaging of magnetic domains with 16 nm resolution [91]. In photoemission studies, the high photon energy of HHG sources is ideally suited to access electrons from the whole Brillouin zone while the intrinsic phase stability enables time-resolved studies [92].

Due to the temporal properties of the emitted radiation, HHG poses as a cornerstone of ultrafast sciences. High-order harmonics are generated parametrically in bursts of attosecond pulses every half cycle of the driving laser in a phase locked manner. This enables time-resolved experiments in a pump-probe scheme free from any timing jitter. By controlling the emission of harmonic radiation it is also possible to select one single attosecond burst and obtain the highest temporal resolution of any known probes [34, 108, 109, 110]. To this end one uses few cycle driving pulses of less than 5 fs duration and applies an additional gating mechanism that selects harmonic emission of only one half cycle. One of the most frequent method is the polarization gating scheme that uses two elliptically polarized pulses which individually cannot efficiently generate high-harmonic radiation. By combining the two counter-rotating elliptical pulses efficient HHG is enabled during a tiny time-gated window. Apart from the enhanced temporal resolution, few cycle driving pulses can generate super continuum spectra with meV spectral resolution. In contrast, longer driving pulses, as used in this work, will lead to discreet harmonics with a spacing of the fundamental photon energy. High-harmonic sources present the workhorse of attosecond spectroscopy and the gating mechanism is mentioned here for completion even though this work uses femtosecond harmonic emission. Nevertheless, many of the methods in this work can be transferred to broadband attosecond sources.

The properties of high-harmonic radiation from solids is very similar to gas-phase harmonics. Solid-state HHG offers similar coherence and a potential for attosecond temporal resolution. However, the underlying microscopic mechanisms are dramatically different as evident from the intensity scaling of the cutoff. For interband harmonic-radiation from solids, the upper energy limit is defined by the maximal band gap. By contrast, high harmonic emission from intraband currents have been observed to scale linearly with the electric field strength [111]. In virtually all experiments with solid targets, a linear scaling and therefore a contribution of the intraband mechanism can be observed [38]. This is in stark contrast to the gas-phase HHG that shows a quadratic scaling [Eq. (2.4)] of the cutoff with respect to the electric field and highlights the huge discrepancies of the HHG mechanisms in solid and gaseous media. It is therefore more challenging to reach high photon energies with solid-state sources, limiting its applicability as light source for core level spectroscopy.

However, the solid-state HHG process itself is ideally suited to study the material properties of the generating medium. During the HHG process the electron travels through the whole band structure of the material and decodes the information in the emitted light. By careful analysis of the harmonic spectra and potential supplementary calculations based on the semiconductor Bloch equations [103] various material properties can be extracted. The list of studies include band reconstructions [62], lattice symmetries [68, 69, 70, 71], phonons [55, 56], Berry curvature [112], orbital tomography [105], carrier dynamics [55, 62, 63], and metal-to-insulator transitions [113]. Especially promising are reconstructions of crystal band structures by solid-state HHG which was previously limited to photoemission experiments. Since photoemission requires ultrahigh vacuum and clean crystal surfaces, HHG is a great alternative with far less prerequisites. Solid-state HHG in the visible does not require vacuum conditions and extensive sample preparation. Using harmonic radiation, directional band structures have already been retrieved in a large variety of materials including strongly-correlated quantum materials and two-dimensional systems [114, 71, 55]. The investigation of solids by the microscopic mechanisms of HHG thus opens a highly promising path and started a very active research field.

2.3 Selection rules and two-color driving fields

As discussed in the preceding section, high-harmonic radiation is emitted near the peak intensities of the alternating laser field every half cycle. In isotropic noble gases both half cycles are equal which prohibits the emission of even harmonics due to destructive interference, similar to a balanced interferometer. More precisely, the driving field fulfills the dynamic symmetry $\mathbf{F}_L(t+T/2) = \hat{P}\mathbf{F}_L(t)$, where $\hat{P}$ is the parity operator and every emitted light field must fulfill the same condition. Therefore, only odd multiples of the laser frequency ω_L are generated in gas-phase HHG, a property that is known as the selection rule of HHG:

$$\omega_{HHG} = \omega_L(2n+1). \tag{2.5}$$

Emission of even harmonics is only achievable if the inversion symmetry is lifted. In SHG within the perturbative regime, this is usually achieved by using a non-inversion symmetric crystal like β-barium borate (BBO). Non-inversion symmetric crystals can also be used for the generation of even order high harmonics. Alternatively, in gas-phase HHG, the emission of even orders is achieved by coherently overlapping the laser at frequency ω with light at some other frequency, e.g. 2ω. Even a weak additional laser field breaks the inversion symmetry of the noble gas and enables the generation of even and odd harmonics [115] leading to the selection rule for two-color (TC) driving fields:

$$\omega_{HHG,TC} = \omega_L n. \tag{2.6}$$

Figure 2.4 shows a spectrum of high-harmonic radiation generated in argon gas with a laser centered at 800 nm wavelength (red). By adding the second harmonic to the driving field (blue), the inversion symmetry is lifted and all orders of harmonics are generated. In addition, the use of a two-color driving field increases the intensity over a large portion of the spectrum. The flux can be raised by one order of magnitude with the addition of the second harmonic and in experiments with the third harmonic, a two orders of magnitude increase was shown [116, 117, 118]. This effect is a result of the increased number of coherent wave mixing processes that yield the same harmonic order [119, 116, 120]. For spectroscopic experiments with gas-phase HHG sources, two-color excitation fields are highly beneficial as they increase the photon count and lead to a denser spectral coverage.

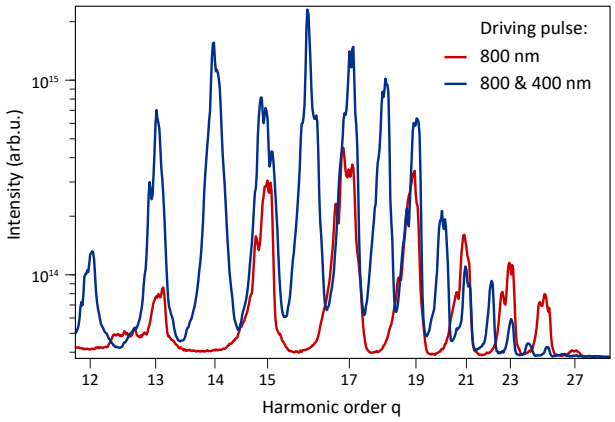

Figure 2.4: Experimental high-harmonic spectrum obtained with a bi-chromatic driving field. Shown are logarithmic intensities of high-harmonic radiation generated by the fundamental at 800 nm wavelength in comparison to a spectrum generated with a bi-chromatic driving field consisting of the fundamental and its second harmonic at 400 nm wavelength. Both fields are linearly polarized with identical orientation.

A combination of two driving fields can be further used to control the polarization state of the harmonic radiation. As discussed in Sec. 2.1.2, circular external fields lead to a diminished recollision probability of the excited electron and prohibit efficient HHG. It is therefore extremely challenging to produce circularly polarized high-harmonic emission. This substantial obstacle is overcome with the use of a two-color driving field. Combining a left-handed circularly polarized fundamental laser field with a right-handed polarized second harmonic allows the efficient generation of circularly polarized high-harmonic radiation [121]. The combined electric driving field has a three-fold cloverleaf shape with near linear polarization at the intensity maxima while simultaneously having angular momentum. A Lissajous curve of the field is shown in Fig. 2.5 (purple) and in greater detail for varied field amplitude ratios in Fig. 6.6. At the peaks of the field, efficient HHG in gases is achieved while the rotating position of the maxima induces a helicity which leads to emission of circularly polarized harmonics. The HHG process can be treated as a combination of photons with ± 1 angular momentum while the second harmonic possesses opposing helicity to the fundamental laser field. Therefore the possible combinations are constrained, such that every third harmonic is absent as specified by the selection rule for threefold fields [121]

$$\omega_{HHG,\mathrm{circ}} = \omega_L(3n \pm 1). \tag{2.7}$$

Here, the harmonic order with $+1$ exhibits the polarization of the fundamental while -1 corresponds to opposing helicity. The selection rule is a great tool to verify the polarization state of the emitted high harmonics. If every third harmonic is found to be suppressed in an experiment, the remaining orders possess defined helicities according to Eq. (2.7).

In solids, the generation of circularly polarized high harmonics is possible with a circularly polarized driving field due to the relaxed recollision constraint and the emission by circular currents within the intraband mechanism [122, 123, 124]. However, this work explores the possibility to use threefold-driving fields for efficient HHG in solids. Most notably, the solid targets show different selection rules, as they superimpose their own symmetry and can contribute angular momentum in the generation process. We analyse the influence of the solid symmetry in conjunction with three-fold driving fields on the efficiency of the HHG in chapter 6. The selection rules for three-fold driving fields in solids are discussed in Sec. 6.4.1.

In practice, the combination of two laser fields is typically achieved with a Mach-Zender interferometer which is prone to timing and beam pointing instabilities that are problematic for the use in HHG. A far simpler design shown in Fig. 2.5 allows for the in-line production of two-color driving fields. In chapter 6 we use the MAZEL-TOV (MAch-ZEhnder-Less for Threefold Optical Virginia spiderwort) device [125], which allows to generate threefold driving fields by using a BBO crystal for SHG and two calcite plates to temporally overlap the two fields. A quaterwaveplate with the fast axis set to 45° converts the linear polarization of fundamental and second harmonic to counter rotating circular polarization. In the same manner, linearly polarized two-color fields are obtained without the quater waveplate in a modified MAZEL-TOV device [Fig. 2.5, bottom]. Since fundamental and second harmonic are generated with perpendicular polarization in the BBO crystal, we utilize a half-wave plate specified for the fundamental that acts as a lambda plate for the second harmonic. The resulting s-polarized driving field minimizes intensity losses in the downstream beam path and maximize the harmonic yield in our setup.

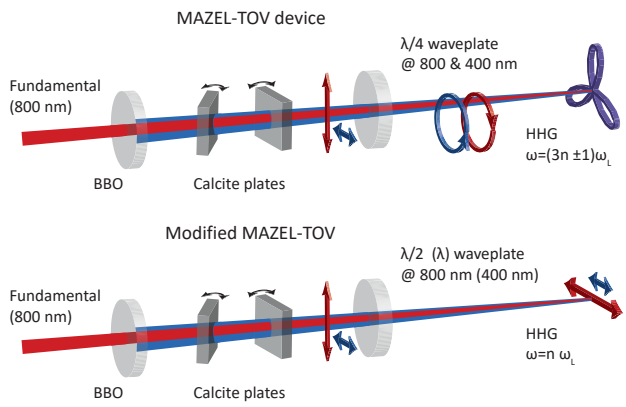

Figure 2.5: In-line production of two-color driving fields. The second harmonic of the fundamental laser (800 nm wavelength) is generated in a β-barium borate (BBO) crystal and temporally overlapped with two rotatable calcite plates. A quarter-wave plate is used to generate a threefold driving field with circular helicity (MAZEL-TOV device introduced in Ref. [125]) and a half wave-plate is used to obtain a two-color linearly polarized excitation field.

2.4 Macroscopic effects of high-harmonic generation

In addition to the discussed microscopic generation mechanisms, macroscopic effects can drastically change the properties of the emitted high-harmonic radiation. The two most important aspects are the phase matching of high-harmonic radiation from individual emitters and the re-absorption. For spectroscopic applications, high intensities and, therefore, good phase matching conditions and minimized re-absorption are of utmost importance. This needs to be considered in the design of the HHG source geometry and its operational parameters. In the following, we will discuss both aspects for solid and gaseous sources and additionally highlight recent developments in structuring of solids which pose a new route for controlling high harmonic emission.

In gases, phase matching can be achieved by adjusting the design of the gas source, the gas pressure, and the laser properties such as intensity, focal length, and mode quality. Ideal phase matching would require an identical phase velocity of the fundamental and the emitted high-harmonic emission. The phase mismatch of harmonic order q is given by the expression [126]:

$$\Delta k \approx \underbrace{-P(1-\eta)q2\pi\lambda_L^{-1}\Delta n}_{\text{Neutral atoms}} + \underbrace{P\eta N_{atm} r_e \lambda_L q}_{\text{Plasma}}, \tag{2.8}$$

where P is the gas pressure, η is the fraction of ionized atoms, r_e is the classical electron radius, N_{atm} is the number density of the gas at 1 atm pressure, and Δn describes the difference in the refractive index between the fundamental and the q-th harmonic. Equation (2.8) approximates the phase matching while neglecting the source geometry [126] and the Gouy phase shift that emerges near the focus of a convergent driving laser [127]. It consist of two parts with opposite sign, the electron plasma dispersion and the dispersion of the neutral gas atoms. By carefully balancing the gas pressure and the level of ionization via the laser intensity, phase matching ($\Delta k = 0$) can be achieved. However, above a certain ionization threshold η_{crit}, the HHG can not be phase matched, effectively limiting the ionization levels to $< 5\%$. This imposes a constraint on the efficient generation of high energy harmonics which is expressed by the phase matching cutoff $E_{PM,cutoff} \propto \lambda_L^{1.6-1.7}$ [84, 128]. While the exact exponent depends on the source geometry, the phase matching cutoff is generally lower than the single atom cutoff [Eq. (2.4)]. In addition, it is clear from Eq. (2.8) that phase matching can not be equally well achieved for the complete comb of high-harmonics. In practice, only a small energy window is

optimally phase matched while harmonic radiation outside this range is sub-optimally generated.

As the phase matching depends very sensitively on gas pressure, laser intensity, and laser mode quality, fluctuations of these parameters are transferred to the high-harmonic intensity. These phase matching fluctuations of the high-harmonic radiation add to the noise originating from the nonlinear, microscopic dependence of the laser power. As a result, the noise floor of HHG light sources is typically around 5% which is roughly ten times larger in comparison to laser systems. The fluctuations are one of the main limiting factors for using HHG as a light source in spectroscopic experiments. Interestingly, phase matching affects every harmonic in a different manner by favouring the macroscopic conversion efficiency at some orders while diminishing the emitted radiation at other orders. This leads to highly correlated fluctuations between different spectral regions. In chapter 7 we analyse the intensity correlations between different wavelengths and use this information for compensation of the HHG source noise in a referencing scheme.

Apart from phase-matching conditions, efficient HHG needs to take the re-absorption of emitted radiation into account. In the XUV region the absorption in noble gases is typically limited to less than a few mm [129] which demands the use of vacuum systems and restrains possible HHG source geometries. It is crucial to achieve low gas pressures in the harmonic beam path while simultaneously realizing a phase matched generation. Different geometries have been tested in order to find the optimal trade off between phase matching and re-absorption. The most frequent geometries include the gas jet [130] that injects high pressure gas in a confined cone, the gas cell [131, 132] filled at low pressure, and the wave guide [133, 134] that confines the mode and allows for large interaction regions. Various experiments analyzed the efficiency of the sources and comparable conversion efficiencies in the XUV range have been found [133, 134, 130, 131, 132]. In this work we use a semi-infinite gas cell [135, 136] [see Fig. 2.1(a), upper] which is an elongated cylinder completely filled with a noble gas. In contrast to small gas cells, it is directly mounted to the vacuum chamber and the laser entrance window is directly attached to one side. Consequentially, it offers higher vibrational stability and physical protection of the vacuum entrance window at similar intensities to other source geometries [135, 136].

In solids, phase matching is not possible in the same manner as it is in the gas phase. In part this drawback is compensated by the denser distribution of emitters and the different microscopic mechanism. The far more severe problem is the re-absorption. Radiation

exceeding the minimal band gap of a solid is strongly absorbed which leads to intense fluorescence lines in the spectrum. It is essential to use a driving laser with a photon energy far below the band gap to avoid strong absorption and a possible destruction of the target material [38]. Therefore, only wide band gap insulators are used for HHG with visible lasers, while semiconductors need to be paired with infrared driving fields. The energy of emitted harmonics typically exceeds the band gap and the resulting strong absorption leads to an extraction depth of only a few tens of nanometers from the surface [137]. Here, it is possible to use a transmission scheme [138] as illustrated in Fig. 2.1 and generate harmonics at the far end of the crystal, or use a reflection geometry [139] shown in Fig. 6.1(a). The latter simplifies the separation of high-harmonic radiation from the intense fundamental beam. Similar to absorption spectroscopy with external light sources, the emitted high-harmonic radiation is absorbed in the near-surface region. Therefore, emitted high-harmonic radiation is not only strongly dependent on the generating process, but also influenced by the material specific absorption coefficient. We utilize this information in chapter 6 to measure the surface magnetism in MgO and the crystalline chirality in quarts.

Recent advances in solid-state HHG with nanostructured solids opened a completely new pathway that was previously impossible with gas sources. By altering the solid morphology or composition on the micrometer and nanometer length-scale, control of the laser light and the HHG process is possible. Various studies used this route for efficient HHG in solids, by enhancing the driving field or tackling the re-absorption. Nanostructures such as gold-sapphire cones used by Han *et al.* [140] can enhance the electric field of the incoming laser radiation. In this study it was shown that the generation of surface-plasmons increase the electric field by ≈ 20 dB at the sapphire tip shown in Fig. 2.6(a) and (b). As a result high harmonics of orders up to 13 could be efficiently generated at significantly lower intensities of $0.1 \times 10^{12} \mathrm{W}/cm^2$ compared to bulk HHG. Further work by Vampa *et al.*. [141] demonstrate an enhanced generation efficiency of factor 5 to 10 from an array of gold nano-antennas. Apart from the local enhancement of electric fields, the high harmonic yields has been optimized by controlling the re-absorption with a periodic array of thin one-dimensional crystalline silicon ridge waveguides [142]. Figure 2.6(c) depicts the working principle, that relies on the confinement of the emitted harmonic radiation to vacuum wave guides between the nano-structured ridges [Fig. 2.6(d)]. Thereby, the propagation is separated from the HHG that preferably occurs at the edges of the silicon and allows high-harmonic emission with a 100-fold increased extraction depth in

contrast to pure silicon. Furthermore, by using an integrated Fresnel zone plate structure Sivis *et al.* [143] focus high harmonics generated in silicon. By implanting gallium ions into the silicon substrate, the HHG efficiency was spatially modulated and the zone plate structure lead to an effective focusing of emitted radiation. As optics for high harmonic radiation in the vacuum ultraviolet (VUV) and XUV region are extremely challenging to realize, integrated lens designs could enable effective focusing. Such advances are particularly relevant for subsequent use of the emitted light in experiments including absorption spectroscopy or photo emission with a solid HHG source.

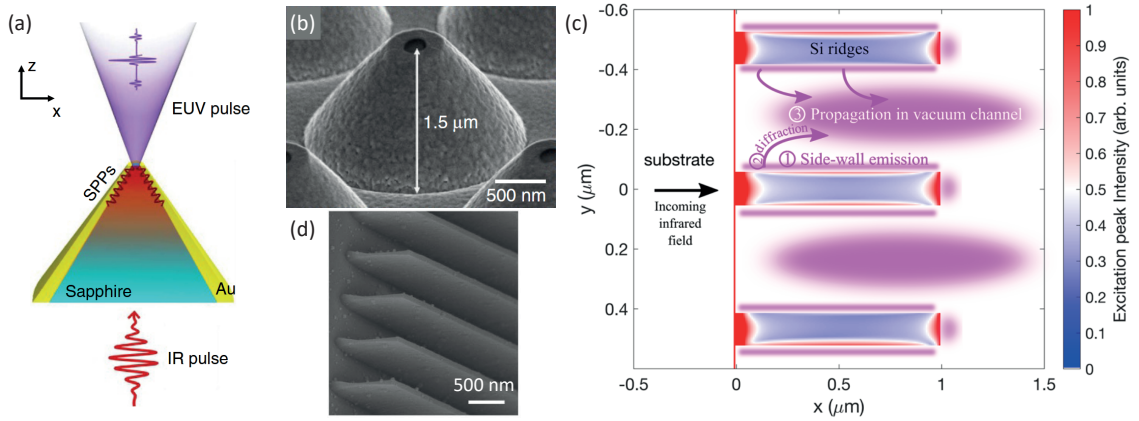

Figure 2.6: Nanoscale structuring of solids for control of HHG. (a) Local enhancement of the infrared (IR) laser pulse by surface plasmon polaritons (SPP) generated at the metal-sapphire interface and traveling to the apex. (b) Scanning electron microscopy images of the nanometer-sized cone. (c) Schematic cross section of the silicon ridges irradiated from the left. The color code displays the infrared intensity which is simulated by the finite-differences frequency domain method. The maximal intensity occurs at the sides of the ridges. Harmonic radiation is generated at the sides and coupled into the vacuum wave guides (purple). (d) Scanning electron microscopy image of the silicon ridges. The scale bar is 500 nm. Subfigures (a) and (b) are adapted from Ref. [140] and (c) and (d) are adapted from Ref. [142] under the Creative Commons Attribution 4.0 International (CC BY 4.0) license.

In summary, gas-phase HHG is a well understood and established light source in the XUV to x-ray region. It is the driver of attosecond spectroscopy and used in many beam lines around the world. It offers great insights into solid-state material systems with unprecedented time resolution. However, the intrinsic fluctuations from the nonlinear process and phase matching are currently limiting the applicability. With advanced sensitivity, high-harmonic radiation has a great potential for a broad range of ultrafast materials research. Furthermore, solid-state HHG has emerged as a great tool for studying intricate

sample systems as shown by the wealth of current studies. It offers the same potential for attosecond time-resolved experiments with minimal requirements regarding sample preparation and vacuum conditions. In addition, the use of nanoscale engineering could be a very powerful tool to control the intensity, the polarization, and the mode profile of high-harmonic radiation from solids. In the future, solid-state HHG will be drastically advanced by the magnitude of existing material engineering methods such as nanostructuring or the production of mono layer material systems [144, 145] and presents a frontier of strong-field and attosecond science [37].

Chapter 3

Elements of ultrafast absorption spectroscopy

Spectroscopic methods investigate the wavelength or frequency dependent interaction of electromagnetic waves with matter. By measuring the intensity of the radiation before and after the interaction, information on the microscopic properties of the specimen are obtained. The material dependent response to electromagnetic waves is well describe by the macroscopic, complex, and frequency dependent refractive index:

$$\underline{n}(\omega) = n(\omega) + ik(\omega). \tag{3.1}$$

Here, $n(\omega) = c/v(\omega)$ describes the phase velocity reduction of the electromagnetic wave in matter while $k(\omega)$ represents its absorption. As the refractive index depends on fine details of the electron orbitals, it includes encoded information about the electronic properties, atomic composition, chemical bonding, structure, and magnetic behaviour. Optical spectroscopy was one of the first methods to access electronic states in atoms and still represents a very powerful tool for modern day solid-state research. Empowered by ultrashort laser pulses, all-optical methods and spectroscopy in particular have long been the forefront of experiments with femtosecond resolution. The combination of electronic sensitivity and a time resolution on the order of electron dynamics yields information about a large variety of material systems. Today, optical spectroscopic methods are still dominant in the field of ultrafast science and present a great tool for investigations of various electronic and structural dynamics on their fundamental timescales [23, 24].

This chapter introduces the basics of ultrafast absorption spectroscopy. At first, we will discuss the microscopic mechanism that dictates the wavelength dependent material absorption with a focus on resonant absorption such as band gap or core level transitions. The Sec. 3.2 discusses *ab-initio* calculations of extreme ultraviolet (XUV) absorption

spectra. Afterwards, the experimental setups used for absorption spectroscopy in the vacuum ultraviolet (VUV) and XUV region are discussed while including the technical aspects of time-resolved studies within a pump probe scheme.

3.1 Absorption of electromagnetic waves in solids

The intensity of an electromagnetic wave that is transmitted through a sample of length L is described by

$$I_t/I_0 = e^{-\mu L}, \tag{3.2}$$

where I_t and I_0 refer to the transmitted and initial intensity while $\mu = 2\frac{\omega}{c}k(\omega)$ represents the absorption coefficient. The characteristic absorption length is defined as $\delta = 1/\mu$. By measuring initial and transmitted intensity, equation (3.2) can be used to extract the imaginary part of the refractive index k by the natural logarithm. However, most experiments use a logarithm of base ten to define the absorbance [146, 35]

$$A = -\log_{10}(I_t/I_0), \tag{3.3}$$

which is also referred to as optical density (OD). With the knowledge of the sample thickness, precise measurements of the transmitted and incident intensity allow to accurately determine the material specific absorption coefficient. On the contrary, the real part of the refractive index can not be obtained in transmission and is usually measured by experiments in a reflection geometry. Here, the reflected intensity I_R is described as a fraction of the incident intensity by the reflectivity $R = \frac{I_R}{I_0}$ which is wavelength dependent and a function of the full complex refractive index. In addition, incident angle and light polarization strongly affect the reflectivity as described by the Fresnel equations. Due to their complexity, reflected spectra are usually harder to interpret as transmitted ones. In principle, it is possible to convert the absorption coefficient determined by absorption to the real part of the refractive index. The Kramers-Kronig equations relate those material constants but require an integration of the known property over the whole frequency domain [147]. As measurements of the refractive index typically do not cover every frequency, missing spectral regions are completed by a theory model or interpolated. Transferring one quantity to the other typically leads to inaccuracies and a direct measurement of the desired

materials constant is always preferred. In the visible, the complete refractive index is usually determined by ellipsometry which measures the reflectivity as a function of the light polarization [148]. Such measurements are widely applied to accurately determine the optical properties of glasses and optical thin films.

For studies of the electronic structure, a complete knowledge of the refractive index is often not needed and parts of the absorption spectrum can be directly related to electronic transitions. Generally, absorption of electromagnetic light is only possible in photon energy quanta of $E_{ph} = \hbar\omega$ and is accompanied by an excitation of an electron to a higher energy level. In the weak perturbation limit, the optical density is proportional to the transition probabilities of electron excitations and can be described by Fermi's Golden rule [149]:

$$A(E_{ph}) \propto \sum_{i,f} |\langle i|\hat{\mathbf{e}}\cdot\mathbf{r}|f\rangle|^2 \delta(E_f - E_i - E_{ph}). \tag{3.4}$$

Here, $|i\rangle$ and $|f\rangle$ are the initial and the final state wave functions with their corresponding energies of E_i and E_f while δ represents the Dirac delta function. Initially, the system is in the ground state while the final state describes an electron in an elevated energy level plus a corresponding electron hole. The interaction of the material with the electromagnetic field is described by the matrix element $\langle i|\hat{\mathbf{e}}\cdot\mathbf{r}|f\rangle$ in the dipole approximation [150] which includes the direction of the light-polarization $\hat{\mathbf{e}} = \mathbf{F}/|\mathbf{F}|$. Equation (3.4) sums up every transition that fulfills the energy conservation of initial state, final state, and photon energy. Directly calculations of the absorbance with Eq. (3.4) is difficult due to the required knowledge of all initial and final state wave functions. In chapter 3.2 we will discuss an alternative approach, the density functional theory (DFT), which uses functionals of the electron density instead of the wave functions.

Despite the dependence of the transition probabilities on the matrix elements, the absorption coefficient can often be qualitatively described by the joint electronic density of states (DOS). The absorption coefficient of a material is larger at photon energies that correspond to a larger number of possible transitions between empty final states and filled initial states. In contrast, if no states fulfill the energy conservation, the material is transparent at this specific frequency. As an example, figure 3.1 illustrates the absorption in a semiconducting or insulating material. These materials exhibit a band gap of E_g that separates the electron-filled valance band from the empty conduction band. Electronic

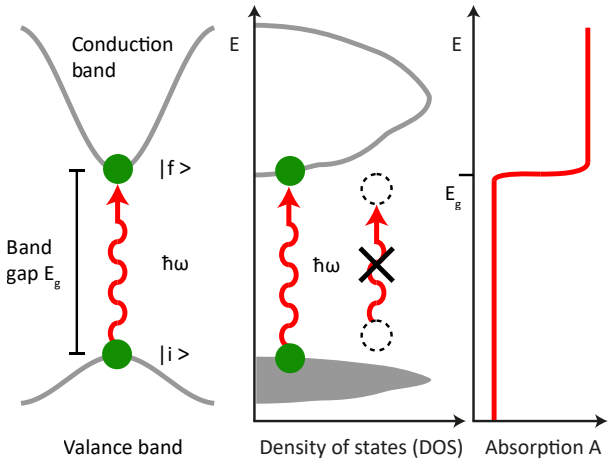

Figure 3.1: Absorption of electromagnetic radiation in semiconductors and insulators. Photons of energy $\hbar\omega > E_g$ excite electrons across the band gap and are strongly absorbed. Lower energy photons can not excite electrons due to the missing initial $|i\rangle$ and final states $|f\rangle$ and pass the material without being absorbed.

transitions with energies smaller than the band gap are not possible such that these materials are almost transparent for photon energies up to the band gap energy. Insulators possess large bad gaps in the multiple eV region which corresponds to the VUV spectrum and are therefore transparent in the visible. On the contrary, semiconductors possess smaller cut-on photon energies in the infrared to visible region. Photons with an energy equal to the band gap are strongly absorbed and these excitations are called resonant. In this work, we explore two different type of resonant excitations. In chapter 6, we discuss the resonant os exciton state in the VUV. Excitons are quasi-particles of bound electron-hole pairs. The coulomb attraction between the two constituents confines their distance in real space and reduces the energy of the exciton to slightly below the band gap. An exciton transition can therefore be identified by an increase in absorption below the band gap. Furthermore, this work discusses XUV spectroscopy of core level excitations in Sec. 8. The theoretical basis for these transitions is presented in the next section.

3.1.1 Core-level transitions

Atomic orbitals with larger binding energies are less involved in chemical bonds and the formation of energy bands. In contrast to the valance and the conduction bands, these core electrons are closely bound to the atomic core. While the conduction and valance band are probed by visible light, photon energies in the XUV to X-ray regime are needed to probe core electrons. In this study, we define the XUV region to roughly 30 eV to 250 eV photon energy and use VUV in the range of approximately 6 eV to 15 eV which is unsuited for core level studies. The field of X-ray absorption spectroscopy showed tremendous success in the identification of chemical compositions and atomic structures [151]. The

XUV region is less frequently used to interrogate core level states. However, shallow core level of most metals can still be successfully probed by XUV radiation allowing access to a large variety of observables including electronic and phononic degrees of freedom.

Figure 3.2(a) illustrates the principle of XUV absorption spectroscopy by means of a fictitious compound consisting of atomic species A and B. The material is assumed to form a solid with an electron filled conduction band and an empty valance band separated by a band gap. At binding energies of roughly 50 eV, accessible by XUV radiation, the $n = 3$ atomic orbital is found for a variety of materials including the first row transition metals [146]. The deeper levels $n = 1,2$ are usually situated at even higher energies in the X-ray region. Upon exceeding the specific energy of the core level, the absorption rapidly increases due to the possible excitations of electrons from the core level to empty states in the valance shell. These sharp features of the spectrum are called K,L or M-edge in correspondence to the atomic orbitals $n = 1,2,3$. The M-edge of our example compound, shown in Fig. 3.2(b), can be decomposed into the core level excitation of atom A and B and therefore offer element specific sensitivity. By analyzing the extended edge region, a variety of material dependent properties can be extracted from the spectra. These include, electron band structures, atomic structure, phonon oscillations, excited carriers, and magnetism [35].

A particularly interesting feature of core level spectra is the occurrence of giant resonances caused by many-body effects in the vicinity of the absorption edge. Microscopically, the incident electromagnetic wave accelerates one electron which transmits the impulse to other electrons and the resulting collective motion leads to strong absorption at a specific resonance frequency. This mechanism is enhanced by strong local screening of surrounding orbitals with large overlapping wave functions. A common example of such collective resonances are plasma oscillations which are found in metals and dominate the visible spectrum. One other example is the many-body peak near core level edges which was first observed in xenon gas [152, 153]. Since semi-core levels such as the M-edge strongly overlap with the valance band, giant resonances are strongly favoured. Recent studies found many-body absorption features in atomic titanium and layered TMDCs [154, 155, 156, 54, 157]. In chapter 8 we will discuss the many body peak in the TMDC $1T$-$TiSe_2$ in detail. In order to fully capture many-body resonances, theoretical calculations of spectra need to incorporate dynamic screening in the form of local field effects which will be discussed in the next section.

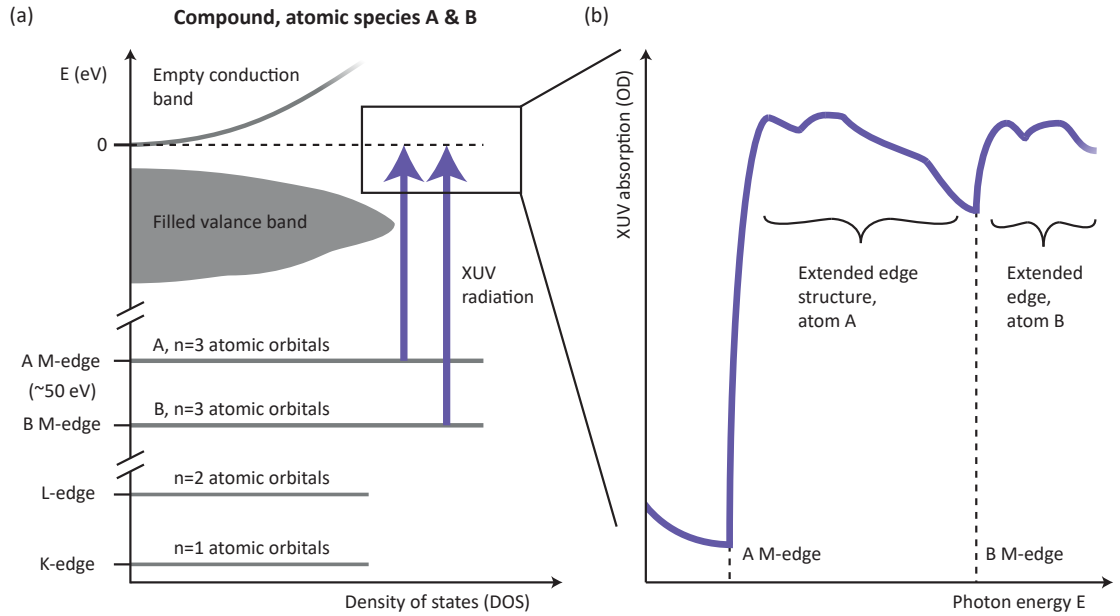

Figure 3.2: Core-level absorption edges in XUV spectra. (a) Band structure of a generic solid compound of atomic species A and B with an electron-filled valance band and an empty conduction band. The transitions of electrons from the atomic core levels (orbitals) are called K,L,M edges corresponding to the principal quantum numbers $n = 1, 2, 3$, respectively. Each element possesses specific core levels with distinct energy. Radiation in the XUV region is suited to probe the M-edges of a variety of materials. (b) The absorption of the XUV radiation drastically increases at the edge. In the extended edge region the absorption is modulated by effects of the band structure yielding valuable spectroscopic information.

3.2 Simulation of XUV absorption spectra with TDDFT

In this section we will discuss a theoretical approach for calculation of XUV absorption spectra in solids. Most works in this spectral region use either the Bethe-Salpeter Equation (BSE) [158, 159, 160] in the context of many body perturbation theory or the time-dependent density functional theory (TDDFT) [161]. Generally, the BSE approach can describe the absorption with greater accuracy but comes with extensive computational costs scaling with the number of atoms. In this work, we use the TDDFT method for calculations of the absorption in $1T$-$TiSe_2$ since the BSE is computationally unfeasible for the large unit cell of this material. The following section introduces the basics of DFT and explains how XUV absorption spectra are derived by subsequent TDDFT calculations within the linear-response theory.

3.2.1 A brief introduction to ground state DFT in solids

Over the last decades, DFT has been evolved to the standard method for calculating the structure and electronic properties of chemical compounds as well as solids [162]. It reformulates the Schrödinger equation which uses a wave function picture in terms of the electron density [163]:

$$n(\mathbf{r}) = \sum_{i}^{N} |\Psi_i(\mathbf{r})|^2, \tag{3.5}$$

where the individual electron wave functions Ψ_i are summed over all N electrons. The theoretical basis for this approach is given by the two Hohenberg-Kohn theorems [164]. The first theorem states that the ground-state electronic wave function is uniquely determined by the ground-state electron density via some unknown functional. In other words, every material property in the ground state is uniquely defined by the ground-state electron density. Further, the second theorem proves that the energy of the electronic system can be calculated by a functional of the density and reaches a minimum for the ground-state density. Thus, it is possible to compute the ground state by finding the ground-state energy with the electron density and abandon the computationally expensive Schrödinger description. The full scale of this methodological advantage becomes clear when comparing the dimension on which the problems need to be solved. The wave function representation requires $3N$ dimensions while the electron density is defined in the 3 dimensional space. In the DFT context the energy is expressed as a functional of the electron density by the equation:

$$V_{KS}\left[n(\mathbf{r})\right] = V\left[n(\mathbf{r})\right] + V_H\left[n(\mathbf{r})\right] + V_{XC}\left[n(\mathbf{r})\right], \tag{3.6}$$

here the potential V describes the coulomb interaction between an electron and the collection of nuclei. The term V_H is called Hartree potential and describes the repulsive coulomb potential of the charge distribution $n(\mathbf{r})$ on a single electron and therefore includes a self-interaction which is nonphysical. In the DFT method, all other terms including the correction for the self-interaction are grouped in the exchange-correlation potential V_{XC} which is unknown but can be approximated by various models. With this convention of the energies, the Schrödinger equation is reformulated in terms of the Kohn-Sham (KS)

equations [165]:

$$\left[-\frac{\hbar^2}{2m_e}\nabla^2 + V_{KS}\right]\psi_i(\mathbf{r}) = E_i\Psi_i(\mathbf{r}). \tag{3.7}$$

This eigenvalue equation yields KS wave functions $\Psi_i(\mathbf{r})$ and the corresponding eigenvalues E_i which are different from the physical wave functions and energies. The strength of DFT is rooted in this replacement of the interacting solid by an equal representation with non-interacting particles. In this context, contributions stemming from the electron-electron interaction are taken care of by the exchange correlation functional. All physical observables are computed from the density as justified by the Hohenberg and Kohn theorems. At this point, it becomes clear that the Kohn-Sham DFT formalism includes a circle reasoning. Calculating the wave functions with the KS equations [Eq. (3.7)] requires the potential defined in Eq. (3.6) which depends on the electron density. The electron density is however calculated by Eq. (3.5) from the wave functions. The DFT problem is therefore solved in a self consistent manner by an iterative workflow:

- Formulate an initial guess of the electron density. This may include the import of a known or approximated crystal structure.
- Calculate the effective Kohn-Sham potential with Eq. (3.6) by choosing a representation of the exchange correlation functional.
- Solve the eigenvalue problem of Eq. (3.7) for the Kohn-Sham wave functions $\Psi_i(\mathbf{r})$.
- Recalculate the electron density with the wave functions [Eq. (3.5)].
- Reiterate until convergence is reached.

The remaining challenge of DFT is the determination of the exchange-correlation functional. Despite the fact that the KS theorem guarantees its existence, the exchange-correlation functional is difficult to obtain and can often only be approximated. Over the years, many exchange-correlation models have been formulated for different material systems. In solids, the most relevant model is the local-density approximation (LDA) [165]. It uses the result of the known exchange correlation of the uniform electron gas where $n(\mathbf{r}) =$ constant. The material specific exchange correlation is then approximated from the local electron density at each position by $V_{XC,LDA}(\mathbf{r}) = V_{XC}^{\text{electron gas}}[n(\mathbf{r})]$. In many solid-state systems with a near homogeneous electron distribution, this approximation

holds reasonably well. However, most material systems exhibit an electron density which is stronger modulated and can not be represented by the local density approach. Especially in the vicinity of atomic nuclei, which needs to be accurately captured for calculations of core level absorption spectra, the electron density is far from homogeneous. To this end, the generalized gradient approximation (GGA) functional incorporates the gradient of the density to include more information [166]. This can be done in a variety of ways, and a large number of GGA models have been developed. One of the most widely used approaches is the Perdew-Burke-Ernzerhof functional [167]. It is a nonempirical model with no free parameters that is constructed by incorporating a variety of physical constrains and known scaling behaviours of the exchange and correlation potentials. Choosing the right exchange potential is non trivial and involves experience and benchmarks on the particular material system with the properties of interest.

For the implementation of DFT by the KS equations, there exists a zoo of software packages and solvers. The "right" choice is again dependent on the material class, the desired accuracy, and the investigated property. The most important difference between the available methods is the choice of basis functions in which the wave functions are represented. Plane wave basis are used in crystalline solid systems by virtue of Bloch theorem whereas Gaussian basis sets dominate in molecular systems. Here, plane waves can not accurately capture the fine details of the wave functions near the nuclei. This problem is solved by hybrid wave functions which incorporate plane waves and locally confined atomic orbitals. Widely applied are augmented plane wave orbitals which are constructed by the muffin-tin approach. It separates the crystal unit cell into spherical, non overlapping regions around the nuclei and the remaining interstitial regime. While the region near the cores is best described by atomic orbitals in terms of the spherical harmonics, the delocalised electrons are best represented by plane waves. The wave functions are constructed in a way, that the boundary and the second derivative are continuous. Linearized methods use a Taylor expansion up to the linear order of the energy in the atomic orbitals which is initially unknown. The energy dependence is absorbed by the coefficients which are determined with the boundary condition. This procedure significantly speeds up the computation as the energy does not need to be estimated in an additional loop. At the same time, the loss of accuracy due to the expansion is well controlled and can even be compensated by dynamically adjusting the basis functions. In addition, some approaches simplify the potential inside the spheres by imposing radial symmetry. Other methods do not reduce the complexity and use the full potential such as the full-potential linearized

augmented plane wave method (FP-LAPW) that is utilized in this work [168, 169, 170]. It can more reliably take the crystal structure into account and more accurately describe the semi-core states which we are most interested in. When the wave functions are expressed by a basis, the KS equation [Eq. (3.7)] can be reformulated in an eigenvalue equation which is efficiently diagonalized. The solutions of the equation are the KS eigenenergies and the coefficients of the basis set.

Once the ground state density is found, other properties such as the electronic band structure or atomic forces can be calculated. If the structure is not precisely known one usually relaxes the structure which means, that the atomic positions are iteratively updated according to the forces in order to minimize the total energy. The forces on the nuclei can also be used to obtain the phonon dispersion. Optical properties cannot be derived from ground state DFT since excitation processes are excluded.

3.2.2 Absorption spectra obtained by linear-response TDDFT

In this section, TDDFT is introduced as an approach to calculate XUV absorption spectra. The field of TDDFT uses similar concepts as ground state DFT to answer the question of excited state properties and the dynamics of the electron system when exposed to external perturbations. Similar to the Hohenberg and Kohn theorems, two existence theorems set the foundation of TDDFT. Runge and Gross established in 1984 that there is a one to one correspondence between the time-dependent densities and external potentials for a fixed initial state of the electronic system [171]. The van Leeuwen theorem generalizes this property by stating that the given initial state, interaction and external potential could be replaced by a different initial state and a corresponding unique external potential to obtain the same density [172]. Similar to the ground state it is possible to express all observables as functionals of the time dependent density $n(\mathbf{r},t)$ which is calculated within a non-interacting electron picture. Thereby the initial state and the potential need to be replaced by the KS representatives. This consideration leads to the formulation of the time dependent Kohn-Sham equations which consider switch-on processes and utilize the solution of the ground state KS equation as an initial condition.

For calculations of XUV absorption spectra, a solution of the time dependent KS equations is not necessary as the system is not driven far from its equilibrium position. Instead, one usually uses the linear response theory that expresses the dynamics of the electron systems by linear response functions. A more thorough discussion of the linear response

within the TDDFT approach is found in Refs. [163, 173, 174]. This theory is well suited to accurately describe optical absorption as it captures the intrinsic dynamics of an excitation process. In the following we recapitulate the fundamentals of the linear response theory for optical absorption in solids within the TDDFT context.

If we consider a weak time-dependent perturbation $\delta H(t)$ to the Hamiltonian of a system, the expectation value $a(t)$ of an observable will be time dependent as well. The difference of the time dependent property to the ground state expectation value is called the response $a(t) - a_0$ and is expanded to linear order by perturbation. In the framework of TDDFT, the most important observable is the electron density. When disturbed by some external potential V_{ext}, the corresponding density change can be expressed by [163]

$$n(\mathbf{r},t) = \int_{-\infty}^{\infty} dt' \int d^3r' \chi(\mathbf{r},\mathbf{r}',t-t') V_{ext}(\mathbf{r}',t') \tag{3.8}$$

with the linear response function:

$$\chi(\mathbf{r},\mathbf{r}',t-t') = -i\theta_{\text{step}}(t-t') \langle \Psi_0 | [n(\mathbf{r},t-t'), n(\mathbf{r}')] | \Psi_0 \rangle , \tag{3.9}$$

where the step function $\theta_{\text{step}}(t-t')$ ensures causality. In words, the response function captures the linear response of the electron density at position $\mathbf{r}$ and time t which is a result of a perturbation at position $\mathbf{r}'$ and time t'. Similar to static DFT, it is possible to compute every material property from the density response function if the material is only perturbatively disturbed. Here, the density response function $\chi(\mathbf{r},\mathbf{r}',t-t')$ can be directly used to obtain the material specific absorption coefficient and calculate XUV absorption spectra [174, 175].

Before we discuss how the response function is obtained within the TDDFT theory let us consider two reformulations of the problem. It is common to treat the response in the frequency domain using the Lehmann representation [176, 163]. Thereby, the integration over the time in Eq. (3.8) is absorbed in the Fourier transform and the density can be described by

$$n(\mathbf{r},\omega) = \int d^3r' \chi(\mathbf{r},\mathbf{r}',\omega) V_{ext}[n](\mathbf{r}',\omega). \tag{3.10}$$

With the definition of the step function

$$\theta_{\text{step}}(\tau) = \lim_{\eta \to 0^+} \frac{i}{2\pi} \int_{-\infty}^{\infty} d\omega' \frac{e^{-i\omega'\tau}}{\omega' + i\eta}, \tag{3.11}$$

the response function [Eq. (3.9)] can now be reformulated as

$$\chi(\mathbf{r}, \mathbf{r}', \omega) = \sum_{m=1}^{\infty} \left[\frac{\langle \Psi_0 | n(\mathbf{r}) | \Psi_m \rangle \langle \Psi_m | n(\mathbf{r}') | \Psi_0 \rangle}{\omega - E_m + E_0 + i\eta} - \frac{\langle \Psi_0 | n(\mathbf{r}') | \Psi_m \rangle \langle \Psi_m | n(\mathbf{r}) | \Psi_o \rangle}{\omega + E_m - E_0 + i\eta} \right]. \tag{3.12}$$

Here, Ψ_0 and Ψ_m represent the wave functions of initial and excited state. This representation is very natural for optical absorption which is recorded as a function of the frequency ω. In extended solids one also abandons the real space picture and represent the response function in the reciprocal space [177, 178]. In crystals it is required that $\chi(\mathbf{r}, \mathbf{r}', \omega) = \chi(\mathbf{r} + \mathbf{R}, \mathbf{r}' + \mathbf{R}, \omega)$, where $\mathbf{R}$ corresponds to the lattice vector. This condition is enforced by the Fourier series

$$\chi(\mathbf{r}, \mathbf{r}', \omega) = \frac{1}{V} \sum_{\mathbf{k}} \sum_{\mathbf{G}, \mathbf{G}'} e^{-i(\mathbf{k}+\mathbf{G})\cdot\mathbf{r}} e^{-i(\mathbf{k}+\mathbf{G}')\cdot\mathbf{r}'} \chi_{\mathbf{G},\mathbf{G}'}(\omega), \tag{3.13}$$

where V is the crystal volume and $\mathbf{G}$ is the reciprocal lattice vector. All other quantities need to be transformed in a similar manner.

Up till now we dealt with the classic linear response theory. The strength of TDDFT is the reformulation of the response function in functionals of the electron density within the framework of non-interacting particles:

$$n(\mathbf{r}, t) = \int_{-\infty}^{\infty} dt' \int d^3 r' \chi^{KS}(\mathbf{r}, \mathbf{r}', t - t') V_{ext}^{KS}[n](\mathbf{r}', t'). \tag{3.14}$$

Here, the response function is replaced by the KS equivalent χ^{KS} and the external potential is substituted by an effective potential [163]

$$V_{ext}^{KS}[n](\mathbf{r}', t') = V_{ext}(\mathbf{r}', t') + f_H + f_{XC}. \tag{3.15}$$

The additional two terms represent the derivatives of the Hartree term and the exchange correlation term, that are known from the static DFT.

It is now possible to formulate an equation to link the non-interacting KS system and

the physical system. The van Leeuwen theory guarantees that the density response in the KS system [Eq. (3.14)] is equal to the density change of the real solid system [Eq. (3.8)]. By combining the two equations with the KS effective potential [Eq. (3.15)] in the frequency and k-space representation, the Dyson equation for the linear response in solids is obtained [175, 179]:

$$\chi_{\mathbf{G},\mathbf{G}'}(\omega) = \chi^{KS}_{\mathbf{G},\mathbf{G}'}(\omega) + \sum_{\mathbf{G},\mathbf{G}'} \chi^{KS}_{\mathbf{G},\mathbf{G}'}(\omega)\left[f_H + f_{XC}(\omega)\right]\chi_{\mathbf{G},\mathbf{G}'}(\omega). \tag{3.16}$$

Here, the $\chi^{KS}_{\mathbf{G},\mathbf{G}'}(\omega)$ term is the KS density response function [179]

$$\chi^{KS}_{\mathbf{G},\mathbf{G}'}(\omega) = \frac{1}{N_{\mathbf{k}}\Omega}\sum_{nm\mathbf{k}} \frac{f_{n\mathbf{k}} - f_{m\mathbf{k}}}{E_{n\mathbf{k}} - E_{m\mathbf{k}} + \omega + i\eta} \times M_{nm\mathbf{k}}(\mathbf{G}) M^{*}_{nm\mathbf{k}}(\mathbf{G}'), \tag{3.17}$$

with the matrix elements in the plane wave expansion

$$M_{nm\mathbf{k}}(\mathbf{G}) = \frac{\sqrt{4\pi}}{|\mathbf{G}|}\left\langle n\mathbf{k}\right| e^{-i\mathbf{G}\mathbf{r}} \left|m\mathbf{k}\right\rangle. \tag{3.18}$$

Here, m and n represent band indices, $|m\mathbf{k}\rangle$ is a plane wave function with crystal momentum $\mathbf{k}$, $N_{\mathbf{k}}$ is the number of electronic states, and Ω is the unit-cell volume. The matrix $M_{nm\mathbf{k}}(\mathbf{G})$ is evaluated by using KS wave functions obtained with static DFT in the FP-LAPW basis set. Electron filling is accounted for by the Fermi function $f_{n\mathbf{k}}$. The Hartree and the exchange-correlation kernel are expressed in the reciprocal space representation by:

$$f_H = \delta(\mathbf{G} - \mathbf{G}')\frac{4\pi}{G^2}, \tag{3.19}$$

$$f_{XC} = \frac{\delta V_{XC}}{\delta n}, \tag{3.20}$$

where $\delta(\mathbf{G} - \mathbf{G}')$ is the delta function. In this work, we use the random phase approximation (RPA) which makes a crude assumption by setting the exchange correlation f_{XC} to zero. The RPA drastically improves the computational complexity of the problem and is fairly well justified in large solid systems. This physically motivated approach was introduced by Bohm and Pines [180, 181, 182] and separates the electronic dynamics in two fundamentally different responses. One part oscillates in phase with the driving field independent of the position of the electron. This is the organised response behaviour of

the system. The other part possesses a phase difference with the external perturbation and depends on the position and the history. Justified by the assumption of randomly distributed positions and phases in a system with a large number of electrons, the second term can be neglected as the individual contributions average out. The RPA has seen huge success in describing the optical properties of solids by the Lindhard theory [183] and is widely used in a similar manner within the context of TDDFT even though it neglects the dynamic part of the exchange correlation. In particular, this approximation can capture the core level screening from local field effects [184, 185, 186].

The solved density response function $\chi_{\mathbf{G},\mathbf{G}'}(\omega)$ can be directly translated to the macroscopic dielectric function $\varepsilon_M(\omega)$ and the refractive index by [175]

$$\varepsilon^{-1}_{\mathbf{G},\mathbf{G}'}(\omega) = 1 + f_H \chi_{\mathbf{G},\mathbf{G}'}(\omega), \tag{3.21}$$

$$\varepsilon_M(\omega) = \underline{n}^2(\omega) = 1/\varepsilon^{-1}_{0,0}(\omega) \tag{3.22}$$

The intermediate step with the microscopic dielectric tensor $\varepsilon_{\mathbf{G},\mathbf{G}'}(\omega)$ is needed to account for the local field effects that are captured by the off diagonal elements in the tensor [187, 188]. The macroscopic dielectric function is the average over the whole unit cell.

In this work, optical spectra are computed with the TDDFT implementation *exciting* [189]. It uses the following scheme:

- Perform static DFT and obtain the Kohn-Sham eigenvalues and wave functions.
- Evaluate the $M_{n,m,\mathbf{k}}(\mathbf{G})$ in the LAPW basis functions on a given k-space mesh. A larger matrix significantly increases the computational load and especially the memory requirements in the calculations.
- For calculations without local fields one can approximate $M_{n,m,\mathbf{k}}(\mathbf{G} \to 0)$.
- Calculate the Kohn-Sham response function in Eq. (3.17). The electron temperature can be adjusted by changing the Fermi-distribution functions $f_{n\mathbf{k}}$ and $f_{m\mathbf{k}}$.
- Solve the Dyson equation [Eq. (3.16)] for the interacting response function.
- Use Eq. (3.21) and Eq. (3.22) to obtain the frequency-dependent refractive index.

In this work, particularly important contributions to the spectra are local field effects which have been reported to play a major role in the XUV absorption in transition metals [154, 155, 156]. These are explicitly included in the calculation and appear in the

off-diagonal elements of the M matrix. The local fields are taken into account up to a specific reciprocal lattice vector G_{max} which was tuned in this work by comparing theoretical spectra to the experimental absorption. Detailed information on parameters of the TDDFT calculations can be found in Sec. 8.5. Even though DFT is a ground state approach, we calculated spectra for increased electron temperature. This has been implemented by using a smeared Fermi-Dirac distribution in Eq. (3.17) and for the calculation of the electron density with Eq. (3.5). Please note, that this treatment is not equivalent to a finite equilibrium temperature which would require complete molecular dynamic simulations of the lattice atoms. The smearing is used to estimate the effect for the laser excited electron system before energy is redistributed to the lattice.

3.3 Practical aspects of time-resolved spectroscopy in the ultraviolet regime

Following the introduction of the theoretical concepts, this section will cover the experimental aspects of performing spectroscopy with high-harmonic generation (HHG) sources. In this work, we utilize two similar setups to measure VUV spectra from a solid-state HHG source and transmission spectra with a gas phase HHG source in the XUV region. Details of the experimental implementations are presented in chapters 6 and 8, respectively. In the following we will give a more general discussion of the involved experimental challenges with a focus on spectrometer design, sample preparation and time-resolved measurements.

Contrary to its visible counterpart, spectrometers for experiments in the VUV and XUV regime need to reduce the re-absorption of the light. Since all materials, even gases at ambient conditions, lead to significant re-absorption on less than a millimeter, the propagation path of the high harmonic radiation needs to be evacuated. As discussed in Sec. 2.4, this is especially challenging for gas-phase HHG sources since the gas ballast need to be handled by a suited pump. Another aspect is the design of customized optical elements that mitigate absorption losses. Transmission optics would need to be limited to sub micrometer thicknesses and can not sufficiently focus VUV and XUV radiation due to the weak dispersions in this wavelength region. Therefore, most experiments rely on reflective optics which are often used at high incident angles to maximize the reflection coefficient. Here, multilayer mirrors allow a wavelength-selective maximization of the

reflection and a widely applied. A toroidally shaped mirror is usually used to focus the incident beam. This allows to collect the divergent beam from the HHG source and create a micrometer scale illumination spot on the sample. Furthermore, a reflective grating is used to generate a spectrum on a charge-coupled device (CCD) camera or a microchannel plate. For focusing onto the detector, it is possible to use a grating printed on a toroidal mirror or separate the two devices. The latter is disfavoured in order to reduce the number of reflective surfaces and minimize losses. In addition, it is possible to correct optical aberrations with precisely and specifically manufactured gratings. Here, the most important distinction is made between toroidal gratings that focus on a sphere and those with a flat field focus. Only a flat field focus can accurately be positioned on flat detectors and yield better spectral resolution while spherical focii are usually used in monochromators. However, as the radius of the sphere focus is usually large in comparison to the detector size, non flat field gratings can still yield good results in spectroscopic applications.

In this work we utilize a spectrometer with a flat field grating and a microchannel plate for the experiments with solid-state HHG in the VUV. Here, accurate spectral information is of great importance, as small spectral shifts are recorded. The vacuum chamber is compact and does not require high throughput pumps since no gas source is present.

For spectroscopy with HHG in solids it has been discussed in Sec. 2.4 that the fundamental laser is required to not exceed the band gap of the investigated material. Therefore, we utilize a titanium sapphire amplifier laser pump in a reflection geometry which permits bulk crystalline materials with a band gap of at least 1.55 eV to be investigated. In combination with the wide band gap insulators MgO and quartz, we observe a high damage threshold which is ideal for high-order harmonic generation. More generally, by tuning the laser wavelength, efficient HHG in a large variety of solids is feasible [190, 37, 38, 104].

For transmission experiments with a gas-phase HHG source we utilize a non-flat field grating and a CCD camera to record XUV spectra. Here, more strict vacuum requirements need to be met. The HHG source chamber is separated by an aluminum filter from the subsequent optics to block the remaining fundamental beam and allow high vacuum conditions which minimize absorption losses and reduce contamination on cooled samples. Since most solid samples show strong re-absorption of XUV radiation on the 100 nm scale, only thin film samples can be investigated in transmission. Such specimens can be fabricated by various methods which include growth on thin substrates, focused ion beam milling, lithography, etching, exfoliation and ultramicrotomy. The last technique

represents a well established procedure for materials research and uses a diamond knife to cut thin flakes from a bulk sample [191]. In this work, we were able to reliably produce 60 nm thick flakes of $1T$-$TiSe_2$ by ultramicrotomy and transfer the specimens onto a silicon membranes of 30 nm thickness. We use silicon membranes since they offer more structural rigidity and thermal contact compared to free standing samples on a grid structure. In comparison to the widely spread silicon nitride membranes, the transmission of XUV radiation is significantly better for similar thicknesses of silicon. Despite the difficulties for the production of thin samples, most materials can, in principle, be used for transmission studies with XUV sources.

Ultrafast transient absorption spectroscopy uses a pump-probe scheme. Here, two optical pulses are overlapped on the sample. The pump pulse triggers some dynamics in the specimen by exciting its electrons, and the probe pulse is transmitted through the sample to interrogate its properties. In practice, one usually compares spectra with (I_{pumped}) and without (I_{unpumped}) the pump beam. This allows to identify pump induced changes in the sample with better precision. To minimize the long term noise, pumped and unpumped spectra are recorded in quick succession by chopping the pump beam with half the frequency of the probe beam. This approach is standard in most beam lines. In chapter 7 we will discuss the use of an advanced referencing approach enhanced by machine learning which further improves the sensitivity by more than one order of magnitude. By varying the delay between the pump and the probe pulses it is possible to obtain a movie of reversible sample dynamics in a stroboscopic fashion. Here, the temporal resolution is determined by the convolution of pump and probe pulse lengths at the sample. Due to the possibility for isolated attosecond pulses, HHG offers unprecedented time resolution. Attosecond XUV absorption spectroscopy with HHG sources is demonstrated and is the workhorse in the attosecond community. However, in this work we utilize femtosecond harmonic radiation as we are mostly interested in somewhat slower lattice dynamics.

Chapter 4

Fitting experimental data with machine learning

One of the biggest obstacles for spectroscopic experiments with gas-phase high-harmonic generation (HHG) sources is the high noise floor which hinders observations of weak absorption changes. Since sample degradation and experimental stability limit the maximal integration time, studies of subtle sample dynamics are very challenging. A variety of referencing approaches have been introduced to mitigate the noise problem and a typical sensitivity of 1 mOD is achieved in current experiments [192, 57, 193, 50, 194]. However, investigations of subtle sample dynamics such as the below-threshold charge density wave (CDW) excitation in 1T-$TiSe_2$, studied in this work, remain below this sensitivity boundary. To overcome this limitation we developed an advanced referencing scheme based on machine learning (ML).

This chapter introduces the basics of data driven models, ML, and artificial neural networks while the application for noise reduction is presented in depth in chapter 7. In the following, the focus will be on *supervised learning* which relies on labeled training data to fit a model which is used for predictions [195]. The two other existing categories of ML are *unsupervised learning* used for clustering or dimensionality reduction [196], and *reinforcement learning* where an agent learns by interacting with an environment [197]. The latter two classes are beyond the scope of this work. In Sec. 4.1, ML and the use of data for predictive modeling is introduced while Sec. 4.2 elucidates the class of artificial neural networks. Chapters 7 and 8 present the use of a neural network for noise reduction in absorption spectroscopy with an HHG source.

4.1 Data driven models and machine learning

In empirical sciences, physics in particular, experimental data and statistics are used to estimate unknown quantities. As an example, this work measures the wavelength dependent transmission of light through a specimen with the goal of determining the material properties. Specifically, mathematical models which previously have been proven to accurately describe physical mechanisms are used to extract particular material constants. The knowledge that is gained from the new data is then used to refine the model in the iterative scientific method. On the contrary, ML is focused on automatically learning from available data in order to make informed choices. It focuses on predicting future data rather than estimating unknown quantities. In most cases, ML uses generic models with a large number of fitting parameters. By adjusting the parameters, the model is "trained", but little information on the underlying mechanism is gained. Nevertheless, in the last years ML models celebrated huge successes and achieved unprecedented accuracy, due to the availability of large data sets. Thanks to their great computational scaling, ML approaches can utilize huge amounts of multi-dimensional data which increases their predictive power. Thereby, a variety of fields in science and industry successfully applied ML to complex problems such as image and voice recognition [198, 199, 200], natural language processing [201, 202], and noise reduction [203, 204, 205].

Despite the great success in other fields, ML has somewhat limited applicability in natural sciences due to the poor interpretability of the results. A prediction of future measurements has limited use when the underlying mechanism cannot be derived from the ML model. Physically motivated models yield much more information. This reduces the applicability of ML to the distinction between the two goals of achieving an accurate prediction or understanding the underlying mechanism. For the application in noise reduction of HHG sources the microscopic mechanism is interesting, but a maximized signal-to-noise level is more important. To this end, ML is ideally suited to be used as a general model which helps to find the best noise reduction during data extraction and evaluation. However, it should be noted that tremendous efforts are focused on the interpretability of ML models such that those models may become more suited in natural sciences in the future [206, 207, 208, 209, 210].

Now that we have established in which context ML is suitable at the current stage, let us discuss how it can utilize training data for future predictions. The fundamental ingredient in *supervised learning* is the data set $D = (\mathbf{X}, \mathbf{Y})$. It is composed by two matrices

consisting of n measurements of a d-dimensional feature vector $\mathbf{x}$ and an m-dimensional, dependent observable vector $\mathbf{y}$. The distinction of the observables from the features is arbitrary and may be chosen according to the problem that is supposed to be solved. In the next step, a ML model with some trainable parameters (= fit parameters) $\mathbf{a}$ is formulated to relate the two quantities by a function $\hat{\mathbf{Y}} = f(\mathbf{X};\mathbf{a})$, $f : \mathbf{x} \rightarrow \hat{\mathbf{y}}$. This function is used to predict the observable from the feature vector. The accuracy of the model is computed by the *cost function* which is usually the mean-squared error (MSE) [211]:

$$C(\mathbf{Y}, f(\mathbf{X};\mathbf{a})) = \frac{1}{m}\sum_{j=1}^{m}\frac{1}{n}\sum_{i=1}^{n}(y_{i,j} - \hat{y}_{i,j}(\mathbf{X},\mathbf{a}))^2. \tag{4.1}$$

When the model and the cost function are defined, the measured data set is used to train the model. Thereby, the cost function is minimized with respect to the fit parameters:

$$\hat{\mathbf{a}} = \arg\min_{\mathbf{a}}\left[C\left(\mathbf{Y}, f(\mathbf{X};\mathbf{a})\right)\right]. \tag{4.2}$$

Minimizing the MSE is known as the method of the least squares and is a common tool in statistics used for experiments with Gaussian noise [211]. However, in some cases it is useful to modify the cost function.

The standard method for finding the global minimum in a complex cost landscape is gradient descent (GD) [212, 195]. Figure 4.1 illustrates an example for a two dimensional energy landscape in which a GD algorithm iteratively approaches the minimum. The basic idea behind the algorithm is to adjust the free parameters $\mathbf{a}$ in the direction of the

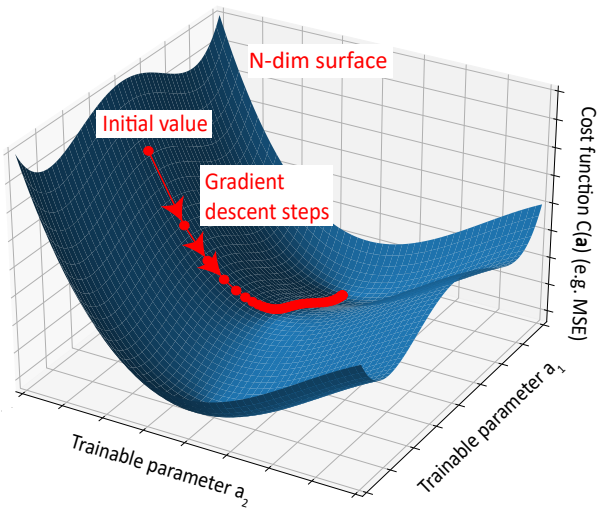

Figure 4.1: Gradient descent. Machine learning models are trained by minimizing the cost function in a large, N-dimensional space of trainable parameters $\mathbf{a}$. The gradient descent algorithm utilizes the local derivative to find the minimum in an iterative fashion.

maximal negative gradient of the cost function. Starting at an initial condition $\mathbf{a}_0$, the fit parameters are iteratively updated by the equation [212, 211]:

$$\mathbf{v}_k = \eta_k \nabla_{\mathbf{a}} C(\mathbf{a}_k), \tag{4.3}$$

$$\mathbf{a}_{k+1} = \mathbf{a}_k - \mathbf{v}_k. \tag{4.4}$$

Here, $\nabla_{\mathbf{a}} C(\mathbf{a}_k)$ is the derivative of the cost function with respect to the fit parameters $\mathbf{a}_k$ at iteration k. The quantity η_k is called step size or learning rate. Determining its magnitude is one of the biggest challenges in GD. Small step sizes will improve the convergence to a minimum but come with a large computational cost. This dilemma is solved by the Newton method which uses the Hessian matrix to dynamically adjust the step size in order to efficiently approach the minimum. However, for practical applications in ML, basic GD causes a variety of problems due to the high dimensionality and the large number of data sets. First, the algorithm might get stuck in local minima or saddle points which are abundant in high-dimensional, non-convex energy landscapes. In addition, the cost function is not known but estimated from the available data which leads to substantial computational costs for computing derivatives and the Hessian matrix. These shortcomings can be overcome by variations of the simple GD which have been developed for practical applications in ML and numeric optimization.

The most common variant of GD is the stochastic gradient descent (SGD) which, as the names suggests, introduces some stochasticity to the algorithm [213, 214, 215]. It forms the foundation of most modern GD codes and is the backbone for training artificial neural networks. The SGD algorithm computes the gradient on subsets of the available data called mini-batches B [212]. Usually the size of these batches range from ten to a few hundred data points, substantially reducing the size of the total data set that is typically in the ten to hundred thousands. By varying the batch B_k for each iteration k, a stochasticity is introduced in the gradient $\nabla_{\mathbf{a}} C^{B_k}(\mathbf{a}_k)$, which helps to avoid local minima and saddle points. The calculation of the gradient on a small subset significantly speeds up the computation. In addition, almost all variants of SGD introduce a momentum term. From a physicists perspective, it is clear that an inertia term will help the algorithm to achieve larger step sizes in the dimensions of small but continuous negative derivatives. At the same time, oscillations in high curvature directions are suppressed. This is particularly useful in combination with mini-batches to keep a large learning rate even if the derivative of a single batch might vanish. The implementation typically uses a running average to

update the fit parameters by [212]

$$\mathbf{v}_k = \gamma \mathbf{v}_{k-1} + \eta_k \nabla_{\mathbf{a}} C^{B_k}(\mathbf{a}_k), \tag{4.5}$$

$$\mathbf{a}_{k+1} = \mathbf{a}_k - \mathbf{v}_k, \tag{4.6}$$

with inclusion of the momentum parameter $\gamma < 1$. In this representation, the SGD already solves most of the mentioned problems but the learning rate η_k is still to be determined. The use of the Hessian matrix or its approximations is computationally unfeasible in high dimensions. To this end algorithms such as AdaSprop, AdaGrad, AdaDelta, RMSprop and ADAM have been developed for an efficient adjustment of the learning rate by the first and second moment of the gradient [212]. Only relying on the first derivative, these algorithms are significantly faster while offering similar accuracy in comparison to second-derivative methods. In this work, we apply the ADAM algorithm that uses a running average of both the gradient and the second moment to adjust the step size. It showed good performance in a large variety of tasks where it slightly outperforms other sophisticated optimizers such as RMSprop [216].

Up to now we have discussed how a specific model is fit to experimental data by adjusting the fit parameters. However, it is still unclear how to choose the model function f and how to predict future data sets. Before going into the details, both questions are answered qualitatively. By using the parameters $\hat{\mathbf{a}}$ obtained with Eq. (4.2), the model is applied to a new data set of the feature space $\mathbf{X}_{test}$ by estimating the corresponding observable $\mathbf{Y}_{pred} = f(\mathbf{X}_{test}; \hat{\mathbf{a}})$. The accuracy of the estimation, which is the main goal in ML, can be calculated by the MSE [Eq. (4.1)] if the observables are additionally recorded. To this end it has become standard in the ML context, to split the available data set into training data $D_{\text{train}} = (\mathbf{X}_{\text{train}}, \mathbf{Y}_{\text{train}})$ and test data $D_{\text{test}} = (\mathbf{X}_{\text{test}}, \mathbf{Y}_{\text{test}})$. Only the training set is used to perform the fitting procedure while the test set is used to calculate the predictive power of the ML model on unseen data. Therefore, the error of the test data is also called out-of-sample error or the generalization error. As we will discuss in detail in the next paragraphs, the out-of-sample error can be used to find the best suited model function. In practice, a collection of different model functions is tested and the one with the lowest generalization error is chosen. It can not be stressed enough that the test data should be kept separate from the training data during the fitting and eventual preprocessing steps to avoid leakage of information. A ratio between training and test data sizes of roughly 80% to 90% has been found to work best for most applications [211].

Let us now have a closer look on the generalization error. Assume an arbitrary ML model f which is fitted by a data set $D = (\mathbf{X}_{\text{train}}, \mathbf{Y}_{\text{train}})$. This data is generated by a true, physical function $\mathbf{y} = g(\mathbf{x}) + \varepsilon$ including some Gaussian noise ε with standard deviation σ_ε. Since the fit parameters of the model are found with Eq. (4.2) by learning from the training data, they are a function of the data set D denoted as $\hat{\mathbf{a}}_D$. In conclusion, the sampling of different data sets from the space of all possible data sets results in varying generalization errors. In order to analyze this behaviour, we construct the hypothetical expectation value $\mathbb{E}_D$ which averages over all possible data sets. In the same manner we may average over all instances of the noise to obtain the noise expectation value $\mathbb{E}_\varepsilon$. A combination of both expectation values yields the expected generalization error [217, 211]:

$$E_{out} := \mathbb{E}_{D,\varepsilon}\left[C(\mathbf{y}, f(\mathbf{x}; a_D))\right] = \mathbb{E}_{D,\varepsilon}\left[\sum_i (\mathbf{y}_i - f(\mathbf{x}_i; a_D))^2\right] \tag{4.7}$$

$$= \sum_i \sigma_\varepsilon^2 + \mathbb{E}_D\left[(g(\mathbf{x}_i) - f(\mathbf{x}_i; a_D))^2\right]. \tag{4.8}$$

Line two inserts the true, physical function and separates the noise term. The second term of Eq. (4.8) can be further expanded as [217]:

$$\mathbb{E}_D\left[(g(\mathbf{x}_i) - f(\mathbf{x}_i; a_D))^2\right] = (g(\mathbf{x}_i) - \mathbb{E}_D\left[f(\mathbf{x}_i; a_D)\right])^2 + \mathbb{E}_D\left[(f(\mathbf{x}_i; a_D) - \mathbb{E}_D[f(\mathbf{x}_i; a_D)])^2\right]. \tag{4.9}$$

Here, the first term is called bias and describes the discrepancy of the chosen model from the true value. In the limit of infinite training data the bias measures how well the model is suited to describe the true generator of the data and is therefore a function of the model itself. The second term is called variance and estimates the fluctuations of the finite training data set. Combining Eq. (4.8) and Eq. (4.9) allows to formulate one of the most important relations in ML which is called the bias-variance decomposition [218]:

$$E_{out} = \text{Bias}^2 + \text{Var} + \text{Noise}. \tag{4.10}$$

The noise which is given by $\sum_i \sigma_\varepsilon^2$ is often call irreducible error as it results from the data acquisition itself and can not be surpassed by any ML model. A typical example in the field of physics would be the shot noise.

To gain a better intuition of the bias-variance decomposition it is useful to discuss some important dependencies. Figure 4.2(a) displays the out-of-sample error and the in-sample error $E_{in} := C(\mathbf{Y}_{\text{train}}, f(\mathbf{X}_{\text{train}}; \mathbf{a}))$ as a function of the training data size. By increasing the amount of training data, the out-of-sample error will decrease due to the improved variance. At the same time, the in-sample error is increased with the data set size. In the limit of infinite training data both values converge to the sum of the noise and the bias of the chosen model. In practice, the training data size is often fixed and cannot be arbitrarily expanded which results in a finite value for the variance. On the contrary, it is simple to change the model complexity which is closely related to the number of fitting parameters. The out-of-sample error as a function of model complexity is depicted in Fig. 4.2(b) and is decomposed into bias and variance. Increasing the model complexity allows to fit more complex phenomena and the bias tends to decrease. At the same time, an increase in model complexity will lead to an increase in the variance. The optimal model complexity is found in the intermediate regime at the minimum of the generalization error. Too large model complexities correspond to an overfitting while too small values result in underfitting. Finding the optimal balance between both is known as the bias-variance tradeoff of ML and one of the most central problems in this field. Due to the finite training data size and large size of ML models, overfitting is typically a more severe problem such that it is often advised to use a high-bias small-variance model [218]. Figure 4.2(c) illustrates the difference between a high-bias, low-variance and a low-bias, high-variance model. The crosses symbolize different data sets with fixed size. In this example, the low-bias model on average describes the truth better, but the limitation to a single fixed data set renders the less complex model more suited to predict the true model. In conclusion, the bias variance decomposition nicely illustrates the significance of underfitting and overfitting and how they relate to the out-of-sample error even if the bias and variance terms can not be calculated in most applications.

For practical applications, many different approaches have been developed to deal with the bias-variance tradeoff. If faced with a large number of fit parameters, like in multivariate linear regression, it is often not favoured to omit any features as they potentially carry valuable information. Instead, it is more useful to introduce some sort of regularization that is often introduced as a penalty term in the cost function. Popular choices are the L_1

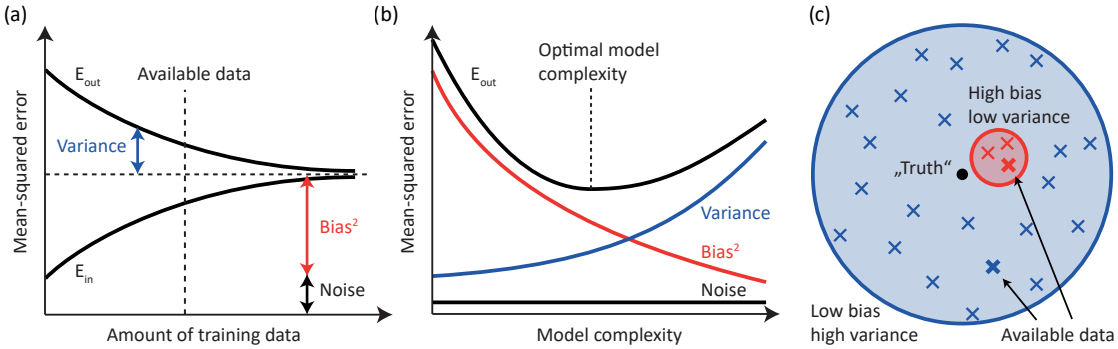

Figure 4.2: The bias-variance tradeoff. (a) The in-sample error E_{in} and the out-of-sample error E_{out} are displayed as a function of the training data size. With increasing number of training samples both quantities converge to a value that is defined by the bias and the noise. In this illustration, the model function is not complex enough to describe the truth. (b) The out-of-sample error E_{out} can be decomposed into variance, bias, and noise terms. With increasing model complexity the bias continuously decreases while the variance increases for a fixed size of available training data. In ML the optimal model complexity is found by a tradeoff between variance and bias. (c) In a two dimensional representation of the out-of-sample error E_{out} the difference between a high-bias, low-variance and a low-bias, high-variance model is visualised. Each cross represents a different training data set of fixed size. A complex model (blue) possesses a smaller bias but a larger variance in comparison to a simpler function (red). In practice, the high-bias model is often better suited for predictions due to limited training data.

or L_2 norm in the form of [219, 220]:

$$C^2(\mathbf{Y}, f(\mathbf{X};\mathbf{a})) = C(\mathbf{Y}, f(\mathbf{X};\mathbf{a})) + \lambda ||\mathbf{a}||_2^2, \tag{4.11}$$

$$C^1(\mathbf{Y}, f(\mathbf{X};\mathbf{a})) = C(\mathbf{Y}, f(\mathbf{X};\mathbf{a})) + \lambda ||\mathbf{a}||_1. \tag{4.12}$$

Here, an additional term with the parameter λ is introduced to the cost function [Eq. (4.1)]. In the context of linear models, the two presented choices are also known as Ridge-regression [220] and Lasso-regression [219], respectively. Both options help to prevent overfitting by favouring small fit parameters and reducing the values of irrelevant features to near zero. However, the modified models introduce the additional hyperparameter λ which needs to be defined.

A different, intuitive approach is the variation of the model complexity. For example, linear regression can be expanded to higher order polynomials. If the model is to complex, the polynomial order needs to be reduced while it is useful to increase the exponent in the high-bias regime. Again, this introduces an additional hyperparameter which is the polynomial degree. But how can the optimal hyperparameters be determined? In short,

the optimal parameter is the one that yields the model with the best generalization error E_{out}. To this end, the test data is used to compute the out-of-sample error and compare different hyperparameters. A typical example of the in-sample and out-of-sample error as a function of the model complexity is shown in Fig. 4.3(a). By increasing the complexity, the in-sample error continuously decreases as the model is better adjusted to the training data. In contrast, the out-of-sample error exhibits an optimum at intermediate complexities as derived in the discussion of the bias-variance decomposition.

Since the hyperparameters are chosen by minimizing the generalization error, the test data set is used in the learning process which is called the model selection bias. As a result, the performance on other, unseen data is worse and the true generalization error can no longer be reliably determined. This problem is solved by using an additional data set which is called the validation data to determine the model complexity. In order to avoid further reduction of the available training data, one usually applies the cross-validation scheme shown in Fig. 4.3(b). After the typical test training split of 80:20, this re-sampling method separates the validation data set from the available training data and uses it to evaluate the hyperparameters. By permutatively using different validation sets and averaging the results of the validation error, training and model selection is performed on the whole training data set. The additional test data is not involved in the fitting or model selection and can estimate the out-of-sample error accurately. Figure 4.3(b) shows a four-fold cross-validation that uses 434 permutations of validation data. In chapter 7, this technique is utilized to find the best suited polynomial function for the referencing of extreme ultraviolet (XUV) spectra.

In this section, the fundamentals of ML have been discussed from a more general perspective. The presented bias-variance tradeoff, the problem of model selection, and the training by SGD are general concepts in the whole field of ML. In particular, artificial neural networks that are discussed in the next section, heavily rely on the presented concepts. In the context of specific ML models, we introduced linear and nonlinear regression, which are applied in chapter 7. Other models in the vast space of ML approaches are not discussed as a part of this work, but can be found in one of the many great textbooks [217, 221, 211, 195, 222].

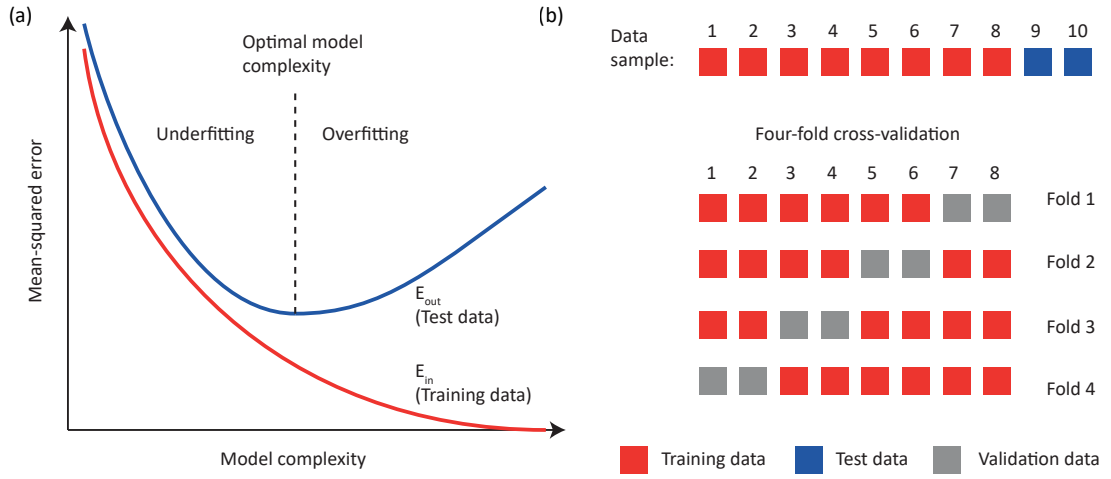

Figure 4.3: Model selection in machine learning. (a) Increasing the model complexity reduces the error of the training data. The out-of-sample error first decreases with increasing model complexity before overfitting sets in. The optimal model minimizes the test error. (b) In ML, the available samples of data are separated into training and testing data and the model's hyperparameters are typically determined by cross-validation. Here, the validation data is permutatively taken from the training data and used to find the best hyperparameters while simultaneously maximizing the available training data.

4.2 Artificial neural networks

In the last decade, artificial neural networks evolved to the most frequently used and most powerful method of ML [223]. Inspired by the biological neural system, artificial neural networks comprise the extension of regression methods to a more powerful general approximator. In particular, deep neural networks, which are sometimes labeled *deep learning*, are capable of incorporating huge data sets to form incredibly accurate predictions. A famous example is the 2012 breakthrough in the ImageNet classification challenge of images [224], which is believed to be the start of modern ML. Today, deep neural networks surpass the human accuracy in a large variety of tasks. In this section, the basics of neural networks will be explained with a focus on supervised learning for regression tasks.

As the name suggests, an artificial neural network is built from individual neurons connected in a certain network architecture. In this work, we employ a simple feed-forward network, that uses layers of neurons as shown in Fig. 4.4(a). Each neuron takes an input vector $\mathbf{x} = x_1, x_2, \ldots$ and produces a scalar output which is used as input for the neurons of the next layer. If a layer is fully connected with its preceding layer it is called dense

and in the example all layers fulfill this property. The first layer takes the provided input, the last layer outputs the prediction and all other layers are labeled *hidden*. A model with a large number of hidden layers is referred to as deep or deep learning. Over the years, many specialised architectures have been developed. Most notably are the convolutional neural networks that utilize convolutions for efficient processing of images [199, 200] and the recurrent neural networks which are suited for sequential inputs [225].

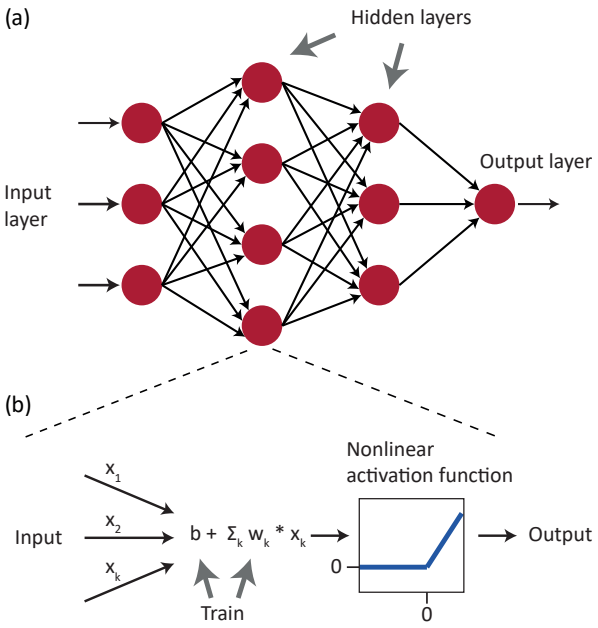

Figure 4.4: Neural network architecture. (a) Feed-forward neural network with two hidden layers. The neurons are fully connected between the layers. (b) The building blocks: Neurons. A neuron is trained by changing the weights and the bias. The linear sum is multiplied by a nonlinear activation function to allow modeling of nonlinear behaviour by the network.

Figure 4.4(b) illustrates how the output of a neuron is calculated. All inputs x_k are multiplied by trainable weights w_k, summed up, and offset by a trainable bias b yielding $z = \sum_k w_k x_k + b$. A neural network is trained by fitting these parameters which essentially weights the importance of the individual inputs. It is essential that the result is multiplied afterwards with a nonlinear activation function $\sigma(z)$ to build a nonlinear ML model. Many different nonlinearities have been tested regarding their accuracy and computational time. Early approaches used the biologically motivated perceptron model which utilizes a step function to compute the output [226]. Other functions are illustrated in Fig. 4.5 and include the sigmoid function which is formally equivalent to the Fermi function, the hyperbolic tangent, and the rectified-linear-unit activation function (ReLU). It was found that the choice of the activation function strongly influences the accuracy and the computational properties. Since neural networks are trained by GD, the algorithm relies on derivatives of the activation function to approach a minimum in the cost function. A vanishing derivative in the case of the perceptron, the sigmoid, and hyperbolic tangent at large

inputs can lead to the training of fit parameters being stuck. As the networks tent to end up at large values, a non vanishing gradient of the activation function is needed. In this work, we utilize the ReLU function which scales linearly without saturation above zero. It is most widely used and shows great performance in a large variety of ML tasks. Other more sophisticated activation functions like leaky ReLU or ELU aim to additionally avoid the vanishing derivative below inputs of zero which is found to improve the training in some cases.

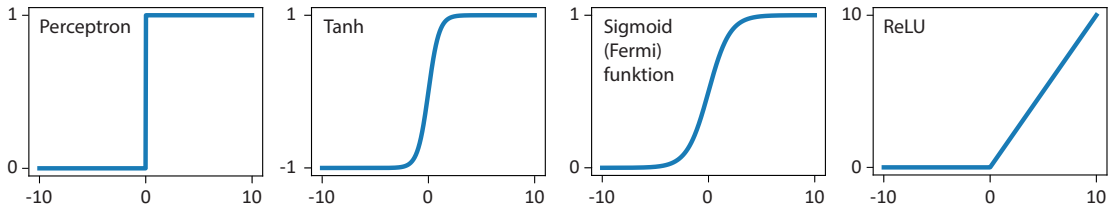

Figure 4.5: Neural-network activation functions. The use of a nonlinear activation function allows to model nonlinear problems with a neural network. The traditionally used functions include the step function (Perceptron), hyperbolic tangents, and the Sigmoid function. In modern architectures, non-saturating functions such as the rectified linear unit (ReLU) are used to improve training efficiency at large input values.

With increasing number of hidden layers and number of neurons, the expressive power of a neural network greatly increases. It is guaranteed by the universal approximation theorem [227], that a sufficiently large feed-forward neural network is capable of approximating any continuous multi-input/multi-output function with arbitrary precision. The proof of this theorem has been provided in a very illustrative and graphical way as shown in Ref. [228]. In short, the use of hidden-layer neurons allows to construct step functions with arbitrary height and width. The more neurons, the more step functions can be constructed. In the limit of an infinite network, any functional behavior can be approximated. Despite this great theoretical foundation, the theorem should not be overemphasised as it does not provide an answer to the size and architecture that should be used.

Similar to the fitting of regression models, a neural network is trained by minimizing the cost function. However, in contrast to well-defined model functions such as linear or polynomial regression, it is not straight forward to compute the derivatives in a layered neural network, where every fit parameter of hidden layers influences the output. To this end, the so-called backpropagation algorithm is used to find the gradient of the cost function. It first propagates the input of a training data set forward in the network and compares it to the desired output. The difference between the obtained output and the

data is used to compute the total cost and the gradient. The latter is nothing else than the desired direction towards which the model should be tuned. By back propagating the gradients back through the network, the derivatives of each trainable parameter is calculated by the chain rule of partial derivatives. The calculated derivatives of every input-output couple in the training data set is averaged to compute the total derivative in every step of the iterative GD.

To gain a better understanding of the backpropagation algorithm, the following paragraph introduces its mathematical foundation. Based on the chain rule of differentiation it is possible to formulate the equations that enable the backpropagation scheme [228]. Assume a network with L layers indicated by index $l = 1, ..., L$. The weights are denoted by $w^l_{j,k}$ to describe the coupling of the kth neuron in layer l to the jth neuron in the succeeding layer. For the corresponding bias, we use b^l_j. In this notation, it is possible to write the output of a neuron, also called activation, as

$$x^l_j = \sigma(z^l_j) = \sigma\left(\sum_k w^l_{jk} x^{l-1}_k + b^l_j\right), \tag{4.13}$$

and thereby relate it to the output of the preceding layer. It follows that the output of the last layer which is used to compute the cost function indirectly depends on all other layers. For the last layer we define the partial derivative of the error with respect to a change of the input z^L_j by:

$$\Delta^L_j := \frac{\partial E}{\partial z^L_j}. \tag{4.14}$$

By analogy, the derivative of a hidden layer is defined by:

$$\Delta^l_j := \frac{\partial E}{\partial z^l_j} = \frac{\partial E}{\partial x^l_j}\sigma'(x^l_j), \tag{4.15}$$

where $\sigma'(a)$ represents the derivative of the activation function which is easy to calculate in the case of the ReLU function. At the same time, it is also possible to express the partial derivative as a differentiation with respect to the bias:

$$\Delta^l_j = \frac{\partial E}{\partial z^l_j} = \frac{\partial E}{\partial b^l_j}\frac{\partial b^l_j}{\partial z^l_j} = \frac{\partial E}{\partial b^l_j}. \tag{4.16}$$

Here, it was used such that the partial derivative $\frac{\partial b_j^l}{\partial z_j^l}$ is equal to one, according to Eq. (4.13). The error of two subsequent layers is connected by the chain rule of differentiation:

$$\Delta_j^l = \frac{\partial E}{\partial z_j^l} = \sum_k \frac{\partial E}{\partial z_k^{l+1}} \frac{\partial z_k^{l+1}}{\partial z_k^l} \tag{4.17}$$

$$= \sum_k \Delta_j^{l+1} \frac{\partial z_k^{l+1}}{\partial z_k^l}. \tag{4.18}$$

This equation allows to propagate the error back through the network. The last important equation of the algorithm calculates the error with respect to the weights:

$$\frac{\partial E}{\partial w_{jk}^l} = \frac{\partial E}{\partial z_j^l} \frac{\partial z_j^l}{\partial w_{jk}^l} = \Delta_j^l x_k^{l-1}. \tag{4.19}$$

Based on the equations it is now possible to find the gradient of the error with respect to all biases $\frac{\partial E}{\partial b_j^l}$ and all weights $\frac{\partial E}{\partial w_{jk}^l}$ in order to perform an SGD step. The backpropagation algorithm consists of fife steps to compute the gradient by [228]:

- Input the experimental data as the activation x^1 in the first layer.
- Propagate through the network and calculate x^l and z^l for every layer l with Eq. (4.13).
- Compute the derivative Δ_j^L of the output layer [Eq. (4.14)].
- Backpropagate the error through the network and compute the error Δ_j^l for each layer and neuron by Eq. (4.18).
- Calculate the gradients of the cost function [Eq. (4.16) and Eq. (4.19)]:

When the gradient in the high-dimensional space is found, SGD is applied to find the minimum in the cost function. As all derivatives can be computed in a single forward and backward pass of the network, the backpropagation algorithm enables layered neural networks to be very efficiently trained. Among other technical aspects, the algorithmic efficiency in computing the gradients allow deep neural networks with a large set of parameters to be efficiently trained in order to approximate complex functional behaviour.

Since neural networks typically possess large model complexities, it is particularly important to balance the bias-variance-tradeoff and counteract overfitting. Most regularization techniques that have been developed for other ML tasks such as L_1 and L_2 penalties

can be transferred to neural networks [223]. A method that is exclusive to neural network models is the *Dropout* procedure [229]. By removing a fraction of neurons with the corresponding connections from the network it is thinned and reduced in complexity. Each neuron has a probability p of being removed at each training step and the predictions are made by using the complete network with corrected weights $w_{test} = p\, w_{train}$. Thereby, the reduction in model complexity prevents overfitting, while the complete network resembles an average over different models similar to ensemble methods that combine multiple different ML models [230].

On of the most important regularization schemes for neural network is the SGD algorithm [231, 223]. As described earlier, SGD divides the training data in mini-batches and performs training on this reduced data set. The stochasticity induced by SGD induces fluctuations that prevent overfitting to fine details in the training data. As the gradient computed with mini-batches does not correspond to the true value, the SGD step will be sub-optimal, but the statistic variation between different batches tend to average out. For long training times, overfitting might still be an issue, but in practice, the model complexity of a neural network trained by SGD only slowly increases. To this end it is very effective to combine SGD with an early stopping routine that monitors the out-of-sample error and interrupts training at the optimal model complexity shown in Fig. 4.3(a). In practice, this combined approach has proven to be very powerful and has become a widely applied tool for regularization [211].

In conclusion, neural networks present a versatile and extremely powerful ML approach. In particular, they can utilize the full information in extremely large data sets to make predictions that outperform every other ML model. In addition, even extensive deep neural networks are trained in reasonable time thanks to the efficient and highly parallelizable backpropagation algorithm. In combination, this explains the success in a large variety of fields where huge amounts of labeled training data is available. We utilize this properties of the neural network for noise reduction in XUV absorption spectroscopy that is discussed in chapter 7. The neural network surpasses other tested ML models in this task with the given amount of training data.

Chapter 5

Charge-density-wave formation in titanium diselenide

In the last decades various new states of condensed matter with surprising and technologically interesting properties have been intensively studied. The list of materials include superconductors, Mott insulators, charge-density-wave (CDW) compounds, antiferromagnets, and topological phases. A particularly interesting class of materials are quasi two-dimensional materials which exhibit a large variety of quantum phases and can be easily engineered through layering. Section 8 of this work investigates the CDW phase of the transition-metal dichalcogenide (TMDC) $1T$-$TiSe_2$. As a brief introduction, this chapter summarizes the basics of CDW formation and highlights previous studies of ultrafast CDW dynamics in $1T$-$TiSe_2$. A more general discussion of CDW formation is found in [8].

5.1 Fundamentals of charge-density-wave formation

Charge density waves are periodic modulations of the electron density in a commensurate or incommensurate fashion with the underlying atomic lattice. Here, the charge density can be written as [8]

$$\rho(\mathbf{r}) = \rho_0(\mathbf{r})\left(1+\rho_1\cos(\mathbf{q}_{\mathrm{CDW}}\mathbf{r}+\Phi)\right), \tag{5.1}$$

where $\rho_0(\mathbf{r})$ describes the unperturbed electron density and ρ_1, $\mathbf{q}_{\mathrm{CDW}}$, and Φ refer to the amplitude, wave vector, and phase of the charge modulation, respectively. A changed electron density will inevitable change the potential energy landscape acting on the atoms

and will lead to a periodic lattice distortion (PLD) in the form of [8]

$$u_n = u_0 \sin(n|\mathbf{q}_{\mathrm{CDW}}|a + \Phi). \tag{5.2}$$

Here u_n describes the displacement at lattice cite n, u_0 is the amplitude of the displacement, and a refers to the lattice constant. Vise versa, a disturbed lattice causes the electrons to move in order to screen the altered ionic polarization and leads to the formation of a CDW. Therefore, a CDW always occurs together with a PLD and it is often challenging to determine the driving factors for this combined phase.

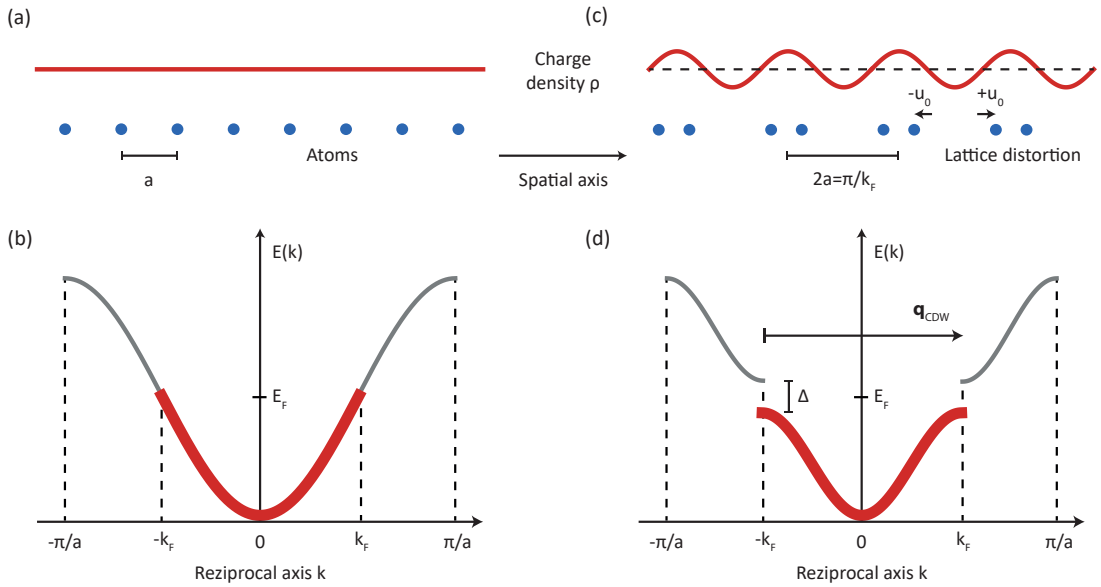

Figure 5.1: Peierls instability in one dimension. (a) One-dimensional chain of atoms spaced by the lattice constant a. The electron density ρ is constant in the normal phase. (b) Electronic band structure of a one-dimensional atomic chain. Every atom contributes one electron to fill a single band up to the Fermi level E_F. The corresponding reciprocal vector k_F spans half the Brillouin zone. (c) In the CDW phase the electron density is modulated with periodicity $2a$ and the atoms are displaced by $\pm u_0$ in positive and negative directions. (d) Band structure in the CDW phase. The Brillouin zone boundary is halved and aligns with the Fermi vector. At the new zone boundary an energy gap of Δ opens and lowers the total electronic energy which favours the formation of a CDW.

To gain a better understanding of the entangled driving forces promoting CDW/PLD formation, the Peierls instability mechanism for the formation of a CDW phase in a one-dimensional atomic chain will be introduced. In the normal state [Fig. 5.1(a)] the atoms

are equally spaced by the lattice parameter a and the electron density ρ is constant. For the corresponding band structure we assume one atomic orbital filled with one electron per atom which results in a half filled band as depicted in Fig. 5.1(b). The electron filling (thick red line) reaches up to the Fermi energy E_F and the corresponding Fermi vector $\mathbf{k}_F$ spans half of the Brillouin zone (π/a). In the CDW state shown in Fig. 5.1(c) electron density and ions are modulated by Eq. (5.1) and Eq. (5.2), respectively. The wavelength of the CDW modulation corresponds to $2a = \pi/k_F$ and the atoms are alternatingly displaced in positive and negative directions by u_0. In the band diagram [Fig. 5.1(d)] the Brillouin zone is halved and coincides with the CDW vector $\mathbf{q}_{\mathrm{CDW}} = 2\mathbf{k}_F$. This leads to a band opening of Δ at the Fermi level which effectively lowers the energy of all occupied states. If the lowered total electronic energy exceeds the increase in lattice strain energy a CDW with an associated PLD is formed.

Within the Peierls instability model in the weak coupling regime it is possible to obtain an analytical criterion for the stability of a CDW phase. By carefully accounting for the gain in electronic energy, the lattice strain term, the coulomb potentials $U_{\mathbf{q}}$, and the exchange energy $V_{\mathbf{q}}$, it is possible to formulate a stability criterion [232]:

$$\frac{4g_{\mathbf{q}}^2}{\hbar\omega_{\mathbf{q}}} - 2U_{\mathbf{q}} + V_{\mathbf{q}} > \frac{1}{\chi_0(\mathbf{q})}. \tag{5.3}$$

Here, $g_{\mathbf{q}}$ represents the strength of the electron-phonon coupling, $\omega_{\mathbf{q}}$ is the phonon frequency, and $\chi_0(\mathbf{q})$ is the non-interacting electronic susceptibility which expresses the potential electronic energy gain. A CDW phase is stable if the equation is met. Several factors can be identified from Eq. (5.3) to promote the formation of a CDW. Favorable are strong electron-phonon and electron-electron couplings, small strain energies, and weak coulomb interactions. However, one of the most important aspect is a diverging or large susceptibility at the CDW wave vector $\mathbf{q}_{\mathrm{CDW}}$. It is reached through a large number of possible electron scattering processes at the Fermi level, the so call "umklapp" processes. It follows that $\mathbf{q}_{\mathrm{CDW}}$ needs to connect portions of the Fermi surface. To achieve a large number of scattering events, the Fermi surface needs to have large parallel sections that can participate in electron scattering. This property is called Fermi surface nesting and occurs naturally in one-dimensional systems as the Fermi surface is planar in the other two dimensions [233]. In higher dimensional systems, parallel sections of the Fermi surface are found less frequent. However, quasi two-dimensional systems like TMDCs are

much more likely to exhibit a CDW compared to bulk materials as they reduce the dimensionality and thereby increase the susceptibility. Special Fermi pockets or other nesting effects leading to large electronic correlations cause CDW formation, superconductivity, and Mott transitions in a variety of two-dimensional materials [8].

While the Peierls model captures the weak coupling regime within a k-space representation, strong interactions are more accurately described in real space. The Band-type Jahn-Teller effect was proposed to explain the CDW formation in strongly coupled materials and focuses on local chemical bonds [234, 235]. A distortion of a highly symmetric lattice can lift the degeneracy of molecular orbitals and, dependent on the electron filling, reduce the total electric energy. This instability can lead to a spontaneous formation of a PLD with an associated CDW. The driving factors are similar to the Peierls transition, but the Jahn-Teller type usually involves stronger atomic displacements and favours commensurate CDW formation [236].

A third mechanism for CDW formation is the excitonic-insulator instability. In a material with a small band gap or overlapping valance and conduction bands, the total energy can be reduced by the formation of excitons. If the charge density and hence the screening is small, the excitons become stable and build a condensate. Such phases are described by the Bardeen-Cooper-Schrieffer theory similar to conventional superconductivity [237]. However, in contrast to cooper pairs, an exciton condensate is insulating due to the binding energy barrier. Since the missing momentum between the valance band maximum and the conduction band minimum needs to be provided by the lattice, this model again requires a sufficiently strong electron-phonon coupling. As a result, the bands hybridize between electronic and phononic dispersion and lead to opening of the electronic bands and the formation of a PLD. Similar to the Peierls transition or Jahn-Teller effect, the formation of a CDW/PLD is favoured by strong electron-electron and electron-phonon coupling.

5.2 The transition-metal dichalcogenide 1*T*-$TiSe_2$

A particularly interesting TMDC is the compound 1*T*-$TiSe_2$. It consists of trilayers of titanium and selenium atoms as shown in Fig. 5.2(a). Within the layers atoms a covalently bound while the layers are hold together by Van der Waals forces [238]. The stacking order of the layers determines the polytype. Compounds of type 1*T* display octahedral coordination with a trigonal (*T*) symmetry and can be described by one unit cell

along the c axis. On the contrary, the 2*H* type is trigonal prismatic with hexagonal (*H*) symmetry and requires a two unit cell representation [233]. The lattice constants of 1*T*-$TiSe_2$ are $a = b = (3.540 \pm 0.001)$ Å and $c = (6.008 \pm 0.003)$ Å [239]. Upon cooling below the critical temperature of $T_c = 200$ K, a CDW forms together with a commensurate $2 \times 2 \times 2$ PLD superstructure shown in Fig. 5.2(b) [240, 241, 242]. The distortion involves 0.085 Å shifts of titanium atoms and 0.028 Å shifts of selenium atoms within the respective planes [241]. Alternating layers possess distortions in opposing directions (black and blue arrows) which leads to a doubling of the unit cell in the c-direction.

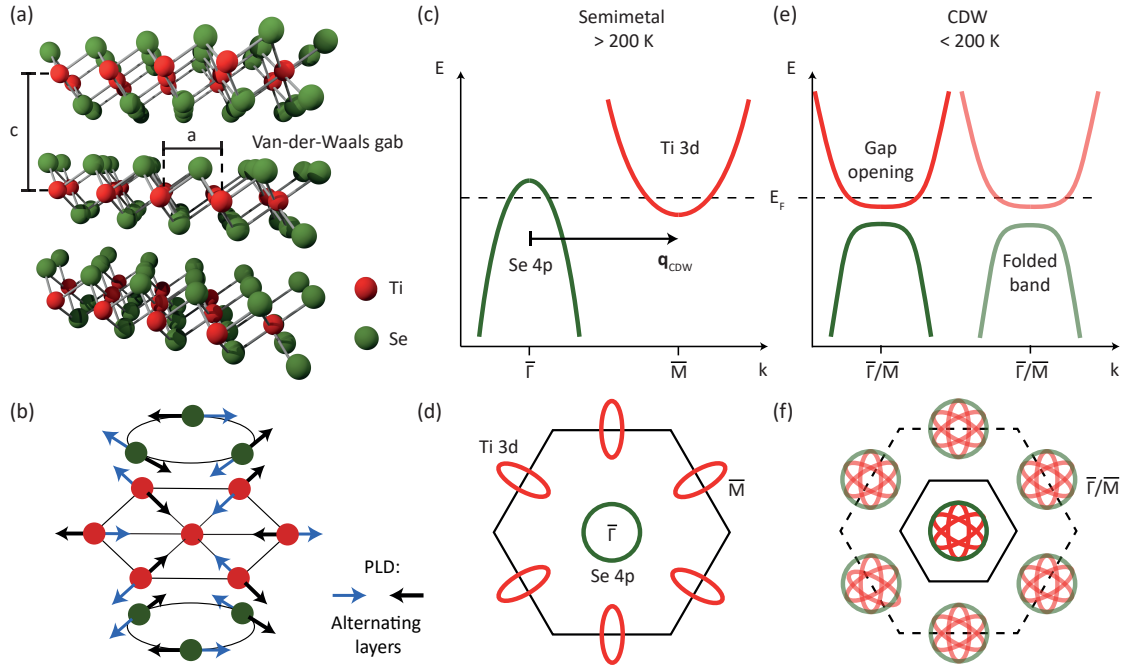

Figure 5.2: Phases of 1*T*-$TiSe_2$. (a) Crystal structure containing trilayers of titanium and selenium atoms. Indicated are the inter layer lattice constant *c* and the smaller intralayer constant *a*. The layers held by van der Waals forces create a quasi two-dimensional material. (b) Periodic lattice distortion. (c) Schematic band structure in the semimetallic high-temperature state. The selenium 4p band at the gamma point slightly overlaps with the titanium 3d level at the M point. (d) Brillouin zone. The Se band is centered around the gamma point and the Ti bands are located at the M point at the zone boundaries. (e) Schematic band structure in the low-temperature CDW phase. The periodic modulation with $\mathbf{q}_{\mathrm{CDW}}$ leads to a backfolding of the titanium band onto the selenium band. As a result the selenium band is downshifted and a band gap is formed. (f) The halving of the Brillouin zone leads to a backfolding of the Ti band on top the Se band.

The origin of the CDW formation in $1T$-$TiSe_2$ is still heavily debated and likely involves both excitonic and electron-phonon coupling mechanism of the Jahn-Teller type. In the high temperature phase, the band structure shows a semimetalic character [243, 241] as shown in Fig. 5.2(c). The selenium 4p band at the center of the Brillouin zone [Fig. 5.2(d)] and the titanium 3d band at the zone boundary overlap by < 120 meV. This small overlap hinders efficient Fermi surface nesting but promotes the formation of excitons due to remarkably strong electron-hole coupling [237]. The momentum mismatch of $\mathbf{q}_{\mathrm{CDW}}$ between valance band maximum and conduction band minimum is accounted for by the PLD. In the low temperature phase, the CDW leads to a backfolding of the bands such that gamma and M point coincide as depicted in Fig. 5.2(e) and (f) [92]. It was found that the transferred spectral weight to back-folded bands is exceptionally large and a comparison to an excitonic insulator model yields good agreement [237, 244]. At the same time, the Se 4p band downshifts which leads to a band gap opening of 110 meV at 100 K [245]. In other studies it was concluded that parallel to the formation of an exciton condensate, one conduction band does not participate in the exciton formation which leads to a conducting state in contrast to excitonic insulator materials [244]. Both, band folding and band gap opening are clear signatures of the electronic part of the CDW.

In contrast, the Jahn-Teller effect is discussed to explain the CDW formation by shortening of the Ti-Se bond length and the subsequent lowering of the Se 4p hole like bands which reduces the total electronic energy [235, 245]. Strong electron phonon coupling is evident from the occurrence of the PLD [246, 247]. It is cause by the Kohn anomaly which is a softening of phonon modes. Upon cooling, the eigenfrequency of the phonon associated with the PLD is reduced. At the transition temperature a frozen-in phonon with a frequency of zero is formed. Below T_c, the so called amplitude mode emerges. This phonon incorporates the same distortions as the frozen-in mode but is centered around the PLD equilibrium position and not the normal state equilibrium.

With the discovery of a superconducting phase in $1T$-$TiSe_2$, the discussion of the CDW driving forces gained additional momentum. Superconductivity was observed at high pressure [248] or when intercalating Cu or Pd atoms [249, 250]. The superconductivity was found to be closely connected to a suppression of the CDW phase and the two phases are mutually exclusive [250, 248]. Hence, to understand the emergence of superconductivity it is essential to study the microscopic mechanisms that stabilize the CDW phase.

5.3 Ultrafast charge-density-wave dynamics in 1*T*-$TiSe_2$

Time-resolved methods have been successfully applied to determine the CDW driving forces in a variety of materials [20]. By observing the laser triggered CDW melting and reformation in real time it is possible to track the microscopic electronic and lattice motions. Since the melting timescales and the dependencies on the laser fluence are determined by the microscopic mechanism, time resolved methods are ideally suited to study the origin of the CDW phase in 1*T*-$TiSe_2$. Various ultrafast experiments have been performed to study different time constants in this material such as angle resolved photo electron spectroscopy (ARPES) [251, 92, 93], x-ray diffraction [252, 253], electron diffraction [254, 255], THz spectroscopy [256], and transient reflection [252, 257]. The following section summarizes the findings of previous time-resolved studies with relevance to the present work.

One of the most interesting properties is the non-thermal melting of the CDW phase in 1*T*-$TiSe_2$ by laser excitation. In 2011 Möhr-Vorobeva *et al.* discovered that the CDW melting can be driven with ultrashort laser pulses below the thermal energy threshold [252]. Here, the energy supplied by the laser is insufficient to drive the transition in thermal equilibrium. In conclusion, the photon doping triggers some electronic kinetics that drive the system out of the CDW phase. It follows that the melted state is metastable. This interesting dynamics was investigated in multiple studies by a variety of probes. The reported threshold fluences are in the $100\,\mu J/cm^2$ regime, far below the typical mJ thermal threshold. It is important to note, that the initial temperature and the photon energy were found to have a large impact on the melting threshold. Some studies also observe a decoupling of electronic and structural part of the CDW/PLD. In ultrafast THz spectroscopy with simultaneous access to electronic and structural degrees of freedom, the PLD and CDW respond different to the 12 fs driving laser pulse. At intermediate fluences, the CDW could be quenched while the PLD persists [256].

Particular promising observables to obtain information on the CDW in connection with the structural counterpart are coherently excited phonon modes. The optical A_{1g} mode and the A_{1g}^* CDW amplitude mode can be driven coherently by laser excitation. The involved atomic displacements are depicted in Fig. 5.3(a). Both modes are well known from Raman experiments [242, 257, 258] shown as an example in Fig. 5.3(b). Here, the optical A_{1g} mode at 6 THz and the E_g mode at 4.2 THz are found in the normal semimetallic state as well as in the CDW phase. Interestingly, the A_{1g}^* mode at 3.5 THz

and the E_g^* mode at 2 THz are only found below the CDW phase transition temperature. In transient reflectivity studies [Fig. 5.3(c)] the A_{1g}^* and the A_{1g} phonon are identified from oscillations of the time dependent signal [257]. Again, a nonthermal threshold was found at which the signal transitions from the amplitude mode to the optical mode. Thereby, the amplitude mode can only be detected below a threshold of $60\,\mu J/cm^2$. The loss of the amplitude-mode signal in transient reflection data hints at a complete suppression of the PLD or a loss of the coherent phonon excitation [257].

Furthermore, the amplitude mode can also be measured in ARPES experiments [251] and was assigned to a displacive excitation mechanism. It has been shown that the top of the valance band possesses binding character while the bottom of the conduction band is antibonding [251]. Therefore, the mid infrared laser directly drives the system from binding to anti binding orbitals which instantaneously changes the potential energy landscape of the atoms and triggers phonon oscillations. This result is a strong indicator of the displacive excitation mechanism, but larger photon energy may involve different lattice responses, as electron cascade processes govern the initial energy relaxation [93].

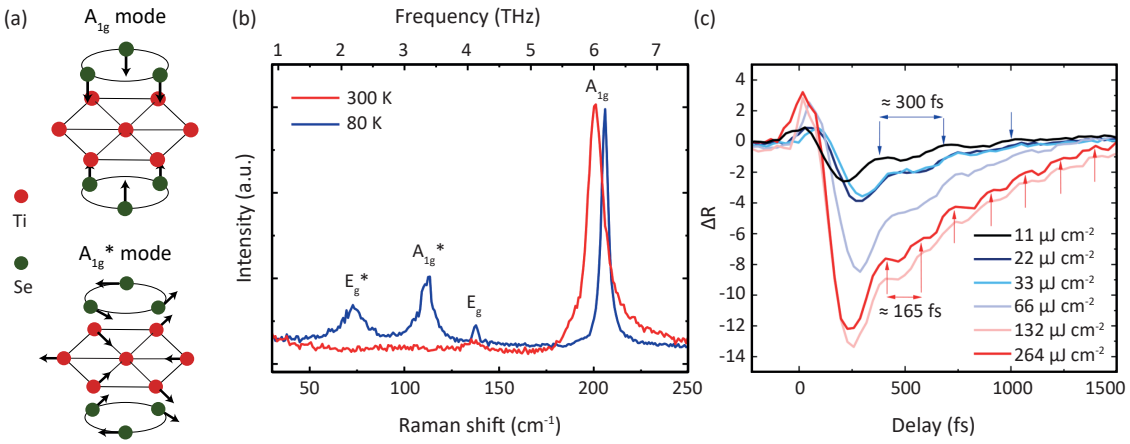

Figure 5.3: Coherently excited phonon modes in 1T-$TiSe_2$. (a) Schematic atomic displacements of the two coherently excited modes. The A_{1g} optical mode only comprises out-of-plane movements of the selenium atoms. On the contrary, the A_{1g}^* mode which is associated with the PLD consists of in-plane movements of selenium and titanium atoms. (b) Raman data obtained in the CDW phase (80 K, blue) and the normal phase (300 K, red). (c) Transient reflection data at various pump fluences. Subfigures (b) and (c) are adapted from Ref. [257] under the Creative Commons Attribution 4.0 International (CC BY 4.0) license.

Motivated by the suppression of the amplitude mode in transient reflectivity experiments, a bottleneck effect has been proposed in connection with supplementary ARPES data. It involves the excitation of strongly-coupled modes, which refers to both the amplitude and the optical mode, hindering the reestablishment of the CDW state above the threshold fluence [257]. The out of equilibrium phonons impede the excited carriers from recombining into excitons and reestablishing the CDW state. Here, the loss of the PLD superlattice causes an abrupt reduction of the damping of the strongly coupled modes and an increase in the exciton dissociation rate [257]. This highlights, the importance of the amplitude mode on the stability of the CDW. However, the involvement of the optical mode on the CDW melting is not clear and it is very challenging to separate both strongly-coupled modes in transient reflection data.

By combining the information gained from various ultrafast time-resolved studies a more thorough picture of the CDW melting emerges. The fast non-thermal melting is believed to be driven by exciton breaking assisted by the structural lattice distortion. This favours a driving mechanism of a combined excitonic and electron-lattice coupling for the CDW and the PLD in 1T-$TiSe_2$ [259, 260]. During the first 100 fs the exceptionally fast suppression of the CDW phase is dominated by the excitonic part via screening of excited carriers [92, 93, 251]. Time-resolved THz spectroscopy showed that the melted state possesses a drastically different plasmon pole which signals a changed electronic screening [256]. Further confirmation of exciton suppression was found in resonant X-ray diffraction by monitoring a space group forbidden superlattice peak which only appears if exciton correlations are present [253]. A complementary quantum-mechanical model of the band structure suggest that excitons and phonons are both necessary to stabilize the CDW phase in 1T-$TiSe_2$ [259, 251]. However, until now it is not entirely clear how the electron-phonon coupling relates to the change in the screening responsible for the exciton breaking.

In this work, chapter 8 focuses on the spectral fingerprints of the A_{1g} optical mode and the A_{1g}^{*} amplitude mode. In particular, the questions regarding their involvement on the CDW melting, the relaxation of the deposited energy, and the connection to electron-screening effects will be discussed.

Chapter 6

Chiral high-harmonic generation and spectroscopy on solid surfaces using polarization-tailored strong fields

T. Heinrich, M. Taucer, O. Kfir, P. B. Corkum, A. Staudte, C. Ropers and M. Sivis
Nat Commun **12**, 3723 (2021)
doi: 10.1038/s41467-021-23999-9,

Strong-field methods in solids enable new strategies for ultrafast nonlinear spectroscopy and provide all-optical insights into the electronic properties of condensed matter in reciprocal and real space. Additionally, solid-state media offers unprecedented possibilities to control high-harmonic generation using modified targets or tailored excitation fields. Here we merge these important points and demonstrate circularly-polarized high-harmonic generation with polarization-matched excitation fields for spectroscopy of chiral electronic properties at surfaces. The sensitivity of our approach is demonstrated for structural helicity and termination-mediated ferromagnetic order at the surface of silicon-dioxide and magnesium oxide, respectively. Circularly polarized radiation emanating from a solid sample now allows to add basic symmetry properties as chirality to the arsenal of strong-field spectroscopy in solids. Together with its inherent temporal (femtosecond) resolution and non-resonant broadband spectrum, the polarization control of high harmonics from condensed matter can illuminate ultrafast and strong field dynamics of surfaces, buried layers or thin films.

Nonlinear spectroscopy has made a huge leap forward with the proof of high-harmonic generation (HHG) in condensed matter [138, 101, 261, 262]. Recently, numerous excellent studies, involving band reconstructions [62], exciton analysis [63], momentum dependent phases [263, 264, 265] and valence-electron mapping [105] have shed new light on various solid-state phenomena. At the same time, the functionalization of solid targets through structural and chemical modifications [143, 266, 267] or nano-confined and tailored excitation fields [267, 140, 141, 268] has led to unprecedented possibilities for the controlled generation of high harmonics. The variation of the excitation field's polarization, in particular, can provide access to crystal orientation-dependent information [68, 69, 70]. When the crystal symmetry is known, the study of phenomena in the sample can be conducted by combining linearly or circularly polarized excitation with a polarization analysis of the harmonic emission. Moreover, in such schemes, the generation of harmonic radiation with elliptical polarization is possible [269, 123, 124]. The use of nontrivial tailored driving fields can significantly enrich solid-state HHG by providing a universal control of the high-harmonic polarizations in arbitrary (symmetric) crystal structures, which is key to efficient generation of circularly polarized radiation and to symmetry-resolved chiral spectroscopy.

In HHG from atoms and molecules, intricate field symmetries already proved their important role, including the probing of orbital angular momentum states with symmetries across the laser wavefront [270, 271, 272] and symmetries at the level of local electric fields [273, 274, 275]. Of great interest for crystalline solids are bi-chromatic light fields with controllable polarization, which can possess discrete rotational symmetries, and are known from circularly-polarized HHG in gases [121, 66]. In the particular case of a bi-circular field comprising counter-rotating fundamental wavelength and its second harmonic, the rotational symmetry is threefold, and the field's angular momentum is imprinted on the generated harmonics. In solids, where the HHG is affected by the crystalline symmetry, such tailored excitation fields would allow for a symmetry-sensitive probing of chiral surface-band features, which is particularly relevant for the study of correlated electronic systems or magnetic properties.

Here, we demonstrate that bi-chromatic rotational symmetric driving fields [121, 66, 276] probe rotational and chiral symmetries at the surfaces of bulk-insulating crystals via HHG. In particular, we match a threefold driving field with threefold, fourfold, and sixfold structures of specific crystal cuts of silicon dioxide (quartz) and magnesium oxide (MgO) and find a high sensitivity of circularly-polarized HHG in solids to structural helicity

and surface magnetism. By evaluating the difference in the resonant, i.e., near-band-edge, absorption between left- and right-circular polarized harmonics we can measure chirality-mediated band shifts in the respective crystal systems. While chiral band shifts in quartz(0001) and at the polar MgO(111) oxygen-terminated surface [277] is expected due to the screw-like structural helicity (P321 space group) [278] and the reconstruction-mediated ferromagnetism at the polar surface [279, 280], respectively, we also discover a chiral footprint also on the cubic non-polar surface of MgO(100).

6.1 Results

6.1.1 High-harmonic generation in solids with bi-circular driving fields

In this study single-crystalline quartz and MgO targets are excited under moderate vacuum conditions ($< 10^{-6}$ mbar pressure) with bi-circular two-color laser pulses (50 fs pulses at 1 kHz repetition rate) comprising a circularly-polarized fundamental field at 800 nm wavelength and a counter-rotating circularly-polarized second harmonic (400 nm wavelength). The field strengths we used (10.5 V nm^{-1} in quartz and 7.7 V nm^{-1} in MgO) are comparable to other studies [262, 68] that observed strong-field HHG in these materials. Figure 6.1a schematically illustrates the experimental setup, where high-harmonic radiation is generated in reflection geometry from a crystal surface and collected with an extreme-ultraviolet spectrometer. The driving bi-circular field exhibits a threefold helical polarization (see Supplementary Fig. 6.6 for details), which we utilized as a spectroscopic probe via circular HHG. Figure 6.1b depicts this principle, which involves rotational symmetry probing by changing the angle θ between the field and the crystal as well as chiral sensitivity through the circular polarization state of the generated harmonics. A typical spectrum spanning from the fifth harmonic (7.75 eV photon energy) to the tenth harmonic (15.5 eV) is shown in Fig. 6.1c for quartz(0001). The spectra for all crystals are shown in Supplementary Fig. 6.7. The near-perfect suppression of every third harmonic is the selection rule that corresponds to circular polarization of the unsuppressed harmonics [121, 66] (see Supplementary section selection rules). More precisely, the circular polarization of the harmonic orders $q = 3n+1$ $(4,7,10,...)$ exhibit the same sense of rotation as the fundamental driving field while the orders $q = 3n-1$ $(5,8,11,...)$ have an opposite polarization helicity (see Fig. 6.1a-c). For a harmonic generation in isotropic targets, such as gases, the radiation symmetries are dominated by the threefold polarization shape of

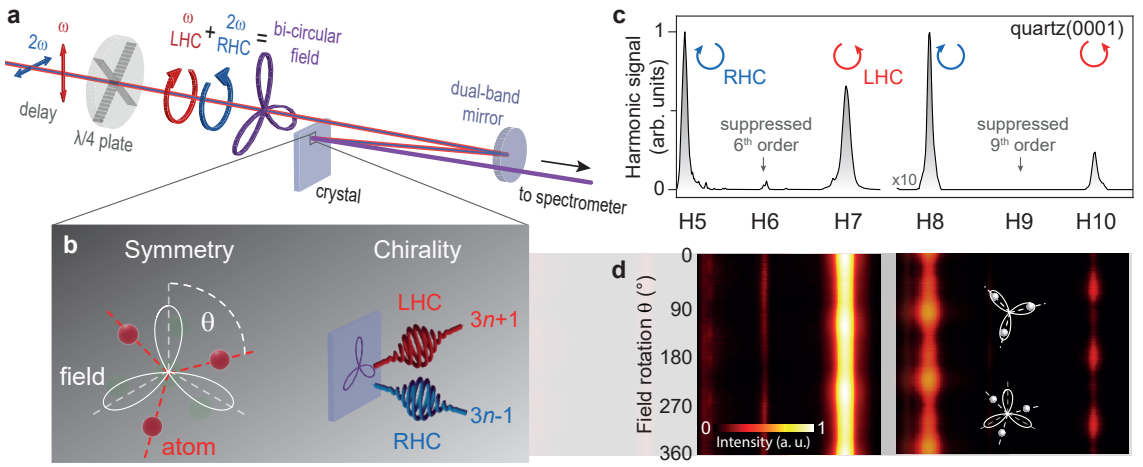

Figure 6.1: Chiral high-harmonic generation in solids. **a** Two-color laser pulses (frequencies marked ω and 2ω) with perpendicular polarization and adjustable phase delay can be converted to circularly-polarized fields with opposite helicity using a dichroic quarter-wave plate with the fast-optical axis set to 45° relative to the laser polarization. The superposition yields a bi-circular field with a three-fold rotation symmetry. The ellipticity and the orientation of the field (see angle θ in (**b**)) depend on the quarter-wave plate rotation and the phase delay between the two spectral field components, respectively. The emitted harmonic radiation is collected with an extreme-ultraviolet spectrometer. LHC: left-handed circular, RHC: right-handed circular. **b** Schematic depiction of the symmetry and chirality probing principle using a bi-circular field for HHG in solids. **c**, High-harmonic spectra from quartz(0001) (harmonic orders label with H5 - H10), showing a suppression of every 3rd harmonic order. The blue and red arrows indicate the helicity of the harmonics. **d** Spectrogram for quartz(0001) as a function of the three-fold field rotation angle θ (see also pictograms), exhibiting a three-fold beating.

the driving bi-circular field. Since threefold and sixfold rotation symmetries inherently conform to the threefold symmetry of the laser field, the same selection rules apply for the termination planes of quartz (0001) and MgO(111) (cf. spectrum in Supplementary Fig. 6.7). Conversely, crystals exhibiting other symmetries, e.g., the fourfold MgO(100), remove the constraints on the selection rules and lead to a less pronounced suppression of every third harmonic (see the spectrum in Supplementary Fig. 6.7 and supplementary information for details on the selection rules). On the other hand, the suppression of every third harmonic confirms the threefold symmetry of the driving field, which allows for the probing of the crystal axes by polarization rotations (see Fig. 6.1b left). The spectrogram in Fig. 6.1d shows allowed harmonic orders which peak every 120°, corresponding to the P3 point-group of the quartz crystal. We attribute the higher angular sensitivity, i.e., the stronger modulation of the signal, for increasing harmonic orders to the nonlinear intensity scaling of the generation process. More specifically, the angular resolution is

determined by the spatial generation anisotropy of the harmonics (whether in the perturbative or non-perturbative regime) and the particular polarization contrast of the threefold excitation field (see Fig. 6.6a). While the influence of the underlying mechanism warrants further investigation, the observed phase differences between individual harmonics (cf. H8 and H10 in Fig. 6.1d) already suggest a non-perturbative generation of higher harmonics [261, 62, 281] in quartz, which could be relevant for the study of diverse solid-state phenomena [62, 105, 112].

6.1.2 Inversion-symmetry probing

The lack of inversion symmetry of bi-circular fields is particularly relevant for the probing of material inversions. Figure 6.2 analyzes the rotational dependence of harmonic

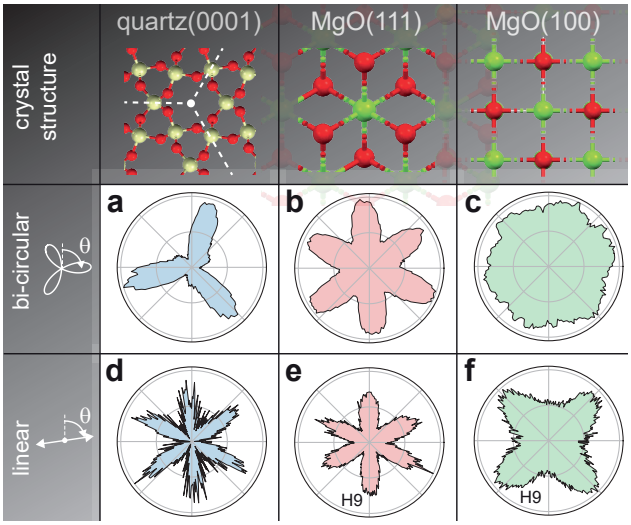

Figure 6.2: Bi-circular and linear polarization rotation scans for quartz and MgO. a-c The yield of the eighth harmonic order (H8) as a function of the rotation angle of the threefold field. **d-f** Yield of H8 as a function of linear polarization angle. For MgO, H8 from linearly polarized drivers is symmetry-forbidden, hence H9 is presented.

generation driven by bi-circular fields and inversion- symmetric linear-polarized fields for different crystals. The solid targets quartz(0001), MgO(111) and MgO(100) represent threefold, sixfold, and fourfold rotational symmetries, respectively. The shown polar plots of the eighth harmonic intensity (ninth harmonic in MgO for linear polarizations) are extracted from the spectrograms (see also Supplementary Figs. 6.7 and 6.8). In quartz, an inversion-symmetry-broken crystal, the bi-circular laser field probes the threefold rotational symmetry and the crystal orientation accurately (Fig. 6.2a). Contrary, a polarization scan with a linearly-polarized field, which possesses a twofold symmetry, exhibits an ambiguous sixfold beating (Fig. 6.2d) corresponding to an inversion-symmetrized threefold rotation. For crystals with sixfold symmetry as MgO(111) (Figs. 6.2b, e) rotating the

bi-circular or linearly polarized field yields similar sixfold patterns. In the case of the fourfold MgO(100) (Fig. 6.2c, f), the harmonic emission from the linearly-polarized fundamental exhibits the expected, fourfold pattern, while for excitation with the bi-circular field the signal loses the appearance of its fourfold symmetry. The convolution of the threefold field and the fourfold crystal should result in a 12-fold signal [282], which is not resolvable. Since in MgO(111) the angular-dependent emission peaks are narrow enough to resolve a 12-fold symmetry, we conclude that the MgO(100) is more isotropic. It may be possible to refine the angular modulation of the harmonic intensity by tuning the parameters of the driving field, such as the amplitude ratio of fundamental and second harmonic, which has an influence on the symmetry modulation of the field, as discussed in "Methods".

6.1.3 Structural and magnetic circular dichroism in solid-state HHG

Chiral electronic properties become apparent when comparing circular HHG for the left and right helicities of the bi-circular field. We find chiral spectral signatures in quartz and MgO and attribute those to structural helicity and ferromagnetic order, respectively. The difference of spectrograms for left and right bi-circular driving fields (see Supplementary Fig. 6.7) in quartz, shown in Fig. 6.3a, reveals a strong angle-dependent spectral shift of the seventh harmonic, as outlined in Fig. 6.3c (gray dots). A similar shift of the fifth harmonic is observed for both crystal cuts of MgO, which is exemplified in Fig. 6.3b, d for MgO(100). Importantly, regardless of the crystal termination planes in MgO (both 100 and 111, cf. Supplementary Fig.6.9), the spectral shifts are independent of the field rotation angle. In both materials, the harmonic orders exhibiting a spectral shift are located near the bandgap energy and we refer to these harmonic orders as "on-resonance" in the following.

Our observations can be explained by circular dichroism, i.e., a helicity-dependent absorption of generated harmonic radiation. This absorption leads to red- and blue-shifted on-resonance harmonics having left- and right-circular polarization, respectively (see red and blue dots in Fig. 6.3e, f). This effect is similar to dichroic absorption measurements with external sources, how ever here, the probe emanates from the sample itself and is sensitive to the crystal symmetry. To evaluate the chiral spectral response, we consider near-band-edge absorption of the opposite circularly-polarized harmonics, with different helicity-dependent absorption channels in both materials. In quartz, the screw-like crystal

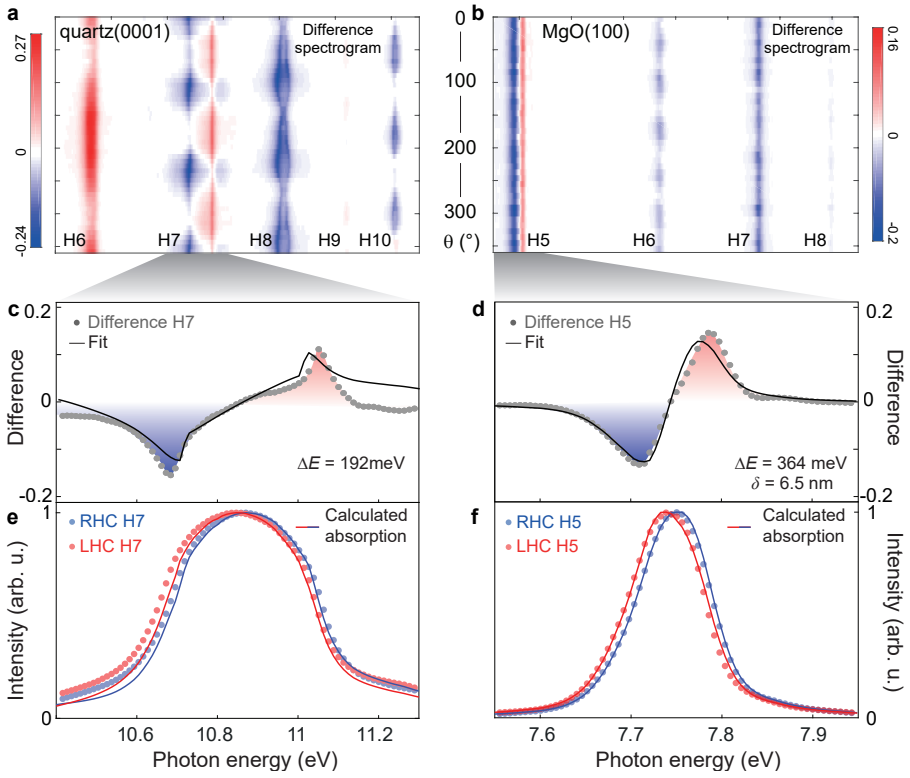

Figure 6.3: Sensitivity of HHG to structural helicity of quartz and surface-ferromagnetic order of MgO. a, **b** Difference signal of two intensity-normalized spectrograms recorded with opposing helicities of the driving field generated in (**a**) quartz(0001) and (**b**) MgO(100). For single helicity spectrograms cf. Fig. 6.1d and Supplementary Fig. 6.7. **c**, **d** Lineouts of the on-resonance harmonic difference signal in (**c**) quartz and (**d**) MgO. The solid lines represent a fit based on calculations of the circular dichroism (fit parameters are the chiral energy splitting ΔE, and the effective interaction length δ). **e**, **f** Normalized intensity of right-handed-circularly (blue, RHC) and left-handed-circularly (red, LHC) polarized harmonics in (**e**) quartz and (**f**) MgO. The solids lines represent the calculated circular dichroism. Lineouts are taken at an angle of $\theta = 120°$ in the case of quartz and averaged over all angles for MgO.

arrangement possesses a structural chirality (see schematics for the 3_1 and 3_2 structure in Fig. 6.4a), where the two enantiomers exhibit different band structures [278], as qualitatively drawn in Fig. 6.4b. Hence, opposing helicities of emitted harmonics probe a different band structure in 3_1 and 3_2 (see purple arrows in the band diagram in Fig. 6.4b). On the other hand, in MgO-being an achiral crystal-the surface ferromagnetism dominates the helicity-selective absorption. Spontaneous symmetry-breaking in the non-stoichiometric surface reconstructions [277, 280, 283] lead to the formation of a ferromagnetic layer with a spin-polarized metallic surface [283, 284]. The oxygen termination of the po-

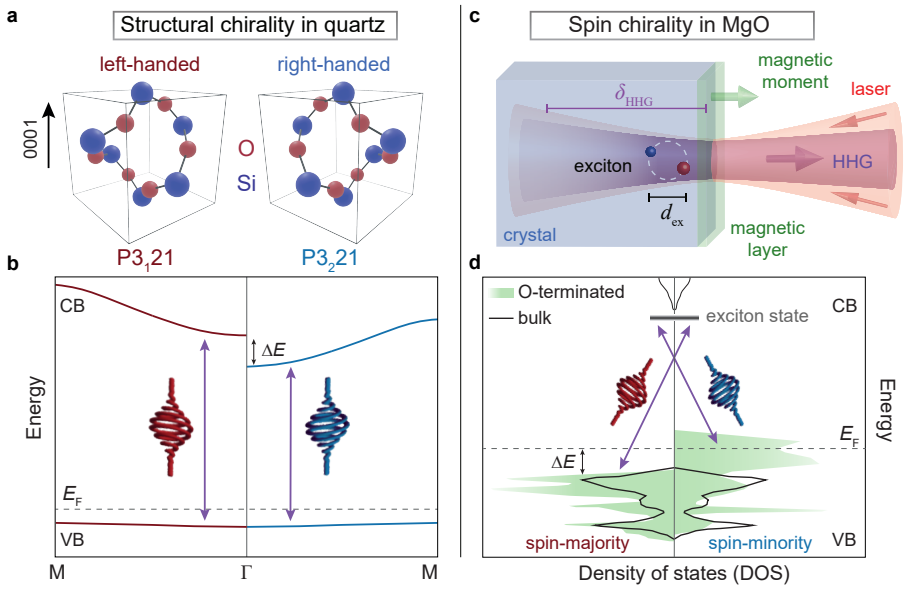

Figure 6.4: Chirality in quartz and MgO. a Schematic of left- and right-handed enantiomers ($P3_121$ and $P3_221$) of quartz(0001). **b** Qualitative band structure of the two quartz(0001) enantiomers, adapted from ref. [278]. **c** Schematic of the high-harmonic generation (HHG) in MgO. Near-surface excitons with exciton diameter d_{ex} may couple to the surface magnetic moment. Harmonic emission generated within the absorption length δ_{HHG} is detected in our experiment. **d** Simplified surface density of states (DOS) for the oxygen-terminated MgO(111) surface (green, see also inset for crystal structure) and bulk MgO (black), adapted from ref. [283] (VB valence band, CB conduction band, E_F fermi energy, ΔE band splitting). The purple arrows mark the excitations with opposite helicities of circularly polarized light.

lar MgO(111) may create a magnetic moment perpendicular at the surface [285], as schematically depicted in Fig. 6.4c. The band structure for the minority and majority spin-polarized charge carriers on the surface of MgO(111) is drawn in Fig. 6.4d. The annotated arrows mark the different absorption for left- and right-circular polarized harmonics (see purple arrows in Fig. 6.4d). In MgO(100), magnetic ordering may arise from vacancies and impurities or faceted surface reconstructions [284, 285], while a bulk ferromagnetism can be excluded at room temperature [280]. The fifth harmonic is sensitive to the ferromagnetism at the MgO surface due to its absorption by excitons, allowing for a penetration depth of only $\delta_{HHG} = 15$ nm (ref. [286]). This attenuation length is comparable to the electron-hole binding distance d_{ex} (about 6 nm in MgO (ref. [287])), which highlights the significance of these surface-localized excitons in our measured spectra.

In order to reproduce the spectral response in Fig. 6.3, we calculate the helicity-dependent absorption of harmonics with left- and right-circular polarization by consider-

ing energetically-shifted absorption coefficients $k(E \pm \Delta E/2)$ for quartz [288] and MgO (ref. [286]). The term $\pm\Delta E/2$ represents the energy shift for opposite circular polarizations (see Supplementary Fig. 6.10). While in the calculation for quartz we consider the entire optical penetration depth (see Eq.6.1 in "Methods"), in the case of MgO, we introduce an effective interaction length δ as an additional parameter (see Eq.6.2 in "Methods") to model a surface sensitivity. We fit the absorption spectra shown in Fig. 6.3e, f to Eq. (6.1) and (6.2) by varying ΔE (and δ, in the case of MgO), and present the final curve alongside the difference spectra in Fig. 6.3c, d (solid lines). In both materials, the absorption model yields significant spectral shifts for the on-resonance harmonic orders while the other harmonic orders show only intensity differences, similar to what we observe in Fig. 6.3a, b. This is consistent with the derivative of the absorption coefficient being largest at the band edge, which justifies the extraction of the band splittings from the on-resonance harmonic signals. The obtained band splitting values of $\Delta E = 192$ meV in quartz (maximum, at 215° field rotation), $\Delta E = 364$ meV in MgO(100), and $\Delta E = 395$ meV in MgO(111) (average over all field rotation angles), are in good agreement with the theoretically predicted changes of the band energy [278, 283, 289] (cf. Fig. 6.4b, d). Furthermore, the obtained interaction length of $\delta = 4-7$ nm in MgO matches the expected exciton diameter, which suggests a coupling of the surface-magnetic moment to exciton states. The intrinsically different origin of the circular dichroism in quartz and MgO is revealed by the remarkably different dependence of their band splitting on the field-rotation angle, as shown in Fig. 6.5. In quartz (Fig. 6.5b), the band splitting is

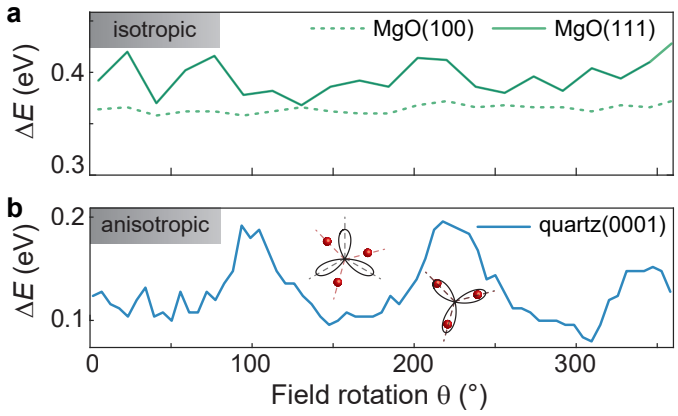

Figure 6.5: Chirality-mediated band shifts. **a**,**b** Band shifts as a function of field rotation for MgO (**a**) and quartz (**b**). The orientation-independent energy splitting in MgO suggests that the chirality originates from spin-polarized surface states.

rotationally anisotropic with a threefold periodicity, indicating a crystal-axis-dependent band structure [278]. On the other hand, the isotropic band splitting in MgO (Fig. 6.5a) can be attributed to the ferromagnetic order on the surface [280]. The accuracy in which

the chiral excitations on the surface explain our observations suggests that further theoretical and experimental analysis using tailored strong-fields under consideration of the energy-dependent emission phases (see Fig. 6.1d) could provide additional microscopic information on chiral systems, possibly even on the atomic level [105].

6.2 Discussion

In conclusion, we demonstrate a distinct symmetry-dependent chiral sensitivity of high harmonics generated from bi-circular laser fields near crystal surfaces. We show that the tailored symmetry and angular momentum of the driving field polarization can be utilized to generate circularly-polarized harmonic radiation in solids with arbitrary crystal structures and allow for symmetry-resolved chiral spectroscopy of the generation medium. Specifically, the harmonic yield depends on the matching between the Lissajous polarization curve and the crystalline axes, which can be harnessed for the detection of inversion symmetry. The circular polarization of the generated harmonics enables probing of the crystalline chirality in quartz and ferromagnetism on the surface of MgO. Using harmonics at the band resonance, we extract the symmetry-resolved energy shearing of helicity-dependent (quartz) and spin-polarized (MgO) bands with a fitting model incorporating a polarization-dependent absorption coefficient. Compared to dichroic absorption spectroscopy with external light sources, the symmetry-sensitive, local generation as well as the large bandwidth and wavelength tunability of the harmonics represent clear advantages. Furthermore, the relaxed requirements on the vacuum conditions and the sample preparation allow for a wider range of materials to be studied. This is particularly relevant for insulating materials for which chiral spectroscopy on thin-film samples is possible but challenging with electron-based methods like spin-resolved photoemission spectroscopy [290, 291] or spin-polarized scanning tunneling microscopy [292, 293, 294] due to surface charge and surface contamination over time [295]. Besides illustrating an all-optical scheme for surface-sensitive spectroscopy, our method also facilitates compact, gas-free extreme-ultraviolet light sources for experiments involving ultra-high vacuum. Moreover, extending the spectroscopic capabilities of our approach, the inherent femtosecond pulse duration of the harmonics and the breaking of expected selection rules imply a powerful, single-shot probe for ultrafast dynamics. In addition to the detection of global properties such as orientation, chirality, or phase transitions, setting the HHG on a particular resonance, e.g., in semiconductors [138, 261, 265, 296] or insulators [262, 105],

will allow to target other surfaces phenomena with the potential of direct or diffractive imaging [143]. Thus, this work opens a path for detailed ultrafast surface spectroscopy and microscopy of dielectric and insulating materials.

6.3 Methods

Crystals

In our experiment we use commercially available (MTI crystals), single-crystalline silicon dioxide (quartz), and magnesium oxide (MgO) targets with 10 mm x 10 mm lateral size and 300 μm thickness. The quartz crystal is oriented along the 0001-direction perpendicular to the z-plane (space group $P3_121$ or $P3_221$). Two additional MgO crystals are cut perpendicular to the [111]- and [100]-direction, respectively

The laser system and two-color bi-circularly-polarized driving fields

The laser system used in this study (Coherent Elite amplifier with Vitesse seed oscillator) delivers milli-Joule-level, 50 femtoseconds (FWHM) pulses with 800 nm central wavelength (see the red spectrum in Supplementary Fig. 6.6b) at a 1 kHz repetition rate. We are able to control the excitation power with a variable attenuator and the incident polarization with a half-wave plate.

Bi-circularly-polarized two-color light fields are generated in an in-line MAZEL-TOV (MAch-ZEhnder-Less for Threefold Optical Virginia spiderwort) apparatus. Supplementary Fig. 6.1a depicts the setup, which consists of a 40 cm plano-convex lens and a BBO crystal for the generation of second-harmonic laser pulses with 400 nm wavelength (see blue spectrum in Supplementary Fig. 6.1b) and a polarization perpendicular to the fundamental polarization direction. Two thick horizontally counter-rotational tiltable calcite plates control the timing (overlap) of the two pulses and a dichroic quarter-wave plate converts the linear polarized pulses to oppositely circularly polarized fields. This configuration allows for the generation of bi-circularly-polarized two-color laser pulses with a defined relative phase, which leads to a three-fold symmetric field distribution with fixed orientation in space. Therefore, the quarter-wave plate's fast optical axis is set to $\pm 45^\circ$ relative to the linearly polarized fundamental where the sign determines the direction of rotation. A wave plate angle of 0° leaves the perpendicular linear-polarizations of the two pulses unchanged. An additional tiltable thin calcite plate mounted on a rotational

stage is placed before the quarter-wave plate, in order to fine-tune and scan the relative phase of the fundamental and the second-harmonic pulses. The phase delay between the fundamental and the second-harmonic pulses controls the relative rotational orientation of the three-fold field distribution to the crystal axis (compare angle θ in Fig. 6.1). More details on the MAZEL-TOV apparatus and the generation principle can be found elsewhere [125]. Removing the MAZEL-TOV apparatus and the quarter-wave plate allows for the use of linearly-polarized laser excitation at the fundamental wavelength, with variable polarization angle via the half-wave plate.

In the experiment the relative power of the second harmonic field to its fundamental was 6% for the measurements on quartz and 1% in the case of MgO. Considering the wavelength-dependent focusing of the 800 nm and 400 nm fields, the field amplitude ratios are 1:2 and 1:5 in the quartz and MgO measurements, respectively, which determines the actual shape to the driving fields in both cases (see Fig: 6.6a). Supplementary figures 6.6c and d show the three-fold driving Lissajous curves for a field amplitude ratio of 1:2 for right- (c) and left- (d) helical rotation. An altered amplitude ratio has no impact on the rotational symmetry of the field nor the helicity of emitted harmonic radiation. It does, however, influence the spatial isotropy, i.e., the degree of angular modulation, of the field, which has an impact on the angle resolution in polarization scans.

We calculated the driving field under consideration of non-optimal quarter-wave plate retardance (see Fig. 6.6b). Therefore, we quantify the specified frequency-dependent retardance $R(\omega)$ with two linear fits at 400 nm and 800 nm wavelength. Additionally, the spectrum of the driving pulse was measured and fitted by two Gaussians. Under the assumption of a Fourier limited pulse, we determined the frequency-dependent electric field $F(\omega)$. The time-dependent electric field can be calculated by a Fourier-transformation $F(t) = \mathfrak{F}\left[F(\omega)e^{(-iR(\omega))}\right]$ and is compared to the field generated with a perfect quarter-wave plate. One optical cycle of the electric field F(t) and its difference ΔF to an undistorted two-color field is shown in Supplementary figures 6.6c, d. The total driving field as well as the difference exhibit a threefold cloverleaf shape. We find that a left- helical field is accompanied by a right-helical residual component and vice versa (see Fig. 6.6c, d). As the residual field counter rotates a weak sixfold beating is expected when scanning the cloverleaf field orientation.

Vacuum system and extreme-ultraviolet spectrometer

We utilize a high-vacuum system at a base pressure of $1e-6$ mbar for the HHG and spectral detection of the emitted extreme-ultraviolet radiation. A lens with 40 cm focal length steers the laser through an optical window into the vacuum chamber. The beam is than retro-reflected of a dual-band dielectric mirror (Eksma, 052-4080-i0) under nearly normal incidence (horizontal and vertical incidence angles $< 1°$) and focused to a focal spot size of $120\,\mu$m in diameter (full-width at half-maximum) on the target crystal surface. Due to the reflection geometry of the setup the incident horizontal angle of the laser beam on the target is 5°, whereas the vertical incident angle is $< 1°$. The generated high-harmonic radiation is collected with a focusing flat-field spectrometer (McPherson, model 234, grating with 1200 grooves/mm) and recorded with a phosphor-screen microchannel plate detector using a CCD camera.

High-harmonic spectra and spectrograms

High-harmonic spectra from the three crystal targets are shown in Supplementary Figs. 6.7a-c. The intensity of high-harmonics generated with the three-fold bi-circular driving field (red) is compared to the signal generated with a two-color perpendicular-linearly polarized field (blue) to assess the suppression of individual harmonic orders. By measuring the spectra with bi-circular excitation as a function of the three-fold field rotation θ we obtain the spectrograms, which are presented in Supplementary Figs. 6.7d-f. The spectrally-integrated signal of the 8th harmonic is used to generate the polar plots in Fig. 6.2a-c.

Helicity-dependent splitting of on-resonant harmonic peaks

The difference spectrograms in Figs. 6.3a, b and Supplementary Fig. 6.9 are determined from spectrograms, similar to those shown in Supplementary Figs. 6.7d-f, which are recorded for both helicities of the fundamental. The fifth harmonic generated in both facets of MgO and the seventh harmonic generated in quartz show a spectral shift which stems from a chiral response in both materials systems.

We model the effect of a magnetic circular dichroism in MgO and a structural circular dichroism in quartz via fitting of a helicity-dependent absorption to the observed spectral shearing of the on-resonant harmonics. Considering an energy splitting ΔE in the absorption channels for the two polarization states of the harmonics (cf. Figs. 6.4b, d) the

helicity-dependent attenuation is described by energetically-shifted literature values of the absorption coefficient $k(E \pm \Delta E/2)$ (Supplementary Fig. 6.10). Here, the signs determine the circular polarization of the high-harmonic radiation. The respective fifth and seventh harmonics are close to the resonances in MgO and quartz, such that even small energetic shifts of k(E) lead to a pronounced change in the absorption of an initial harmonic intensity $I_0(E)$. The intensity of shifted harmonics with left- and right-circular polarization ($I_{L,R}(E)$) then result from the following two equations for the respective crystal systems:

$$I_{L,R}^{\text{Quartz}}(E) = \int_0^\infty I_0(E) e^{-\frac{4\pi}{\lambda} x k\left(E \pm \frac{\Delta E}{2}\right)} dx = \frac{\lambda}{4\pi} I_0(E) k^{-1}\left(E \pm \frac{\Delta E}{2}\right), \tag{6.1}$$

$$I_{L,R}^{\text{MgO}}(E) = I_0(E) e^{-\frac{4\pi}{\lambda} \delta k\left(E \pm \frac{\Delta E}{2}\right)}, \tag{6.2}$$

where I_0 is the initially unshifted harmonic peak and λ is the wavelength of the harmonic. We used equations (6.1) and (6.2) to calculation the emitted harmonic intensity by estimating $I_0(E)$ as the mean of the recorded left- and right-circular polarized spectra. In the case of quartz, the spectrum was additionally fitted by a gaussian function to compensate for the saturated signal in the corresponding measurement. A helicity-dependent bulk effect is expected in quartz harmonics generated from every depth x and weighted by their chiral absorption contribute to the emitted intensity. Contrary, in MgO we use an additional fit parameter δ to describe the interaction length in a near-surface region where the absorption is helicity-dependent. We assume that all generated harmonic radiation passes this surface near region, neglecting the generation in the layer itself. This is justified since the major portion of the detected radiation is generated beyond this surface region as can be approximated by the penetration depth δ_{HHG}.

In addition to a chiral material response, we also considered the energy splitting of excitonic states due to an optical stark effect from the residual field as a possible cause for shifted high-harmonics. Since changing of the fundamental helicity lead to inversion of all helicities including the residual fields (see Fig. 6.6c, d), we can conclude that no symmetry-breaking field is present and no stark shift signal is expected in our case [297, 298]. Linear field components that result from the near-normal incidence of the bi-circular field on the crystal could lead to a symmetry-broken excitation. However, under consideration of the Fresnel coefficients, the calculated field values are many orders of magnitude too low for a significant optical stark effect.

Data availability

The data that support the finding of this study are available from the corresponding author upon reasonable request.

Acknowledgements

The authors thank Hugo Lourenço-Martins for helpful comments on the manuscript. This work was funded with resources from the Gottfried Wilhelm Leibniz Prize. O.K. gratefully acknowledges funding from the European Union's Horizon 2020 research and innovation program under the Marie Skłodowska-Curie grant agreement No. 752533. P.B.C. acknowledges funds from the United States Air Force Office of Scientific Research (AFOSR) under award numbers FA9550-16-1-0109.

Author contributions

M.S. conceived and designed the experiment with contributions from M.T. and O.K. M.S., T.H. and M.T. conducted the experiments with contributions from O.K., analyzed the data, and prepared the manuscript with contributions from O.K. P.B.C., A.S. and C.R. All authors discussed the results and interpretation.

Funding

Open Access funding enabled and organized by Projekt DEAL.

Competing interests

The authors declare no competing interests.

6.4 Supplementary information

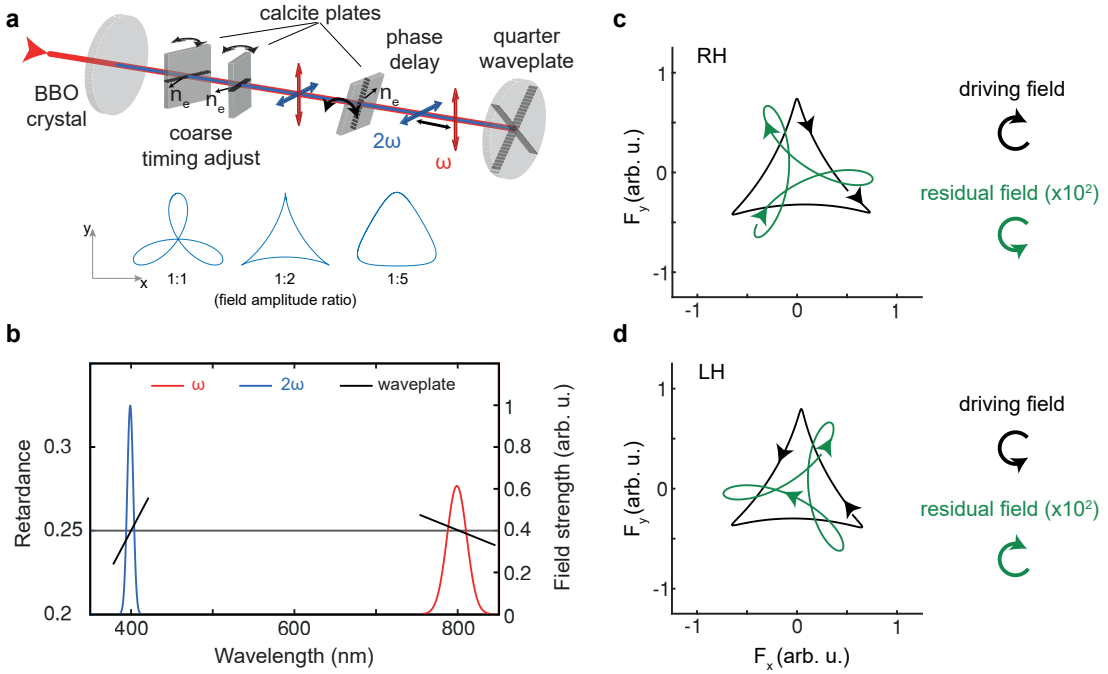

Figure 6.6: Three-fold bi-chromatic driving field. a, Schematic representation of the MAZELTOV apparatus used for generation of the bi-chromatic three-fold driving field. The timing between fundamental and second harmonic is adjusted to zero by a pair of calcite plates. An additional calcite plate is used to fine tune the phase and allow tunability of the cloverleaf orientation. **b**, Shown are gaussian fits of the measured incident spectrum (red and blue) and the specified retardance of the quarter-wave plate (black). **c**,**d**, Lissajous curve of the total three-fold right-helical (RH) and left-helical (LH) driving field (black) and the residual field (green). n_e; optical axis, ω; fundamental frequency, 2ω second harmonic frequency, $F_{x,y}$; electric field components.

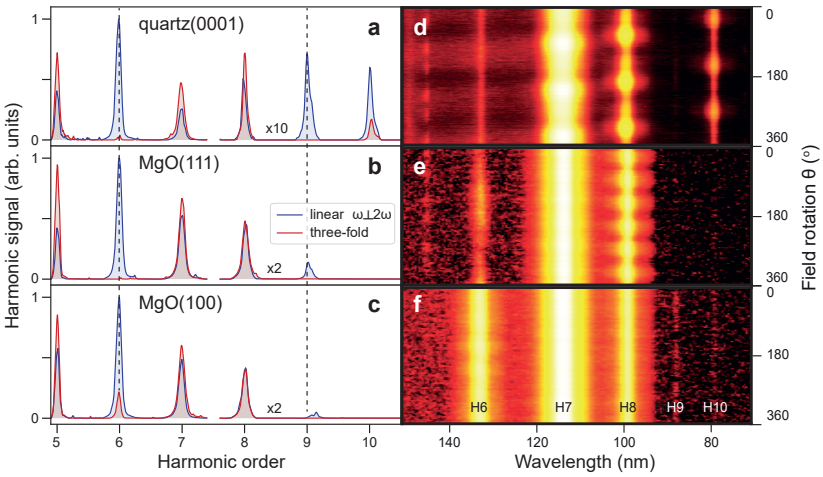

Figure 6.7: High-harmonic spectra. (**a**) quartz(0001), (**b**) MgO(111) and (**c**) MgO(100) spectra for two-color excitation with perpendicular-linear (blue) and bi-circular (red) polarization. Spectrograms for (**d**) quartz(0001), (**e**) MgO(111) and (**f**) MgO(100) as a function of three-fold field rotation angle θ with logarithmic color scale. The 8^{th} harmonic of the spectrograms is used to generate Figs. 6.2a-c.

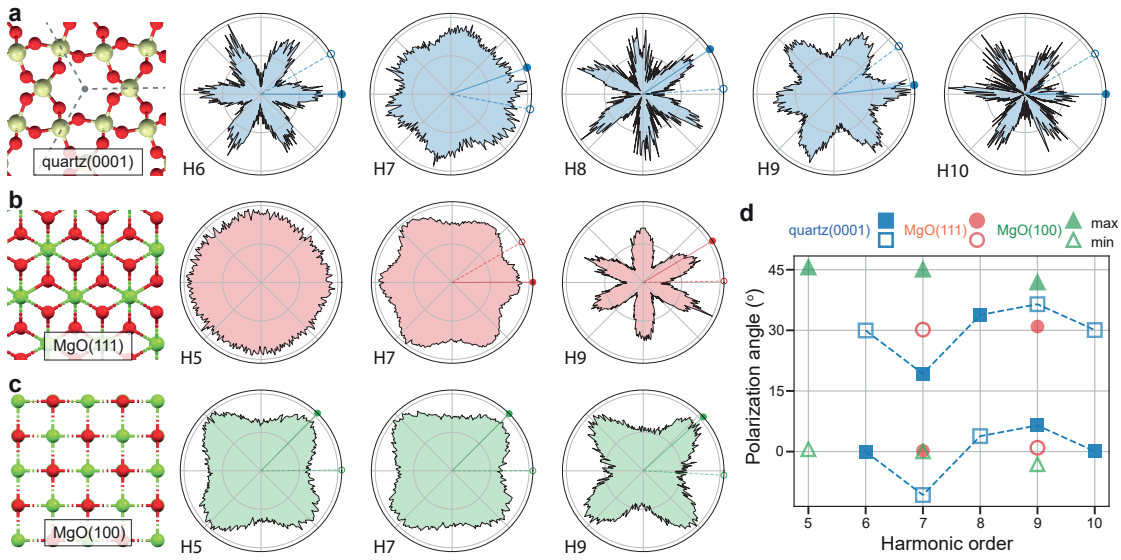

Figure 6.8: Linear Polarization Scans. Harmonic yields as a function of angle of linear polarization with respect to the fixed crystal, for (**a**) quartz(0001), (**b**) MgO(111), and (**c**) MgO(100), and their crystal structures. Dashed lines and filled/empty circles indicate angles corresponding to maxima/minima of the harmonic signal. **d** Polarization angles corresponding to maximum and minimum signal for each material as a function of harmonic order (filled and empty shapes, respectively).

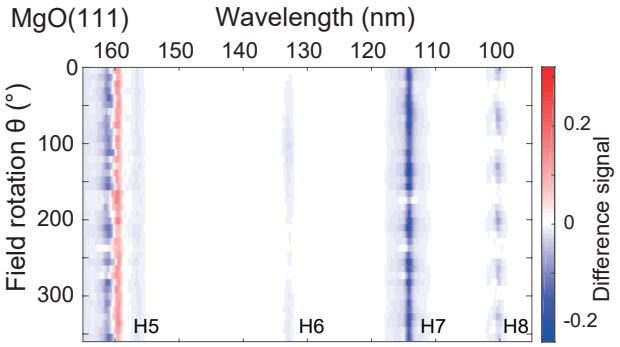

Figure 6.9: Field rotation scans on MgO(111). Difference signal from two intensity-normalized phase scans, recorded with left- and right-helical bi-circular driving fields, respectively.

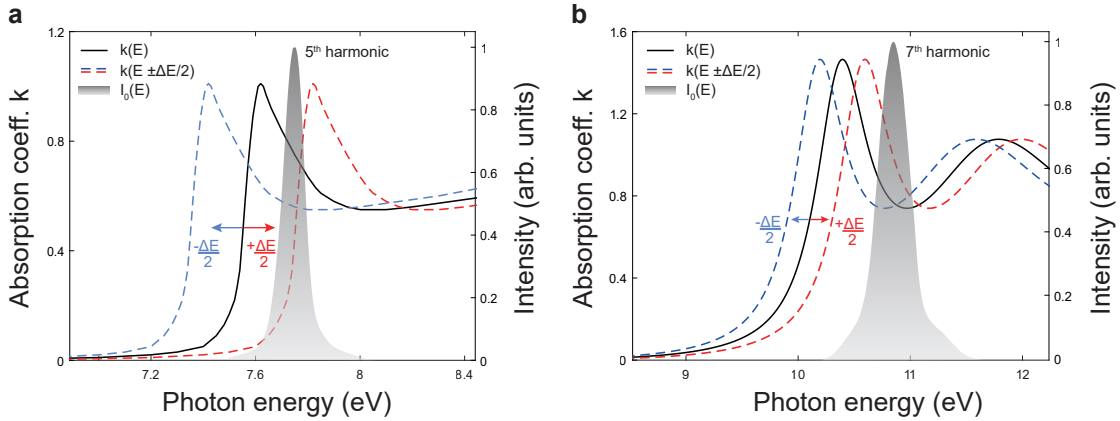

Figure 6.10: Model of shifted absorption edges. The imaginary part of the refractive index $k(E)$ (black line) for (**a**) MgO and (**b**) quartz. An energetically up (red) and down (blue) shifted edges model the effective absorption for left and right circular harmonics. The intensities $I_0(E)$ of the 5^{th} and 7^{th} harmonics are indicated

6.4.1 Selection rules for bi-circularly polarized HHG in solids

Harmonic generation is a multi-photon process which can involve many photons of each light field. Since the emitted photon can only have ± 1 unit of angular momentum, and the two-color light fields used in this study have opposite circular polarizations, the possible combinations are constrained. In the case of an anisotropic solid, the lattice itself participates in the process and can give or take angular momentum on a femtosecond timescale, but only in quantized units given by its rotational symmetry. Allowed processes for harmonic generation must obey

$$q - 3n = 2lN \pm 2,$$

where q is the order of the emitted harmonic, n is the number of ω-photons, N refers to the rotational symmetry of the N-fold crystal, l is the number of quanta of angular momentum contributed by the lattice, and the sign determines the polarization state of the harmonic. This selection rule is substantially different from the one derived for single color circular fields [299, 123]. By energy conservation, the number of 2ω-photons must be $m = (q-n)/2$. Elementary algebra shows that when N and q are both multiples of three, there exist no solutions. That is, three- and six-fold materials forbid the production of harmonics 3, 6, 9, 12, etc. The relevant rotational symmetries in this case refer to rotation about the propagation axis of the light. This yields an explanation for the presence or absence of a selection rule depending upon the crystal orientation in the case of MgO. Figure 6.7 shows the high harmonic spectra emitted from the quartz(0001), MgO(111) and MgO(100) surface for bi-circular (red) polarization. Spectra recorded with perpendicular polarized linear pulses (blue) serve as a reference experiment. The high harmonic intensity generated by the bi-circular driving field shows near-perfect suppression of H6 and H9 for quartz(0001) and MgO(111). In the case of MgO(100) a much less pronounced suppression indicates a lifting of the selection rule by the four-fold rotational symmetry.

6.4.2 Linear polarization scans

For each crystal, we also performed angle-dependent measurements with linearly-polarized, single-color driving fields. As the 800 nm driving polarization is rotated with respect to the fixed crystals, we see variations in the harmonic yields (Fig. 6.8 and 6.2d-f). Maxima (minima) for each harmonic are indicated by a solid line and a filled (empty) circle. In these linear polarization scans, quartz(0001) and MgO(111) show a six-fold response, while MgO(100) appears four-fold, consistent with the respective three-fold, six-fold and four-fold crystal symmetries. For MgO, figure 6.7b and c, the maxima and minima are always along high-symmetry directions, although in the case of MgO(111) there is a reversal between harmonics 7 and 9. On the other hand, quartz(0001) shows a more complex angle-dependence, with each harmonic maximized along a different direction, as shown in figure 6.8d. The relative phase of the harmonics has been intensively studied and applied in various studies[69, 281, 112, 62, 105]. In a real space picture, the phase is determined by the electron trajectory of the individual harmonics. The more complex angle-dependence of quartz can likely be attributed to its more complex crystal structure. For example, the projections of chemical bonds onto the surface, evident in the left panels

of figure 6.8a-c, are at several non-trivial angles for quartz, compared to the relatively simple bonding character of MgO.

Chapter 7

High-sensitivity extreme-ultraviolet transient absorption spectroscopy enabled by machine learning

T. Gutberlet, H.-T. Chang, S. Zayko, M. Sivis and C. Ropers
Optics Express 31, 39757-39764 (2023)
doi: 10.1364/OE.495821, reprinted under the terms of the Optica Open Access Publishing Agreement

We present a novel denoising scheme for spectroscopy experiments employing broadband light sources and demonstrate its capabilities using transient absorption measurements with a high-harmonic source. Our scheme relies on measuring the probe spectra before and after interacting with the sample while capturing correlations between spectral components through machine learning approaches. With the present setup we achieve up to a tenfold improvement in noise suppression in XUV transient absorption spectra compared to the conventional pump on/ pump off referencing method. By utilizing strong spectral correlations in source fluctuations, the use of an artificial neural network facilitates pixel-wise noise reduction without requiring wavelength calibration of the reference spectrum. Our method can be adapted to a wide range of experiments and may be particularly advantageous for low repetition-rate systems, such as free electron lasers as well as laser-driven plasma and HHG sources. The enhanced sensitivity enables the investigation of subtle electron and lattice dynamics in the weak excitation regime, which is relevant for studying photovoltaics and photo-induced phase transitions in strongly correlated materials.

Table-top optical-extreme-ultraviolet (XUV) transient absorption spectroscopy is a powerful tool to investigate photoinduced electronic and structural dynamics in atoms, molecules, and solids [108, 35, 72, 300]. In this approach, a sample material is excited by an optical pulse and subsequently probed in reflection or transmission with a time-delayed XUV pulse produced by high-harmonic generation (HHG). Photons in the XUV spectrum can excite core electrons, and thus enable element-specific probing of the optically induced dynamics with intrinsic attosecond timing precision due to the phase-locked generation [301]. In addition, the HHG process allows for single isolated attosecond pulses. These properties enable unprecedented time resolution for the observation of sub-cycle electron dynamics [108, 109, 110].

Despite its wide range of applications, table-top optical-XUV transient absorption spectroscopy has been mainly utilized in the high-pump-fluence regime ($>$1 mJ/cm^2) that induce large transient signals. This is largely due to the strong nonlinearities in HHG that greatly amplify fluctuations of the driving laser pulse, leading to a typical noise floor of 0.1 - 1 mOD in state-of-the-art experiments [192, 57, 193, 50, 194], which presents a formidable challenge for the observation of small pump-induced XUV absorbance changes. This far-from-shot-noise-limited sensitivity hinders studies of dynamics in the low-excitation regime, as involved in carrier dynamics in photovoltaics and electronic and structural phase transitions in solids [107, 6, 252]. For example, in a solar cell, the excited carrier density by sunlight is typically on the order of 10^{14}-10^{17} cm^{-3} [302, 303], whereas the carrier density in a 200 nm thick silicon membrane excited by 800 nm laser irradiation with fluence of 1 mJ/cm^2 exceeds 10^{18} cm^{-3} [75].

Substantial efforts have already been made to enhance the signal-to-noise ratio of transient absorption spectroscopy in the context of HHG sources. The most common method to trace long-term fluctuations involves a successive recording of pumped and un-pumped spectra [193, 57]. Additionally, noise reduction is possible by referencing, using the laser power [304], the spectral regions unaffected by the pump-induced dynamics [192, 305], or a second spectrum of the XUV pulse before the sample [306, 307]. It is also possible to use an almost common path referencing by splitting up the XUV beam [308, 309, 310]. However, these approaches typically impose requirements on the sample and experimental geometry and can not be easily used in a large variety of beam lines. Although approaches with a second spectrum may also overcome noise due to both long and short term fluctuations, imperfectly matched spectra can lead to far-from-ideal noise suppression.

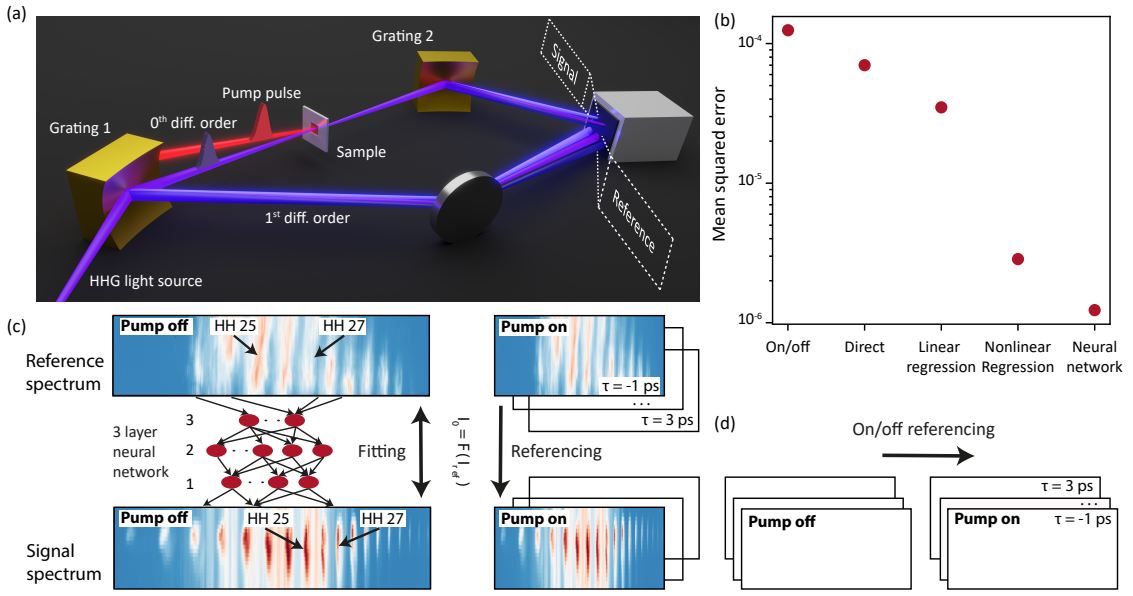

Figure 7.1: (a) Experimental setup for extreme ultraviolet transient absorption spectroscopy with a reference spectrum. (b) Comparison of different referencing algorithms. (c) Scheme for referencing with a neural network, trained on the un-pumped data. The model is applied at every pump-probe time delay τ. (d) Noise control scheme by comparing pumped and un-pumped signal (on/off) spectrum without additional reference spectrum.

In this work, we utilize machine learning to find the optimal referencing given an imperfect reference spectrum. Linear and polynomial regression and a neural network model are evaluated for signal enhancement of experimental XUV transient absorption spectra. In experiments with a 60 nm thick 1T-$TiSe_2$ sample at low fluences (0.66 mJ/cm^2), we find that a three-layer neural network surpasses all other methods and enables studies of coherent lattice vibrations and a phase transition in this material [311]. Moreover, we exploit the capability of performing a pixel-wise referencing with sub harmonic spectral resolution using the neural network.

The experimental setup is illustrated in Fig. 7.1(a). We investigate a 1T-$TiSe_2$ sample with XUV pulses produced by HHG with a 2 mJ, 35-fs-duration, 800-nm-wavelength driving pulse and its second harmonic from a Ti:sapphire laser operating at 1 kHz repetition rate with 0.28 % RMS shot-to-shot stability. A second femtosecond optical pump pulse at 2 μm wavelength produced by optical parametric amplification from the same laser system is used to excite the sample. We employ discrete harmonics that are even and odd multiples of the 1.55 eV fundamental photon energy and fluctuate by 4 % RMS.

The total flux exceeds 6 x 10^9 photons/s/harmonic for 38 nm wavelength at the source. In contrast to conventional XUV absorption experiments scheme [57] where the XUV beam is focused onto the sample with a toroidal mirror, here the focusing mirror before the sample is replaced by a toroidal grating (Grating 1) and the first-order diffracted XUV beam from the grating is taken as the *reference* spectrum. The zeroth-order beam probes the sample and is dispersed by a second grating producing the *signal* spectrum. The signal and the reference XUV beam illuminate the upper and lower half of a charged-coupled device (CCD, 1024 $\times$ 255 pixels), respectively. By recording the reference beam intensity I_{ref}, the noise of each acquisition of the signal spectrum I_{sig} may be directly compensated. However, noise originating from the beam path after the reference grating such as vibrations of the sample cannot be accounted for. Transient absorption experiments measure the change of absorbance $\Delta A = -\log_{10}(I_{sig}/I_0)$, defined as the logarithm of the pumped signal spectrum normalized by I_0 which corresponds to the transmitted probe spectrum without the pump. The time-dependent information of I_{sig} is obtained by varying the delay τ between pump and probe pulse.

Most experiments use successive recording of pumped and unpumped (on/off) signal spectra (I_0 corresponds to a subsequently acquired signal spectrum without the pump) to trace fluctuations on timescales exceeding the camera acquisition time (see Fig. 7.1(d)). However, noise originating from fluctuations on the acquisition timescale can only be fully suppressed if I_0 and I_{sig} are known simultaneously. In a two-spectrometer configuration, the normalization spectrum I_0 can be calculated by the simultaneously acquired reference spectrum $I_0 = F(I_{ref})$. Here, F is a function that relates the reference spectrum with the unpumped sample absorption.

In its simplest form, F merely contains the averaged ratio between the intensity of the unpumped signal and reference spectrum (*direct* referencing):

$$F(\lambda, I_{ref}) = I_{ref}(\lambda) \times \langle I_{sig}(\lambda)/I_{ref}(\lambda) \rangle, \tag{7.1}$$

with λ denoting the wavelength.In practice, however, the signal and reference beams may be subjected to different noise levels which prevents successful signal extraction. For example, the reference and signal beams may vary drastically in intensity and spectral purity induced by the differences in optics and path lengths between the two beams. Furthermore, the two spectra may cover different spectral regions due to their respective beam paths and it can be very challenging to precisely calibrate CCD pixels and corresponding

wavelength for both spectra at the same time. To address these issues, machine learning, which is capable of *learning* intensity relations between different wavelengths [192, 305], is utilized to establish the pixel-wise relationship between the signal and reference spectrum. The model function F is trained by 58240 sets (80%) of data to learn the relation between I_0 and I_{ref}. The training data is acquired without optical pump. The efficacy of the models are tested by another 14560 sets (20%) of unpumped data. In the following, we introduce three different machine learning models: linear and polynomial regression, and a three-layer neural network. The performance of the three approaches are evaluated by comparing their mean squared error to *direct* referencing and on/off referencing using the same dataset (Fig. 7.1(b)). Due to the discrete nature of the harmonics in our experiment and the described problems for *direct* and on/off approaches, we use the individual harmonics (7 in the reference and 15 in the signal spectrum) as pixels in the comparison.

In the nonlinear polynomial regression model of degree N, the intensity of I_0 at pixel s is expressed as

$$I_{0,s} = F(s, I_{ref}) = a_0^s + \sum_{k=1}^{N} \sum_{r_1,\ldots,r_k} a^s_{r_1,\ldots,r_k} I_{ref,r_1} \times \cdots \times I_{ref,r_k}\,, \tag{7.2}$$

where indices r_i run through all pixels containing the reference beam and a_0^s and $a^s_{r_0,\ldots,r_k}$'s are fitting coefficients. The linear regression model uses $N = 1$ with $(7+1) \times 15 = 120$ fitting parameters. As the number of fitting parameters increases exponentially with N, nonlinear polynomial regression models with different N's are tested by 5-fold cross validation to avoid over-fitting [312]. Here, 20% of the randomly ordered training data are permutatively taken out to evaluate the degree of over-fitting. In this data set, over-fitting sets in at polynomial orders larger than 5 which correspond to 30030 fitting parameters.

The neural network model can be viewed as a further generalization, capable of fitting an arbitrary, non-polynomial function $F(I_{ref})$ to the data [227]. In the present work, we employ a three-layer feed-forward neural network (see Fig. 7.1(c)) constructed with libraries *Keras* and *TensorFlow* [313]. The code is available at [314]. In the model, the number of neurons from hidden layers 1-3 are 250, 100, 70, and 200, 100, 20 for correlating intensity data of each pixel and each harmonic, respectively. These numbers have been empirically tested on the presented data and equivalent data sets recorded with the same setup and slightly changed HHG parameters. Larger models were found to yield no further accuracy improvements. A rectified-linear-unit activation function [315,

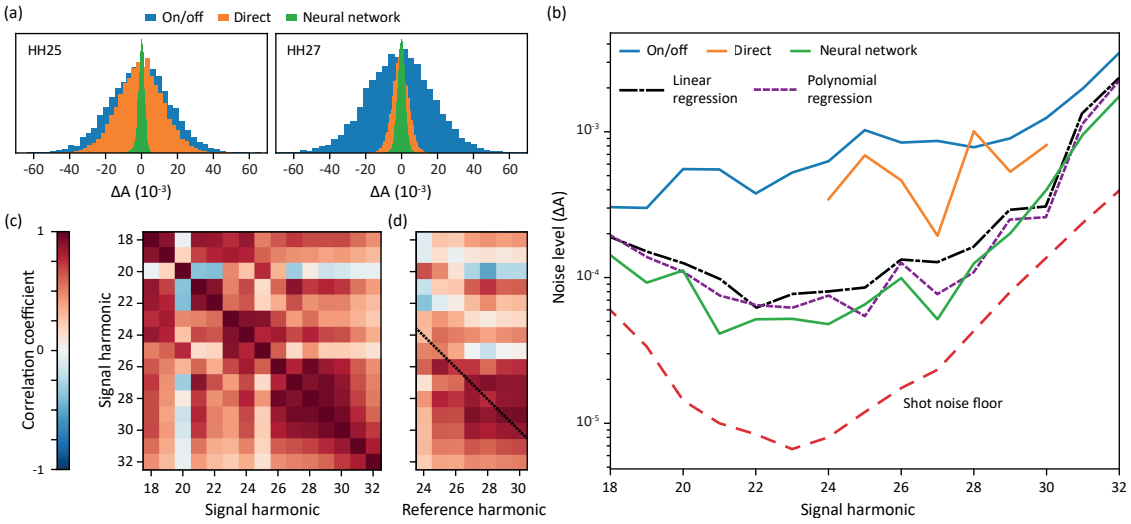

Figure 7.2: (a) Histograms of optical density difference before time zero for harmonics 25 and 27. (b) Noise levels of the discussed referencing techniques derived by the histogram standard deviation as a function of the harmonic order. (c) Autocorrelation of the signal spectrum. (d) Cross-correlation between reference and signal spectrum. Diagonal elements (black line) are used for *direct* referencing.

316] was used. The networks of 24435 and 193170 trainable parameters, corresponding to individual harmonic and pixel wise models, are optimized with stochastic gradient descent on the mean-squared error with the Adam optimizer [216] and batches of 50 data points [317]. Training of the larger model by 58240 data sets is achieved in less than three hours on a personal computer without parallelization, which presents a very moderate computational cost. In order to avoid over-fitting, the fitting is stopped when the error minimization of the testing data saturates. The presented architecture of a simple 3 layer neural network poses a good foundation for a model to describe the connection of signal and reference spectrum without any prior knowledge. In the future, more sophisticated designs may be employed to further improve the already great performance and accuracy.

Among the different models, the mean squared error (Fig. 7.1(b)) of the pumped spectrum before time zero and a subsequently acquired unpumped spectrum (on/off) is the largest. Marginal improvements are obtained by *direct* referencing (Eq. (7.1)) and linear regression. The polynomial regression method can reach better approximation with much smaller error, but is still surpassed by the neural network model. This indicates the importance to account for non-polynomial intensity noise imprinted by the highly nonlinear HHG process. To further analyze the performance of the different approaches,

the models are applied to experimental XUV transient absorption data before time zero. Here, the pump pulse arrives *after* the XUV probe and we expect the transient absorption in this material system to be zero. In Fig. 7.2(a) the absorbance change of the 25^{th} and 27^{th} harmonic are compared between the on/off method, *direct* referencing and the neural network. The on/off approach shows the largest noise which is given by the standard deviation of the histograms. *Direct* referencing improves the noise level, but is highly dependent on the harmonic order. This may result from various effects including clipping of some intensity and the unequal imaging condition such as optical aberrations, imperfect simultaneous alignment of both focal planes, and spectral impurity caused by the different beam paths and optical elements. Significantly better results are achieved with the neural network yielding similar noise levels at both harmonics.

A comprehensive analysis of the noise level derived from the standard deviations as a function of harmonic order is presented in Fig. 7.2(b). While the *direct* referencing improves the on/off approach at almost all wavelengths, the resulting noise strongly varies between harmonics. Please note that due to geometric constraints, only harmonic 24 to 30 can be recorded in the reference spectrum, limiting the spectral applicability of the *direct* referencing. The machine learning approaches which includes linear and polynomial regression and the neural network show significantly better performance with less deviation over the whole spectral region. We find that the neural network outperforms the other techniques at almost all orders of harmonics for the presented data. While the linear regression shows already good results and could be applied as a simpler model, the difference to the neural network approach is still significant. The results are compared with the photon shot noise that defines the lower noise limit. At the utilized 200 msec integration time and 3 MHz readout rate, the dark current of 0.02 counts and the readout noise of 30 counts are negligible in comparison to the measured signal of $> 10^5$ counts per pixel. The machine learning referencing reduces the noise level significantly and roughly matches the photon shot noise spectral dependence. The remaining discrepancy is likely to result form imperfect matching of signal and reference spectrum due to the different optical elements and beam paths. Furthermore, the spectral region which is not covered by the reference spectrum is prone to additional error.

To validate the predictive power when the reference and signal spectra do not share the exact same wavelength ranges, we study the intensity correlation of different harmonic orders between the unpumped signal and reference spectra. Figures 7.2(c) and 7.2(d) show the correlation coefficients among harmonics of the signal spectrum and between

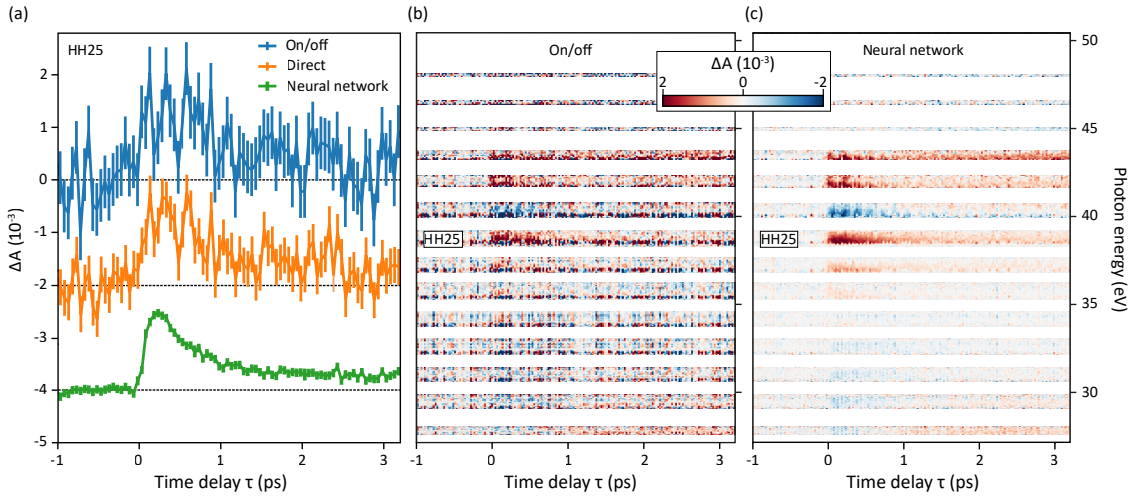

Figure 7.3: (a) Transient absorption of the 25$^{\text{th}}$ harmonic evaluated with different referencing techniques. The error bars are identical for every delay and defined by the standard deviation at the particular harmonic. (b) Pixel wise spectrum obtained with the conventional on/off approach. (c) Same as (b) but with the neural network referencing.

signal and reference spectrum, respectively. Most off-diagonal elements in both correlation maps have > 0.4 magnitude, indicating that the intensities of different harmonics are strongly correlated by the HHG process. The black line in Fig. 7.2(d) shows components that are used in *direct* referencing. As the intensities between different regions of the harmonic spectrum are highly correlated, it is feasible to predict the signal spectrum using a reference spectrum with partially overlapped spectral region. In addition, the off diagonal components provides additional information, which are used by the linear regression model. Nonlinear correlations fitted by the polynomial regression and the neural network model are not captured by the correlation coefficients. In principle, any other correlated quantity, like laser power, HHG source variables or total XUV intensity could be used for de-noising with machine learning.

Finally, we demonstrate the signal enhancement capability by showing a pump-probe trace of the 25$^{\text{th}}$ harmonic for on/off, *direct* and neural network referencing in Fig. 7.3(a). The 9.4×10^{-4} OD standard deviation of the spectrum with on/off referencing aligns with the typical noise level ≈ 1 mOD found in most transient absorption studies [192] and can be improved by a factor of two with *direct* referencing. An improvement by more than one order of magnitude in sensitivity to 9×10^{-5} OD is achieved with the neural network. In addition, the neural network model can be applied to obtain a pixel-wise correlation

between the signal and reference spectra. As most attosecond sources offer a broadband supercontinuum covering large portions of the XUV region, pixel-wise correlation offers noise-reduction without the loss of spectral resolution due to binning. Transient absorption spectra as a function of pump-probe delays and XUV photon energies are compared in Fig. 7.3(b) and Fig. 7.3(c) between the established on/off approach and the neural network referencing, respectively. For clarity, the spectral regions with low XUV intensities (owing to the discrete nature of harmonics) are omitted. While the pump induced response remains at a similar level, the neural network referencing drastically improves the visibility of the pump probe data. Again one order of magnitude improvement down to roughly 10^{-4} OD is visible. Note that while polynomial regression can also handle nonlinearities in the spectral correlation, it is computationally unfeasible to fit single pixel spectra due to the large number of fit parameters. For example, in the case of a 1024-pixel detector, 10^{14} fit parameters would be needed to model a polynomial of 5^{th} degree in polynomial regression.

The feasibility of single pixel referencing renders the neural network algorithm ideally suited for normalizing the broadband spectra from a wide range of attosecond beam lines. The reference spectrum can be acquired without wavelength calibration or complete coverage of the signal spectrum. Furthermore, instead of implementing a second spectrum, any measured quantity which is correlated to the harmonic intensity such as laser power, total XUV intensity, pulse duration, pulse shape, gas pressure or beam position may be use as input in the machine learning algorithm. As a side note, the neural network should always be trained during the data acquisition on the unpumped data such that the model can accurately capture fluctuations of the HHG source during the measurement. Comparing with the widely used on/off referencing, the neural network method does not require additional experiment time since pumped data are recorded by default for the on/off referencing in quick succession to un-pumped spectra. Note that when using a pre-trained model for noise-reduction of datasets in a different experiment, the performance of the model may degrade due to differences in HHG parameters.

In summary, we developed an algorithm for optimal noise correction in transient absorption spectroscopy with a reference spectrum. Thereby, we extend the applications of data driven algorithms in optics and photonics [318] which already showed great success in X-ray diffraction and spectroscopy for noise suppression and signal extraction [319]. Among the tested algorithms, the three-layer neural network approach shows the best result and improves the noise level by an order of magnitude compared to the established

on/off referencing method. This sensitivity increase opens the field of femtosecond to attosecond XUV transient absorption spectroscopy in the weak excitation regime such as photoinduced phase transitions in photovoltaics *in operando* or strongly correlated materials like 1T-$TiSe_2$. As the neural network approach utilizes the nonlinear intensity correlation between different pixels, it does not require wavelength-calibrated reference spectra, nor does it rely on signal and reference beams covering the same spectral region. This largely relaxes the conditions for experimental instrumentation and highlights the wide application of our method to both narrowband and broadband sources in the field of transient spectroscopy. On a broader scale, the presented combination of referencing with machine learning may be applied to a large variety of experiments with fluctuating probes to enhance the sensitivity.

Funding

Alexander von Humboldt-Stiftung; Deutsche Forschungsgesellschaft; Gottfried Wilhelm Leibniz Prize; Max-Planck-Gesellschaft.

Disclosures

The authors declare no conflicts of interest.

Data availability

Data underlying the results presented in this paper are not publicly available at this time but may be obtained from the authors upon reasonable request.

Chapter 8

Electronic and structural fingerprints of charge-density-wave excitations in extreme ultraviolet transient absorption spectroscopy

T. Heinrich, H.-T. Chang, S. Zayko, K. Rossnagel, M. Sivis and C. Ropers
Phys. Rev. X **13**, 021033 (2023)
doi: 10.1103/PhysRevX.13.021033, reprinted under (CC BY 4.0) license

Femtosecond core-level transient absorption spectroscopy is utilized to investigate photoinduced dynamics of the charge density wave in 1*T*-$TiSe_2$ at the Ti $M_{2,3}$ edge (32-50 eV). Photoexcited carriers and phonons are found to primarily induce spectral redshifts of core-level excitations, and a carrier relaxation time and phonon heating time of approximately 360 fs and 1.0 ps are extracted, respectively. Pronounced oscillations in delay-dependent absorption spectra are assigned to coherent excitations of the optical A_{1g} phonon (6.0 THz) and the A_{1g}^* charge density wave amplitude mode (3.3 THz). By comparing the measured spectra with time-dependent density functional theory simulations, we determine the directions of the momentary atomic displacements of both coherent modes and estimate their amplitudes. Interestingly, the spectral fingerprint of the amplitude mode can be associated with many-body electron screening, strengthening the importance of electron-electron and simultaneous electron-phonon interaction for the stability of the charge density wave. In addition, we find that 10% and 13% of the absorbed energy is stored in the A_{1g} and A_{1g}^* coherent modes, respectively. This work presents a first look on charge density wave excitations with tabletop core-level transient absorption spectroscopy, enabling simultaneous access to electronic and lattice excitation and relaxation.

8.1 Introduction

Electronic processes in quantum materials including superconductors, Mott insulators, and charge density wave (CDW) compounds encompass a wide range of phenomena with collective excitations involving coupled electronic, vibrational, and spin dynamics [8, 6, 106, 107]. The layered transition metal dichalcogenide 1T-$TiSe_2$ features CDW formation below a critical temperature (T_c) of 200 K [241], linked to a periodic lattice distortion (PLD) in the form of a $2 \times 2 \times 2$ supercell [240], shown in Fig. 8.1(a). Various mechanisms, including Jahn-Teller effects and exciton condensation, were proposed to explain the CDW formation yet the exact mechanism of CDW formation is still unclear and subject of many studies [234, 235, 245, 259, 237, 244, 320, 236]. Recent experiments on ultrafast nonthermal melting of the CDW in 1T-$TiSe_2$ suggest that the electronic and vibrational degrees of freedom are strongly coupled in the CDW quenching process [252, 321, 92, 246, 20, 93, 251, 322, 257, 253, 323, 324, 255], and different timescales of the loss of electronic and structural orders have been observed [256, 254].

To understand such complex photophysical phenomena, simultaneous probing of the electronic and lattice subsystems in a single experiment is highly beneficial, as it allows for a study of both degrees of freedom at identical experimental conditions. Core-level transient absorption spectroscopy, in which the sample is pumped with a femtosecond optical pulse and subsequently probed by an extreme ultraviolet (XUV) pulse, is ideally suited for this purpose. This method has been successfully utilized to simultaneously observe the decay of photoexcited carriers and coherent phonons in $MoTe_2$ [51] and to disentangle the intricate electron phonon dynamics in graphite [53]. However, up to now, XUV radiation has not been used to study excitations of CDWs. In this work, we apply core-level spectroscopy at the Ti $M_{2,3}$ edge (32-50 eV) to investigate photoinduced excitations of the CDW in 1T-$TiSe_2$. Thereby, we analyze the transient absorption by comparing with *ab initio* simulations conducted with time-dependent density functional theory (TDDFT). We distinguish the electronic and phonon contributions to the core-level transient absorption spectra, extract the timescales of hot electron cooling and phonon heating, separate contributions from different coherent phonon modes by spectral fingerprints, and identify their corresponding atomic displacements, excitation efficiency, and dephasing times.

8.2 Results

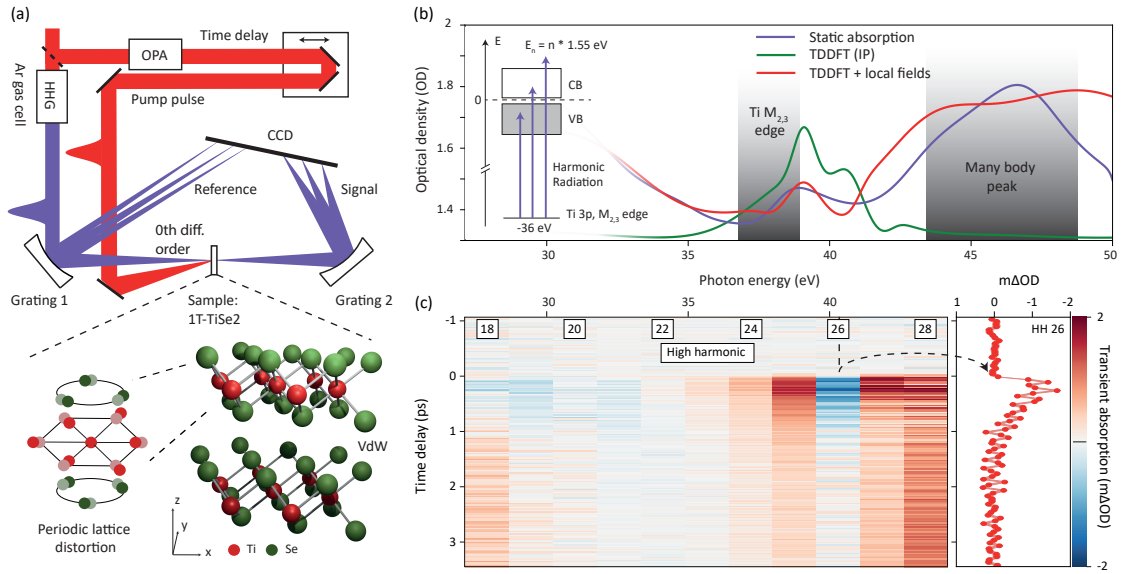

Figure 8.1: (a) Setup for extreme ultraviolet (XUV) transient absorption spectroscopy, where fluctuations of the high-harmonic generation (HHG) source are tracked with a reference spectrum for noise reduction. The $1T$-$TiSe_2$ specimen consists of layers held by van der Waals (vdW) forces and shows a charge density wave with an associated periodic lattice distortion. (b) Static absorption spectrum recorded with a continuous HHG source (purple line) [157]. Time-dependent density functional theory (TDDFT) calculations under independent particle (IP) approximation (green line) and with the inclusion of local field effects (red line). The latter qualitatively reproduces the Ti $M_{2,3}$-edge (approximately 36.5 eV) as well as the many-body absorption peak at 42 eV – 49 eV. Inset: Titanium M edge originating from transitions of the Ti 3p orbital to empty states in the valence (VB) and conduction band (CB). (c) Exemplary transient absorption spectrum recorded with discrete harmonics spaced by 1.55 eV. Relative changes to an unpumped sample are shown for various time delays of the pump pulse.

The core-level transient absorption experiment is conducted with a 65-nm-thick $1T$-$TiSe_2$ flake on a 30-nm-thick silicon membrane (Appendix 8.5) at a temperature of 110 K. Details of the experimental setup [Fig. 8.1(a)] are described in Appendix 8.5 and Ref. [325]. In brief, the sample is optically excited by a 40-fs laser pulse centered at 2-μm wavelength and probed by a time-delayed XUV beam covering the spectral range of 25-50 eV. The XUV radiation is produced through high-harmonic generation (HHG) driven by 35-fs-long laser pulses (800 nm center wavelength) and their second harmonic in an Ar-filled gas cell. The two-color field creates both even and odd harmonics of the fundamental driving beam centered at 1.55 eV. The absorption of the XUV radiation in

the investigated spectral range is dominated by transitions of the Ti $3p$ electrons into the valence shell [Fig. 8.1(b)]. The pump-induced change of the XUV absorbance is defined as the difference between the absorbance [optical density, OD] with and without optical excitation ($\Delta\text{OD} = \text{OD}_{\text{pumped}} - \text{OD}_{\text{unpumped}}$). An additional reference spectrum of the harmonic source is simultaneously collected for noise suppression, which provides an improved sensitivity beyond 10^{-4} OD [325] and enables the detection of subtle CDW dynamics, as found in $1T$-$TiSe_2$ at low pump fluences. More specifically, the investigation of CDW excitations is largely restricted to fluences below the threshold for nonthermal CDW melting [254].

Figure 8.1(b) displays a static absorption spectrum of $1T$-$TiSe_2$ (purple line), recorded with a spectrally continuous source [157]. Here, the Ti $M_{2,3}$-edge exhibits a small peak with an onset at approximately 36.5 eV and another strong absorption peak centered at about 47 eV. The absorption below the edge (< 36.5 eV) results from excitations of electrons within the valence shell, which are dominated by the bulk plasmon peak centered at 20 eV [326]. This contribution to the absorption decreases with increasing photon energy such that only the tail is seen in the XUV spectra below 36 eV. As this spectral region does not involve excitations of core-level states, it is expected to behave differently from the M-edge spectrum at energies larger than 36 eV. To understand the Ti $M_{2,3}$-edge transitions, we compare the measured static spectrum with TDDFT simulations (Appendix 8.5) in the linear response theory under random phase approximation. The simulated transitions within the independent particle (IP) approximation [Fig. 8.1(b), green line] overlap with only the approximately 39 eV small peak in the empirical spectrum, whereas the strong peak at approximately 47 eV is absent. Calculations including local field effects [Fig. 8.1(b), red line] [155], where many-body interactions in electronic excitations are partially accounted for, qualitatively reproduce the empirical spectrum. This suggests that the small peak at the onset of the Ti $M_{2,3}$-edge (36.5 eV) mainly constitutes single-particle excitations from the Ti $3p$ orbitals to the conduction band. In addition, the strong peak at approximately 47 eV can be identified as a giant resonance [327, 328] comprising transitions from the Ti $3p$ levels to the conduction band, accompanied by valence-shell excitations from below to above the Fermi level through configuration interactions. Here, the local screening to the core electron results in a collective resonance above the core-level edge in addition to the single-electron transitions. In transition metals and transition-metal dichalcogenides, it has been found that the many-body resonance is highly sensitive to the local charge density around the excited atom [156, 329]. To this end, the spectral region

of the giant resonance at approximately 47 eV is ideally suited to study the charge density wave dynamics in $1T$-$TiSe_2$.

The photoinduced dynamics in $1T$-$TiSe_2$ are tracked by recording XUV absorption spectra as a function of the pump-probe time delay τ [Fig. 8.1(c)]. Because of the discrete spectrum of the harmonic source (Appendix 8.5) and the weak pump-induced signals ($< 10^{-3}$ OD), the spectra are binned to the center of each harmonic peak, separated by the photon energy of the fundamental driving laser (1.55 eV). At pump-probe overlap ($\tau \approx 0$), the absorbance decreases at energies below 35 eV. An increase in absorbance is observed in both the Ti $M_{2,3}$ near-edge region (35-39 eV) and at the onset of the many-body giant resonance (42-45 eV). In between the tail of the lower-energy peak of Ti $M_{2,3}$ edge (39 eV) and the onset of the giant resonance (42 eV), a decrease in absorbance is found. At long time delays ($\tau > 3$ ps), an absorbance increase is seen across the entire spectrum. At time delays up to about 3 ps, oscillations in transient absorption signals are evident from the 26th to the 31th harmonic [Fig. 8.1(c), right]. In the following sections, we analyze the transient absorption signals at pump-probe overlap and > 3 ps time delay (Sec. 8.2.1), discuss the origin of the oscillations (Sec. 8.2.2), and extract the timescales of the underlying physical processes.

8.2.1 Hot electron dynamics and lattice heating

Transient absorption signals at $\tau = 50$ fs and 3 ps are plotted in Fig. 8.2(a) (dots) for a pump fluence of 0.66 mJ/cm^2. As the energy transfer from the electrons to the lattice typically occurs on the hundreds of femtoseconds to picosecond timescale [257, 255], photoexcited carriers are expected to be the main contributor to the transient absorption signal at 50-fs delay. This time delay is intentionally chosen to show only the effects of the excited electron system shortly after the laser pulse excitation. In many materials, photoexcited carriers contribute to a positive core-level transient absorption signal below the edge and a negative signal above the edge due to holes and electrons below and above the Fermi level, respectively [57, 58, 59, 60, 51, 61]. However, at the onset of the Ti $M_{2,3}$ edge, the transient absorption signal exhibits an increase with energy, contrary to the expected signal contribution from electronic state blocking. This can be explained by significant many-body effects affecting the core-level transitions [156, 330, 157].

Previous studies observe an electron-temperature-induced derivative absorption feature in a variety of materials [51, 331, 332, 60, 156, 330] which is assigned to a band gap

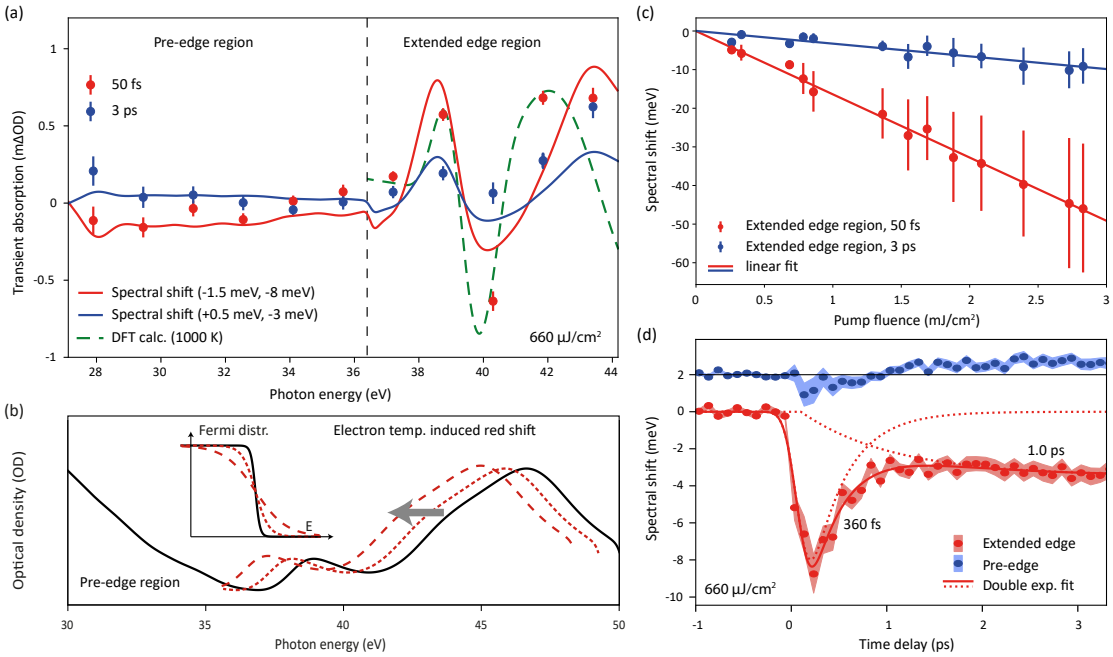

Figure 8.2: (a) Transient absorption spectra. The energy-dependent response can be modeled with selective spectral shifts of the static spectrum [Fig. 1 (b)]. To this end, the spectral range is separated into the pre-edge ($< 36.5\,\mathrm{eV}$) and extended edge ($> 36.5\,\mathrm{eV}$) regions. Complementary TDDFT calculation for elevated electron temperature (green dashed line) shows a similar spectral change. The spectral width of the harmonics is < 250 meV. (b) Schematic spectral changes induced by electronic heating. (c) Fluence dependence of the extended edge shifts, showing a linear scaling in support of thermal mechanisms. (d) Temporal dynamics of spectral shifts in the pre-edge and extended edge region. A double-exponential fit extracts electronic excitation decaying on approximately 360 fs and contributions of the phonon bath that emerge on the picosecond time scale.

renormalization in semiconductors and chemical potential changes plus changes in electronic screening in metals. Both effects lead to a shift of the empty final states, which are overlapped by a broadening of the absorption edge. In addition, the changed electronic screening may also shift the energy of the core level [333]. In a complex semimetal like 1T-$TiSe_2$, it is nontrivial to assign a specific microscopic mechanism, but all mentioned effects are well described by a spectral shift plus some broadening of the static absorption spectrum [330]. We apply such an analysis by first separating the spectrum into two regions: the region containing the Ti $M_{2,3}$-edge transitions (>36.5 eV), and the region mainly contributed by the tail of the bulk plasmon excitation (<36.5 eV, cf. Fig. 1(b)), which does not include a core-level excitation and is, therefore, not further discussed in

this work. By applying redshifts of 1.5 and 8 meV to the static absorption spectrum below and above 36.5 eV, respectively, the resulting spectrum shows reasonable agreement with the empirical transient absorption data (Fig. 8.2(a) red line and dots). We do not observe a pronounced broadening of the Ti M edge in 1T-$TiSe_2$. At photon energies of > 44 eV, the energy cutoff of our HHG light source is reached, which leads to higher noise levels overshadowing the signal. Therefore, we cannot resolve the small redshift in this spectral region that is predicted by the simulations.

We compare the measured transient absorption spectrum at 50 fs with TDDFT simulations to explore whether a hot (quasithermalized) electronic population is consistent with the observed absorption changes. Figure 8.2(a) (green dashed line) shows the difference between the core-level absorption spectrum simulated for an electronic temperature of 1000 and 110 K. Here, the electron temperature is adjusted by the Fermi distribution in the calculation, and the calculation also accounts for the electron-temperature-induced band changes described in the previous paragraph. According to fluence-dependent measurements [Fig. 8.2(c)], the behavior of the spectral redshift does not differ below and above the thermal CDW transition threshold. Therefore, we use the normal state of 1T-$TiSe_2$ instead of the PLD supercell, as the CDW is not expected to significantly influence the spectral signature of excited electrons. The fluence-dependent measurements are further discussed in a later paragraph. A temperature of 1000 K corresponds to the estimated electron temperature at the pump fluence of 0.66 mJ/cm^2, calculated in the free electron gas model. The simulation shows good agreement with the experimental spectrum, suggesting that at 50 fs an excited electronic population leads to a redshift qualitatively shown in Fig. 8.2(b). Notably, the TDDFT calculation is in even better agreement with the data compared to the simplified spectral shift model.

In contrast to the dominance of photoexcited electrons in the transient absorption spectrum at 50-fs time delay, the spectrum at 3-ps delay is expected to be dominated by the heated phonon bath. An increase in the lattice temperature can influence the XUV spectrum by thermal expansion [60, 75] and electron-phonon coupling, which was previously observed to shrink the band gap and also lead to a derivative-shaped absorption feature [60, 57, 51, 75]. The effect has been analyzed in comparison to the Debye-Waller effect from electron diffraction data [60], and it was found that at large time delays the near edge spectral changes can be assigned to the lattice temperature. In this study, we estimate a lattice and electron temperature of 30 K at equilibrium using the pump fluence (see Appendix C). At this temperature, the expected contribution from the electronic

temperature increase is only 0.3 meV and can be neglected. Thus the empirical transient absorption spectrum at 3 ps can be attributed to lattice heating and approximated by a much larger redshift of the static absorption spectrum. Figure 8.2(a) (blue line and dots) shows that the transient absorption below 36.5 eV is diminished to almost zero, while the spectrum above 36.5 eV can be qualitatively described by a 3-meV redshifted static absorption spectrum. The agreement between the empirical data and energy-shifted static spectrum degrades in the >40-eV region. This may be explained by the different response to photoexcitations between the Ti $M_{2,3}$-edge onset, which is mainly due to one-body core-level excitations, and the giant resonance at >42 eV, where many-body effects dominate. The absorption in the >40 eV region is therefore expected to be influenced by both mechanisms. As the fitting only incorporates one spectral shift parameter, the behavior of the transient absorption signal cannot be properly described here.

To substantiate the relationship between the spectral shifts and electron and lattice temperatures, we conduct fluence-dependent measurements at these two time delays. The resulting spectral shifts from fitted spectra at >36.5 eV depend linearly on pump fluence [Fig. 8.2(c)], indicating that the spectral shifts also depend linearly on the electron temperature and phonon populations. Potential nonlinearities induced by the second-order phase transition at the thermal transition threshold with corresponding pump fluence of 1.8 mJ/cm^2 (see Appendix 8.5 for more details) are not observed. This agrees with the negligible discontinuity of the derivative of the specific heat near the transition threshold [334].In conclusion, the redshift is found to be a good measure of the thermal electron and phonon excitation. In this regard, it is justified to compare TDDFT calculations that omit CDW effects. In the temperature and fluence range explored in this study, we find that the nonlinearities arising from the temperature-dependent electronic and lattice specific heat are below the experimental sensitivity. The integration of the specific heat [334] reveals a deviation of less than 5% of the fluence-dependent temperature from a linear scaling. In addition, calculations at different electron temperatures confirm a linear dependence of the spectral shift on the electron temperature in the relevant fluence regime. In photoemission studies that offer a more detailed view on the electronic structure, it was shown that electron-electron scattering leads to a quasiequilibrium within the electron subsystem at a timescale of 200 fs [93]. In comparison, the spectral redshift is expected to be less sensitive to the finer details of the carrier distribution but serves as a good measure for the effective strength of electronic excitation, as indicated by the linear fluence dependence and the TDDFT calculations. As the ab *initio* simulations of lattice temperature

effects are much more computationally intensive, comparison of simulation and experimentally measured spectra at 3-ps delay is beyond the scope of this work. However, we show that the spectrum at 3 ps is dominated by the lattice temperature contribution corresponding to a 30-K temperature increase, which is directly related to an increased electron temperature of 1000 K at 50 fs. Between 50 fs and 3 ps time delays, both electronic and lattice heating effects are present. Hence, by extracting the spectral shifts at each time delay, the time-dependent electron and lattice temperature can be qualitatively tracked. Figure 8.2(d) (red line) displays the fitted spectral shifts of the extended edge region as a function of the time delay. We fit the time-dependent redshift with two time constants (dashed lines) for the electronic (T_e) and phononic systems (T_b), which corresponds to a three-temperature model. In this model, a third system may store and exchange energy with the electrons and the phonon bath. The fitting yields a $T_e = 0.36 \pm 0.04$ ps decay and a $T_b = 1.0 \pm 0.3$ ps rise, which we assign as the electronic population decay time and phonon population rise time, respectively. A fit with a single time constant is incapable of describing the slight increase of the redshift between 1 and 3.3 ps and, more importantly, yields an unreasonable fast time constant of 280 fs for the lattice system which is expected to heat up on the 1 ps timescale [255].

8.2.2 Coherent phonon dynamics

The XUV transient absorption spectra exhibit oscillations as a function of the time delay [Fig. 8.1(c), right side] that stem from coherently excited lattice modes. In 1T-$TiSe_2$, harmonic orders 26 to 31 display oscillations at 3.3 and 6.0 THz as shown in Figs. 8.3(a)&(b), 8.7, and 8.8. From phonon frequencies identified in previous Raman and optical pump-probe studies [324, 242], the 6- and 3.3-THz oscillations are assigned to the A_{1g} optical mode and the A_{1g}^* CDW amplitude mode, respectively.

The optical mode consists of purely out-of-plane oscillations of all selenium atoms. In contrast, the amplitude mode, which involves the coherent oscillation of the PLD, comprises in-plane movements of both Ti and Se atoms. For comparison, the eigenvectors of these modes are depicted in Fig. 8.3(c). As the amplitude mode is found only in the PLD-ordered state below the critical temperature [242], a loss of its signal is interpreted as a partial suppression of the PLD order [324]. In this study, we observe a corresponding suppression of the amplitude mode by increasing the pump fluence from $F = 260\,\mu\mathrm{J/cm^2}$ to $F = 660\,\mu\mathrm{J/cm^2}$. At the higher fluence, the 3.3-THz signature is no longer discernible

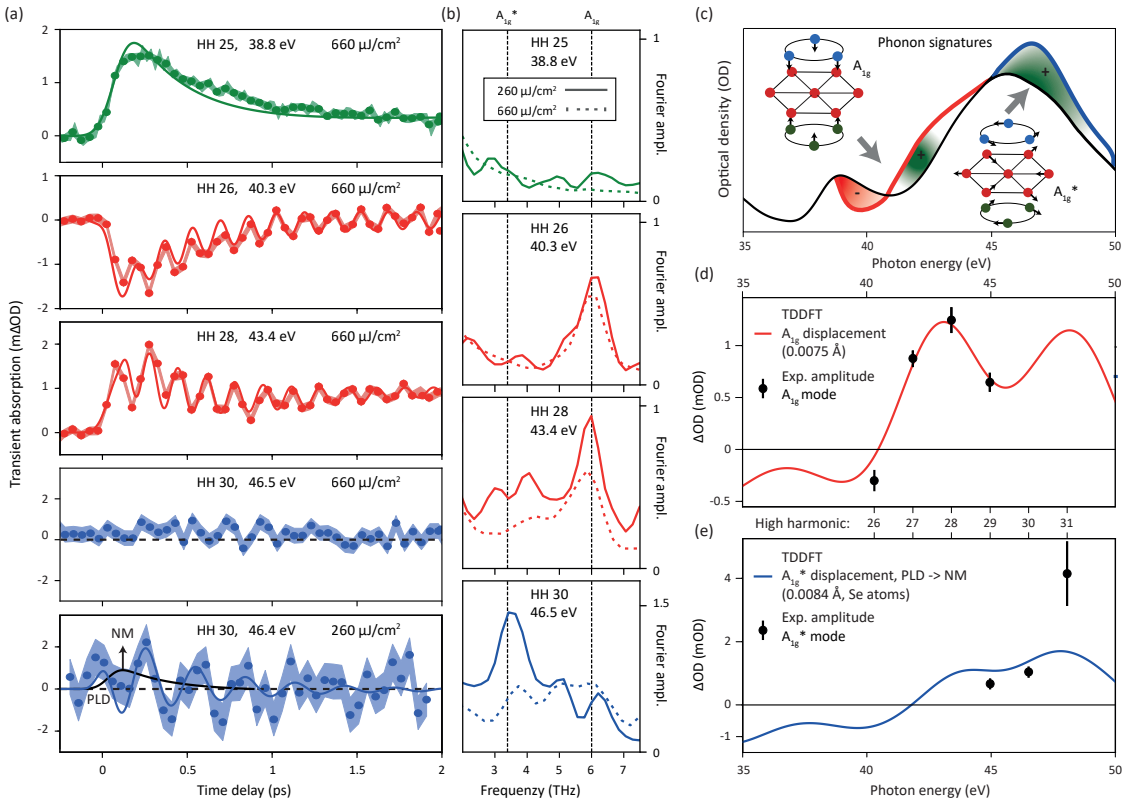

Figure 8.3: (a) Selected transient absorption traces of $1T$-$TiSe_2$. Pump-probe traces are recorded for $F = 260\,\mu J/cm^2$ and $F = 660\,\mu J/cm^2$ at 110 K in the CDW phase. The sign of ΔOD is related to the direction of lattice displacement (see TDDFT calculations) and allows for assigning the displacements from the PLD to the high temperature, normal metallic (NM) state of $1T$-$TiSe_2$ for positive absorption changes at harmonic 30. (b) Fourier spectra of pump-probe traces. The observed 6 and 3 THz oscillations are attributed to the A_{1g} optical mode and the $A_{1g}{}^*$ amplitude mode of $1T$-$TiSe_2$. The optical mode is largely independent of the pump fluence while the signature of the amplitude mode is suppressed at large excitation. (c) Schematic sketch of the phonon mode spectral fingerprints. The optical and the amplitude mode can be assigned to a characteristic change in the spectrum which are qualitatively illustrated here. (d) Spectral change of the A_{1g} displacement calculated by TDDFT compared to the initial oscillation amplitude in the pump-probe traces. (e) The same as (d) but for the $A_{1g}{}^*$ amplitude mode.

[HH 30, Figs. 8.3(a)&(b)], whereas the optical mode amplitude is largely unaffected.

Interestingly, the spectral changes induced by the two phonon modes are energy separated, and these spectral fingerprints are schematically drawn in Fig. 8.3(c). From the lineouts shown in Figs. 8.3(a) and 8.7 as well as their Fourier components displayed in Figs. 8.3(b) and 8.8, we identify three spectral regions with different contributions to the transient absorption signal. First, at photon energies below 38.7 eV (HH 25, green), no

coherent oscillations are visible. Between 40.3 and 45 eV (red), the transient absorption spectra are dominated by the 6-THz oscillations assigned to the A_{1g} optical mode. Finally, the 3.3-THz oscillations corresponding to the amplitude mode appears only above 45 eV (blue).

The spectral fingerprints of the observed oscillations are further analyzed by direct comparison with TDDFT calculations. Here, the spectra are computed for small atomic displacements along the phonon eigenmodes predicted by DFT simulations [335], which are schematically shown as black arrows in Fig. 8.3(c). By comparing the spectra to the absorption of an undistorted lattice, the expected change in the optical density is calculated (see Appendix 8.5 for more information). In Figs. 8.3(d) and 8.3(e), the calculated OD change is compared to the experimentally observed oscillation amplitude near time zero. The spectral fingerprints are well reproduced by the DFT model. The simulated ΔOD for the amplitude mode shows a maximum amplitude at the 31st harmonic and a smaller response at the 30th and 29th harmonic. A very different spectral response at harmonics 26-29 is observed for the optical mode. Here, the sign reversal between harmonics 26 and 27, which can also be seen by comparing HH 26 and HH 28 in Fig. 8.3(a), is faithfully reproduced by the calculations. At larger photon energies, the optical mode signal can no longer be clearly distinguished from the noise level despite being predicted by the simulations. This is due to the increased noise at the cutoff wavelength of our light source. Thus, potential signatures of the optical mode that could be seen in the Fourier spectra at harmonics 30 and 31 in Figs. 8.3(b) and 8.8 are not included in the above discussion.

With the link to real-space coordinates provided by the TDDFT calculations, the direction of the atomic movements related to positive or negative absorption changes can be unambiguously identified. For the amplitude mode, positive absorption changes correspond to an atomic movement from the PLD toward the high-temperature, normal (semi)metallic (NM) phase. In the case of the optical mode, a positive transient absorption of harmonics 27-29 is indicative of a contraction movement like shown in Fig. 8.3(c).

Besides the qualitative agreement, a comparison of TDDFT data to the experiment allows us to quantify the initial amplitude of the coherent oscillations. For the optical mode, the experimental absorption change is reproduced by Se atoms displaced by 0.0075 Å, and for the amplitude mode by reducing the PLD by 30% (0.0084 Å for Se atoms and 0.0255 Å for Ti atoms). The energy stored in the modes can, thus, be estimated from the real-space displacements and the phonon frequencies. Under the assumption of a homogeneous excitation over the entire sample region probed, stored energies per normal-phase

unit cell (u.c.) of 0.65 and 0.8 meV/u.c. are obtained for the optical and amplitude mode near time zero, respectively (Appendix 8.5). These values represent a significant fraction of the 260 μJ/cm^2 pump fluence, which translates to an absorbed energy of 6 meV/u.c. (Appendix 8.5). Interestingly, at the larger fluence of 660 μJ/cm^2 the amplitude of the optical mode excitation remains largely unchanged compared to the low-fluence data, implying that the efficiency of phonon excitation is nonlinear. This is further discussed in Sec. 8.3.

In order to obtain meaningful damping times of the coherent modes, we use a global fit that simultaneously fits a single oscillation with a frequency f and a common damping T_p to multiple harmonics (see Appendix 8.5 for details). Here, we use all harmonics that display either the optical or the amplitude mode to extract the intrinsic phonon dephasing times. Resulting fits are shown as solid lines in Figs. 8.3(a) and 8.7, and details of the fit parameters are described in Appendix 8.5. The optical mode shows a dephasing time of $T_p = 1.3 \pm 0.5$ ps and $T_p = 1.0 \pm 0.2$ ps for the 260 and the 660 μJ/cm^2 fluence measurement, respectively. For the amplitude mode we extract a damping of $T_p = 0.6 \pm 0.2$ ps. We find that the obtained time constants of both phonon modes are in good agreement with previous studies [257]. In the global fit model, we exclude harmonic 26 from the global fit of the optical mode as the phonon signature at this harmonic is strongly affected by the electron and lattice-induced redshift [Fig. 8.2(a)]. This leads to the seemingly stark difference between the strong damping of harmonic 28 and the weaker damping of harmonic 26 as shown in Fig. 8.3(a). We discuss the influence of the redshift on the measured damping times in more detail in Appendix 8.5 and Fig. 8.6.

While harmonic 30 does not show any contribution of an elevated electron temperature at the larger fluence of 660 μJ/cm^2, the oscillation of the amplitude mode is found to be displaced to positive optical density changes within the first picosecond at 260 μJ/cm^2 excitation [black line in Fig. 8.3(a)]. A similar behavior of an additional positive absorption change is visible at harmonic 29 in Fig. 8.7. We assign this component to an additional displaced atomic position. This short-lived positive absorption change can be associated with a mean displacement of the amplitude mode from the PLD state toward the high-temperature NM phase, in accordance with the TDDFT calculations. Such transient oscillation around a new equilibrium position may be associated to a displacive excitation mechanism that is expected for the amplitude mode in 1T-$TiSe_2$ [253, 251]. However, usually the oscillation of displacive excitation occurs around a new equilibrium position and relaxes on larger timescales.

8.3 Discussion

In this study, we spectrally separate coherent excitations of the A_{1g}^{*} amplitude mode and the simultaneously excited A_{1g} optical mode in $1T$-$TiSe_2$. We find that only the amplitude mode is suppressed above a certain threshold fluence in agreement with the previously reported nonthermal CDW suppression [253, 252, 254, 256]. For better comparison to previous experiments, the incident fluences used in this work ($F = 260\,\mu J/cm^2$ and $F = 660\,\mu J/cm^2$) are converted to deposited energy per unit cell (u.c.) (see Appendix 8.5) resulting in 6 and 15 meV/u.c., respectively. At the lower excitation density of 6 meV/u.c., the amplitude mode is well visible and suppressed at 15 meV/u.c. deposited energy. Considering the stark differences in the experimental setup, sample, temperature, and pump wavelength, this threshold is still in reasonable agreement with the previously reported threshold value of 4 meV/u.c. [257]. Since the nonthermal melting of the CDW strongly depends on the exact electron excitation mechanism, different excitation configurations and especially different pump wavelengths lead to deviating threshold fluences. In conclusion, a comparison of absolute fluences and microscopic mechanisms between two separate experiments is often challenging. This highlights the value of simultaneous observations on electronic and phononic subsystems by the same probe, which facilitate a direct comparison. As the amplitude mode exists only in the PLD-ordered state, its suppression is a clear indication of a loss of PLD order. We estimate a temperature increase of approximately 30 K for the fluence of 0.66 mJ/cm^2, which is insufficient to drive the system above the transition temperature of 200 K. Nevertheless, this fluence still leads to a suppression of the PLD as indicated by the vanishing of the amplitude mode. Various mechanisms have been proposed to describe this nonthermal melting of $1T$-$TiSe_2$, ranging from exciton breaking to a loss of 3D coherence [253, 252, 254, 256].

To gain more insights into the mechanism of CDW excitations in $1T$-$TiSe_2$, understanding the photoinduced dynamics and the interplay of the electronic and phononic systems is of great importance. The spectral redshift is found to qualitatively track electronic and lattice heating. An effect of the CDW or PLD melting on the spectral shift is not observed. This is confirmed by the linear fluence dependence, shown at 50 fs and 3 ps pump-probe delays in Fig. 8.2. Additionally, we find that the signal from the optical mode persists independent of the fluence, and we do not observe any direct involvement of the optical mode on the quenching of the CDW or PLD state. The observed nonlinear dependence of the excitation efficiency on the fluence is consistent with previous work. A sublinear scal-

ing has been reported above the threshold [257], and our work extends this observation to lower fluences. A possible mechanism could be the indirect influence of the nonlinearly excited electronic system which determines the excitation efficiency of the phonon mode. While the optical mode's spectral fingerprint resides near the absorption edge, the spectral region of the amplitude mode coincides with the many-body absorption peak. As the many-body resonance results from local dynamic screening effects, we find strong evidence of a coupling of the amplitude mode to a perturbation of the electronic screening and cooperative electron motion [328, 186]. Specifically, coherent excitations of the amplitude mode, associated with the PLD, lead to an altered electronic screening at the Ti atoms, which is reflected by the spectral changes in the many-body peak. This result supports an interplay of electron-electron interactions and electron-phonon coupling for the CDW stability in light of the ongoing discussion regarding the CDW driving mechanism in $1T$-$TiSe_2$ [234, 235, 245, 259, 237, 244, 320, 236]. Conversely, a perturbed electron-electron correlation may be one cause of the amplitude mode excitation. However, it should be noted that while our results provide important insights into the interplay between electron-electron interactions and electron-phonon coupling in the stability of the CDW in $1T$-$TiSe_2$, a complete understanding of the relative contributions of excitonic and electron-phonon coupling mechanisms to the CDW transition requires further investigation. Therefore, future studies should aim to explore the exact nature of the excitonic or electron-phonon coupling and their roles in the CDW transition of $1T$-$TiSe_2$. Additionally, we find weak implications of a displacive phonon excitation. It describes the mechanism of an instantaneous change in the atomic potential landscape after electronic excitation, which leads to a motion toward a new equilibrium structure. The cosine phase that is often used as indication of displacive excitation cannot be applied in this study, as such phase assignments are beyond the sensitivity of our probe. However, we observe that the optically excited electronic system drives the atoms toward the normal metallic state. For displacive excitations the system oscillates around the new equilibrium position before slowly relaxing back [25]. In this study, we find a very weak displacement toward the normal metallic state of $1T$-$TiSe_2$ which decays within the first picosecond. Such a fast relaxation is unusual for displacive excitation and may hint at a more complex excitation pathway that warrants further investigation.

At larger timescales in the picosecond regime, energy transfer between the phonon modes drastically influences the dynamics. Both the optical mode and the amplitude mode are strongly excited and transiently store a significant fraction of the excitation

energy, which is redistributed on their respective damping timescales. We find that 11% of the 6 meV/u.c. excitation ($F = 260\,\mu\mathrm{J/cm^2}$) are initially deposited in the optical mode while 14% are transferred to the amplitude mode. The effect of transient energy storage in the phonon modes can be seen when comparing the extracted timescales. The lattice heats up significantly slower on the 1 ps timescale compared to the cooling of the electronic system, which occurs on roughly 360 fs. In this regard, we find evidence of a bottleneck effect that hinders the heating of the lattice due to the transient energy which is stored in hot phonon modes. After laser irradiation, coherent modulations of the A_{1g} and A_{1g}^{*} modes are triggered together with electronic excitation. The electron subsystem relaxes on the approximately 300 fs timescale while further exciting incoherent populations of strongly coupled phonon modes [257], to which the A_{1g} and the A_{1g}^{*} mode also belong. These hot phonons store a significant amount of energy that is redistributed on a timescale close to or larger than the 1-ps dephasing time measured in this study.

8.4 Conclusion

In this work, we use high-sensitivity transient absorption spectroscopy with a HHG source to investigate and distinguish various electronic and lattice contributions of the weakly excited CDW in 1T-$TiSe_2$. Thereby, we paid particular attention to the coherently excited phonon modes. The out-of-plane A_{1g} optical phonon can be separated from the ${A_{1g}}^{*}$ amplitude mode, as each mode hosts a specific spectral fingerprint. We find that the amplitude mode signature is rooted in the many-body absorption peak of the static absorption spectrum indicating that an excited ${A_{1g}}^{*}$ mode strongly changes the local electron screening. These results closely link the CDW amplitude mode to the many-body screening which is dominated by the local electron density around the Ti core. In a reciprocal manner, a perturbation of the electron-electron correlation may, therefore, be the cause of the amplitude mode excitation. Using TDDFT, the spectral fingerprints can be reproduced and linked to real-space lattice displacements. With the knowledge of displacements and frequencies, the deposited energies and the excitation efficiencies of the two modes are thus estimated. In this work, the unique sensitivity of XUV absorption spectroscopy allows us to simultaneously measure the excitation efficiency of the A_{1g} out-of-plane oscillations and the A_{1g}^{*} in-plane CDW mode. Complementary analysis of spectral shifts enables simultaneous extraction of the timescales of electronic cooling and phonon-bath heating on the same dataset. This allows us to obtain a more refined picture

of the energy relaxation in $1T$-$TiSe_2$, where the heating of the lattice is delayed due to excitations of strongly coupled hot phonons.

This work exemplifies the potential of high-sensitivity transient absorption spectroscopy for the investigation of quantum materials by simultaneously probing electronic and lattice degrees of freedom. A simultaneous sensitivity to the presented degrees of freedom by other means is extremely challenging. In future experiments, our approach may be combined with spectrally continuous sources to enable simultaneous access to coherent phonon dynamics and detailed information on electron and hole interactions on attosecond timescales [332]. The extracted spectral fingerprints of the phonon modes may prove valuable in further experiments, such as imaging with high-harmonic sources. In addition, the presented approach may be applied to a variety of phenomena with strongly coupled dynamics of electronic and lattice systems like CDW formation, metal-to-insulator transitions and superconductivity.

Acknowledgments

This work was funded with resources from the Gottfried Wilhelm Leibniz Prize and the Deutsche Forschungsgesellschaft (DFG). We thank Stephen R. Leone for providing lab instruments to record continuous XUV spectra of $1T$-$TiSe_2$, which was funded by the Air Force Office of Scientific Research (FA9550-19-1-0314 and FA9550-20-1-0334). H.-T. C. acknowledges support from Air Force Office of Scientific Research (FA9550-19-1-0314 and FA9550-20-1-0334). The simulations were conducted at the Scientific Compute Cluster at GWDG, the joint data center of Max Planck Society for the Advancement of Science (MPG) and University of Göttingen.

8.5 Appendix

Sample preparation

This study uses $1T$-$TiSe_2$ flakes grown by chemical vapor transport [336] and cut to $L = 65\,\text{nm}$ thickness at lateral sizes of approximately $300\,\mu\text{m}$ by ultramicrotomy. The flakes are positioned on a commercial TEM membrane of 30-nm-thick nanocrystalline, porous silicon (SiMPore) consisting of eight $100\,\text{x}\,100\,\mu\text{m}$ and one $350\,\mu\text{m}\,\text{x}\,100\,\mu\text{m}$ windows. By aligning the sample with the windows, some are fully covered while others remain empty to allow for absolute transmission measurements compared to the pure silicon transmission. A schematic sample is depicted in Fig. 8.4(a).

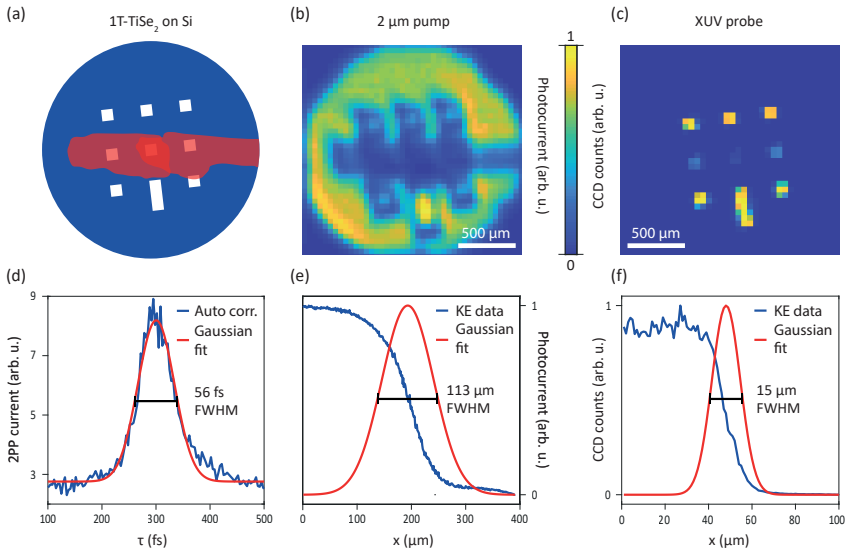

Figure 8.4: (a) Schematic of nine window Si membrane apertures and a $1T$-$TiSe_2$ flake positioned on top. (b) & (c) Transmitted intensity of pump and probe beam used for spatial overlapping of both beams. (d) Intensity autocorrelation of the pump pulse recorded by two-photon absorption. (e) & (f) Knife-edge (KE) measurements of pump and probe beam and estimated Gaussian beam profile.

Transient absorption setup

Infrared-pump XUV-probe core-level transient absorption measurements are carried out with a tabletop high-harmonic source [Figs. 8.1(a) and 8.5]. It is driven by a 1-kHz Ti:sapphire 35-fs laser amplifier with a central wavelength of 800 nm and generates XUV radiation with spectral range of 25-50 eV in an Ar-filled gas cell. The high-harmonic

spectrum comprises peaks with 1.55 eV spacing, achieved by a bicolor laser excitation scheme [125]. It consists of a β-barium borate (BBO) crystal to generate the second harmonic and two calcite plates to adjust the temporal overlap with respect to the fundamental pulse. The sample is excited by a 2-μm laser pulse with 40-fs pulse duration and an incidence angle of 5° generated in an optical parametric amplifier (OPA). The wavelength is chosen to achieve a homogeneous absorption profile in the depth of the sample. Our setup consists of two toroidal gratings that spectrally disperse the XUV beam before the sample and after transmission through the sample. The two spectra, referred to as the reference and signal spectrum, are simultaneously detected on a charge-coupled device (CCD) camera. In combination with feed-forward neural network fitting [325], this procedure achieves a sensitivity of $< 10^{-4}$ OD. Pump-probe traces are recorded with alternating pumped and unpumped frames and randomly distributed timing delays, to avoid systematic drifts in time. By evaluating the spot sizes on the detector, we estimate a spectral width of approximately 250 meV (FWHM) for the harmonics as an upper limit, given the aberration broadening of the optical system.

Spatial overlap of pump and probe beams is achieved by scanning the sample in the focal plane and obtaining the position of the pump and probe beams through maps of the transmitted intensity. Two example transmission maps are shown in Figs. 8.4(b) and 8.4(c). The integrated CCD counts and photocurrent of an additional infrared photodiode placed in the transmitted pump beam path measure the transmittance. In addition, these scans can be used for knife-edge measurements to estimate the probe and pump beam sizes on the sample as shown in Figs. 8.4(e) and 8.4(f). The spot profiles are analyzed by Gaussian fits to estimate spot diameters of $d_{\text{pump}} = 113\,\mu$m and $d_{\text{probe}} = 15\,\mu$m for pump and probe beam at full width at half maximum (FWHM), respectively. These dimensions are chosen such that the probe can be positioned well within the 100 μm windows while ensuring homogeneous excitation by the pump beam.

To estimate the temporal resolution, the pump and probe pulse durations and the wavefront tilt originating from the noncollinear excitation are considered. By utilizing two-photon photoabsorption in a conventional silicon diode, intensity autocorrelation is performed on the 2-μm pump pulse. An autocorrelation width of $\tau_{\text{a.c.}} = 56$ fs is extracted by fitting a Gaussian pulse shape as shown in Fig. 8.4(d). The resulting pulse length of $\tau_{\text{pump}} = \tau_{\text{a.c.}}/\sqrt{2} = 40$ fs is significantly larger than the expected $\tau_{\text{XUV}} \approx 10$ fs pulse length of the XUV beam [337]. An additional contribution stems from the 5° pulse front tilt between pump and probe pulses. This additional temporal shear over the probed length

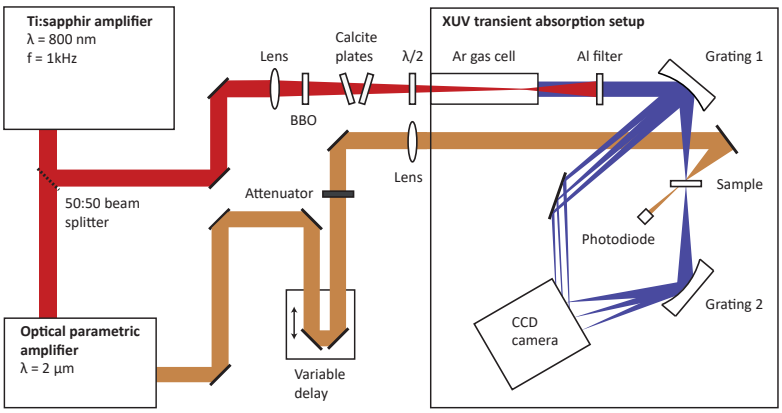

Figure 8.5: Schematic of the transient absorption setup.

of $d = 15\,\mu$m can be computed by $\tau_{\text{tilt}} = d_{\text{probe}} \times \sin(5^\circ)/c$ (c is the speed of light) and is found to be 4.5 fs. The combined temporal resolution is governed by the pump pulse width and is estimated to be 41 fs by convolution.

Absorbed energy

With the assumption of a Gaussian spot profile and nearly collinear excitation, the incident fluence is calculated as

$$F = P/(f \times r_{\text{pump}}^2 \times \pi)\,. \tag{8.1}$$

Here, the $1/e$ radius of the pump pulse $r_{\text{pump}} = d_{\text{pump}}/[2\sqrt{\ln(2)}]$, the laser repetition rate f, and the measured pump power P are used. Furthermore, the absorbed fluence can be estimated by subtracting reflected and transmitted portions for samples of length L:

$$F_{abs} = F \times (1-R) \times [1 - e^{-L/\delta} \times (1-R)]. \tag{8.2}$$

From the literature, a reflectivity of R = 60% (Ref. [338]) and an absorption length of $\delta = 41$ nm (Ref. [338]) are used for the $2\,\mu$m pump wavelength. To obtain an accurate measure of the excitation density the absorbed fluence is converted to deposited energy per Ti atom (normal state unit cell) by:

$$E_{u.c.} = F_{abs}/(L \times \rho)\,, \tag{8.3}$$

with the atomic density $\rho = 1.536 \times 10^{22}\,\mathrm{u.c./cm^3}$ (Ref. [239]). However, for reflection studies on bulk samples, the formalism needs to be adjusted. Specifically, the length L is set to half of the probe attenuation depth, and a second reflection is omitted. Table 8.1 compares the incident fluence and absorbed energy of this work to selected literature values. Under the assumption of homogeneous excitation and full equilibration, the expected temperature increase due to laser excitation is calculated by integrating the known heat capacity [334]. For the temperature increase from 110 K to the equilibrium phase transition temperature of 200 K, we find a fluence of 1.8 mJ/cm^2. By contrast, the fluence of 660 μJ/cm^2 leads to a temperature increase of roughly 30 K, which cannot drive the CDW melting through a thermal mechanism.

Dataset	Fluence F (μJ/cm^2)	Energy $E_{u.c.}$ (meV)
This work	260, 660	5.9, 15.0
Hedeyat *et al.* [257]	62	4.0

Table 8.1: Excitation fluences and deposited energy per unit cell normalized to the probed sample volume.

A significant portion of the absorbed energy is initially stored in the coherently excited phonon modes ${A_{1g}}^*$ and A_{1g}. From the TDDFT calculation, the maximal elongation from the equilibrium position x_i of the atoms (i =Ti, Se) can be estimated, which allows one to calculate the potential energy for a specific phonon mode in the spring model by

$$E = 0.5 \times \sum_i \alpha_i \omega^2 x_i^2 M_i \,. \tag{8.4}$$

Here, ω is the phonon oscillation frequency, M_i is the atomic mass of the atom, and α_i is the number of moving atoms per normal phase unit cell. For the A_{1g} optical mode, both Se atoms ($\alpha_{Se} = 2$, $\alpha_{\mathrm{Ti}} = 0$) in the unit cell are displaced by $x_{\mathrm{Se}} = 0.0075\,$Å. In the case of the amplitude mode ${A_{1g}}^*$, we use $\alpha_{\mathrm{Se}} = \frac{6}{4}$, $\alpha_{\mathrm{Ti}} = \frac{3}{4}$, $x_{\mathrm{Se}} = 0.0084\,$Å and $x_{\mathrm{Ti}} = 0.0255\,$Å, since only a fraction of the atoms participate in the mode. This leads to an energy of $E = 0.65\,\mathrm{meV/u.c.}$ and $E = 0.8\,\mathrm{meV/u.c.}$, stored in the coherently excited amplitude of the A_{1g} and the ${A_{1g}}^*$ mode, respectively. Incoherent excitations of the modes are not captured here, and the total stored energy might be even larger. For the calculation, the excitation is assumed to be homogeneous over the sample, such that each unit cell is equally excited.

Fitting procedure

Phonon damping timescales are extracted by global fits with the equation

$$\begin{aligned}\Delta OD(\tau) =& 0.5 \times \left[\mathrm{erf}\left(\frac{\tau}{T_{r1}}\right)+1\right] \times \left\{A_e \times \exp\left(-\frac{\tau}{T_e}\right) + A_b \times \left[1-\exp\left(-\frac{\tau}{T_b}\right)\right]\right\} \\ &+ 0.5 \times \left[\mathrm{erf}\left(\frac{\tau}{T_{r2}}\right)+1\right] \times A_p \times \sin(2\pi f \tau + \phi) \times \exp\left(-\frac{\tau}{T_p}\right).\end{aligned} \tag{8.5}$$

Here, T_{r1} and T_{r2} represent the rise times after excitation, A_e, A_b and A_p the amplitude of the electron, phonon bath and coherent phonon contributions and T_e, T_b and T_p the corresponding damping times, respectively. The values of $T_e = 0.36 \pm 0.04$ ps and $T_b = 1.0 \pm 0.3$ ps are taken from the result of the time-dependent spectral redshift [Fig. 8.2(c)], as these time constants should be independent of the harmonic order. We distinguish the rise times of the electronic T_{r1} and phononic system T_{r2} to incorporate the different physical excitation mechanisms which exceed the duration of the pump pulse. For the extraction of phonon dephasing times we use a global fit incorporating all harmonics that show a signature of the individual phonon mode. Here, a single phonon oscillation at frequency f, its associated phase ϕ, and damping constant T_p are fit to multiple harmonics in a single fitting. Only the amplitudes are allowed to vary between different wavelengths. For the amplitude mode ($F = 260\,\mu\mathrm{J/cm^2}$) harmonics 29-31 are utilized, while for the optical mode the fit includes harmonic 27 and 28. At $F = 660\,\mu\mathrm{J/cm^2}$, harmonics 27-29 are used in the fitting. The fittings are displayed in Figs. 8.3(a) and 8.7 and the fitting parameters for both phonon modes are shown in Table 8.2 for both fluences. Since the time zero is not independently known, the phase is used as a time-zero offset and cannot directly be used to extract a cosine behavior indicative of displacive excitation.

In the global fit, harmonic 26 is neglected, as it is significantly modulated by the redshift leading to a much larger damping time. A separate fit of this harmonic reveals a damping time of 2.3 ± 0.5 ps, which is significantly larger than the 1 ps extracted by the global fit. The modulation of the apparent phonon amplitude by a redshift is schematically shown in Fig. 8.6. The black curve indicates the expected phonon signature of the A_{1g} optical mode. A redshift of this spectral fingerprint (red lines) leads to a significant reduction of the amplitude at harmonic 26 and minor changes at larger photon energies, indicated by the arrows. The modulation is particularly strong at harmonic 26 as it is

situated near the maximal slope and the zero crossing of the phonon spectral signature. As shown in Fig. 8.2(d), the redshift induced by electronic and lattice heating is strongly time dependent, which affects the observed phonon amplitude and damping at harmonic 26. Specifically, a large redshift near time zero reduces the observed amplitude. However, during the initial decay of the redshift on the timescale of 360 fs, the observed phonon amplitude is artificially increased leading to an overestimation of the phonon damping time. Afterward, the redshift is constant and the apparent phonon relaxation thus remains unaltered. Therefore, the influence of the redshift on the observed timescales can be significant near the zero crossing as shown in the case of the harmonic 26. However, in the spectral region of harmonics 27-29 a global fit can be safely used to extract the phonon damping timescale.

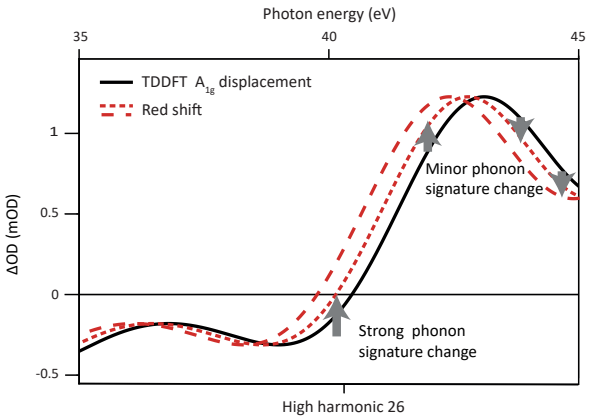

Figure 8.6: Schematic illustration of the influence of the spectral shift on the optical mode signature. At a given probe energy, the redshifted spectral signature can increase or decrease the visible phonon signal. The apparent signal at harmonic 26 is strongly reduced by a redshift, as it is situated near the maximal slope and the zero crossing of the phonon signature. At larger photon energies, in the plateau region of the phonon fingerprint the effects of the redshift are only minor.

Phonon	Fluence	Harmonics	T_{r1} (fs)	T_{r2} (fs)	f (THz)	ϕ	T_p (ps)
A_{1g}^*	260 μJ/cm^2	29, 30, 31	-	90 ± 70	3.4 ± 0.1	3.4 ± 0.3	0.6 ± 0.2
A_{1g}	260 μJ/cm^2	27, 28	100 ± 30	50 ± 50	5.9 ± 0.1	0.7 ± 0.2	1.3 ± 0.5
A_{1g}	660 μJ/cm^2	27, 28, 29	80 ± 10	60 ± 50	6.0 ± 0.1	0.8 ± 0.2	1.0 ± 0.2

Table 8.2: Fitting parameters of the global fit for the A_{1g} and $A_{1g}{}^*$ phonon modes.

Simulations with Density Functional Theory (DFT)

The Ti $M_{2,3}$ edge absorption spectra in Fig. 8.1(b), Fig. 8.2(b), and Fig. 8.3(d,e) are simulated with time-dependent density functional theory (TDDFT) in the random phase approximation and the full-potential linearized augmented plane wave method using the

exciting software package [189, 160, 161]. We employ the framework of TDDFT in the linear response theory to capture the dynamical core-level excitation process that leads to the absorption of XUV radiation. The calculations are performed with a Perdew-Burke-Ernzerhof exchange-correlation functional [167], and local field effects are included in all TDDFT calculations to incorporate the effects of many-body interactions on the core-level absorption [339, 155, 156]. Spectral calculations with atomic displacements along the A_{1g} optical mode are conducted with a single unit cell on a $12 \times 12 \times 6$ k grid. Equilibrium atomic positions are obtained via geometry optimization by relaxing the structure and minimizing internal forces with initial atomic positions taken from Ref. [340]. The atomic displacements of the optical mode are taken from subsequent phonon calculations at the Γ point. Simulations of the core-level absorption spectra with displacements along the amplitude mode are conducted with a $2 \times 2 \times 2$ supercell. The atomic positions for the CDW and normal phase are taken from Ref. [335]. Here, the ground state DFT calculations are first carried out on a $12 \times 12 \times 6$ k grid, and the following TDDFT spectral simulations are conducted on a $6 \times 6 \times 3$ k grid. Simulations at increased electron temperature are conducted by adjusting the electron occupation with the Fermi distributions at finite temperature in the calculation of the density [341]. As a result, the calculated electronic bands as well as the occupation account for the increased electron temperature.

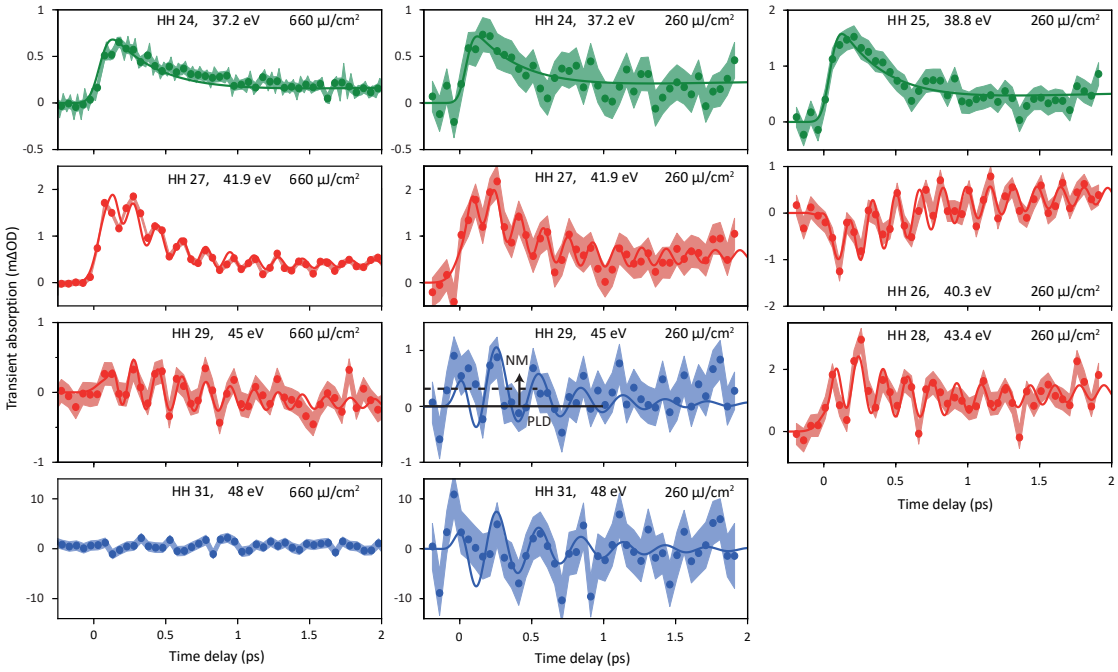

Figure 8.7: Transient absorption traces of $1T$-$TiSe_2$. Pump probe traces are recorded for $F = 260\,\mu J/cm^2$ and $F = 660\,\mu J/cm^2$.

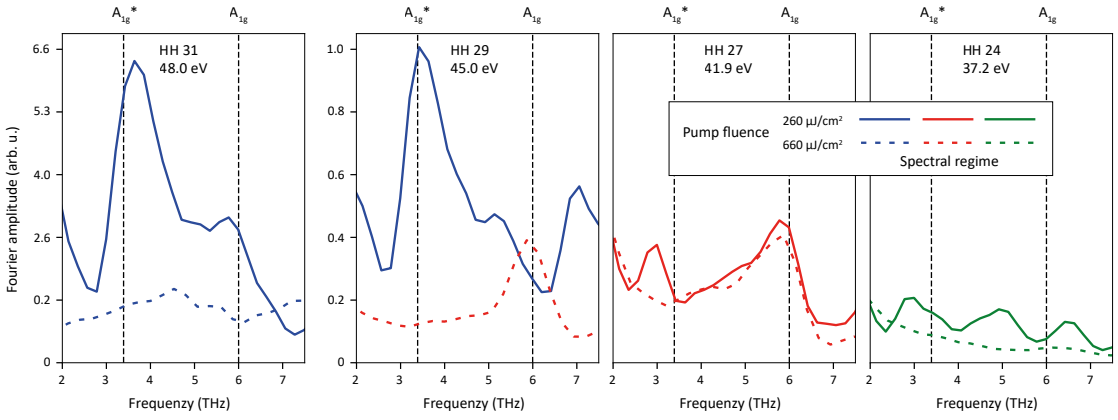

Figure 8.8: Fourier spectra of pump-probe traces.

Chapter 9

Discussion

High-harmonic light sources have been proven to be versatile tools for material studies. In recent years, the focus of this field shifted from investigations of atoms and molecules to solid-state systems. Both, solid-state high-harmonic generation (HHG) and extreme ultraviolet (XUV) transient absorption spectroscopy in solids present new means for the study of entangled degrees of freedom in complex quantum materials. In this work, the control of HHG source parameters allows the efficient generation of circularly polarized harmonics in solids. By using a bi-circular driving field to generate high-harmonic radiation in the vacuum ultraviolet (VUV), magnetic and crystalline chirality are recorded in MgO and quartz, respectively. In the field of XUV absorption spectroscopy with gas-phase HHG sources, a machine learning based referencing is developed which improves the sensitivity to absorption changes by more than one order of magnitude. This significant advance allows the investigation of subtle absorption changes that occur in connection with below-threshold excitation of the charge density wave (CDW) in 1T-$TiSe_2$.

Sections 9.1-9.3 provide a summary of the previous work and highlight the most relevant results and put them into perspective. Specifically, our methods of generating circularly polarized harmonics and noise reduction are discussed in the broad context of solid-state probing with HHG sources. Here, possible alternatives to generate circularly polarized harmonics with elliptical driving fields and alternatives for noise reduction are elucidated. Moreover, it is reflected how complex and correlated materials such as 1T-$TiSe_2$ can be investigated by XUV absorption. Potential future applications of the presented work will be discussed in Sec. 9.4 in more detail.

9.1 Solid-state HHG as a probe for crystal symmetries

Chapter 6 reports on the generation of circularly polarized high harmonics from solid media with the use of a bi-circular driving field. By overlapping the left-handed circularly polarized fundamental beam with its right-handed circularly polarized second-harmonic, a threefold cloverleaf field with angular momentum is obtained. By inverting the helicities of the field the chiral properties of MgO and quartz are probed. In addition, the rotational symmetries of the crystals are investigated by rotation of the driving field.

As an alternative to threefold driving fields, circularly polarized high harmonics can be generated by circular and elliptical driving fields in solids [122]. In stark contrast to gas phase sources which do not allow HHG with circularly polarized lasers, solids systems relax this re-collision constraint. As explained in Sec. 2.1, the ionization and recombination of electron and hole is not limited to the same atomic site. In conclusion, a broad range of quasiparticle trajectories can participate in the HHG process which allow elliptically and circularly polarized driving fields. It was found that the interplay of intra- and inter-band mechanism strongly influences the degree of the harmonic elipticity [342]. In particular, the emitted circularly polarized harmonics depend on the solids symmetry class and, in the case of elliptical driving fields, are influenced by the fine details of the intraband mechanism, the field strength, and the band structure [123, 124]. By enabling reliable and efficient generation of circularly polarized high harmonics through tailoring of the driving fields, our work relaxes this material requirement.

The material-independent generation of circularly polarized high harmonics is applied to study two different chiral material properties. In particular, we investigate the crystalline chirality in quartz and the surface magnetism in MgO which is otherwise challenging to access. Near-surface generation of harmonic radiation is ideally suited to probe such material properties on bulk samples in an all-optical manner. Therefore, this method poses very little limitations on material selection and experimental requirements. In comparison to electron probe methods, all-optical approaches do not require ultra high vacuum conditions and clean sample surfaces. Especially, dielectric and insulating materials such as MgO or quartz are not easy to investigate by electron probe techniques due to charging.

With the presented work, we demonstrate rotational symmetry probing with solid-state HHG by means of sample rotation and selection rules. The bi-circular driving fields distinguishes threefold-symmetric crystals from six-fold symmetric materials by rotating the fields angle with respect to the crystal axes. This is not possible with linearly polarized

driving fields. In addition, the potential for utilizing the HHG selection rules as symmetry probe is discussed in Sec. 2.3 and Sec. 6.4.1. This route has been further explored by Tzur *et al.* [46]. In solids, the combined symmetries of the solid and the irradiated field result in a selection criterion, which prohibits the generation of certain harmonic orders. By generalizing the bi-circular fields to bi-elliptically polarized driving pulses, a framework for probing a large variety of symmetry broken states is presented in Ref. [46]. In the context of ultrafast material research, this approach is particularly promising for the study of dynamical symmetry breaking such as phonon or magnon excitations [46], topological insulators [47], CDW materials [49], and superconductivity [48].

Although not part of the current work, the advances of solid-state HHG in the context of material micro-engineering are worth highlighting. Changing the properties of emitted radiation through material manipulation has the potential to create the next generation of VUV and XUV light sources with customizable properties. Section 2.4 reports on the current state in this field. Such light sources are particularly useful for photoelectron spectroscopy while circularly polarized harmonics can be used to access the spin degrees of freedom [343, 344, 345]. The gas-free generation of high harmonics is well suited for ultra-high vacuum conditions and VUV light allows the emission of electrons at high momenta [92]. A solid-state HHG source can be positioned close to the sample without the need for additional optics, as the emitted radiation can be focused by the modification of the generation target [143]. With the current work, we expand the toolbox of tailored light sources by enabling the generation of circularly polarized light in arbitrary crystal structures. This offers more flexibility for additional material engineering.

In summary, the extension of threefold driving fields to solid-state HHG provides essential controls for the study of materials systems. In particular, the investigation of magnetic properties will greatly benefit from the presented material-independent generation of circularly polarized high harmonics. Section 9.4.1 highlights future application of ultrafast chiral probing with threefold driving fields.

9.2 Noise reduction in XUV absorption spectroscopy

Chapter 7 reports on a tenfold increase in sensitivity of XUV absorption experiments with the use of machine learning (ML) based referencing. By utilizing strong correlations between different harmonic orders, a spectrum of the HHG source is fed into a neural network to find the optimal reference for the transient sample spectrum. As a proof of

concept, this method is applied to a pixel-wise spectrum to show its applicability for broadband attosecond sources.

The limited sensitivity is one of the biggest challenges in XUV absorption spectroscopy for solid-state research. This issue becomes even more severe for time-resolved experiments, since the required integration time is multiplied by the number of time steps. Furthermore, experimental stability and sample degradation often render longer integration times unfeasible. As a result, there is a sensitivity limit to dynamics that can be probed by XUV transient absorption spectroscopy with HHG sources. In our work, accessing the CDW in $1T$-$TiSe_2$ requires cooling below the phase transition temperature which leads to sample contamination over time. Since the CDW dynamics in this material are only accessible at low fluences the expected absorption changes are weak as elucidated in Sec. 5.3. Therefore, enhancing the sensitivity of the experiment is essential to investigate the CDW phase.

Different measures are taken in this work and other studies to maximize the signal-to-noise ratio in absorption spectroscopy with HHG sources. Before discussing potential solutions, it is illustrative to list the sources of the intensity noise in the XUV spectrum. It largely results from the highly nonlinear microscopic mechanism and the phase matching of the HHG process which is discussed in Sec. 2.4. Laser power, beam pointing, and temporal pulse shape of the driving field are the most crucial parameters in HHG as they dictate the ionization level and, hence, the phase matching conditions. The backing pressure of the gas source is typically stable but may drift over time. Mechanical vibrations are an additional concern for the HHG source and the optical elements. Vibrations of the vacuum pumps are often reduced by flexible tubing in combination with anchoring of other vacuum parts. In addition, beam pointing can be taken care by active stabilization, pulse propagation effects can be mitigated by evacuating the beam path, and structural rigidity of optical elements is achieved by reinforced mounting and ambient temperature control. Further noise reduction is pursued by referencing approaches which have been discussed in chapter 7. Long term drifts of gas pressure, laser intensity, pulse duration and spectral changes of the fundamental can be traced by on/off referencing which is the standard noise reduction in most XUV absorption experiments. Here, pulse-to-pulse fluctuations are only partially accounted for by extensive averaging and binning.

A key finding of this work is that referencing with an additional spectrum of the HHG source in connection with ML yields a tenfold increase in sensitivity. We find that the HHG source is highly correlated in a nonlinear, non-polynomial fashion between har-

monic orders. It is therefore possible to use a second spectrum for referencing of disjunct spectral regions. This is a huge advantage as the requirements for the reference spectrum are less strict. At the same time, we show that linear or polynomial models fail to fit the reference data to the signal spectrum. In this respect, the neural network significantly outperforms linear regression, polynomial regression as well as direct referencing. The surprisingly little signal-to-noise improvements of direct referencing can be explained by imperfections of the experimental spectra. Due to the use of different optical elements in combination with optical aberrations and strong wavelength dependencies of reflections, the intensity noise at a specific wavelength is unequal between the signal and reference spectrum. In addition, it is expected that the measured spectra are imperfect and different wavelengths intermix on each CCD pixel.

Using a neural network for fitting the non-polynomial dependence between the reference and the signal spectrum constitutes a powerful and practical solution to the high noise level of HHG sources. A neural network is more suited to model the nonlinear correlations (universal approximation theorem, Sec. 4.2) and it also outperforms other ML approaches in terms of computational complexity. In our study we used a personal computer without graphical processing units acceleration to train the neural network within a couple of hours. With such moderate computational costs the training could even run in parallel to the data acquisition. Furthermore, a neural network can utilize large input data sets such as individual camera pixels for noise reduction of broadband spectra. The polynomial model is found to yield comparable results for single harmonic referencing, but its complexity scales exponentially with the number of pixels and prohibits the use in broadband experiments.

In summary, achieving a tenfold sensitivity increase with the use of a reference spectrum in combination with an artificial neural network is the key prerequisite for probing of subtle sample dynamics. The following section presents, how the increased sensitivity is used within this work to study weakly excited CDW dynamics. The presented neural network based referencing approach is transferable to other beamlines with broadband attosecond sources. This avenue will be further discussed in Sec. 9.4.2.

9.3 Disentangling CDW dynamics in XUV absorption spectra

The application of high sensitivity XUV spectroscopy for studies of CDW dynamics in the TMDC 1T-$TiSe_2$ is presented in chapter 8. These investigations are enabled by var-

ious experimental capabilities developed for this purpose within the current work. In XUV absorption spectroscopy experiments, the most important quantities are the spectral resolution and the signal-to-noise level. The last section evaluated different measures to enhance the stability of the HHG source. In this work, we utilized the described methods except active beam stabilization and evacuation of the fundamental beam path. Due to a short propagation distance from the laser to the experiment, the beam pointing is stable, and the majority of the noise results from other sources. A semi infinite gas cell is used as an HHG source offering improved stability and low maintenance in comparison to other sources discussed in Sec. 2.4. Furthermore, the use of a two-color driving field allows the generation of even and odd harmonics due to symmetry, maximizing the spectral sensitivity. The increased flux of this approach also improves the signal-to-noise ratio for a given integration time. By using the inline scheme introduced in Sec. 2.3 for second harmonic generation (SHG) and temporal control, a highly stable bi-color field is achieved. In addition, ML based referencing is applied to further enhance the sensitivity by more than one order of magnitude. A sensitivity of 0.1 mOD is achieved at the Ti M-edge which allows to study below-threshold dynamics of CDW in 1T-$TiSe_2$.

Core level spectra include a wealth of information, but disentangling different contributions is not a trivial task. To this end, we employed TDDFT calculations to reproduce the experimental spectra. In Sec. 3.2 and Sec. 8.5 details of the TDDFT based simulations of XUV core level spectra are presented. The focus of the simulation has been to accurately describe photon excitation processes at the shallow Ti 3p-core level. It was found that the TDDFT within the linear response theory is capable to accurately describe the many body absorption peak near the Ti core edge. Specifically, the *ab-initio* calculations are used to link real space atomic displacements of phonon modes to the corresponding spectral changes. In addition, a smearing of the Fermi distribution proves to be a good tool to study the photoinduced electron temperature increase. Therefore, the TDDFT was found invaluable for the interpretation of the transient XUV absorption changes.

By studying 1T-$TiSe_2$, the presented results are very valuable in order to understand how electronic and phononic part of the CDW phase transition interact. The results from the XUV absorption clarify that the A_{1g}^* mode found at 3.5 Thz belongs to the amplitude distortion and is suppressed non-thermally at low fluences. We link this mode to screening dynamics of the electronic system via its spectral response in the many body resonance peak of the spectrum. On the contrary, the A_{1g} mode identified at 6 Thz is excited independently of the pump fluence and shows a signature in the extended edge region below

the many body resonance. We conclude, that this mode is not directly related to the CDW phase. Furthermore, in connection with TDDFT data the energies stored in both coherent modes could be extracted and were found to be surprisingly large. By combining this information with the extracted electronic and lattice temperatures we are able to strengthen a bottleneck effect induced by the strongly excited phonon modes.

In summary, the presented work resolves weak absorption changes in the XUV region of 1T-$TiSe_2$, induced by below-threshold excitations of the CDW. In combination with TDDFT, detailed information is extracted from the spectrum revealing the real space coordinates of coherently excited phonon modes. These results provide new insights on the CDW stability in 1T-$TiSe_2$ while more detailed XUV absorption studies, that will be discussed in Sec. 9.4.3, present a very promising route to form an even more complete picture of the CDW melting.

9.4 Outlook

9.4.1 Ultrafast solid-state HHG

Due to the intrinsically short pulse lengths in the femto- to attosecond regime, solid-state HHG is ideally suited for time resolved experiments. Here, an additional pump pulse is added to the fundamental driving field as depicted in Fig. 9.1(a). The pump beam triggers some sample dynamics which change the microscopic HHG and the subsequent absorption. Alternatively, two co-linear driving pulses enable band reconstructions by control of their relative timing [62].

The presented work opens a path for time resolved symmetry probing. Specifically, chiral properties and magnetism are accessible by HHG with threefold driving fields. Circularly polarized harmonic emission allows to study ultrafast magnetization dynamics similar to XUV absorption spectroscopy [40, 41, 64]. However, due to the lower photon energy, core levels can usually not be accessed in solid-state HHG and the sensitivity depends on a dichroism in the visible and VUV region such as the spin-selective band gap in the case of e.g. MgO surface layers.

A different chiral property that gained large interest in recent years is the valley polarization. Two dimensional materials with broken inversion symmetry such as strained graphene, hexagonal boron nitride or 2H-MoS_2 form two distinct valleys at the edge of the Brillouin zone with different crystal momenta, also called pseudo spins [11]. Optical

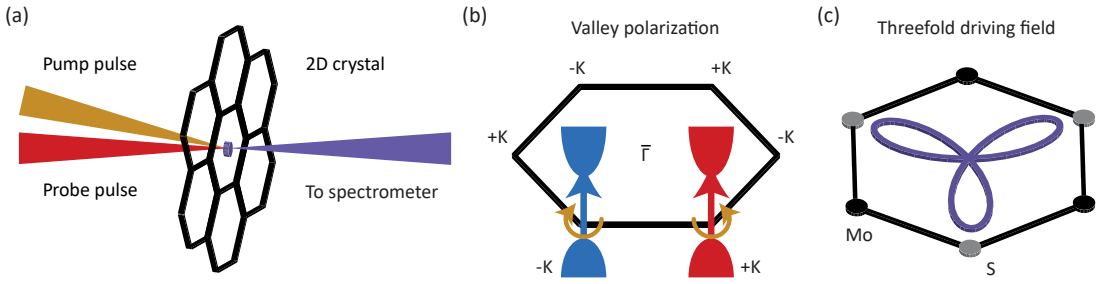

Figure 9.1: Ultrafast solid-state HHG. (a) Pump probe geometry of solid-state HHG in transmission. (d) The electron bands of non inversion symmetric two-dimensional materials form distinguishable valleys at the edges of the Brillouin zone. The +K and -K are selectively excited by circularly polarized light (yellow arrow). (c) Threefold driving fields are tailored to trigonal materials such as MoS_2 and selectively lift the degeneracy at high symmetry points.

selection rules lift the degeneracy of the valleys for circularly polarized light [346]. Here, resonant excitation with circularly polarized light selectively excites carriers at either the +K or the -K valley dependent on the lights polarization as shown in Fig. 9.1(b) [347, 346]. The valley polarization is a particularly promising route for energy efficient information storage and processing [11].

Similar to circularly polarized light, threefold fields [Fig. 9.1(c)] carry angular momentum and induce asymmetric carrier excitation between the two distinct valleys. By using of-resonant excitation in 2*H*-MoS_2, a modulation of the band gap at the high symmetry points +K and -K has been shown in Refs. [348, 349]. Here, the threefold field matches the trigonal crystal structure of 2*H*-MoS_2 and selectively drives electrons along the crystal directions as depicted in Fig. 9.1(c) [349]. This allows to selectively lift the valley degeneracy by rotation of the threefold field. The valley polarization that is induced by the threefold field can be probed by harmonic generation of linear pulses at 3ω [350]. Alternatively, the valley selective dichroism is accessible by the emitted high-harmonic radiation from the threefold driving fields. In theoretical studies, valley selective emission of harmonics is proven [351]. Thus, in future experimental work, HHG is a promising candidate for efficient writing and reading of valley polarization and offers detailed information about the nature of the bands and berry curvature at the high symmetry points.

The field of ultrafast solid-state HHG is still developing, but in the last years many studies showed its great potential. A good example of a current work in this field is the investigation of the ultrafast metal to insulator transition in VO_2 [113]. In the same ma-

terial, coherent phonon oscillation are observed in the emitted high-harmonic spectrum. This highlights the capabilities of studying dynamics in complex and correlated quantum materials with solid-state HHG in future experiments. In this regard, the use of bi-circular driving fields facilitate investigations of chiral properties such as ultrafast magnetism or valleytronics.

9.4.2 Application of ML based referencing

The experimental breakthrough (discussed in chapter 7) that enabled high sensitive XUV spectroscopy in this work was the development of a referencing scheme with a neural network. In this endeavour we paid particular attention on the transferability of our approach to other XUV beamlines. We show that the neural network is capable of efficiently fitting broadband spectra found in attosecond experiments. Therefore, our method is applicable to a large variety of spectroscopic experiments with high-harmonic radiation or other light sources such as free electron lasers. The best results are obtained when a reference spectrum is introduced to the setup. Here, the second spectrum does not need to be calibrated which is a huge benefit for practicality. In many setups it is possible to replace the focusing toroidal mirror by a toroidal grating and position a detector in the first diffraction order. When there is enough space in the vacuum setup, this approach can be implemented directly.

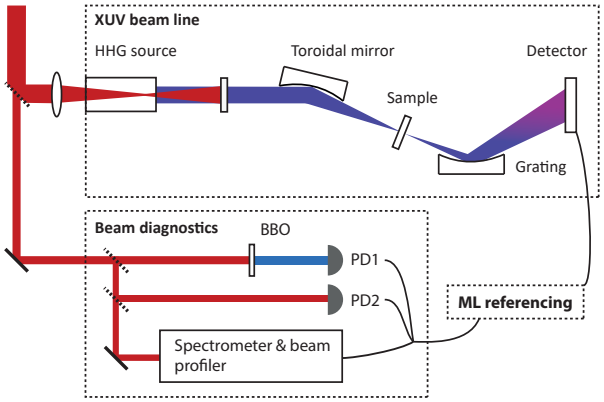

Figure 9.2: Non-invasive referencing in HHG beamlines. In contrast to a spectrum of the HHG source, other correlated variables such as the beam properties of the fundamental are suitable as a reference. This approach allows noise reduction without changing the existing XUV beamline. Two photodiodes (PD1 and PD2) are used to measure the intensity of the fundamental and the second harmonic. In Addition, a spectrum and the beam pointing of the driving laser are recorded. All properties are fed into an ML algorithm as a reference.

If a second spectrum of the HHG source can not be implemented, monitoring other correlated properties is a promising alternative. In Ref. [304] the laser power was successfully applied as a reference. Our work suggests that it is useful to include several quantities simultaneously. Therefore, figure 9.2 highlights a referencing scheme that utilizes multiple parameters of the fundamental pulses. The driving laser is coupled out before entering the vacuum chamber and routed to a beam analysing station. Parameters for the referencing may include the laser power, measured with a photodiode (PD), the beam pointing, and the pulse duration. The latter is estimated by the intensity of the second harmonic in connection with a spectrum of the fundamental. By employing nonlinear conversions like SHG in a β-barium borate (BBO) crystal, the mode quality is indirectly measured. Since the majority of the short term noise results from instabilities of the driving laser, other quantities such as the gas pressure are expected to yield minor noise reduction. The great advantage of this approach for existing beamlines is that the complete vacuum chamber and XUV spectrometer can be left unchanged. Syncing of the signals is easily achieved in connection with a shutter or the camera readout trigger.

Furthermore, the applicability of an ML based referencing is not limited to XUV beamlines. Deep learning has been recently applied in Electroencephalography to enhance the signal-to-noise ratio. In this field, electric currents of the brain are supposed to be measured with contact electrodes. However, involuntary muscle movements induce additionally currents that are corrected with the use of a second reference electrode. In a study by Porr *et al.* successful real time noise reduction by more than 4 decibel was demonstrated with the use of a deep neural network [352]. Referencing is also closely connected to active noise cancelling which is widely applied in headphones. Here the signal of a single or multiple microphones need to be translated to an optimal output at a spatially separated speaker. The optimal noise reduction of the acoustic waves is achieved if the speaker produces in-phase destructive waves. This is challenging as the propagation between the microphone and the speaker influences the sound waves. Referencing with multiple sources is found to benefit largely from the use of a neural network [353, 354].

The presented examples highlight the great potential of ML methods for referencing tasks of fluctuating light sources, overlapping signals or added noise due to propagation effects. Possible future applications range from industrial sensing and active stabilization to experiments with highly fluctuating probes such as HHG or free electron lasers.

9.4.3 High sensitivity attosecond XUV absorption spectroscopy of quantum materials

In this work, we show simultaneous probing of multiple coherent phonon modes by XUV absorption spectroscopy. With complementary TDDFT calculations, the spectral changes are linked to real space atomic displacements and the energy that is stored in the modes is estimated. For laser excited CDW dynamics, the developed technique represents an ideal platform to study CDW related amplitude modes. A potential candidate for future experiments is the transition-metal dichalcogenide (TMDC) 1T-$TaTe_2$. In this sample system the amplitude mode is not exactly known and still debated [355]. Here, the presented spectroscopic method may yield valuable information by linking the spectral changes of oscillations to real space atomic coordinates. This can be used to unambiguously link the periodic lattice distortion [356] to the related amplitude-phonon mode.

While coherent phonon modes are well accessed with the presented setup, some observables are still beyond the capabilities of our beamline. First, in our experiments the spectral cutoff is situated right at the many body resonance of 1T-$TiSe_2$. This reduces the sensitivity at photon energies larger than harmonic 45 eV (harmonic 29) as seen in Fig. 7.2(b). Second, the the use of 35 fs driving pulses leads to discrete harmonics limiting the time and spectral resolution.

Advancing the capabilities of our setup has great potential for more accurate and complete studies of correlated dynamics. With the use of few cycle driving fields and the polarization gating mechanism introduced in Sec. 2.2 our setup could be advanced to broad band attosecond XUV spectra which enable more detailed spectral information. This would allow for studies of complete relaxation pathways after laser excitation, as illustrated in Fig. 9.3. In this regards, several studies showed probing of different quantities from the attosecond to picosecond regime. Core-hole-screening dynamics was found to modulate the many body absorption peak on attosecond timescale in atomic titanium and TMDCs [154, 155, 156]. Figure 9.3(a) shows significant absorption changes shortly after laser excitation at 10 fs and 22 fs. The entangles spectral changes can be decomposed into band renormalization, state filling effects, and local screening contributions shown in Fig. 9.3(b). On the multiple-femtosecond time scale, carrier relaxation dynamics is visible in the XUV spectral response. In germanium, transient absorption spectroscopy traces the relaxation of electrons and holes simultaneously with meV spectral resolution as shown in Fig. 9.3(c) [57]. At larger timescales in the picosecond regime, lattice dy-

namics such as coherently excited phonon modes [Fig. 9.3(d)] are imprinted on the XUV absorption spectrum.

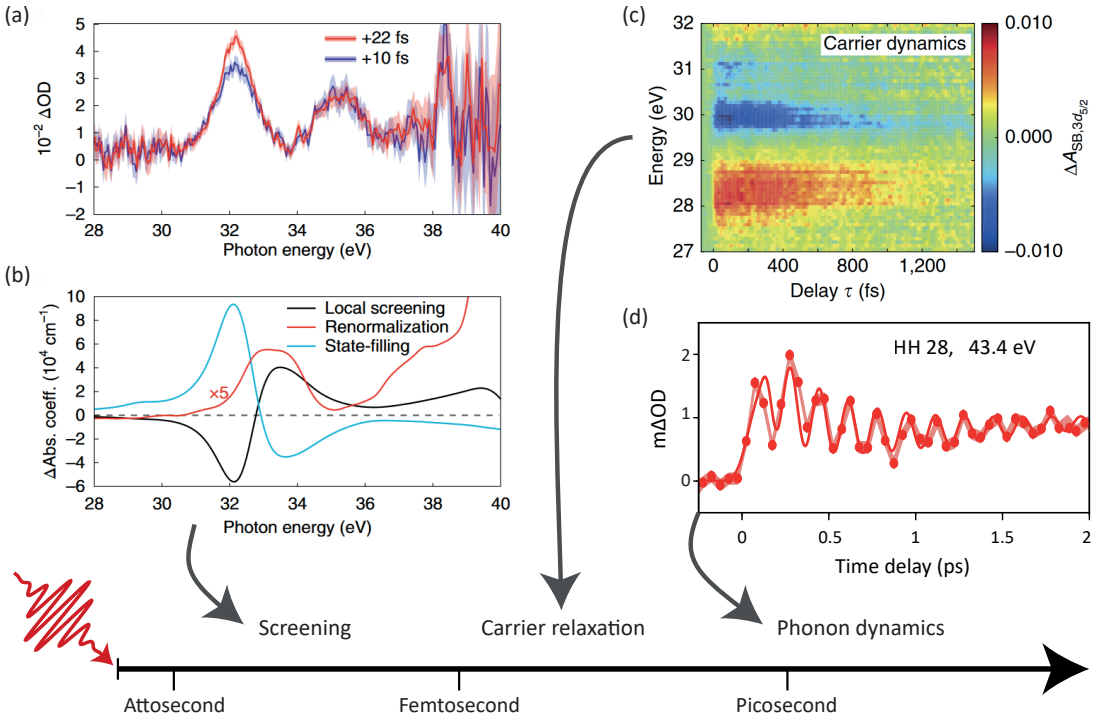

Figure 9.3: Correlated properties probed with XUV absorption at ultrafast time scales. (a) and (b) Local screening of electrons alter the absorption of titanium on the attosecond timescale. (c) Electron and hole contribution to the transient absorption change are simultaneously traces in germanium. (d) Coherently excited phonon modes modulated the XUV absorption change at certain photon energies. Subfigures (a) and (b) are reproduced with permission from Springer Nature, Ref. [156]. Subfigure (c) is adapted from Ref. [57] and (d) is adapted form [311] under the Creative Commons Attribution 4.0 International (CC BY 4.0) license.

With the potential advancement of our setup to an attosecond broadband source, complementary information such as electronic relaxation and ultrafast screening yield valuable information on the CDW stability of 1T-$TiSe_2$. Carrier relaxation has been reported to play a major role in the excitation process and accelerates the suppression of the CDW phase[93]. In this regard, electron and hole relaxation in 1T-$TiSe_2$ can be traced simultaneously by XUV absorption. On similar or even shorter timescales, the electron screening dynamics is of particular interest. With this work we have started the process of investigating the connection of screening dynamics and CDW suppression by using the many

body absorption peak. We observe oscillations of the many body absorption which we relate to a coherently excited amplitude mode. In addition, a direct influence of the exciton breaking and melting of the CDW in the same spectral region is expected. This should materialize as a non oscillating, spectral dependent absorption change which is currently beyond the capabilities of our setup. Here, an extension of the HHG cutoff beyond 50 eV would greatly enhance the sensitivity at the many body absorption peak and facilitate more precise measurements of screening dynamics. This can be done by changing the focusing conditions of the fundamental beam or the gas species.

In summary, future applications of the presented method may yield valuable information on phonon dynamics such as amplitude mode excitations in CDW materials. The extension of our setup to an attosecond light source, offers great potential for simultaneous probing of electronic and lattice degrees of freedom in novel quantum materials.

Bibliography

[1] Tokura, Y., Kawasaki, M., and Nagaosa, N. Emergent functions of quantum materials. *Nature Physics*, 13(11):1056–1068, November 2017. doi:10.1038/nphys4274. Cited on p. 1

[2] Basov, D. N., Averitt, R. D., and Hsieh, D. Towards properties on demand in quantum materials. *Nature Materials*, 16(11):1077–1088, November 2017. doi:10.1038/nmat5017. Cited on p. 1

[3] Paglione, J. and Greene, R. L. High-temperature superconductivity in iron-based materials. *Nature Physics*, 6(9):645–658, September 2010. doi:10.1038/nphys1759. Cited on p. 1

[4] Bardeen, J., Cooper, L. N., and Schrieffer, J. R. Theory of Superconductivity. *Physical Review*, 108(5):1175–1204, December 1957. doi:10.1103/PhysRev.108.1175. Cited on p. 1

[5] Ginzburg, V. L. and Landau, L. D. On the theory of superconductivity. In *On Superconductivity and Superfluidity: A Scientific Autobiography*, pages 113–137. Springer Berlin Heidelberg, Berlin, Heidelberg, 2009. doi:10.1007/978-3-540-68008-6_4. Cited on p. 1

[6] Imada, M., Fujimori, A., and Tokura, Y. Metal-insulator transitions. *Rev. Mod. Phys.*, 70:1039–1263, Oct 1998. doi:10.1103/RevModPhys.70.1039. Cited on p. 1, 15, 90, 100

[7] Yang, Z., Ko, C., and Ramanathan, S. Oxide Electronics Utilizing Ultrafast Metal-Insulator Transitions. *Annual Review of Materials Research*, 41(1):337–367, August 2011. doi:10.1146/annurev-matsci-062910-100347. Cited on p. 1

[8] Grüner, G. *Density Waves in Solids*. Number v. 89 in Frontiers in Physics. Addison-Wesley Pub. Co., Advanced Book Program, Reading, Mass, 1994. doi:10.1201/9780429501012. Cited on p. 1, 15, 59, 60, 62, 100

[9] Geim, A. K. and Novoselov, K. S. The rise of graphene. *Nature Materials*, 6(3): 183–191, March 2007. doi:10.1038/nmat1849. Cited on p. 1

[10] Manzeli, S., Ovchinnikov, D., Pasquier, D., Yazyev, O. V., and Kis, A. 2D transition metal dichalcogenides. *Nature Reviews Materials*, 2(8):17033, June 2017. doi:10.1038/natrevmats.2017.33. Cited on p. 1

[11] Schaibley, J. R., Yu, H., Clark, G., Rivera, P., Ross, J. S., Seyler, K. L., Yao, W., and Xu, X. Valleytronics in 2D materials. *Nature Reviews Materials*, 1(11):1–15, August 2016. doi:10.1038/natrevmats.2016.55. Cited on p. 1, 4, 129, 130

[12] Saito, Y., Nojima, T., and Iwasa, Y. Highly crystalline 2D superconductors. *Nature Reviews Materials*, 2(1):1–18, December 2016. doi:10.1038/natrevmats.2016.94. Cited on p. 1

[13] Luo, B., Liu, G., and Wang, L. Recent advances in 2D materials for photocatalysis. *Nanoscale*, 8(13):6904–6920, 2016. doi:10.1039/C6NR00546B. Cited on p. 1

[14] Siwick, B. J., Dwyer, J. R., Jordan, R. E., and Miller, R. J. D. An Atomic-Level View of Melting Using Femtosecond Electron Diffraction. *Science*, 302(5649): 1382–1385, November 2003. doi:10.1126/science.1090052. Cited on p. 1

[15] Vogelgesang, S., Storeck, G., Horstmann, J. G., Diekmann, T., Sivis, M., Schramm, S., Rossnagel, K., Schäfer, S., and Ropers, C. Phase ordering of charge density waves traced by ultrafast low-energy electron diffraction. *Nature Physics*, 14(2): 184–190, February 2018. doi:10.1038/nphys4309. Cited on p. 1

[16] Danz, T., Domröse, T., and Ropers, C. Ultrafast nanoimaging of the order parameter in a structural phase transition. *Science*, 371(6527):371–374, January 2021. doi:10.1126/science.abd2774. Cited on p. 1

[17] Cao, Y., Mazzone, D. G., Meyers, D., Hill, J. P., Liu, X., Wall, S., and Dean, M. P. M. Ultrafast dynamics of spin and orbital correlations in quantum materials: An energy- and momentum-resolved perspective. *Philosophical Transactions of the*

Royal Society A: Mathematical, Physical and Engineering Sciences, 377(2145): 20170480, May 2019. doi:10.1098/rsta.2017.0480. Cited on p. 1

[18] Buzzi, M., Först, M., Mankowsky, R., and Cavalleri, A. Probing dynamics in quantum materials with femtosecond X-rays. *Nature Reviews Materials*, 3(9):299–311, September 2018. doi:10.1038/s41578-018-0024-9. Cited on p. 1

[19] Smallwood, C. L., Kaindl, R. A., and Lanzara, A. Ultrafast angle-resolved photoemission spectroscopy of quantum materials. *EPL (Europhysics Letters)*, 115(2): 27001, July 2016. doi:10.1209/0295-5075/115/27001. Cited on p. 1

[20] Hellmann, S., Rohwer, T., Kalläne, M., Hanff, K., Sohrt, C., Stange, A., Carr, A., Murnane, M. M., Kapteyn, H. C., Kipp, L., Bauer, M., and Rossnagel, K. Time-domain classification of charge-density-wave insulators. *Nature Communications*, 3(1):1–8, September 2012. doi:10.1038/ncomms2078. Cited on p. 1, 65, 100

[21] Zhou, X., He, S., Liu, G., Zhao, L., Yu, L., and Zhang, W. New developments in laser-based photoemission spectroscopy and its scientific applications: A key issues review. *Reports on Progress in Physics*, 81(6):062101, June 2018. doi:10.1088/1361-6633/aab0cc. Cited on p. 1

[22] Sobota, J. A., He, Y., and Shen, Z.-X. Angle-resolved photoemission studies of quantum materials. *Reviews of Modern Physics*, 93(2):025006, May 2021. doi:10.1103/RevModPhys.93.025006. Cited on p. 1

[23] Giannetti, C., Capone, M., Fausti, D., Fabrizio, M., Parmigiani, F., and Mihailovic, D. Ultrafast optical spectroscopy of strongly correlated materials and high-temperature superconductors: A non-equilibrium approach. *Advances in Physics*, 65(2):58–238, March 2016. doi:10.1080/00018732.2016.1194044. Cited on p. 1, 25

[24] Orenstein, J. Ultrafast spectroscopy of quantum materials. *Physics Today*, 65(9): 44–50, September 2012. doi:10.1063/PT.3.1717. Cited on p. 1, 25

[25] Zeiger, H. J., Vidal, J., Cheng, T. K., Ippen, E. P., Dresselhaus, G., and Dresselhaus, M. S. Theory for displacive excitation of coherent phonons. *Physical Review B*, 45 (2):768–778, January 1992. doi:10.1103/PhysRevB.45.768. Cited on p. 1, 112

[26] Stojchevska, L., Vaskivskyi, I., Mertelj, T., Kusar, P., Svetin, D., Brazovskii, S., and Mihailovic, D. Ultrafast Switching to a Stable Hidden Quantum State in an Electronic Crystal. *Science*, 344(6180):177–180, April 2014. doi:10.1126/science.1241591. Cited on p. 1

[27] Rudner, M. S. and Lindner, N. H. Band structure engineering and non-equilibrium dynamics in Floquet topological insulators. *Nature Reviews Physics*, 2(5):229–244, May 2020. doi:10.1038/s42254-020-0170-z. Cited on p. 1

[28] Oka, T. and Kitamura, S. Floquet Engineering of Quantum Materials. *Annual Review of Condensed Matter Physics*, 10(1):387–408, March 2019. doi:10.1146/annurev-conmatphys-031218-013423. Cited on p. 1

[29] Bao, C., Tang, P., Sun, D., and Zhou, S. Light-induced emergent phenomena in 2D materials and topological materials. *Nature Reviews Physics*, 4(1):33–48, January 2022. doi:10.1038/s42254-021-00388-1. Cited on p. 1

[30] Cavalleri, A., Tóth, Cs., Siders, C. W., Squier, J. A., Ráksi, F., Forget, P., and Kieffer, J. C. Femtosecond Structural Dynamics in VO_2 during an Ultrafast Solid-Solid Phase Transition. *Physical Review Letters*, 87(23):237401, November 2001. doi:10.1103/PhysRevLett.87.237401. Cited on p. 1

[31] Jager, M. F., Ott, C., Kraus, P. M., Kaplan, C. J., Pouse, W., Marvel, R. E., Haglund, R. F., Neumark, D. M., and Leone, S. R. Tracking the insulator-to-metal phase transition in VO2 with few-femtosecond extreme UV transient absorption spectroscopy. *Proceedings of the National Academy of Sciences*, 114(36):9558–9563, September 2017. doi:10.1073/pnas.1707602114. Cited on p. 1

[32] Perfetti, L., Loukakos, P. A., Lisowski, M., Bovensiepen, U., Berger, H., Biermann, S., Cornaglia, P. S., Georges, A., and Wolf, M. Time Evolution of the Electronic Structure of 1T-Ta_2 through the Insulator-Metal Transition. *Physical Review Letters*, 97(6):067402, August 2006. doi:10.1103/PhysRevLett.97.067402. Cited on p. 1

[33] Beaurepaire, E., Merle, J.-C., Daunois, A., and Bigot, J.-Y. Ultrafast Spin Dynamics in Ferromagnetic Nickel. *Physical Review Letters*, 76(22):4250–4253, May 1996. doi:10.1103/PhysRevLett.76.4250. Cited on p. 2

[34] Gaumnitz, T., Jain, A., Pertot, Y., Huppert, M., Jordan, I., Ardana-Lamas, F., and Wörner, H. J. Streaking of 43-attosecond soft-X-ray pulses generated by a passively CEP-stable mid-infrared driver. *Optics Express*, 25(22):27506, October 2017. doi:10.1364/OE.25.027506. Cited on p. 2, 15

[35] Geneaux, R., Marroux, H. J. B., Guggenmos, A., Neumark, D. M., and Leone, S. R. Transient absorption spectroscopy using high harmonic generation: A review of ultrafast X-ray dynamics in molecules and solids. *Philosophical Transactions of the Royal Society A: Mathematical, Physical and Engineering Sciences*, 377 (2145):20170463, May 2019. doi:10.1098/rsta.2017.0463. Cited on p. 2, 8, 26, 29, 90

[36] Zong, A., Nebgen, B. R., Lin, S.-C., Spies, J. A., and Zuerch, M. Emerging ultrafast techniques for studying quantum materials. *Nature Reviews Materials*, 8(4): 224–240, February 2023. doi:10.1038/s41578-022-00530-0. Cited on p. 2

[37] Ghimire, S. and Reis, D. A. High-harmonic generation from solids. *Nature Physics*, 15(1):10–16, January 2019. doi:10.1038/s41567-018-0315-5. Cited on p. 2, 7, 8, 9, 24, 40

[38] Goulielmakis, E. and Brabec, T. High harmonic generation in condensed matter. *Nature Photonics*, May 2022. doi:10.1038/s41566-022-00988-y. Cited on p. 2, 8, 9, 16, 22, 40

[39] Li, J., Lu, J., Chew, A., Han, S., Li, J., Wu, Y., Wang, H., Ghimire, S., and Chang, Z. Attosecond science based on high harmonic generation from gases and solids. *Nature Communications*, 11(1):2748, June 2020. doi:10.1038/s41467-020-16480-6. Cited on p. 2, 4

[40] Rudolf, D., La-O-Vorakiat, C., Battiato, M., Adam, R., Shaw, J. M., Turgut, E., Maldonado, P., Mathias, S., Grychtol, P., Nembach, H. T., Silva, T. J., Aeschlimann, M., Kapteyn, H. C., Murnane, M. M., Schneider, C. M., and Oppeneer, P. M. Ultrafast magnetization enhancement in metallic multilayers driven by superdiffusive spin current. *Nature Communications*, 3(1):1037, September 2012. doi:10.1038/ncomms2029. Cited on p. 2, 3, 129

[41] La-O-Vorakiat, C., Siemens, M., Murnane, M. M., Kapteyn, H. C., Mathias, S., Aeschlimann, M., Grychtol, P., Adam, R., Schneider, C. M., Shaw, J. M., Nembach, H., and Silva, T. J. Ultrafast Demagnetization Dynamics at the M Edges of Magnetic Elements Observed Using a Tabletop High-Harmonic Soft X-Ray Source. *Physical Review Letters*, 103(25):257402, December 2009. doi:10.1103/PhysRevLett.103.257402. Cited on p. 2, 3, 129

[42] Vojta, M. Quantum phase transitions. *Reports on Progress in Physics*, 66(12): 2069, nov 2003. doi:10.1088/0034-4885/66/12/R01. Cited on p. 2

[43] Chen, P., Chan, Y. H., Fang, X. Y., Zhang, Y., Chou, M. Y., Mo, S. K., Hussain, Z., Fedorov, A. V., and Chiang, T. C. Charge density wave transition in single-layer titanium diselenide. *Nature Communications*, 6(1):8943, November 2015. doi:10.1038/ncomms9943. Cited on p. 2

[44] Gegenwart, P., Si, Q., and Steglich, F. Quantum criticality in heavy-fermion metals. *Nature Physics*, 4(3):186–197, March 2008. doi:10.1038/nphys892. Cited on p. 2

[45] Giamarchi, T., Rüegg, C., and Tchernyshyov, O. Bose–Einstein condensation in magnetic insulators. *Nature Physics*, 4(3):198–204, March 2008. doi:10.1038/nphys893. Cited on p. 2

[46] Tzur, M. E., Neufeld, O., Bordo, E., Fleischer, A., and Cohen, O. Selection rules in symmetry-broken systems by symmetries in synthetic dimensions. *Nature Communications*, 13(1):1312, March 2022. doi:10.1038/s41467-022-29080-3. Cited on p. 2, 125

[47] Ma, C., Bian, X.-B., and Du, T.-Y. Role of symmetry breaking in high-order harmonic generation from Su-Schrieffer-Heeger systems. *Physical Review B*, 106(12): 125117, September 2022. doi:10.1103/PhysRevB.106.125117. Cited on p. 2, 125

[48] Daou, R., Chang, J., LeBoeuf, D., Cyr-Choinière, O., Laliberté, F., Doiron-Leyraud, N., Ramshaw, B. J., Liang, R., Bonn, D. A., Hardy, W. N., and Taillefer, L. Broken rotational symmetry in the pseudogap phase of a high-Tc superconductor. *Nature*, 463(7280):519–522, January 2010. doi:10.1038/nature08716. Cited on p. 2, 125

[49] Li, H., Zhao, H., Ortiz, B. R., Park, T., Ye, M., Balents, L., Wang, Z., Wilson, S. D., and Zeljkovic, I. Rotation symmetry breaking in the normal state of a kagome superconductor KV3Sb5. *Nature Physics*, 18(3):265–270, March 2022. doi:10.1038/s41567-021-01479-7. Cited on p. 2, 125

[50] Weisshaupt, J., Rouzée, A., Woerner, M., Vrakking, M. J. J., Elsaesser, T., Shirley, E. L., and Borgschulte, A. Ultrafast modulation of electronic structure by coherent phonon excitations. *Physical Review B*, 95(8):081101, February 2017. doi:10.1103/PhysRevB.95.081101. Cited on p. 2, 43, 90

[51] Attar, A. R., Chang, H.-T., Britz, A., Zhang, X., Lin, M.-F., Krishnamoorthy, A., Linker, T., Fritz, D., Neumark, D. M., Kalia, R. K., Nakano, A., Ajayan, P., Vashishta, P., Bergmann, U., and Leone, S. R. Simultaneous observation of carrier-specific redistribution and coherent lattice dynamics in 2H-MoTe. Cited on p. 2, 3, 100, 103, 105

[52] Géneaux, R., Timrov, I., Kaplan, C. J., Ross, A. D., Kraus, P. M., and Leone, S. R. Coherent energy exchange between carriers and phonons in peierls-distorted bismuth unveiled by broadband xuv pulses. *Phys. Rev. Res.*, 3:033210, Sep 2021. doi:10.1103/PhysRevResearch.3.033210. Cited on p. 2

[53] Sidiropoulos, T. P. H., Di Palo, N., Rivas, D. E., Severino, S., Reduzzi, M., Nandy, B., Bauerhenne, B., Krylow, S., Vasileiadis, T., Danz, T., Elliott, P., Sharma, S., Dewhurst, K., Ropers, C., Joly, Y., Garcia, M. E., Wolf, M., Ernstorfer, R., and Biegert, J. Probing the Energy Conversion Pathways between Light, Carriers, and Lattice in Real Time with Attosecond Core-Level Spectroscopy. *Physical Review X*, 11(4):041060, December 2021. doi:10.1103/PhysRevX.11.041060. Cited on p. 2, 100

[54] Oh, J., Chang, H.-T., Chen, C. T., Aloni, S., Schwartzberg, A., and Leone, S. R. Carrier and Phonon Dynamics in Multilayer WSe_2 Captured by Extreme Ultraviolet Transient Absorption Spectroscopy. *The Journal of Physical Chemistry C*, 127 (10):5004–5012, March 2023. doi:10.1021/acs.jpcc.2c07695. Cited on p. 2, 3, 29

[55] Heide, C., Kobayashi, Y., Johnson, A. C., Liu, F., Heinz, T. F., Reis, D. A., and Ghimire, S. Probing electron-hole coherence in strongly driven 2d ma-

terials using high-harmonic generation. *Optica*, 9(5):512–516, May 2022. doi:10.1364/OPTICA.444105. Cited on p. 2, 16

[56] Hu, S.-Q., Zhao, H., Liu, X.-B., Chen, D.-Q., and Meng, S. Probing Phonon dynamics and Electron-Phonon Coupling by High Harmonic Generation in Solids. *arXiv e-prints*, 2023. doi:10.48550/arXiv.2304.09459. Cited on p. 2, 16

[57] Zürch, M., Chang, H.-T., Borja, L. J., Kraus, P. M., Cushing, S. K., Gandman, A., Kaplan, C. J., Oh, M. H., Prell, J. S., Prendergast, D., Pemmaraju, C. D., Neumark, D. M., and Leone, S. R. Direct and simultaneous observation of ultrafast electron and hole dynamics in germanium. *Nature Communications*, 8(1):1–11, June 2017. doi:10.1038/ncomms15734. Cited on p. 2, 43, 90, 92, 103, 105, 133, 134

[58] Zürch, M., Chang, H.-T., Kraus, P. M., Cushing, S. K., Borja, L. J., Gandman, A., Kaplan, C. J., Oh, M. H., Prell, J. S., Prendergast, D., Pemmaraju, C. D., Neumark, D. M., and Leone, S. R. Ultrafast carrier thermalization and trapping in silicon-germanium alloy probed by extreme ultraviolet transient absorption spectroscopy. *Structural Dynamics*, 4(4):044029, 06 2017. doi:10.1063/1.4985056. Cited on p. 2, 103

[59] Schlaepfer, F., Lucchini, M., Sato, S. A., Volkov, M., Kasmi, L., Hartmann, N., Rubio, A., Gallmann, L., and Keller, U. Attosecond optical-field-enhanced carrier injection into the GaAs conduction band. *Nature Physics*, 14(6):560–564, June 2018. doi:10.1038/s41567-018-0069-0. Cited on p. 2, 103

[60] Lin, M.-F., Verkamp, M. A., Leveillee, J., Ryland, E. S., Benke, K., Zhang, K., Weninger, C., Shen, X., Li, R., Fritz, D., Bergmann, U., Wang, X., Schleife, A., and Vura-Weis, J. Carrier-Specific Femtosecond XUV Transient Absorption of PbI_2 Reveals Ultrafast Nonradiative Recombination. *The Journal of Physical Chemistry C*, 121(50):27886–27893, December 2017. doi:10.1021/acs.jpcc.7b11147. Cited on p. 2, 103, 105

[61] Verkamp, M., Leveillee, J., Sharma, A., Lin, M.-F., Schleife, A., and Vura-Weis, J. Carrier-Specific Hot Phonon Bottleneck in CH3NH3PbI3 Revealed by Femtosecond XUV Absorption. *Journal of the American Chemical Society*, 143(48): 20176–20182, December 2021. doi:10.1021/jacs.1c07817. Cited on p. 2, 103

[62] Vampa, G., Hammond, T. J., Thiré, N., Schmidt, B. E., Légaré, F., McDonald, C. R., Brabec, T., Klug, D. D., and Corkum, P. B. All-Optical Reconstruction of Crystal Band Structure. *Physical Review Letters*, 115(19):193603, November 2015. doi:10.1103/PhysRevLett.115.193603. Cited on p. 2, 13, 16, 70, 73, 87, 129

[63] Langer, F., Hohenleutner, M., Schmid, C. P., Poellmann, C., Nagler, P., Korn, T., Schüller, C., Sherwin, M. S., Huttner, U., Steiner, J. T., Koch, S. W., Kira, M., and Huber, R. Lightwave-driven quasiparticle collisions on a subcycle timescale. *Nature*, 533(7602):225–229, May 2016. doi:10.1038/nature17958. Cited on p. 2, 16, 70

[64] Kfir, O., Zayko, S., Nolte, C., Sivis, M., Möller, M., Hebler, B., Arekapudi, S. S. P. K., Steil, D., Schäfer, S., Albrecht, M., Cohen, O., Mathias, S., and Ropers, C. Nanoscale magnetic imaging using circularly polarized high-harmonic radiation. *Science Advances*, 3(12):eaao4641, December 2017. doi:10.1126/sciadv.aao4641. Cited on p. 3, 129

[65] Rouxel, J. R. and Mukamel, S. Molecular Chirality and Its Monitoring by Ultrafast X-ray Pulses. *Chemical Reviews*, 122(22):16802–16838, November 2022. doi:10.1021/acs.chemrev.2c00115. Cited on p. 3

[66] Kfir, O., Grychtol, P., Turgut, E., Knut, R., Zusin, D., Popmintchev, D., Popmintchev, T., Nembach, H., Shaw, J. M., Fleischer, A., Kapteyn, H., Murnane, M., and Cohen, O. Generation of bright phase-matched circularly-polarized extreme ultraviolet high harmonics. *Nature Photonics*, 9(2):99–105, February 2015. doi:10.1038/nphoton.2014.293. Cited on p. 3, 70, 71

[67] Baykusheva, D. and Wörner, H. J. Chiral Discrimination through Bielliptical High-Harmonic Spectroscopy. *Physical Review X*, 8(3):031060, September 2018. doi:10.1103/PhysRevX.8.031060. Cited on p. 3

[68] You, Y. S., Reis, D. A., and Ghimire, S. Anisotropic high-harmonic generation in bulk crystals. *Nature Physics*, 13(4):345–349, April 2017. doi:10.1038/nphys3955. Cited on p. 3, 13, 16, 70, 71

[69] Luu, T. T. and Wörner, H. J. Observing broken inversion symmetry in solids using

two-color high-order harmonic spectroscopy. *Physical Review A*, 98(4):041802, October 2018. doi:10.1103/PhysRevA.98.041802. Cited on p. 3, 16, 70, 87

[70] Jiang, S., Chen, J., Wei, H., Yu, C., Lu, R., and Lin, C. D. Role of the Transition Dipole Amplitude and Phase on the Generation of Odd and Even High-Order Harmonics in Crystals. *Physical Review Letters*, 120(25):253201, June 2018. doi:10.1103/PhysRevLett.120.253201. Cited on p. 3, 16, 70

[71] Yue, L., Hollinger, R., Uzundal, C. B., Nebgen, B., Gan, Z., Najafidehaghani, E., George, A., Spielmann, C., Kartashov, D., Turchanin, A., Qiu, D. Y., Gaarde, M. B., and Zuerch, M. Signatures of Multiband Effects in High-Harmonic Generation in Monolayer MoS 2. *Physical Review Letters*, 129(14):147401, September 2022. doi:10.1103/PhysRevLett.129.147401. Cited on p. 3, 16

[72] Liu, H., Klein, I. M., Michelsen, J. M., and Cushing, S. K. Element-specific electronic and structural dynamics using transient XUV and soft X-ray spectroscopy. *Chem*, 7(10):2569–2584, October 2021. doi:10.1016/j.chempr.2021.09.005. Cited on p. 3, 90

[73] Mathias, S., La-o-vorakiat, C., Shaw, J. M., Turgut, E., Grychtol, P., Adam, R., Rudolf, D., Nembach, H. T., Silva, T. J., Aeschlimann, M., Schneider, C. M., Kapteyn, H. C., and Murnane, M. M. Ultrafast element-specific magnetization dynamics of complex magnetic materials on a table-top. *Journal of Electron Spectroscopy and Related Phenomena*, 189:164–170, August 2013. doi:10.1016/j.elspec.2012.11.013. Cited on p. 3

[74] Chatziathanasiou, S., Kahaly, S., Skantzakis, E., Sansone, G., Lopez-Martens, R., Haessler, S., Varju, K., Tsakiris, G., Charalambidis, D., and Tzallas, P. Generation of Attosecond Light Pulses from Gas and Solid State Media. *Photonics*, 4:26, March 2017. doi:10.3390/photonics4020026. Cited on p. 4

[75] Cushing, S. K., Lee, A., Porter, I. J., Carneiro, L. M., Chang, H.-T., Zürch, M., and Leone, S. R. Differentiating Photoexcited Carrier and Phonon Dynamics in the Δ, L , and Γ Valleys of Si(100) with Transient Extreme Ultraviolet Spectroscopy. *The Journal of Physical Chemistry C*, 123(6):3343–3352, February 2019. doi:10.1021/acs.jpcc.8b10887. Cited on p. 4, 90, 105

[76] Castro Neto, A. H., Guinea, F., Peres, N. M. R., Novoselov, K. S., and Geim, A. K. The electronic properties of graphene. *Reviews of Modern Physics*, 81(1):109–162, January 2009. doi:10.1103/RevModPhys.81.109. Cited on p. 4

[77] MAIMAN, T. H. Stimulated Optical Radiation in Ruby. *Nature*, 187(4736):493–494, August 1960. doi:10.1038/187493a0. Cited on p. 7

[78] Franken, P. A., Hill, A. E., Peters, C. W., and Weinreich, G. Generation of Optical Harmonics. *Physical Review Letters*, 7(4):118–119, August 1961. doi:10.1103/PhysRevLett.7.118. Cited on p. 7

[79] Kaiser, W. and Garrett, C. G. B. Two-Photon Excitation in Ca F 2 : Eu 2 +. *Physical Review Letters*, 7(6):229–231, September 1961. doi:10.1103/PhysRevLett.7.229. Cited on p. 7

[80] Boyd, R. W. *Nonlinear Optics, Third Edition*. Academic Press, Inc., USA, 3rd edition, 2008. Cited on p. 7

[81] Bloembergen, N. Nonlinear optics: Past, present, and future. *IEEE Journal of Selected Topics in Quantum Electronics*, 6(6):876–880, 2000. doi:10.1007/978-94-011-2536-9$_1$. Cited on p. 7

[82] Reintjes, J., Eckardt, R. C., She, C. Y., Karangelen, N. E., Elton, R. C., and Andrews, R. A. Generation of Coherent Radiation at 53.2 nm by Fifth-Harmonic Conversion. *Physical Review Letters*, 37(23):1540–1543, December 1976. doi:10.1103/PhysRevLett.37.1540. Cited on p. 7

[83] Pfeifer, T., Spielmann, C., and Gerber, G. Femtosecond x-ray science. *Reports on Progress in Physics*, 69(2):443–505, February 2006. doi:10.1088/0034-4885/69/2/R04. Cited on p. 7

[84] Popmintchev, T., Chen, M.-C., Popmintchev, D., Arpin, P., Brown, S., Ališauskas, S., Andriukaitis, G., Balčiunas, T., Mücke, O. D., Pugzlys, A., Baltuška, A., Shim, B., Schrauth, S. E., Gaeta, A., Hernández-García, C., Plaja, L., Becker, A., Jaron-Becker, A., Murnane, M. M., and Kapteyn, H. C. Bright Coherent Ultrahigh Harmonics in the keV X-ray Regime from Mid-Infrared Femtosecond Lasers. *Science*, 336(6086):1287–1291, June 2012. doi:10.1126/science.1218497. Cited on p. 7, 20

[85] McPherson, A., Gibson, G., Jara, H., Johann, U., Luk, T. S., McIntyre, I. A., Boyer, K., and Rhodes, C. K. Studies of multiphoton production of vacuum-ultraviolet radiation in the rare gases. *Journal of the Optical Society of America B: Optical Physics*, 4(4):595–601, April 1987. doi:10.1364/JOSAB.4.000595. Cited on p. 7

[86] Ferray, M., L'Huillier, A., Li, X. F., Lompre, L. A., Mainfray, G., and Manus, C. Multiple-harmonic conversion of 1064 nm radiation in rare gases. *Journal of Physics B: Atomic, Molecular and Optical Physics*, 21(3):L31–L35, February 1988. doi:10.1088/0953-4075/21/3/001. Cited on p. 7

[87] Strickland, D. and Mourou, G. Compression of amplified chirped optical pulses. *Optics Communications*, 55(6):447–449, October 1985. doi:10.1016/0030-4018(85)90151-8. Cited on p. 7

[88] Corkum, P. B. Plasma perspective on strong field multiphoton ionization. *Physical Review Letters*, 71(13):1994–1997, September 1993. doi:10.1103/PhysRevLett.71.1994. Cited on p. 7, 8, 9, 11

[89] Luu, T. T., Yin, Z., Jain, A., Gaumnitz, T., Pertot, Y., Ma, J., and Wörner, H. J. Extreme–ultraviolet high–harmonic generation in liquids. *Nature Communications*, 9 (1):3723, December 2018. doi:10.1038/s41467-018-06040-4. Cited on p. 7

[90] Young, L., Ueda, K., Gühr, M., Bucksbaum, P. H., Simon, M., Mukamel, S., Rohringer, N., Prince, K. C., Masciovecchio, C., Meyer, M., Rudenko, A., Rolles, D., Bostedt, C., Fuchs, M., Reis, D. A., Santra, R., Kapteyn, H., Murnane, M., Ibrahim, H., Légaré, F., Vrakking, M., Isinger, M., Kroon, D., Gisselbrecht, M., L'Huillier, A., Wörner, H. J., and Leone, S. R. Roadmap of ultrafast x-ray atomic and molecular physics. *Journal of Physics B: Atomic, Molecular and Optical Physics*, 51(3):032003, February 2018. doi:10.1088/1361-6455/aa9735. Cited on p. 8

[91] Zayko, S., Kfir, O., Heigl, M., Lohmann, M., Sivis, M., Albrecht, M., and Ropers, C. Ultrafast high-harmonic nanoscopy of magnetization dynamics. *Nature Communications*, 12(1):6337, December 2021. doi:10.1038/s41467-021-26594-0. Cited on p. 8, 15

[92] Rohwer, T., Hellmann, S., Wiesenmayer, M., Sohrt, C., Stange, A., Slomski, B., Carr, A., Liu, Y., Avila, L. M., Kalläne, M., Mathias, S., Kipp, L., Rossnagel, K., and Bauer, M. Collapse of long-range charge order tracked by time-resolved photoemission at high momenta. *Nature*, 471(7339):490–493, March 2011. doi:10.1038/nature09829. Cited on p. 8, 15, 64, 65, 67, 100, 125

[93] Mathias, S., Eich, S., Urbancic, J., Michael, S., Carr, A. V., Emmerich, S., Stange, A., Popmintchev, T., Rohwer, T., Wiesenmayer, M., Ruffing, A., Jakobs, S., Hellmann, S., Matyba, P., Chen, C., Kipp, L., Bauer, M., Kapteyn, H. C., Schneider, H. C., Rossnagel, K., Murnane, M. M., and Aeschlimann, M. Self-amplified photo-induced gap quenching in a correlated electron material. *Nature Communications*, 7(1):12902, December 2016. doi:10.1038/ncomms12902. Cited on p. 8, 65, 66, 67, 100, 106, 134

[94] Kulander, K. C., Schafer, K. J., and Krause, J. L. Dynamics of Short-Pulse Excitation, Ionization and Harmonic Conversion. In Piraux, B., L'Huillier, A., and Rzążewski, K., editors, *Super-Intense Laser-Atom Physics*, NATO ASI Series, pages 95–110. Springer US, Boston, MA, 1993. doi:10.1007/978-1-4615-7963-2$_1$0. Cited on p. 8, 9

[95] Schafer, K. J., Yang, B., DiMauro, L. F., and Kulander, K. C. Above threshold ionization beyond the high harmonic cutoff. *Physical Review Letters*, 70(11):1599–1602, March 1993. doi:10.1103/PhysRevLett.70.1599. Cited on p. 8, 9

[96] Lewenstein, M., Balcou, Ph., Ivanov, M. Yu., L'Huillier, A., and Corkum, P. B. Theory of high-harmonic generation by low-frequency laser fields. *Physical Review A*, 49(3):2117–2132, March 1994. doi:10.1103/PhysRevA.49.2117. Cited on p. 8, 9, 12

[97] Keldysh, L. V. Ionization in the field of a strong electromagnetic wave. *Sov. Phys. JETP*, 20(5), 1965. Cited on p. 10

[98] Parks, A. M., Ernotte, G., Thorpe, A., McDonald, C. R., Corkum, P. B., Taucer, M., and Brabec, T. Wannier quasi-classical approach to high harmonic generation in semiconductors. *Optica*, 7(12):1764, December 2020. doi:10.1364/OPTICA.402393. Cited on p. 11, 13

[99] Houston, W. V. Acceleration of Electrons in a Crystal Lattice. *Physical Review*, 57 (3):184–186, February 1940. doi:10.1103/PhysRev.57.184. Cited on p. 13

[100] McDonald, C. R., Vampa, G., Corkum, P. B., and Brabec, T. Interband Bloch oscillation mechanism for high-harmonic generation in semiconductor crystals. *Physical Review A*, 92(3):033845, September 2015. doi:10.1103/PhysRevA.92.033845. Cited on p. 13

[101] Schubert, O., Hohenleutner, M., Langer, F., Urbanek, B., Lange, C., Huttner, U., Golde, D., Meier, T., Kira, M., Koch, S. W., and Huber, R. Sub-cycle control of terahertz high-harmonic generation by dynamical Bloch oscillations. *Nature Photonics*, 8(2):119–123, February 2014. doi:10.1038/nphoton.2013.349. Cited on p. 13, 70

[102] Ghimire, S., DiChiara, A. D., Sistrunk, E., Szafruga, U. B., Agostini, P., DiMauro, L. F., and Reis, D. A. Redshift in the Optical Absorption of ZnO Single Crystals in the Presence of an Intense Midinfrared Laser Field. *Physical Review Letters*, 107 (16):167407, October 2011. doi:10.1103/PhysRevLett.107.167407. Cited on p. 13

[103] Golde, D., Meier, T., and Koch, S. W. High harmonics generated in semiconductor nanostructures by the coupled dynamics of optical inter- and intraband excitations. *Physical Review B*, 77(7):075330, February 2008. doi:10.1103/PhysRevB.77.075330. Cited on p. 13, 16

[104] Luu, T. T., Garg, M., Kruchinin, S. Y., Moulet, A., Hassan, M. T., and Goulielmakis, E. Extreme ultraviolet high-harmonic spectroscopy of solids. *Nature*, 521 (7553):498–502, May 2015. doi:10.1038/nature14456. Cited on p. 13, 40

[105] Lakhotia, H., Kim, H. Y., Zhan, M., Hu, S., Meng, S., and Goulielmakis, E. Laser picoscopy of valence electrons in solids. *Nature*, 583(7814):55–59, July 2020. doi:10.1038/s41586-020-2429-z. Cited on p. 13, 16, 70, 73, 78, 87

[106] Dagotto, E. Complexity in Strongly Correlated Electronic Systems. *Science*, 309 (5732):257–262, July 2005. doi:10.1126/science.1107559. Cited on p. 15, 100

[107] Basov, D. N., Averitt, R. D., van der Marel, D., Dressel, M., and Haule, K. Electrodynamics of correlated electron materials. *Reviews of Modern Physics*, 83(2): 471–541, June 2011. doi:10.1103/RevModPhys.83.471. Cited on p. 15, 90, 100

[108] Krausz, F. and Ivanov, M. Attosecond physics. *Reviews of Modern Physics*, 81(1): 163–234, February 2009. doi:10.1103/RevModPhys.81.163. Cited on p. 15, 90

[109] Krausz, F. and Stockman, M. I. Attosecond metrology: From electron capture to future signal processing. *Nature Photonics*, 8(3):205–213, March 2014. doi:10.1038/nphoton.2014.28. Cited on p. 15, 90

[110] Zhao, K., Zhang, Q., Chini, M., Wu, Y., Wang, X., and Chang, Z. Tailoring a 67 attosecond pulse through advantageous phase-mismatch. *Optics Letters*, 37(18): 3891–3893, September 2012. doi:10.1364/OL.37.003891. Cited on p. 15, 90

[111] Ghimire, S., DiChiara, A. D., Sistrunk, E., Agostini, P., DiMauro, L. F., and Reis, D. A. Observation of high-order harmonic generation in a bulk crystal. *Nature Physics*, 7(2):138–141, February 2011. doi:10.1038/nphys1847. Cited on p. 16

[112] Luu, T. T. and Wörner, H. J. Measurement of the Berry curvature of solids using high-harmonic spectroscopy. *Nature Communications*, 9(1):916, March 2018. doi:10.1038/s41467-018-03397-4. Cited on p. 16, 73, 87

[113] Bionta, M. R., Haddad, E., Leblanc, A., Gruson, V., Lassonde, P., Ibrahim, H., Chaillou, J., Émond, N., Otto, M. R., Jiménez-Galán, Á., Silva, R. E. F., Ivanov, M., Siwick, B. J., Chaker, M., and Légaré, F. Tracking ultrafast solid-state dynamics using high harmonic spectroscopy. *Physical Review Research*, 3(2):023250, June 2021. doi:10.1103/PhysRevResearch.3.023250. Cited on p. 16, 130

[114] Liu, H., Li, Y., You, Y. S., Ghimire, S., Heinz, T. F., and Reis, D. A. High-harmonic generation from an atomically thin semiconductor. *Nature Physics*, 13(3):262–265, March 2017. doi:10.1038/nphys3946. Cited on p. 16

[115] Perry, M. D. and Crane, J. K. High-order harmonic emission from mixed fields. *Physical Review A*, 48(6):R4051–R4054, December 1993. doi:10.1103/PhysRevA.48.R4051. Cited on p. 17

[116] Kim, I. J., Kim, C. M., Kim, H. T., Lee, G. H., Lee, Y. S., Park, J. Y., Cho, D. J., and Nam, C. H. Highly Efficient High-Harmonic Generation in an Orthogonally Polarized Two-Color Laser Field. *Physical Review Letters*, 94(24):243901, June 2005. doi:10.1103/PhysRevLett.94.243901. Cited on p. 17

[117] Jin, C., Wang, G., Wei, H., Le, A.-T., and Lin, C. D. Waveforms for optimal sub-keV high-order harmonics with synthesized two- or three-colour laser fields. *Nature Communications*, 5(1):4003, September 2014. doi:10.1038/ncomms5003. Cited on p. 17

[118] Jin, C., Stein, G. J., Hong, K.-H., and Lin, C. D. Generation of Bright, Spatially Coherent Soft X-Ray High Harmonics in a Hollow Waveguide Using Two-Color Synthesized Laser Pulses. *Physical Review Letters*, 115(4):043901, July 2015. doi:10.1103/PhysRevLett.115.043901. Cited on p. 17

[119] Eichmann, H., Egbert, A., Nolte, S., Momma, C., Wellegehausen, B., Becker, W., Long, S., and McIver, J. K. Polarization-dependent high-order two-color mixing. *Physical Review A*, 51(5):R3414–R3417, May 1995. doi:10.1103/PhysRevA.51.R3414. Cited on p. 17

[120] Watanabe, S., Kondo, K., Nabekawa, Y., Sagisaka, A., and Kobayashi, Y. Two-Color Phase Control in Tunneling Ionization and Harmonic Generation by a Strong Laser Field and Its Third Harmonic. *Physical Review Letters*, 73(20):2692–2695, November 1994. doi:10.1103/PhysRevLett.73.2692. Cited on p. 17

[121] Fleischer, A., Kfir, O., Diskin, T., Sidorenko, P., and Cohen, O. Spin angular momentum and tunable polarization in high-harmonic generation. *Nature Photonics*, 8(7):543–549, July 2014. doi:10.1038/nphoton.2014.108. Cited on p. 18, 70, 71

[122] Klemke, N. *High harmonic generation from solids with elliptically polarized laser pulses*. PhD thesis. Cited on p. 19, 124

[123] Saito, N., Xia, P., Lu, F., Kanai, T., Itatani, J., and Ishii, N. Observation of selection rules for circularly polarized fields in high-harmonic generation from a crystalline solid. *Optica*, 4(11):1333–1336, November 2017. doi:10.1364/OPTICA.4.001333. Cited on p. 19, 70, 87, 124

[124] Klemke, N., Mücke, O. D., Rubio, A., Kärtner, F. X., and Tancogne-Dejean, N. Role of intraband dynamics in the generation of circularly polarized high harmonics from solids. *Physical Review B*, 102(10):104308, September 2020. doi:10.1103/PhysRevB.102.104308. Cited on p. 19, 70, 124

[125] Kfir, O., Bordo, E., Ilan Haham, G., Lahav, O., Fleischer, A., and Cohen, O. In-line production of a bi-circular field for generation of helically polarized high-order harmonics. *Applied Physics Letters*, 108(21):211106, May 2016. doi:10.1063/1.4952436. Cited on p. 19, 80, 116

[126] Popmintchev, T., Chen, M.-C., Cohen, O., Grisham, M. E., Rocca, J. J., Murnane, M. M., and Kapteyn, H. C. Extended phase matching of high harmonics driven by mid-infrared light. *Optics Letters*, 33(18):2128, September 2008. doi:10.1364/OL.33.002128. Cited on p. 20

[127] L'Huillier, A., Schafer, K. J., and Kulander, K. C. Higher-order harmonic generation in xenon at 1064 nm: The role of phase matching. *Physical Review Letters*, 66(17):2200–2203, April 1991. doi:10.1103/PhysRevLett.66.2200. Cited on p. 20

[128] Popmintchev, T., Chen, M.-C., Bahabad, A., Gerrity, M., Sidorenko, P., Cohen, O., Christov, I. P., Murnane, M. M., and Kapteyn, H. C. Phase matching of high harmonic generation in the soft and hard X-ray regions of the spectrum. *Proceedings of the National Academy of Sciences*, 106(26):10516–10521, June 2009. doi:10.1073/pnas.0903748106. Cited on p. 20

[129] Constant, E., Garzella, D., Breger, P., Mével, E., Dorrer, Ch., Le Blanc, C., Salin, F., and Agostini, P. Optimizing High Harmonic Generation in Absorbing Gases: Model and Experiment. *Physical Review Letters*, 82(8):1668–1671, February 1999. doi:10.1103/PhysRevLett.82.1668. Cited on p. 21

[130] Hädrich, S., Klenke, A., Rothhardt, J., Krebs, M., Hoffmann, A., Pronin, O., Pervak, V., Limpert, J., and Tünnermann, A. High photon flux table-top coherent extreme-ultraviolet source. *Nature Photonics*, 8(10):779–783, October 2014. doi:10.1038/nphoton.2014.214. Cited on p. 21

[131] Chen, M.-C., Gerrity, M. R., Backus, S., Popmintchev, T., Zhou, X., Arpin, P., Zhang, X., Kapteyn, H. C., and Murnane, M. M. Spatially coherent, phase matched, high-order harmonic EUV beams at 50 kHz. *Optics Express*, 17(20): 17376, September 2009. doi:10.1364/OE.17.017376. Cited on p. 21

[132] Tamaki, Y., Itatani, J., Nagata, Y., Obara, M., and Midorikawa, K. Highly Efficient, Phase-Matched High-Harmonic Generation by a Self-Guided

Laser Beam. *Physical Review Letters*, 82(7):1422–1425, February 1999. doi:10.1103/PhysRevLett.82.1422. Cited on p. 21

[133] Rundquist, A., Durfee, C. G., Chang, Z., Herne, C., Backus, S., Murnane, M. M., and Kapteyn, H. C. Phase-Matched Generation of Coherent Soft X-rays. *Science*, 280(5368):1412–1415, May 1998. doi:10.1126/science.280.5368.1412. Cited on p. 21

[134] Durfee, C. G., Rundquist, A. R., Backus, S., Herne, C., Murnane, M. M., and Kapteyn, H. C. Phase Matching of High-Order Harmonics in Hollow Waveguides. *Physical Review Letters*, 83(11):2187–2190, September 1999. doi:10.1103/PhysRevLett.83.2187. Cited on p. 21

[135] Papadogiannis, N., Kalpouzos, C., Goulielmakis, E., Nersisyan, G., Charalambidis, D., Augé, F., Weihe, F., and Balcou, Ph. Kilohertz extreme-ultraviolet light source based on femtosecond high-order harmonic generation from noble gases. *Applied Physics B: Lasers and Optics*, 73(7):687–692, November 2001. doi:10.1007/s003400100734. Cited on p. 21

[136] Steingrube, D. S., Vockerodt, T., Schulz, E., Morgner, U., and Kovačev, M. Phase matching of high-order harmonics in a semi-infinite gas cell. *Physical Review A*, 80(4):043819, October 2009. doi:10.1103/PhysRevA.80.043819. Cited on p. 21

[137] Ghimire, S., DiChiara, A. D., Sistrunk, E., Ndabashimiye, G., Szafruga, U. B., Mohammad, A., Agostini, P., DiMauro, L. F., and Reis, D. A. Generation and propagation of high-order harmonics in crystals. *Physical Review A*, 85(4):043836, April 2012. doi:10.1103/PhysRevA.85.043836. Cited on p. 22

[138] Ghimire, S., DiChiara, A. D., Sistrunk, E., Agostini, P., DiMauro, L. F., and Reis, D. A. Observation of high-order harmonic generation in a bulk crystal. *Nature Physics*, 7(2):138–141, February 2011. doi:10.1038/nphys1847. Cited on p. 22, 70, 78

[139] Vampa, G., You, Y. S., Liu, H., Ghimire, S., and Reis, D. A. Observation of backward high-harmonic emission from solids. *Optics Express*, 26(9):12210–12218, April 2018. doi:10.1364/OE.26.012210. Cited on p. 22

[140] Han, S., Kim, H., Kim, Y. W., Kim, Y.-J., Kim, S., Park, I.-Y., and Kim, S.-W. High-harmonic generation by field enhanced femtosecond pulses in metal-sapphire nanostructure. *Nature Communications*, 7(1):13105, October 2016. doi:10.1038/ncomms13105. Cited on p. 22, 23, 70

[141] Vampa, G., Ghamsari, B. G., Siadat Mousavi, S., Hammond, T. J., Olivieri, A., Lisicka-Skrek, E., Naumov, A. Y., Villeneuve, D. M., Staudte, A., Berini, P., and Corkum, P. B. Plasmon-enhanced high-harmonic generation from silicon. *Nature Physics*, 13(7):659–662, July 2017. doi:10.1038/nphys4087. Cited on p. 22, 70

[142] Liu, H., Vampa, G., Zhang, J. L., Shi, Y., Buddhiraju, S., Fan, S., Vuckovic, J., Bucksbaum, P. H., and Reis, D. A. Beating absorption in solid-state high harmonics. *Communications Physics*, 3(1):192, December 2020. doi:10.1038/s42005-020-00472-5. Cited on p. 22, 23

[143] Sivis, M., Taucer, M., Vampa, G., Johnston, K., Staudte, A., Naumov, A. Y., Villeneuve, D. M., Ropers, C., and Corkum, P. B. Tailored semiconductors for high-harmonic optoelectronics. *Science*, 357(6348):303–306, July 2017. doi:10.1126/science.aan2395. Cited on p. 23, 70, 79, 125

[144] Liu, H., Li, Y., You, Y. S., Ghimire, S., Heinz, T. F., and Reis, D. A. High-harmonic generation from an atomically thin semiconductor. *Nature Physics*, 13(3):262–265, March 2017. doi:10.1038/nphys3946. Cited on p. 24

[145] Yoshikawa, N., Tamaya, T., and Tanaka, K. High-harmonic generation in graphene enhanced by elliptically polarized light excitation. *Science*, 356(6339):736–738, May 2017. doi:10.1126/science.aam8861. Cited on p. 24

[146] Attwood, D. *Soft X-Rays and Extreme Ultraviolet Radiation: Principles and Applications*. Cambridge University Press, first edition, August 1999. doi:10.1017/CBO9781139164429. Cited on p. 26, 29

[147] Lucarini, V., Saarinen, J. J., Peiponen, K.-E., and Vartiainen, E. M. *Kramers-Kronig Relations in Optical Materials Research*. April 2005. doi:10.1007/b138913. Cited on p. 26

[148] Tompkins, H. G. and Irene, E. A., editors. *Handbook of Ellipsometry*. William Andrew Publishing, Norwich, NY, 2005. doi:10.1016/B978-081551499-2.50015-0. Cited on p. 27

[149] Rehr, J. Theory and calculations of X-ray spectra: XAS, XES, XRS, and NRIXS. *Radiation Physics and Chemistry*, 75(11):1547–1558, November 2006. doi:10.1016/j.radphyschem.2005.11.014. Cited on p. 27

[150] Griffiths, D. J. and Schroeter, D. F. *Introduction to quantum mechanics*. Cambridge University Press, Cambridge ; New York, NY, third edition edition, 2018. doi:10.1017/9781316995433. Cited on p. 27

[151] Yano, J. and Yachandra, V. K. X-ray absorption spectroscopy. *Photosynthesis Research*, 102(2-3):241–254, December 2009. doi:10.1007/s11120-009-9473-8. Cited on p. 28

[152] Becker, U., Prescher, T., Schmidt, E., Sonntag, B., and Wetzel, H. E. Decay channels of the discrete and continuum Xe *4d* resonances. *Physical Review A*, 33(6): 3891–3899, June 1986. doi:10.1103/PhysRevA.33.3891. Cited on p. 29

[153] Shiner, A. D., Schmidt, B. E., Trallero-Herrero, C., Wörner, H. J., Patchkovskii, S., Corkum, P. B., Kieffer, J.-C., Légaré, F., and Villeneuve, D. M. Probing collective multi-electron dynamics in xenon with high-harmonic spectroscopy. *Nature Physics*, 7(6):464–467, June 2011. doi:10.1038/nphys1940. Cited on p. 29

[154] Krasovska, O. V., Antonov, V. N., Krasovskii, E. E., and Schattke, W. Effect of off-diagonal dielectric response on optical properties of latio3. *physica status solidi (b)*, 243(8):1885–1892, 2006. doi:10.1002/pssb.200642012. Cited on p. 29, 38, 133

[155] Krasovskii, E. E. and Schattke, W. Local field effects in optical excitations of semicore electrons. *Physical Review B*, 60(24):R16251–R16254, December 1999. doi:10.1103/PhysRevB.60.R16251. Cited on p. 29, 38, 102, 121, 133

[156] Volkov, M., Sato, S. A., Schlaepfer, F., Kasmi, L., Hartmann, N., Lucchini, M., Gallmann, L., Rubio, A., and Keller, U. Attosecond screening dynamics mediated by electron localization in transition metals. *Nature Physics*, 15(11):1145–1149,

November 2019. doi:10.1038/s41567-019-0602-9. Cited on p. 29, 38, 102, 103, 121, 133, 134

[157] Chang, H.-T., Guggenmos, A., Chen, C. T., Oh, J., Géneaux, R., Chuang, Y.-D., Schwartzberg, A. M., Aloni, S., Neumark, D. M., and Leone, S. R. Coupled valence carrier and core-exciton dynamics in WS_2 probed by few-femtosecond extreme ultraviolet transient absorption spectroscopy. *Physical Review B*, 104(6): 064309, August 2021. doi:10.1103/PhysRevB.104.064309. Cited on p. 29, 101, 102, 103

[158] Hedin, L. New Method for Calculating the One-Particle Green's Function with Application to the Electron-Gas Problem. *Physical Review*, 139(3A):A796–A823, August 1965. doi:10.1103/PhysRev.139.A796. Cited on p. 30

[159] Salpeter, E. E. and Bethe, H. A. A relativistic equation for bound-state problems. *Phys. Rev.*, 84:1232–1242, Dec 1951. doi:10.1103/PhysRev.84.1232. Cited on p. 30

[160] Vorwerk, C., Aurich, B., Cocchi, C., and Draxl, C. Bethe–Salpeter equation for absorption and scattering spectroscopy: Implementation in the exciting code. *Electronic Structure*, 1(3):037001, August 2019. doi:10.1088/2516-1075/ab3123. Cited on p. 30, 121

[161] Sagmeister, S. and Ambrosch-Draxl, C. Time-dependent density functional theory versus Bethe–Salpeter equation: An all-electron study. *Physical Chemistry Chemical Physics*, 11(22):4451, 2009. doi:10.1039/b903676h. Cited on p. 30, 121

[162] Orio, M., Pantazis, D. A., and Neese, F. Density functional theory. *Photosynth Res*, page 11, 2009. doi:10.1007/s11120-009-9404-8. Cited on p. 31

[163] Marques, M. A. L. *Time-Dependent Density Functional Theory*. Number 706 in Lecture Notes in Physics. Springer, Berlin, 2006. doi:10.1007/b11767107. Cited on p. 31, 35, 36

[164] Hohenberg, P. and Kohn, W. Inhomogeneous Electron Gas. *Physical Review*, 136(3B):B864–B871, November 1964. doi:10.1103/PhysRev.136.B864. Cited on p. 31

[165] Kohn, W. and Sham, L. J. Self-Consistent Equations Including Exchange and Correlation Effects. *Physical Review*, 140(4A):A1133–A1138, November 1965. doi:10.1103/PhysRev.140.A1133. Cited on p. 32

[166] Perdew, J. P., Chevary, J. A., Vosko, S. H., Jackson, K. A., Pederson, M. R., Singh, D. J., and Fiolhais, C. Atoms, molecules, solids, and surfaces: Applications of the generalized gradient approximation for exchange and correlation. *Physical Review B*, 46(11):6671–6687, September 1992. doi:10.1103/PhysRevB.46.6671. Cited on p. 33

[167] Perdew, J. P., Burke, K., and Ernzerhof, M. Generalized Gradient Approximation Made Simple. *Physical Review Letters*, 77(18):3865–3868, October 1996. doi:10.1103/PhysRevLett.77.3865. Cited on p. 33, 121

[168] Andersen, O. K. Linear methods in band theory. *Physical Review B*, 12(8):3060–3083, October 1975. doi:10.1103/PhysRevB.12.3060. Cited on p. 34

[169] Wimmer, E., Krakauer, H., Weinert, M., and Freeman, A. J. Full-potential self-consistent linearized-augmented-plane-wave method for calculating the electronic structure of molecules and surfaces: O_2 molecule. *Physical Review B*, 24(2):864–875, July 1981. doi:10.1103/PhysRevB.24.864. Cited on p. 34

[170] Grotendorst, J., Blügel, S., and John von Neumann-Institut für Computing, editors. *Computational Nanoscience: Do It Yourself! Winter School, 14 - 22 February 2006, Forschungszentrum Jülich, Germany ; Lecture Notes*. Number 31 in NIC Series. NIC-Secretariat, Research Centre Jülich, Jülich, 2006. Cited on p. 34

[171] Runge, E. and Gross, E. K. U. Density-Functional Theory for Time-Dependent Systems. *Physical Review Letters*, 52(12):997–1000, March 1984. doi:10.1103/PhysRevLett.52.997. Cited on p. 34

[172] van Leeuwen, R. Mapping from Densities to Potentials in Time-Dependent Density-Functional Theory. *Physical Review Letters*, 82(19):3863–3866, May 1999. doi:10.1103/PhysRevLett.82.3863. Cited on p. 34

[173] Marques, M. A., Maitra, N. T., Nogueira, F. M., Gross, E., and Rubio, A., editors. *Fundamentals of Time-Dependent Density Functional Theory*, volume 837 of

Lecture Notes in Physics. Springer Berlin Heidelberg, Berlin, Heidelberg, 2012. doi:10.1007/978-3-642-23518-4. Cited on p. 35

[174] Ullrich, C. *Time-Dependent Density-Functional Theory: Concepts and Applications*. Oxford Graduate Texts. Oxford University Press, Oxford ; New York, 2012. Cited on p. 35

[175] Hybertsen, M. S. and Louie, S. G. Ab initio static dielectric matrices from the density-functional approach. I. Formulation and application to semiconductors and insulators. *Physical Review B*, 35(11):5585–5601, April 1987. doi:10.1103/PhysRevB.35.5585. Cited on p. 35, 37, 38

[176] Lehmann, H. Über Eigenschaften von Ausbreitungsfunktionen und Renormierungskonstanten quantisierter Felder. *Il Nuovo Cimento (1943-1954)*, 11 (4):342–357, April 1954. doi:10.1007/BF02783624. Cited on p. 35

[177] Hanke, W. Dielectric theory of elementary excitations in crystals. *Advances in Physics*, 27(2):287–341, March 1978. doi:10.1080/00018737800101384. Cited on p. 36

[178] Gurtubay, I. G., Pitarke, J. M., Ku, W., Eguiluz, A. G., Larson, B. C., Tischler, J., Zschack, P., and Finkelstein, K. D. Electron-hole and plasmon excitations in 3 d transition metals: *Ab initio* calculations and inelastic x-ray scattering measurements. *Physical Review B*, 72(12):125117, September 2005. doi:10.1103/PhysRevB.72.125117. Cited on p. 36

[179] Petersilka, M., Gossmann, U. J., and Gross, E. K. U. Excitation Energies from Time-Dependent Density-Functional Theory. *Physical Review Letters*, 76(8): 1212–1215, February 1996. doi:10.1103/PhysRevLett.76.1212. Cited on p. 37

[180] Bohm, D. and Pines, D. A Collective Description of Electron Interactions. I. Magnetic Interactions. *Physical Review*, 82(5):625–634, June 1951. doi:10.1103/PhysRev.82.625. Cited on p. 37

[181] Pines, D. and Bohm, D. A Collective Description of Electron Interactions: II. Collective vs Individual Particle Aspects of the Interactions. *Physical Review*, 85 (2):338–353, January 1952. doi:10.1103/PhysRev.85.338. Cited on p. 37

[182] Bohm, D. and Pines, D. A Collective Description of Electron Interactions: III. Coulomb Interactions in a Degenerate Electron Gas. *Physical Review*, 92(3):609–625, November 1953. doi:10.1103/PhysRev.92.609. Cited on p. 37

[183] Lindhard, J. On the properties of a gas of charged particles. *Kgl. Danske Videnskab. Selskab Mat.-fys. Medd.* Cited on p. 38

[184] Schwitalla, J. and Ebert, H. Electron Core-Hole Interaction in the X-Ray Absorption Spectroscopy of 3d Transition Metals. *Physical Review Letters*, 80(20): 4586–4589, May 1998. doi:10.1103/PhysRevLett.80.4586. Cited on p. 38

[185] Zangwill, A. and Soven, P. Density-functional approach to local-field effects in finite systems: Photoabsorption in the rare gases. *Physical Review A*, 21(5):1561–1572, May 1980. doi:10.1103/PhysRevA.21.1561. Cited on p. 38

[186] Ankudinov, A. L., Nesvizhskii, A. I., and Rehr, J. J. Dynamic screening effects in x-ray absorption spectra. *Physical Review B*, 67(11):115120, March 2003. doi:10.1103/PhysRevB.67.115120. Cited on p. 38, 112

[187] Wiser, N. Dielectric Constant with Local Field Effects Included. *Physical Review*, 129(1):62–69, January 1963. doi:10.1103/PhysRev.129.62. Cited on p. 38

[188] Adler, S. L. Quantum Theory of the Dielectric Constant in Real Solids. *Physical Review*, 126(2):413–420, April 1962. doi:10.1103/PhysRev.126.413. Cited on p. 38

[189] Gulans, A., Kontur, S., Meisenbichler, C., Nabok, D., Pavone, P., Rigamonti, S., Sagmeister, S., Werner, U., and Draxl, C. Exciting: A full-potential all-electron package implementing density-functional theory and many-body perturbation theory. *Journal of Physics: Condensed Matter*, 26(36):363202, September 2014. doi:10.1088/0953-8984/26/36/363202. Cited on p. 38, 121

[190] Park, J., Subramani, A., Kim, S., and Ciappina, M. F. Recent trends in high-order harmonic generation in solids. *Advances in Physics: X*, 7(1):2003244, December 2022. doi:10.1080/23746149.2021.2003244. Cited on p. 40

[191] Malis, T. F. and Steele, D. Ultramicrotomy for Materials Science. *MRS Online Proceedings Library (OPL)*, 199:3, January 1990. doi:10.1557/PROC-199-3. Cited on p. 41

[192] Géneaux, R., Géneaux, R., Géneaux, R., Chang, H.-T., Schwartzberg, A. M., Marroux, H. J. B., and Marroux, H. J. B. Source noise suppression in attosecond transient absorption spectroscopy by edge-pixel referencing. *Optics Express*, 29 (2):951–960, January 2021. doi:10.1364/OE.412117. Cited on p. 43, 90, 93, 96

[193] Stooß, V., Hartmann, M., Birk, P., Borisova, G. D., Ding, T., Blättermann, A., Ott, C., and Pfeifer, T. XUV-beamline for attosecond transient absorption measurements featuring a broadband common beam-path time-delay unit and *in situ* reference spectrometer for high stability and sensitivity. *Review of Scientific Instruments*, 90(5):053108, May 2019. doi:10.1063/1.5091069. Cited on p. 43, 90

[194] Kato, K., Mashiko, H., Kunihashi, Y., Omi, H., Gotoh, H., and Oguri, K. Highly sensitive transient reflection measurement in extreme ultraviolet region for tracking carrier and coherent phonon dynamics. *Optics Express*, 28(2):1595–1602, January 2020. doi:10.1364/OE.381585. Cited on p. 43, 90

[195] Bishop, C. M. and Nasrabadi, N. M. *Pattern Recognition and Machine Learning*, volume 4. Springer, 2006. Cited on p. 43, 45, 51

[196] Ghahramani, Z. Unsupervised Learning. In Bousquet, O., von Luxburg, U., and Rätsch, G., editors, *Advanced Lectures on Machine Learning: ML Summer Schools 2003, Canberra, Australia, February 2 - 14, 2003, Tübingen, Germany, August 4 - 16, 2003, Revised Lectures*, Lecture Notes in Computer Science, pages 72–112. Springer, Berlin, Heidelberg, 2004. doi:10.1007/978-3-540-28650-9_5. Cited on p. 43

[197] Sutton, R. S. and Barto, A. G. *Reinforcement Learning, Second Edition: An Introduction*. MIT Press, November 2018. Cited on p. 43

[198] Lecun, Y., Bottou, L., Bengio, Y., and Haffner, P. Gradient-based learning applied to document recognition. *Proceedings of the IEEE*, 86(11):2278–2324, November 1998. doi:10.1109/5.726791. Cited on p. 44

[199] Abdel-Hamid, O., Deng, l., and Yu, D. Exploring convolutional neural network structures and optimization techniques for speech recognition. 08 2013. doi:10.21437/Interspeech.2013-744. Cited on p. 44, 53

[200] LeCun, Y. and Bengio, Y. *Convolutional Networks for Images, Speech, and Time Series*, page 255â258. MIT Press, Cambridge, MA, USA, 1998. ISBN 0262511029. Cited on p. 44, 53

[201] Hirschberg, J. and Manning, C. D. Advances in natural language processing. *Science*, 349(6245):261–266, 2015. doi:10.1126/science.aaa8685. Cited on p. 44

[202] Vaswani, A., Shazeer, N., Parmar, N., Uszkoreit, J., Jones, L., Gomez, A. N., Kaiser, L. u., and Polosukhin, I. Attention is all you need. In Guyon, I., Luxburg, U. V., Bengio, S., Wallach, H., Fergus, R., Vishwanathan, S., and Garnett, R., editors, *Advances in Neural Information Processing Systems*, volume 30. Curran Associates, Inc., 2017. Cited on p. 44

[203] Ormiston, R., Nguyen, T., Coughlin, M., Adhikari, R. X., and Katsavounidis, E. Noise reduction in gravitational-wave data via deep learning. *Physical Review Research*, 2(3):033066, July 2020. doi:10.1103/PhysRevResearch.2.033066. Cited on p. 44

[204] Isogawa, K., Ida, T., Shiodera, T., and Takeguchi, T. Deep Shrinkage Convolutional Neural Network for Adaptive Noise Reduction. *IEEE Signal Processing Letters*, 25(2):224–228, February 2018. doi:10.1109/LSP.2017.2782270. Cited on p. 44

[205] Acquarelli, J., van Laarhoven, T., Gerretzen, J., Tran, T. N., Buydens, L. M. C., and Marchiori, E. Convolutional neural networks for vibrational spectroscopic data analysis. *Analytica Chimica Acta*, 954:22–31, February 2017. doi:10.1016/j.aca.2016.12.010. Cited on p. 44

[206] Brunton, S. L., Proctor, J. L., and Kutz, J. N. Discovering governing equations from data by sparse identification of nonlinear dynamical systems. *Proceedings of the National Academy of Sciences*, 113(15):3932–3937, April 2016. doi:10.1073/pnas.1517384113. Cited on p. 44

[207] Thuerey, N., Holl, P., Mueller, M., Schnell, P., Trost, F., and Um, K. *Physics-based Deep Learning*. WWW, 2021. Cited on p. 44

[208] Rudin, C., Chen, C., Chen, Z., Huang, H., Semenova, L., and Zhong, C. Interpretable Machine Learning: Fundamental Principles and 10 Grand Challenges. *arXiv e-prints*, July 2021. doi:10.48550/arXiv.2103.11251. Cited on p. 44

[209] Molnar, C. *Interpretable Machine Learning*. 2 edition, 2022. Cited on p. 44

[210] Rudin, C. Stop explaining black box machine learning models for high stakes decisions and use interpretable models instead. *Nature Machine Intelligence*, 1(5): 206–215, May 2019. doi:10.1038/s42256-019-0048-x. Cited on p. 44

[211] Mehta, P., Bukov, M., Wang, C.-H., Day, A. G., Richardson, C., Fisher, C. K., and Schwab, D. J. A high-bias, low-variance introduction to machine learning for physicists. *Physics Reports*, 810:1–124, 2019. doi:10.1016/j.physrep.2019.03.001. Cited on p. 45, 46, 47, 48, 51, 57

[212] Ruder, S. An overview of gradient descent optimization algorithms. *arXiv e-prints*, 2017. doi:10.48550/arXiv.1609.04747. Cited on p. 45, 46, 47

[213] Bottou, L. Large-scale machine learning with stochastic gradient descent. In Lechevallier, Y. and Saporta, G., editors, *Proceedings of COMPSTAT'2010*, pages 177–186, Heidelberg, 2010. Physica-Verlag HD. doi:10.1007/978-3-7908-2604-3_1. Cited on p. 46

[214] Bottou, L. Stochastic Gradient Descent Tricks. In Montavon, G., Orr, G. B., and Müller, K.-R., editors, *Neural Networks: Tricks of the Trade*, volume 7700, pages 421–436. Springer Berlin Heidelberg, Berlin, Heidelberg, 2012. doi:10.1007/978-3-642-35289-$8_2$5. Cited on p. 46

[215] Rumelhart, D. E., Hinton, G. E., and Williams, R. J. Learning representations by back-propagating errors. *Nature*, 323(6088):533–536, 1986. doi:10.1038/323533a0. Cited on p. 46

[216] Kingma, D. P. and Ba, J. Adam: A Method for Stochastic Optimization. *arXiv e-prints*, January 2017. doi:10.48550/arXiv.1412.6980. Cited on p. 47, 94

[217] Abu-Mostafa, Y. S., Magdon-Ismail, M., and Lin, H.-T. *Learning From Data*. AMLBook, 2012. Cited on p. 48, 51

[218] Geman, S., Bienenstock, E., and Doursat, R. Neural Networks and the Bias/Variance Dilemma. *Neural Computation*, 4(1):1–58, January 1992. doi:10.1162/neco.1992.4.1.1. Cited on p. 48, 49

[219] Tibshirani, R. Regression Shrinkage and Selection Via the Lasso. *Journal of the Royal Statistical Society: Series B (Methodological)*, 58(1):267–288, 1996. doi:10.1111/j.2517-6161.1996.tb02080.x. Cited on p. 50

[220] Hoerl, A. E. and Kennard, R. W. Ridge Regression: Biased Estimation for Nonorthogonal Problems. *Technometrics*, 12(1):55–67, February 1970. doi:10.1080/00401706.1970.10488634. Cited on p. 50

[221] Murphy, K. P. *Machine learning: A probabilistic perspective*. MIT Press, 2013. Cited on p. 51

[222] Hastie, T., Tibshirani, R., and Friedman, J. *The elements of statistical learning: data mining, inference and prediction*. Springer, 2 edition, 2009. doi:10.1007/978-0-387-84858-7. Cited on p. 51

[223] Goodfellow, I., Bengio, Y., and Courville, A. *Deep Learning*. Adaptive computation and machine learning. MIT Press, 2016. Cited on p. 52, 57

[224] Krizhevsky, A., Sutskever, I., and Hinton, G. E. ImageNet classification with deep convolutional neural networks. *Communications of the ACM*, 60(6):84–90, May 2017. doi:10.1145/3065386. Cited on p. 52

[225] Medsker, L. and Jain, L. C. *Recurrent Neural Networks: Design and Applications*. CRC Press, December 1999. doi:10.1201/9781003040620. Cited on p. 53

[226] Rosenblatt, F. The perceptron: A probabilistic model for information storage and organization in the brain. *Psychological Review*, 65:386–408, 1958. doi:10.1037/h0042519. Cited on p. 53

[227] Hornik, K., Stinchcombe, M., and White, H. Multilayer feedforward networks are universal approximators. *Neural Networks*, 2(5):359–366, January 1989. doi:10.1016/0893-6080(89)90020-8. Cited on p. 54, 93

[228] Nielsen, M. A. *Neural Networks and Deep Learning*. Determination press, 2015. Cited on p. 54, 55, 56

[229] Srivastava, N., Hinton, G. E., Krizhevsky, A., Sutskever, I., and Salakhutdinov, R. Dropout: a simple way to prevent neural networks from overfitting. *Journal of Machine Learning Research*, 15(1):1929–1958, 2014. Cited on p. 57

[230] Dietterich, T. G. Ensemble Methods in Machine Learning. In *Multiple Classifier Systems*, Lecture Notes in Computer Science, pages 1–15, Berlin, Heidelberg, 2000. Springer. doi:10.1007/3-540-45014-9$_1$. Cited on p. 57

[231] Wilson, A. C., Roelofs, R., Stern, M., Srebro, N., and Recht, B. The marginal value of adaptive gradient methods in machine learning. In *Proceedings of the 31st International Conference on Neural Information Processing Systems*, NIPS'17, page 4151â4161, Red Hook, NY, USA, 2017. Curran Associates Inc. Cited on p. 57

[232] Chan, S.-K. and Heine, V. Spin density wave and soft phonon mode from nesting Fermi surfaces. *Journal of Physics F: Metal Physics*, 3(4):795–809, April 1973. doi:10.1088/0305-4608/3/4/022. Cited on p. 61

[233] Chen, C.-W., Choe, J., and Morosan, E. Charge density waves in strongly correlated electron systems. *Reports on Progress in Physics*, 79(8):084505, July 2016. doi:10.1088/0034-4885/79/8/084505. Cited on p. 61, 63

[234] Hughes, H. P. Structural distortion in $TiSe_2$ and related materials-a possible Jahn-Teller effect? *Journal of Physics C: Solid State Physics*, 10(11):L319–L323, June 1977. doi:10.1088/0022-3719/10/11/009. Cited on p. 62, 100, 112

[235] Whangbo, M. H. and Canadell, E. Analogies between the concepts of molecular chemistry and solid-state physics concerning structural instabilities. Electronic origin of the structural modulations in layered transition metal dichalcogenides. *Journal of the American Chemical Society*, 114(24):9587–9600, November 1992. doi:10.1021/ja00050a044. Cited on p. 62, 64, 100, 112

[236] Rossnagel, K. On the origin of charge-density waves in select layered transition-metal dichalcogenides. *Journal of Physics: Condensed Matter*, 23(21):213001, May 2011. doi:10.1088/0953-8984/23/21/213001. Cited on p. 62, 100, 112

[237] Cercellier, H., Monney, C., Clerc, F., Battaglia, C., Despont, L., Garnier, M. G., Beck, H., Aebi, P., Patthey, L., Berger, H., and Forró, L. Evidence for an Excitonic Insulator Phase in 1T-$TiSe_2$. *Physical Review Letters*, 99(14):146403, October 2007. doi:10.1103/PhysRevLett.99.146403. Cited on p. 62, 64, 100, 112

[238] Wilson, J. and Yoffe, A. The transition metal dichalcogenides discussion and interpretation of the observed optical, electrical and structural properties. *Advances*

in Physics, 18(73):193–335, May 1969. doi:10.1080/00018736900101307. Cited on p. 62

[239] Riekel, C. Structure refinement of $TiSe_2$ by neutron diffraction. *Journal of Solid State Chemistry France*, 17(4):389–392, January 1976. doi:10.1016/S0022-4596(76)80008-4. Cited on p. 63, 118

[240] Woo, K. C., Brown, F. C., McMillan, W. L., Miller, R. J., Schaffman, M. J., and Sears, M. P. Superlattice formation in titanium diselenide. *Physical Review B*, 14 (8):3242–3247, October 1976. doi:10.1103/PhysRevB.14.3242. Cited on p. 63, 100

[241] Di Salvo, F. J., Moncton, D. E., and Waszczak, J. V. Electronic properties and superlattice formation in the semimetal $TiSe_2$. *Physical Review B*, 14(10):4321–4328, November 1976. doi:10.1103/PhysRevB.14.4321. Cited on p. 63, 64, 100

[242] Holy, J. A., Woo, K. C., Klein, M. V., and Brown, F. C. Raman and infrared studies of superlattice formation in Ti Se 2. *Physical Review B*, 16(8):3628–3637, October 1977. doi:10.1103/PhysRevB.16.3628. Cited on p. 63, 65, 107

[243] Zunger, A. and Freeman, A. J. Band structure and lattice instability of $TiSe_2$. *Physical Review B*, 17(4):1839–1842, February 1978. doi:10.1103/PhysRevB.17.1839. Cited on p. 64

[244] Monney, C., Schwier, E. F., Garnier, M. G., Mariotti, N., Didiot, C., Cercellier, H., Marcus, J., Berger, H., Titov, A. N., Beck, H., and Aebi, P. Probing the exciton condensate phase in 1T-$TiSe_2$ with photoemission. *New Journal of Physics*, 12 (12):125019, December 2010. doi:10.1088/1367-2630/12/12/125019. Cited on p. 64, 100, 112

[245] Rossnagel, K., Kipp, L., and Skibowski, M. Charge-density-wave phase transition in 1 T-$TiSe_2$: Excitonic insulator versus band-type Jahn-Teller mechanism. *Physical Review B*, 65(23):235101, May 2002. doi:10.1103/PhysRevB.65.235101. Cited on p. 64, 100, 112

[246] Weber, F., Rosenkranz, S., Castellan, J.-P., Osborn, R., Karapetrov, G., Hott, R., Heid, R., Bohnen, K.-P., and Alatas, A. Electron-Phonon Coupling and the Soft

Phonon Mode in TiSe 2. *Physical Review Letters*, 107(26):266401, December 2011. doi:10.1103/PhysRevLett.107.266401. Cited on p. 64, 100

[247] Holt, M., Zschack, P., Hong, H., Chou, M. Y., and Chiang, T.-C. X-ray studies of phonon softening in $TiSe_2$. *Phys. Rev. Lett.*, 86:3799–3802, Apr 2001. doi:10.1103/PhysRevLett.86.3799. Cited on p. 64

[248] Kusmartseva, A. F., Sipos, B., Berger, H., Forró, L., and Tutiš, E. Pressure Induced Superconductivity in Pristine 1T-$TiSe_2$. *Phys. Rev. Lett.*, 103(23):236401, November 2009. doi:10.1103/PhysRevLett.103.236401. Cited on p. 64

[249] Morosan, E., Wagner, K. E., Zhao, L. L., Hor, Y., Williams, A. J., Tao, J., Zhu, Y., and Cava, R. J. Multiple electronic transitions and superconductivity in Pd_xTiSe_2. *Physical Review B*, 81(9):094524, March 2010. doi:10.1103/PhysRevB.81.094524. Cited on p. 64

[250] Morosan, E., Zandbergen, H. W., Dennis, B. S., Bos, J. W. G., Onose, Y., Klimczuk, T., Ramirez, A. P., Ong, N. P., and Cava, R. J. Superconductivity in Cu_xTiSe_2. *Nature Physics*, 2(8):544–550, August 2006. doi:10.1038/nphys360. Cited on p. 64

[251] Monney, C., Puppin, M., Nicholson, C. W., Hoesch, M., Chapman, R. T., Springate, E., Berger, H., Magrez, A., Cacho, C., Ernstorfer, R., and Wolf, M. Revealing the role of electrons and phonons in the ultrafast recovery of charge density wave correlations in 1 T-$TiSe_2$. *Physical Review B*, 94(16):165165, October 2016. doi:10.1103/PhysRevB.94.165165. Cited on p. 65, 66, 67, 100, 110

[252] Möhr-Vorobeva, E., Johnson, S. L., Beaud, P., Staub, U., De Souza, R., Milne, C., Ingold, G., Demsar, J., Schaefer, H., and Titov, A. Nonthermal Melting of a Charge Density Wave in $TiSe_2$. *Physical Review Letters*, 107(3):036403, July 2011. doi:10.1103/PhysRevLett.107.036403. Cited on p. 65, 90, 100, 111

[253] Burian, M., Porer, M., Mardegan, J. R. L., Esposito, V., Parchenko, S., Burganov, B., Gurung, N., Ramakrishnan, M., Scagnoli, V., Ueda, H., Francoual, S., Fabrizi, F., Tanaka, Y., Togashi, T., Kubota, Y., Yabashi, M., Rossnagel, K., Johnson, S. L., and Staub, U. Structural involvement in the melting of the charge density wave in 1T-$TiSe_2$. *Physical Review Research*, 3(1):013128, February 2021. doi:10.1103/PhysRevResearch.3.013128. Cited on p. 65, 67, 100, 110, 111

[254] Cheng, Y., Zong, A., Li, J., Xia, W., Duan, S., Zhao, W., Li, Y., Qi, F., Wu, J., Zhao, L., Zhu, P., Zou, X., Jiang, T., Guo, Y., Yang, L., Qian, D., Zhang, W., Kogar, A., Zuerch, M. W., Xiang, D., and Zhang, J. Light-induced dimension crossover dictated by excitonic correlations. *Nature Communications*, 13(1):963, December 2022. doi:10.1038/s41467-022-28309-5. Cited on p. 65, 100, 102, 111

[255] Otto, M. R., Pöhls, J.-H., René de Cotret, L. P., Stern, M. J., Sutton, M., and Siwick, B. J. Mechanisms of electron-phonon coupling unraveled in momentum and time: The case of soft phonons in $TiSe_2$. *Science Advances*, 7(20):eabf2810, May 2021. doi:10.1126/sciadv.abf2810. Cited on p. 65, 100, 103, 107

[256] Porer, M., Leierseder, U., Ménard, J.-M., Dachraoui, H., Mouchliadis, L., Perakis, I. E., Heinzmann, U., Demsar, J., Rossnagel, K., and Huber, R. Non-thermal separation of electronic and structural orders in a persisting charge density wave. *Nature Materials*, 13(9):857–861, September 2014. doi:10.1038/nmat4042. Cited on p. 65, 67, 100, 111

[257] Hedayat, H., Sayers, C. J., Bugini, D., Dallera, C., Wolverson, D., Batten, T., Karbassi, S., Friedemann, S., Cerullo, G., van Wezel, J., Clark, S. R., Carpene, E., and Da Como, E. Excitonic and lattice contributions to the charge density wave in 1 T-$TiSe_2$ revealed by a phonon bottleneck. *Physical Review Research*, 1(2):023029, September 2019. doi:10.1103/PhysRevResearch.1.023029. Cited on p. 65, 66, 67, 100, 103, 110, 111, 112, 113, 118

[258] Sugai, S., Murase, K., Uchida, S., and Tanaka, S. Raman studies of lattice dynamics in 1T-$TiSe_2$. *Solid State Communications*, 35(5):433–436, August 1980. doi:10.1016/0038-1098(80)90175-1. Cited on p. 65

[259] Van Wezel, J., Nahai-Williamson, P., and Saxena, S. S. Exciton-phonon-driven charge density wave in $TiSe_2$. *Physical Review B*, 81(16):165109, April 2010. doi:10.1103/PhysRevB.81.165109. Cited on p. 67, 100, 112

[260] Porer, M. *Ultrafast low-energy dynamics of strongly correlated systems*. PhD thesis, Universität Regensburg, Regensburg, 2014. Cited on p. 67

[261] Vampa, G., Hammond, T. J., Thiré, N., Schmidt, B. E., Légaré, F., McDonald, C. R., Brabec, T., and Corkum, P. B. Linking high harmonics from gases and

solids. *Nature*, 522(7557):462–464, June 2015. doi:10.1038/nature14517. Cited on p. 70, 73, 78

[262] Luu, T. T., Garg, M., Kruchinin, S. Y., Moulet, A., Hassan, M. T., and Goulielmakis, E. Extreme ultraviolet high-harmonic spectroscopy of solids. *Nature*, 521 (7553):498–502, May 2015. doi:10.1038/nature14456. Cited on p. 70, 71, 78

[263] Bauer, D. and Hansen, K. K. High-Harmonic Generation in Solids with and without Topological Edge States. *Physical Review Letters*, 120(17):177401, April 2018. doi:10.1103/PhysRevLett.120.177401. Cited on p. 70

[264] Silva, R. E. F., Jiménez-Galán, Á., Amorim, B., Smirnova, O., and Ivanov, M. Topological strong-field physics on sub-laser-cycle timescale. *Nature Photonics*, 13(12):849–854, December 2019. doi:10.1038/s41566-019-0516-1. Cited on p. 70

[265] Bai, Y., Fei, F., Wang, S., Li, N., Li, X., Song, F., Li, R., Xu, Z., and Liu, P. High-harmonic generation from topological surface states. *Nature Physics*, pages 1–5, November 2020. doi:10.1038/s41567-020-01052-8. Cited on p. 70, 78

[266] Liu, H., Guo, C., Vampa, G., Zhang, J. L., Sarmiento, T., Xiao, M., Bucksbaum, P. H., Vučković, J., Fan, S., and Reis, D. A. Enhanced high-harmonic generation from an all-dielectric metasurface. *Nature Physics*, 14(10):1006–1010, October 2018. doi:10.1038/s41567-018-0233-6. Cited on p. 70

[267] Gauthier, D., Kaassamani, S., Franz, D., Nicolas, R., Gomes, J.-T., Lavoute, L., Gaponov, D., Février, S., Jargot, G., Hanna, M., Boutu, W., and Merdji, H. Orbital angular momentum from semiconductor high-order harmonics. *Optics Letters*, 44 (3):546–549, February 2019. doi:10.1364/OL.44.000546. Cited on p. 70

[268] Imasaka, K., Kaji, T., Shimura, T., and Ashihara, S. Antenna-enhanced high harmonic generation in a wide-bandgap semiconductor ZnO. *Optics Express*, 26(16): 21364–21374, August 2018. doi:10.1364/OE.26.021364. Cited on p. 70

[269] Langer, F., Hohenleutner, M., Huttner, U., Koch, S. W., Kira, M., and Huber, R. Symmetry-controlled temporal structure of high-harmonic carrier fields from a bulk crystal. *Nature Photonics*, 11(4):227–231, April 2017. doi:10.1038/nphoton.2017.29. Cited on p. 70

[270] Gariepy, G., Leach, J., Kim, K. T., Hammond, T. J., Frumker, E., Boyd, R. W., and Corkum, P. B. Creating High-Harmonic Beams with Controlled Orbital Angular Momentum. *Physical Review Letters*, 113(15):153901, October 2014. doi:10.1103/PhysRevLett.113.153901. Cited on p. 70

[271] Kong, F., Zhang, C., Larocque, H., Bouchard, F., Li, Z., Taucer, M., Brown, G., Severino, S., Hammond, T. J., Karimi, E., and Corkum, P. B. Spin-constrained orbital-angular-momentum control in high-harmonic generation. *Physical Review Research*, 1(3):032008, October 2019. doi:10.1103/PhysRevResearch.1.032008. Cited on p. 70

[272] Pisanty, E., Machado, G. J., Vicuña-Hernández, V., Picón, A., Celi, A., Torres, J. P., and Lewenstein, M. Knotting fractional-order knots with the polarization state of light. *Nature Photonics*, 13(8):569–574, August 2019. doi:10.1038/s41566-019-0450-2. Cited on p. 70

[273] Ayuso, D., Neufeld, O., Ordonez, A. F., Decleva, P., Lerner, G., Cohen, O., Ivanov, M., and Smirnova, O. Synthetic chiral light for efficient control of chiral light–matter interaction. *Nature Photonics*, 13(12):866–871, December 2019. doi:10.1038/s41566-019-0531-2. Cited on p. 70

[274] Neufeld, O., Podolsky, D., and Cohen, O. Floquet group theory and its application to selection rules in harmonic generation. *Nature Communications*, 10(1):1–9, January 2019. doi:10.1038/s41467-018-07935-y. Cited on p. 70

[275] Zayko, S., Kfir, O., Bordo, E., Fleischer, A., Cohen, O., and Ropers, C. A dynamical symmetry triad in high-harmonic generation revealed by attosecond recollision control. *New Journal of Physics*, 22(5):053017, May 2020. doi:10.1088/1367-2630/ab82bd. Cited on p. 70

[276] Long, S., Becker, W., and McIver, J. K. Model calculations of polarization-dependent two-color high-harmonic generation. *Physical Review A*, 52(3):2262–2278, September 1995. doi:10.1103/PhysRevA.52.2262. Cited on p. 70

[277] Noguera, C. Polar oxide surfaces. *Journal of Physics: Condensed Matter*, 12(31): R367–R410, August 2000. doi:10.1088/0953-8984/12/31/201. Cited on p. 71, 75

[278] Yu, C., Zhang, X., Jiang, S., Cao, X., Yuan, G., Wu, T., Bai, L., and Lu, R. Dependence of high-order-harmonic generation on dipole moment in Si O 2 crystals. *Physical Review A*, 94(1):013846, July 2016. doi:10.1103/PhysRevA.94.013846. Cited on p. 71, 75, 76, 77

[279] Hu, J., Zhang, Z., Zhao, M., Qin, H., and Jiang, M. Room-temperature ferromagnetism in MgO nanocrystalline powders. *Applied Physics Letters*, 93(19):192503, November 2008. doi:10.1063/1.3021085. Cited on p. 71

[280] Singh, J. P. and Chae, K. H. D° Ferromagnetism of Magnesium Oxide. *Condensed Matter*, 2(4):36, December 2017. doi:10.3390/condmat2040036. Cited on p. 71, 75, 76, 77

[281] Luu, T. T. and Wörner, H. J. High-order harmonic generation in solids: A unifying approach. *Physical Review B*, 94(11):115164, September 2016. doi:10.1103/PhysRevB.94.115164. Cited on p. 73, 87

[282] Jia, G.-R., Wang, X.-Q., Du, T.-Y., Huang, X.-H., and Bian, X.-B. High-order harmonic generation from 2D periodic potentials in circularly and bichromatic circularly polarized laser fields. *The Journal of Chemical Physics*, 149(15):154304, October 2018. doi:10.1063/1.5051598. Cited on p. 74

[283] Goniakowski, J. and Noguera, C. Characteristics of Pd deposition on the MgO(111) surface. *Physical Review B*, 60(23):16120–16128, December 1999. doi:10.1103/PhysRevB.60.16120. Cited on p. 75, 76, 77

[284] Martínez-Boubeta, C., Beltrán, J. I., Balcells, Ll., Konstantinović, Z., Valencia, S., Schmitz, D., Arbiol, J., Estrade, S., Cornil, J., and Martínez, B. Ferromagnetism in transparent thin films of MgO. *Physical Review B*, 82(2):024405, July 2010. doi:10.1103/PhysRevB.82.024405. Cited on p. 75, 76

[285] Gallego, S., Beltrán, J. I., Cerdá, J., and Muñoz, M. C. Magnetism and half-metallicity at the O surfaces of ceramic oxides. *Journal of Physics: Condensed Matter*, 17(43):L451–L457, October 2005. doi:10.1088/0953-8984/17/43/L04. Cited on p. 76

[286] Roessler, D. M. and Walker, W. C. Optical Constants of Magnesium Oxide and Lithium Fluoride in the Far Ultraviolet*. *Journal of the Optical Society of America*, 57(6):835, June 1967. doi:10.1364/JOSA.57.000835. Cited on p. 76, 77

[287] Wang, J., Tu, Y., Yang, L., and Tolner, H. Theoretical investigation of the electronic structure and optical properties of zinc-doped magnesium oxide. *Journal of Computational Electronics*, 15(4):1521–1530, December 2016. doi:10.1007/s10825-016-0906-2. Cited on p. 76

[288] Palik, E. D. *Handbook of Optical Constants of Solids*. Academic Press, Orlando, 1985. doi:10.1016/C2009-0-20920-2. Cited on p. 77

[289] Gao, F., Hu, J., Yang, C., Zheng, Y., Qin, H., Sun, L., Kong, X., and Jiang, M. First-principles study of magnetism driven by intrinsic defects in MgO. *Solid State Communications*, 149(21):855–858, June 2009. doi:10.1016/j.ssc.2009.03.010. Cited on p. 77

[290] Johnson, P. D. Spin-polarized photoemission. *Reports on Progress in Physics*, 60(11):1217–1304, November 1997. doi:10.1088/0034-4885/60/11/002. Cited on p. 78

[291] Plötzing, M., Adam, R., Weier, C., Plucinski, L., Eich, S., Emmerich, S., Rollinger, M., Aeschlimann, M., Mathias, S., and Schneider, C. M. Spin-resolved photoelectron spectroscopy using femtosecond extreme ultraviolet light pulses from high-order harmonic generation. *Review of Scientific Instruments*, 87(4):043903, April 2016. doi:10.1063/1.4946782. Cited on p. 78

[292] Heinrich, A. J., Gupta, J. A., Lutz, C. P., and Eigler, D. M. Single-Atom Spin-Flip Spectroscopy. *Science*, 306(5695):466–469, October 2004. doi:10.1126/science.1101077. Cited on p. 78

[293] Bode, M., Heide, M., von Bergmann, K., Ferriani, P., Heinze, S., Bihlmayer, G., Kubetzka, A., Pietzsch, O., Blügel, S., and Wiesendanger, R. Chiral magnetic order at surfaces driven by inversion asymmetry. *Nature*, 447(7141):190–193, May 2007. doi:10.1038/nature05802. Cited on p. 78

[294] Wiesendanger, R. Spin mapping at the nanoscale and atomic scale. *Reviews of Modern Physics*, 81(4):1495–1550, November 2009. doi:10.1103/RevModPhys.81.1495. Cited on p. 78

[295] Woodruff, D. P. Quantitative Structural Studies Of Corundum and Rock-salt Oxide Surfaces. *Chemical Reviews*, 113(6):3863–3886, June 2013. doi:10.1021/cr3002998. Cited on p. 78

[296] Langer, F., Schmid, C. P., Schlauderer, S., Gmitra, M., Fabian, J., Nagler, P., Schüller, C., Korn, T., Hawkins, P. G., Steiner, J. T., Huttner, U., Koch, S. W., Kira, M., and Huber, R. Lightwave valleytronics in a monolayer of tungsten diselenide. *Nature*, 557(7703):76–80, May 2018. doi:10.1038/s41586-018-0013-6. Cited on p. 78

[297] Combescot, M. Optical Stark effect of the exciton. II. Polarization effects and exciton splitting. *Physical Review B*, 41(6):3517–3533, February 1990. doi:10.1103/PhysRevB.41.3517. Cited on p. 82

[298] Joffre, M., Hulin, D., Migus, A., and Combescot, M. Laser-Induced Exciton Splitting. *Physical Review Letters*, 62(1):74–77, January 1989. doi:10.1103/PhysRevLett.62.74. Cited on p. 82

[299] Tang, C. L. and Rabin, H. Selection Rules for Circularly Polarized Waves in Nonlinear Optics. *Physical Review B*, 3(12):4025–4034, June 1971. doi:10.1103/PhysRevB.3.4025. Cited on p. 87

[300] Biswas, S. and Baker, L. R. Extreme Ultraviolet Reflection–Absorption Spectroscopy: Probing Dynamics at Surfaces from a Molecular Perspective. *Accounts of Chemical Research*, 55(6):893–903, March 2022. doi:10.1021/acs.accounts.1c00765. Cited on p. 90

[301] Huppert, M., Jordan, I., and Wörner, H. J. Attosecond beamline with actively stabilized and spatially separated beam paths. *Review of Scientific Instruments*, 86 (12):123106, December 2015. doi:10.1063/1.4937623. Cited on p. 90

[302] Wu, J., Cha, H., Du, T., Dong, Y., Xu, W., Lin, C.-T., and Durrant, J. R. A Comparison of Charge Carrier Dynamics in Organic and Perovskite Solar Cells. *Advanced Materials*, 34(2):2101833, 2022. doi:10.1002/adma.202101833. Cited on p. 90

[303] Uprety, P., Subedi, I., Junda, M. M., Collins, R. W., and Podraza, N. J. Photogenerated Carrier Transport Properties in Silicon Photovoltaics. *Scientific Reports*, 9 (1):19015, December 2019. doi:10.1038/s41598-019-55173-z. Cited on p. 90

[304] Volkov, M., Pupeikis, J., Phillips, C. R., Schlaepfer, F., Gallmann, L., and Keller, U. Reduction of laser-intensity-correlated noise in high-harmonic generation. *Optics Express*, 27(6):7886–7895, March 2019. doi:10.1364/OE.27.007886. Cited on p. 90, 132

[305] Faccialà, D., Toulson, B. W., and Gessner, O. Removal of correlated background in a high-order harmonic transient absorption spectra with principal component regression. *Optics Express*, 29(22):35135, October 2021. doi:10.1364/OE.435008. Cited on p. 90, 93

[306] Willems, F., Schmising, C. v. K., Strüber, C., Schick, D., Engel, D. W., Dewhurst, J. K., Elliott, P., Sharma, S., and Eisebitt, S. Optical inter-site spin transfer probed by energy and spin-resolved transient absorption spectroscopy. *Nature Communications*, 11(1):1–7, February 2020. doi:10.1038/s41467-020-14691-5. Cited on p. 90

[307] Johnsen, P. C., Ryan, S. A., Gentry, C., Grafov, A., Kapteyn, H., and Murnane, M. A beamline for ultrafast extreme ultraviolet magneto-optical spectroscopy in reflection near the shot noise limit. *Review of Scientific Instruments*, 94(3):033001, 03 2023. doi:10.1063/5.0127119. Cited on p. 90

[308] Heldt, T., Dubois, J., Birk, P., Borisova, G. D., Lando, G. M., Ott, C., and Pfeifer, T. Attosecond Real-Time Observation of Recolliding Electron Trajectories in Helium at Low Laser Intensities. *Physical Review Letters*, 130(18):183201, May 2023. doi:10.1103/PhysRevLett.130.183201. Cited on p. 90

[309] Camper, A., Park, H., Hageman, S. J., Smith, G., Auguste, T., Agostini, P., and DiMauro, L. F. High relative-phase precision beam duplicator for mid-infrared femtosecond pulses. *Optics Letters*, 44(22):5465, November 2019. doi:10.1364/OL.44.005465. Cited on p. 90

[310] Abel, J. J., Wiesner, F., Nathanael, J., Reinhard, J., Wünsche, M., Schmidl, G., Gawlik, A., Hübner, U., Plentz, J., Rödel, C., Paulus, G. G., and Fuchs, S. Absolute

EUV reflectivity measurements using a broadband high-harmonic source and an in situ single exposure reference scheme. *Optics Express*, 30(20):35671, September 2022. doi:10.1364/OE.463216. Cited on p. 90

[311] Heinrich, T., Chang, H.-T., Zayko, S., Rossnagel, K., Sivis, M., and Ropers, C. Electronic and Structural Fingerprints of Charge-Density-Wave Excitations in Extreme Ultraviolet Transient Absorption Spectroscopy. *Physical Review X*, 13(2): 021033, June 2023. doi:10.1103/PhysRevX.13.021033. Cited on p. 91, 134

[312] Cawley, G. C. and Talbot, N. L. C. On Over-fittingg inModel Selectionn andSubsequent Selection Biass inPerformance Evaluation. page 29, 2010. Cited on p. 93

[313] Chollet, F. et al. Keras. `https://keras.io`, 2015. Cited on p. 93

[314] Heinrich, T. Referencing-neural-network. `https://github.com/tobheinrich/referencing-neural-network`, 2022. Cited on p. 93

[315] Nair, V. and Hinton, G. E. Rectified Linear Units Improve Restricted Boltzmann Machines. In *Proceedings of the Twenty Seventh International Conference on Artificial Intelligence and Statistics*, pages 807–814, 2010. Cited on p. 93

[316] Glorot, X., Bordes, A., and Bengio, Y. Deep Sparse Rectifier Neural Networks. In *Proceedings of the Fourteenth International Conference on Artificial Intelligence and Statistics*, Proceedings of Machine Learning Research, pages 315–323, April 2011. Cited on p. 94

[317] Shirish Keskar, N., Mudigere, D., Nocedal, J., Smelyanskiy, M., and Tang, P. T. P. On Large-Batch Training for Deep Learning: Generalization Gap and Sharp Minima. *arXiv e-prints*, September 2016. doi:10.48550/arXiv.1609.04836. Cited on p. 94

[318] Genty, G., Salmela, L., Dudley, J. M., Brunner, D., Kokhanovskiy, A., Kobtsev, S., and Turitsyn, S. K. Machine learning and applications in ultrafast photonics. *Nature Photonics*, 15(2):91–101, February 2021. doi:10.1038/s41566-020-00716-4. Cited on p. 97

[319] Chen, Z., Andrejevic, N., Drucker, N. C., Nguyen, T., Xian, R. P., Smidt, T., Wang, Y., Ernstorfer, R., Tennant, D. A., Chan, M., and Li, M. Machine learning on

neutron and x-ray scattering and spectroscopies. *Chemical Physics Reviews*, 2(3): 031301, July 2021. doi:10.1063/5.0049111. Cited on p. 97

[320] Kogar, A., Rak, M. S., Vig, S., Husain, A. A., Flicker, F., Joe, Y. I., Venema, L., MacDougall, G. J., Chiang, T. C., Fradkin, E., van Wezel, J., and Abbamonte, P. Signatures of exciton condensation in a transition metal dichalcogenide. *Science*, 358(6368):1314–1317, December 2017. doi:10.1126/science.aam6432. Cited on p. 100, 112

[321] Huber, M., Lin, Y., Dale, N., Sailus, R., Tongay, S., Kaindl, R. A., and Lanzara, A. Mapping the dispersion of the occupied and unoccupied band structure in photoexcited 1T-TiSe2. *Journal of Physics and Chemistry of Solids*, 168:110740, 2022. doi:10.1016/j.jpcs.2022.110740. Cited on p. 100

[322] Karam, T. E., Hu, J., and Blake, G. A. Strongly Coupled Electron–Phonon Dynamics in Few-Layer $TiSe_2$ Exfoliates. *ACS Photonics*, 5(4):1228–1234, April 2018. doi:10.1021/acsphotonics.7b00878. Cited on p. 100

[323] Duan, S., Cheng, Y., Xia, W., Yang, Y., Xu, C., Qi, F., Huang, C., Tang, T., Guo, Y., Luo, W., Qian, D., Xiang, D., Zhang, J., and Zhang, W. Optical manipulation of electronic dimensionality in a quantum material. *Nature*, 595(7866):239–244, July 2021. doi:10.1038/s41586-021-03643-8. Cited on p. 100

[324] Hedayat, H., Sayers, C. J., Ceraso, A., van Wezel, J., Clark, S. R., Dallera, C., Cerullo, G., Da Como, E., and Carpene, E. Investigation of the non-equilibrium state of strongly correlated materials by complementary ultrafast spectroscopy techniques. *New Journal of Physics*, 23(3):033025, March 2021. doi:10.1088/1367-2630/abe272. Cited on p. 100, 107

[325] Heinrich, T., Chang, H.-T., Zayko, S., Sivis, M., and Ropers, C. High-sensitivity extreme-ultraviolet transient absorption spectroscopy enabled by machine learning. *arXiv e-prints*, May 2023. doi:10.48550/arXiv.2305.02236. Cited on p. 101, 102, 116

[326] Shu, G.-J., Zhou, Y., Kao, M.-Y., Klingshirn, C. J., Huang, M. R. S., Huang, Y.-L., Liang, Y., Kuo, W. C. H., and Liou, S.-C. Investigation of the π plasmon and plasmon-exciton coupling in titanium diselenide ($TiSe_2$) by momentum-resolved

electron energy loss spectroscopy. *Applied Physics Letters*, 114(20):202103, May 2019. doi:10.1063/1.5097023. Cited on p. 102

[327] Connerade, J. P., Esteva, J. M., and Karnatak, R. C., editors. *Giant Resonances in Atoms, Molecules, and Solids*, volume 151 of *NATO ASI Series*. Springer US, Boston, MA, 1987. doi:10.1007/978-1-4899-2004-1. Cited on p. 102

[328] Amusia, M. Y. and Connerade, J.-P. The theory of collective motion probed by light. *Reports on Progress in Physics*, 63(1):41–70, January 2000. doi:10.1088/0034-4885/63/1/202. Cited on p. 102, 112

[329] Schumacher, Z., Sato, S., Neb, S., Niedermayr, A., Gallmann, L., Rubio, A., and Keller, U. Ultrafast electron localization and screening in a transition metal dichalcogenide. *Proceedings of the National Academy of Sciences*, 120(15): e2221725120, 2023. doi:10.1073/pnas.2221725120. Cited on p. 102

[330] Chang, H.-T., Guggenmos, A., Cushing, S. K., Cui, Y., Din, N. U., Acharya, S. R., Porter, I. J., Kleineberg, U., Turkowski, V., Rahman, T. S., Neumark, D. M., and Leone, S. R. Electron thermalization and relaxation in laser-heated nickel by few-femtosecond core-level transient absorption spectroscopy. *Physical Review B*, 103 (6):064305, February 2021. doi:10.1103/PhysRevB.103.064305. Cited on p. 103, 104

[331] Bévillon, E., Colombier, J. P., Recoules, V., and Stoian, R. Free-electron properties of metals under ultrafast laser-induced electron-phonon nonequilibrium: A first-principles study. *Physical Review B*, 89(11):115117, March 2014. doi:10.1103/PhysRevB.89.115117. Cited on p. 103

[332] Schultze, M., Ramasesha, K., Pemmaraju, C. D., Sato, S. A., Whitmore, D., Gandman, A., Prell, J. S., Borja, L. J., Prendergast, D., Yabana, K., Neumark, D. M., and Leone, S. R. Attosecond band-gap dynamics in silicon. *Science*, 346(6215): 1348–1352, December 2014. doi:10.1126/science.1260311. Cited on p. 103, 114

[333] Cushing, S. K., Zürch, M., Kraus, P. M., Carneiro, L. M., Lee, A., Chang, H.-T., Kaplan, C. J., and Leone, S. R. Hot phonon and carrier relaxation in Si(100) determined by transient extreme ultraviolet spectroscopy. *Structural Dynamics*, 5 (5):054302, September 2018. doi:10.1063/1.5038015. Cited on p. 104

[334] Craven, R., Di Salvo, F., and Hsu, F. Mechanisms for the 200 K transition in $TiSe_2$: A measurement of the specific heat. *Solid State Communications*, 25(1): 39–42, January 1978. doi:10.1016/0038-1098(78)91165-1. Cited on p. 106, 118

[335] Bianco, R., Calandra, M., and Mauri, F. Electronic and vibrational properties of $TiSe_2$ in the charge-density-wave phase from first principles. *Physical Review B*, 92 (9):094107, September 2015. doi:10.1103/PhysRevB.92.094107. Cited on p. 109, 121

[336] Wang, J., Zheng, H., Xu, G., Sun, L., Hu, D., Lu, Z., Liu, L., Zheng, J., Tao, C., and Jiao, L. Controlled Synthesis of Two-Dimensional 1T-$TiSe_2$ with Charge Density Wave Transition by Chemical Vapor Transport. *Journal of the American Chemical Society*, 138(50):16216–16219, December 2016. doi:10.1021/jacs.6b10414. Cited on p. 115

[337] Igarashi, H., Makida, A., Ito, M., and Sekikawa, T. Pulse compression of phase-matched high harmonic pulses from a time-delay compensated monochromator. *Opt. Express*, 20(4):3725–3732, Feb 2012. doi:10.1364/OE.20.003725. Cited on p. 116

[338] Bayliss, S. C. and Liang, W. Y. Reflectivity, joint density of states and band structure of group IVb transition-metal dichalcogenides. *Journal of Physics C: Solid State Physics*, 18(17):3327–3335, June 1985. doi:10.1088/0022-3719/18/17/010. Cited on p. 117

[339] Aryasetiawan, F., Gunnarsson, O., Knupfer, M., and Fink, J. Local-field effects in NiO and Ni. *Physical Review B*, 50(11):7311–7321, September 1994. doi:10.1103/PhysRevB.50.7311. Cited on p. 121

[340] Persson, K. Materials Data on $TiSe_2$ (SG:164) by Materials Project. February 2016. doi:10.17188/1197256. Cited on p. 121

[341] Sato, S. A., Shinohara, Y., Otobe, T., and Yabana, K. Dielectric response of laser-excited silicon at finite electron temperature. *Physical Review B*, 90(17):174303, November 2014. doi:10.1103/PhysRevB.90.174303. Cited on p. 121

[342] Tancogne-Dejean, N., Mücke, O. D., Kärtner, F. X., and Rubio, A. Ellipticity dependence of high-harmonic generation in solids originating from coupled intraband and interband dynamics. *Nature Communications*, 8(1):745, December 2017. doi:10.1038/s41467-017-00764-5. Cited on p. 124

[343] Fano, U. Spin Orientation of Photoelectrons Ejected by Circularly Polarized Light. *Physical Review*, 178(1):131–136, February 1969. doi:10.1103/PhysRev.178.131. Cited on p. 125

[344] Liu, Y., Bian, G., Miller, T., and Chiang, T.-C. Visualizing Electronic Chirality and Berry Phases in Graphene Systems Using Photoemission with Circularly Polarized Light. *Physical Review Letters*, 107(16):166803, October 2011. doi:10.1103/PhysRevLett.107.166803. Cited on p. 125

[345] Sánchez-Barriga, J., Varykhalov, A., Braun, J., Xu, S.-Y., Alidoust, N., Kornilov, O., Minár, J., Hummer, K., Springholz, G., Bauer, G., Schumann, R., Yashina, L. V., Ebert, H., Hasan, M. Z., and Rader, O. Photoemission of Bi_2Se_3 with circularly polarized light: Probe of spin polarization or means for spin manipulation? *Physical Review X*, 4(1):011046, March 2014. doi:10.1103/PhysRevX.4.011046. Cited on p. 125

[346] Liu, Y., Gao, Y., Zhang, S., He, J., Yu, J., and Liu, Z. Valleytronics in transition metal dichalcogenides materials. *Nano Research*, 12(11):2695–2711, November 2019. doi:10.1007/s12274-019-2497-2. Cited on p. 130

[347] Mak, K. F., He, K., Shan, J., and Heinz, T. F. Control of valley polarization in monolayer MoS2 by optical helicity. *Nature Nanotechnology*, 7(8):494–498, August 2012. doi:10.1038/nnano.2012.96. Cited on p. 130

[348] Tyulnev, I., Poborska, J., Jiménez-Galán, Á., Vamos, L., Smirnova, O., Ivanov, M., and Biegert, J. Polarization-Shaped Strong Field Control over Valley Polarization with Mid-IR Light. *arXiv e-prints*, September 2022. doi:10.48550/arXiv.2209.04928. Cited on p. 130

[349] Tyulnev, I., Jiménez-Galán, Á., Poborska, J., Vamos, L., Silva, R. F., Russell, S. J., Tani, F., Smirnova, O., Ivanov, M., and Biegert, J. Valleytronics in bulk MoS2

by optical control of parity and time symmetries. *arXiv e-prints*, February 2023. doi:10.48550/arXiv.2302.12564. Cited on p. 130

[350] Mrudul, M. S., Jiménez-Galán, Á., Ivanov, M., and Dixit, G. Light-induced valleytronics in pristine graphene. *Optica*, 8(3):422–427, March 2021. doi:10.1364/OPTICA.418152. Cited on p. 130

[351] He, Y.-L., Guo, J., Gao, F.-Y., and Liu, X.-S. Dynamical symmetry and valley-selective circularly polarized high-harmonic generation in monolayer molybdenum disulfide. *Physical Review B*, 105(2):024305, January 2022. doi:10.1103/PhysRevB.105.024305. Cited on p. 130

[352] Porr, B., Daryanavard, S., Bohollo, L. M., Cowan, H., Porr, B., and Dahiya, R. Real-time noise cancellation with Deep Learning. *arXiv e-prints*, September 2022. doi:10.48550/arXiv.2011.03466. Cited on p. 132

[353] Zhang, H. and Wang, D. A Deep Learning Method to Multi-Channel Active Noise Control. In *Interspeech 2021*, pages 681–685. ISCA, August 2021. doi:10.21437/Interspeech.2021-1512. Cited on p. 132

[354] Cha, Y.-J., Mostafavi, A., and Benipal, S. S. DNoiseNet: Deep learning-based feedback active noise control in various noisy environments. *Engineering Applications of Artificial Intelligence*, 121:105971, May 2023. doi:10.1016/j.engappai.2023.105971. Cited on p. 132

[355] Hu, T. C., Wu, Q., Wang, Z. X., Shi, L. Y., Liu, Q. M., Yue, L., Zhang, S. J., Li, R. S., Zhou, X. Y., Xu, S. X., Wu, D., Dong, T., and Wang, N. L. Optical spectroscopy and ultrafast pump-probe study of the structural phase transition in 1 T′-$TaTe_2$. *Physical Review B*, 105(7):075113, February 2022. doi:10.1103/PhysRevB.105.075113. Cited on p. 133

[356] Siddiqui, K. M., Durham, D. B., Cropp, F., Ophus, C., Rajpurohit, S., Zhu, Y., Carlström, J. D., Stavrakas, C., Mao, Z., Raja, A., Musumeci, P., Tan, L. Z., Minor, A. M., Filippetto, D., and Kaindl, R. A. Ultrafast optical melting of trimer superstructure in layered 1T'-$TaTe_2$. *Communications Physics*, 4(1):1–7, July 2021. doi:10.1038/s42005-021-00650-z. Cited on p. 133

Author Contributions

This chapter describes the specific contributions of the author in the publications that constitute chapters 6, 7 and 8. The cumulative thesis comprises the following articles:

(1) Tobias Heinrich, Marco Taucer, Ofer Kfir, P. B. Corkum, André Staudte, Claus Ropers, and Murat Sivis. "Chiral high-harmonic generation and spectroscopy on solid surfaces using polarization-tailored strong fields", Nat Commun, **12**, 3723 (2021).

(2) Tobias Gutberlet, Hung-Tzu Chang, Sergey Zayko, Murat Sivis, and Claus Ropers. "High-sensitivity extreme-ultraviolet transient absorption spectroscopy enabled by machine learning", Optics Express 31, 39757-39764 (2023).

(3) Tobias Heinrich, Hung-Tzu Chang, Sergey Zayko, Kai Rossnagel, Murat Sivis, and Claus Ropers."Electronic and structural fingerprints of charge density wave excitations in extreme ultraviolet transient absorption spectroscopy", Phys. Rev. X,**13**, 021033 (2023).

These publications present original work by the author (T.G.) concerning the design, setup and conduction of all experiments in (1),(2) and (3), as well as the analysis of the collected data unless mentioned below. An exception is publication (1), which constitutes of experimental work done in a collaboration of M.S., M.T. and T.G. with contributions of O.K.. M.S. conceived and designed the experiment with contributions from M.T. and O.K. The density functional theory calculations in (3) were conducted by H-T. C. with input from T.G. and evaluated by T.G.. The manuscripts (2) and (3) were written by T.G., H-T. C. and C.R. and (1) was written by T.G., M.T. and M.S.. All authors discussed the results of the respective publications.

Danksagung

An dieser Stelle möchte ich einmal allen Personen danke sagen, die mich auf dem Weg zur Promotion unterstützt haben.

Zuallererst danke ich meinem Doktorvater Prof. Dr. Claus Ropers, mir diese Arbeit ermöglicht zu haben. Ich bedanke mich für das entgegengebrachte Vertrauen und die Freiheit bei der Umsetzung meiner Ideen.

Weiterhin danke ich meinem Betreuungsausschuss, bestehend aus Prof. Dr. Stefan Mathias und PD Dr. Salvatore Manmana, für das Feedback und die vielen konstruktiven Diskussionen. Prof. Dr. Stefan Mathias möchte ich darüber hinaus für die freundliche Übernahme des Korreferats danken.

Während meiner Promotion und bereits davor habe ich Methoden, experimentelles Arbeiten und vieles mehr von meinen "Postdoc Mentoren" gelernt. An dieser Stelle möchte ich Dr. Hung-Tzu Chang, Dr. Ofer Kfir, Dr. Murat Sivis und Dr. Sergey Zayko für die Zeit im Labor und am Whiteboard danken. Außerdem gebührt Dank der gesamten Arbeitsgruppe für die freundliche Atmosphäre und Unterstützung.

Den langen Weg zur Promotion haben mich meine Freunde aus dem ersten Semester begleitet. Ich möchte mich bei euch für die vielen tollen Stunden und die Unterstützung während des Studiums bedanken.

Außerordentlicher Dank gilt meinen Eltern, die mir dieses Studium ermöglicht haben. Ich danke euch, dass ihr mich immer bei meinen Entscheidungen unterstützt und motiviert habt.

Nicht zuletzt gilt ganz besonderer Dank meiner geliebten Frau Marie. Als emotionale Stütze und auch fachlich hast du maßgeblich zum Gelingen dieser Arbeit beigetragen.